Materials Today Chemistry 27 (2023) 101238

Contents lists available at ScienceDirect

Materials Today Chemistry

journal homepage: www.journals.elsevier.com/materials-today-chemistry/

Current progresses in two-dimensional MXene-based framework: prospects from superficial synthesis to energy conversion and storage applications

Zeeshan Ajmal [a], Abdul Qadeer [b], Ubaid Khan [c], Muhammad Bilal Hussain [d], Muhammad Irfan [e], Rashid Mehmood [f], Muhammad Abid [g], Ridha Djellabi [h], Anuj Kumar [i], Hamid Ali [j], A. Kalam [k, l], A.G. Al-Sehemi [k, l], H. Algarni [k, m], Yas Al-Hadeethi [n, o], Jin Qian [a, **], Asif Hayat [p, q, *], Huaqiang Zeng [a, ***]

[a] School of Chemistry and Chemical Engineering, Northwestern Polytechnical University, Xian, China
[b] State Key Laboratory of Environmental Criteria and Risk Assessment, National Engineering Laboratory for Lake Pollution Control and Ecological Restoration, Chinese Research Academy of Environmental Sciences, 10012, Beijing, China
[c] Electronic Materials Research Laboratory, School of Electronic Science and Engineering, Xi'an Jiaotong University, Xi'an 710049, Shaanxi, China
[d] School of Energy and Power Engineering, Shandong University, Jinan 250061, China
[e] School of Environmental Science and Engineering, Tianjin University, Tianjin, 300354, People's Republic of China
[f] Institute of Chemical Sciences, Bahaudin Zakariya University, Multan, Pakistan
[g] Department of Ocean Science and Engineering, Southern University of Science and Technology, Shenzhen, China
[h] Department of Chemical Engineering, Universitat Rovira I Virgili, 43007, Tarragona, Spain
[i] Nanotechnology Laboratory, Department of Chemistry, GLA, University, Mathura, Uttar Pradesh, 281406, India
[j] Multiscale Computational Materials Facility, Key Laboratory of Eco-Materials Advanced Technology, College of Materials Science and Engineering, Fuzhou University, Fuzhou 350100, China
[k] Research Center for Advanced Materials Science (RCAMS), King Khalid University, P.O. Box 9004, Abha, 61413, Saudi Arabia
[l] Department of Chemistry, College of Science, King Khalid University, P.O. Box 9004, Abha 61413, Saudi Arabia
[m] Department of Physics, Faculty of Science, King Khalid University, P.O. Box 9004, Abha 61413, Saudi Arabia
[n] Department of Physics, Faculty of Science, King Abdulaziz University, Jeddah 21589, Saudi Arabia
[o] Lithography in Devices Fabirication Research Group, Deanship of Scientific Research, King Abdulaziz University, Jeddah 21589, Saudi Arabia
[p] College of Chemistry and Life Sciences, Zhejiang Normal University, Jinhua 321004, Zhejiang PR, China
[q] College of Geography and Environmental Sciences, Zhejiang Normal University, Jinhua, 321004, China

ARTICLE INFO

Article history:
Received 1 July 2022
Received in revised form
24 September 2022
Accepted 5 October 2022
Available online xxx

Keywords:
2D MXenes
Synthesis strategies
Different properties
Morphological aspects
Distinctive composition
Potential applications

ABSTRACT

MXenes are regarded as a type of two-dimensional (2D) inorganic material, mainly comprising a number of transition metal carbides, nitrides, or carbonitrides atomic planes. Nevertheless, the scientific community is continuously interested in exploring and structuring the engineered-based multifunctional material for numerous applications. The MXenes-based materials in this context, have emerged as highly active compounds owing to their superior surface area, substantial interlayer spacing, highly reactive surface-active sites and surface functional group, even though, recent studies have shown significant scientific and theoretical progress related to enormous prospects in MXenes, chemical nature, robust electrochemistry and high hydrophilicity of MXenes. The role of MXenes in all kinds of strategies is still in an upgrading phase for their further improvement, and is not sufficiently summarized in the literature now. To begin with this, herein, present review article is intended to critically discuss the diversity of MXenes with respect to different composition, formulation, plasmonic, complexation, and numerous geometric and morphological aspects, along with novel construction strategies to improve their surface characteristics in all aforesaid multidimensional applications. Following that, in terms of broadening the application, this review article is envisaged to endorse the use of MXenes and their hybrid configuration in a series of emerging environmental decontamination via adsorption, photodegradation, photocatalytic fuel production via hydrogen evolution, CO_2 reduction, electrocatalytic sensing, along with membrane

* Corresponding author.
** Corresponding author.
*** Corresponding author.
E-mail addresses: qianjin@nwpu.edu.cn (J. Qian), asifncp11@yahoo.com (A. Hayat), hqzeng@nwpu.edu.cn (H. Zeng).

https://doi.org/10.1016/j.mtchem.2022.101238

distillation and energy storage. In addition, comprehensive information about existing obstacles and future perspectives have been addressed. Finally, an overview is succinctly summarized and discussed regarding the emerging prospects of MXenes for their potential uses in numerous research fields. At the end, it is anticipated that this review article will pave the way for the effective use of MXenes in different fields of environmental remediation, energy conversion, storage and biomedical applications as an innovative, reliable, and multifunctional material.

1. Introduction

Recently, 2D materials (graphene and other different kinds of layered materials) have received substantial research attention due to their outstanding optoelectronic and astonishing electrochemical characteristics [1–19]. The integration of 2D layered materials for improving activities of many conventional devices has been demonstrated as a most auspicious way. The related devices include photodetectors, photothermal therapies, rechargeable lithium-ion batteries, solar steam, and fuel production [20–34]. Amongst all different 2D materials, the phosphorene, MoS_2 and graphene, along with their derivatives are more widely explored [35,36]. Nevertheless, a comprehensive overview and understanding regarding the potential use of MXenes in a wide range of research applications is still missing, particularly in terms of their process integration, mass production, and overall properties [37–41]. Belonging to the family of 2D layered structures, the MXenes were basically discovered more than 10 years ago in 2011, but they are still at the initial stage of understanding, and not fully investigated till now (Fig. 2) [3,42,43]. This might be due to its limited preparation routes, as well as the use of hazardous hydrofluoric acid over a longer period. The ongoing research mainly related to the diverse applications of MXenes has been diverted into a new era after the discovery of alternate LiF salt precursor in 2014, which further leads to the fabrication and discovery of a novel MXene with unique characteristics by expanding their ultimate applications in a wide range of scientific fields. Recently, MXenes mainly consisting of layered transition metal nitride, carbides, and carbonitrides have received enormous research interest in the field of material science along with appearing as a novel class of 2D-based graphene-like carbon materials [42,44–55]. The MXenes have a general chemical formula $M_{n+1}X_nT_x$ ($n = 1, 2,$ or 3), where M represents early d-block transition metals (e.g. Ta, Hf, Ti, Mo, Nb, Sc, Zr, Cr, V, and W), X represents carbon (C) and/or nitrogen (N), and Tx denotes surface groups such as ^{-}O, ^{-}OH, and ^{-}F [56]. Gogotsi et al. firstly discovered the titanium (III) carbide ($Ti_3C_2T_x$) based MXene in 2011 [57]. After that, a wide variety of MXene derivatives have been prepared and reported till now [58]. They include V_2CT_x [59], $Ti_3C_2T_x$ [60], Zr_3C_2 [61], Lu_2C [62], $Nb_4C_3T_x$ [63], $Ti_4N_3T_x$ [64], along with some of the potential MXenes reported via theoretical calculation [61,65].

Among all the investigated MXenes, the titanium-based $Ti_3C_2T_x$ and Ti_2CT_x have been widely explored especially for environmental decontamination related to their non-toxicity and elemental abundance [66]. The use of MXenes has received considerable interest in numerous applications, because of rigorous chemistry and inimitable combination of excellent properties. These types of outstanding properties included superior surface area characteristics, which is related to exceptional 2D layered morphology, elemental configuration tenability, ultralarge interlayer spacing, ample surface active sites, exceptional biocompatibility, hydrophilic properties, superior thermal mechanical stability, outstanding electrical conductivity ($\approx$6000–8000 S/cm), more surface functional groups (^{-}OH and ^{-}O), configuration, as well as environmental friendly nature [67]. Such kind of well-defined characteristic ultimately leads to the potential use of MXenes in such a wide spectrum of applications such as fuel cells [68], water desalination [69], photocatalysis [70], gas sensors [71], electromagnetic interference shielding [72], hydrogen storage [73], lithium-ion batteries [74], supercapacitors [75], semiconductors [76], and environmental remediation [66]. The alternative utmost characteristic of MXenes is related to its excellent affinity towards metal ions owing to their vanadium (V), titanium (Ti) element, which has the enough capability for the adsorption of Hg [77], Cu [78], Cr [79] and Pb [80], radionuclides [81], and organic dyes (Methyl green, rhodium B, acid blue 80 and Methylene blue [82]. In addition to offering ample active sites for the direct ion exchange process [83], the surface functional groups in MXenes-based material encompass sufficient ability to adsorb the radionuclides and immobilize via electrostatic and chemical attraction [84]. Owing to the outstanding thermal and chemical stability, the MXenes-based materials show considerable confrontation against strong radiations, which is essential for the material to be applied as an effective hazardous pollutant adsorbent for the treatment of contaminated environments [85]. For that aim, exfoliation and intercalation of MXenes via suitable intercalants could effectively tune the interlayer spacing of the layer-structured of MXenes [86], in an efficient manners towards adsorption, photocatalysis, energy conversion (HER, OER and CO_2 reduction), energy storage (battery application) and bacterial disinfection applications. The wide layer d-spacing is an important aspect, which has greater impact on ion exchange capacity as the surface interface interaction capability of functional group strongly increases through wide layer spacing strategy and thus leads to the enhanced capability of MXenes as a robust and multifunctional compound in all kinds of applications [87–89]. Indeed, Mxenes are considered as a cost-effective material owing to their scalable synthesis on a large scale via wet chemical method and its non-toxic nature ascribable to their non-toxic element constituents (nitrogen [N], carbon [C] and titanium [Ti]) [89–91]. Such kind of remarkable properties demonstrates MXenes as the most promising material in environmental remediation, electrocatalytic sensors, energy conversion, storage and bacterial disinfection. Therefore, a timely critical review specifically focusing onto the state-of-the-art progress of the rational design modulation and its further widespread applications is expected to provide up-to-date milestones and information in the history of this material by promoting their (MXenes) application in a wide variety of research fields [92–94]. Thus, this review article is designed to provide a concise description regarding the recent advancements in the structural composition and rational design modulation of 2D MXenes as a robust and multifunctional compound along with their potential practical applications in a diverse range of environmental remediation via adsorption, photocatalysis, electrocatalytic sensing, energy conversion, storage and antibacterial field (Fig. 1). For that purpose, in the first section, we will begin with discussing the structural properties, intercalation/

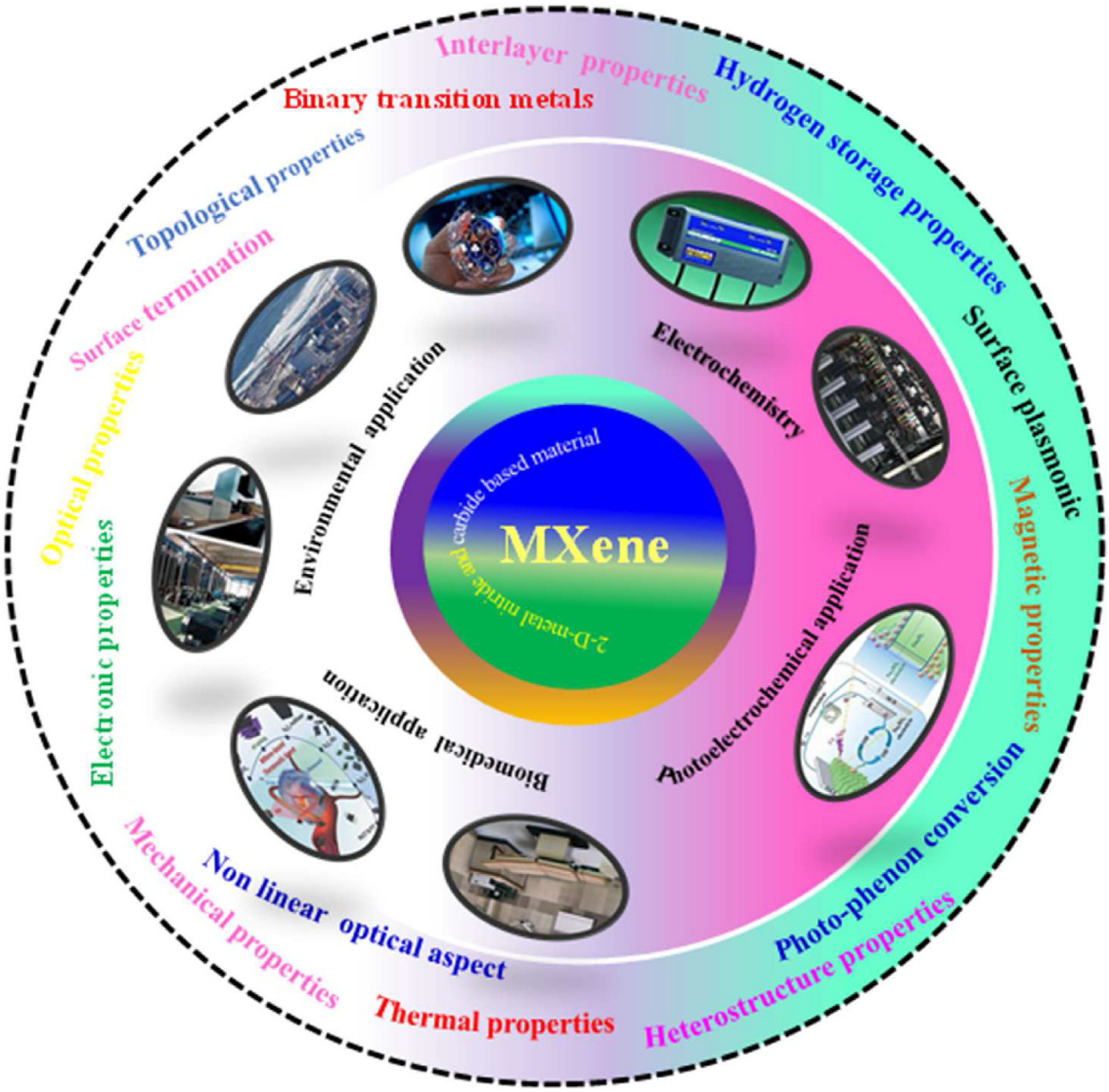

Fig. 1. Graphical representation of MXenes uses in a wide range of research field.

delamination and perspective tuning of MXenes for said applications. Thereafter, we will provide a brief overview regarding the existing contests in using MXenes-based materials for overall environmental remediation strategies, photocatalytic degradation, CO_2 reduction, energy conversion to storage and bacterial disinfection. At the end, we will concisely describe the future perspectives of MXenes regarding their potential applications in a broad range of research fields.

2. MXenes in brief

After the first invention of stable 2D atomic carbon layer graphene, the 2D MXenes with obvious advantages of remarkable configuration as compared to that of bulk counterparts, has received considerable attention in a wide range of scientific fields [97,98]. Nevertheless, the application of graphene is yet limited to certain extent owing to their challenging chemical configuration, perpetual crystal and elemental and structure as well as gapless band structure. Therefore, the stoichiometric doping based material strategy has swiftly received immense attraction via other elements including Bi [99], Te [100,101], P [102], Ge [103] and Si [104], as well as compounds Bi_2Te_3 [105] and MoS_2 [106] along with various excellent properties those contest well with certain demands. Gogotsi et al. [107] presented new 2D transition metal nitride, carbides, and carbon nitrides based MXenes in 2011, igniting a new upsurge in ongoing research to search more innovative thoughts and their auspicious application in the field. The universal formula of MXenes is $Mn_{+1}X_nT_x$, where M indicates early transition metal (i.e. Mn, Mo, Cr, Ta, Nb, V, Hf, Ti,Sc, Zr), X is C and N, and T are surface functional group unit (e.g. fluorine, oxygen or hydroxyl), and $n = 1, 2$, or 3. The more obvious outer layer of MXenes, which is chemically active in turn, leads to the development of surface functional groups (terminations). On these bases, MXenes based materials have been categorized in different types of classes (ordered mono-M, ordered double-M and solid-solution M) based on their composition and atomic lattice (M) (Fig. 3). The production of MXenes is mainly accomplished via selective acid etching of their MAX/non-MAX precursor, where A denotes A-group elements (usually 13 and 14 groups elements of periodic table), bottom-up construction techniques and chemical transformations. Usually, the first technique is considered to be more desirable than the other two methods, owing to their

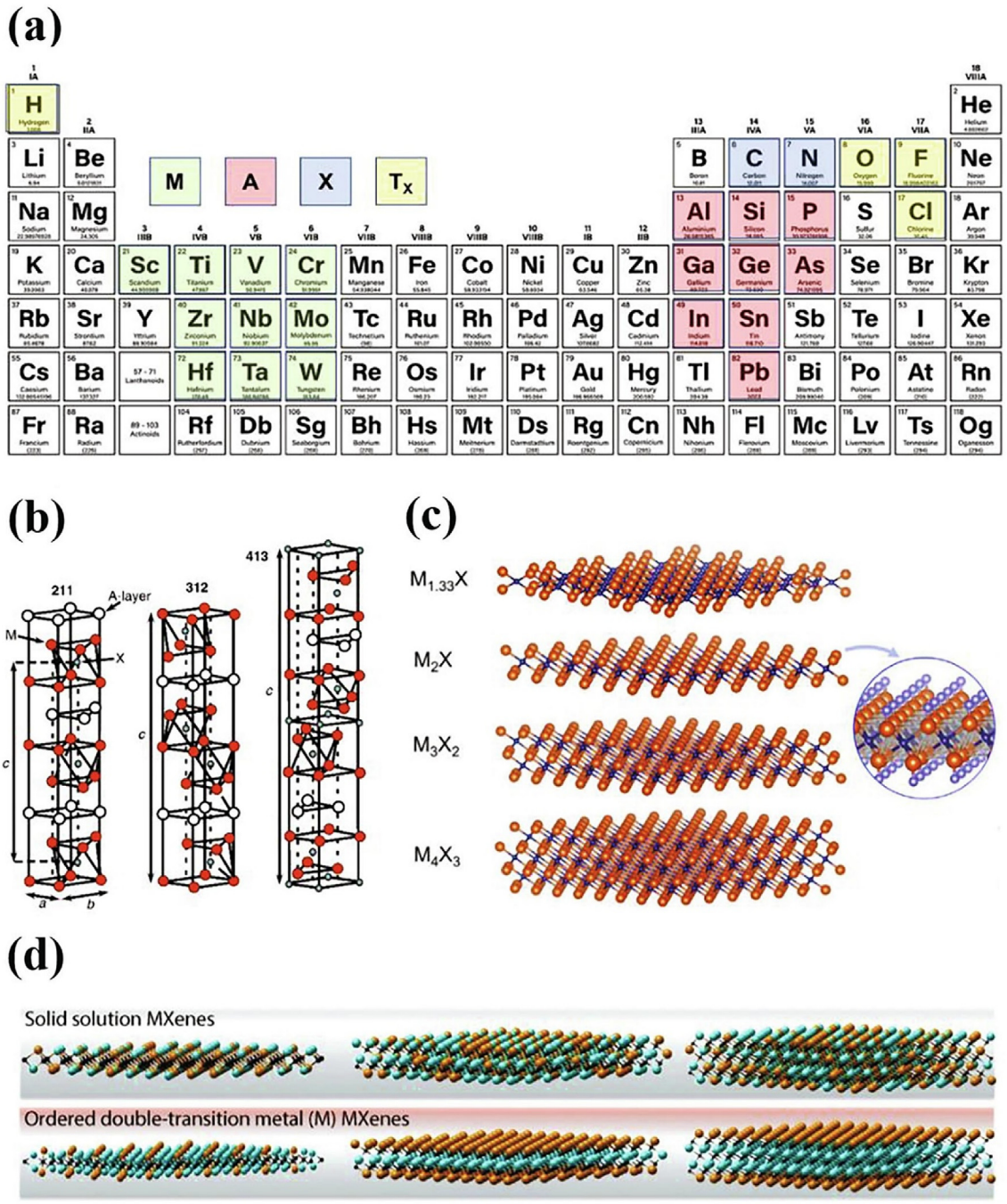

Fig. 2. (a) MXenes are made up of chemical components. (b) 211 (n = 1), 312 (n = 2), and 413 (n = 3) MAX-phase units cell architectures. Reproduced with permission from Ref. [95]. Elsevier (c) Framework of mono-M MXenes. Reprinted with permission from Ref. [96]. Cell Press, (d) The configuration of MXenes is made up of two metallic elements. Reprinted with permission from Ref. [42]. Copyright, American chemical society.

process viability, cost effectiveness and better yields. A wide variety of ternary nitride and carbide based over 70 kinds of numerous MAX phases had been invented [108], which exhibited incredible distinctions in the family of MXenes. Among them, almost thirty kinds of MXenes have been discovered via an experimental approach while that of many more are in the pipeline and being invented through revealing theoretical calculation [109]. The concise description along with timeline progress about MXenes based materials is shown in Fig. 3 [110]. The surface termination and rich stoichiometry equip 2D MXenes by having extremely flexible structure with tailorable chemical and physical properties. For example, the ultra-low optical diminution, utmost ability to interpolate the ions, huge elastic moduli, higher electrical conductivity along with capacity, tunable bandgap and considerable compatibility with organic solvents and water have been significantly established. And a list of comprehensive reviews have been reported related to the synthesis [111,112], electronics [113], sensors [114], catalysis [115,116], MXenes-assisted energy conversion and storage [108,117], as well as its biomedical applications [118]. However, there is scarce information available in literature regarding the electro-magnetic properties and their corresponding applications [119]. Extensive

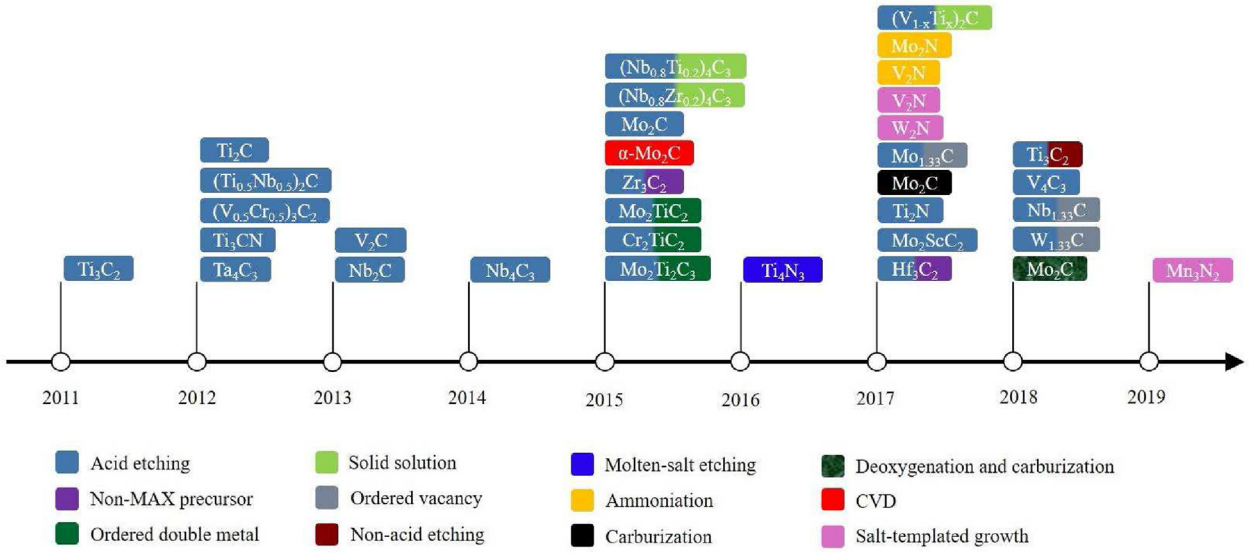

Fig. 3. The timeframe of the MXenes' evolution. Reprinted with permission from Ref. [110], Copyright Elsevier.

applications of MXenes and their novel opto-electro-magnetic phenomena have been recently established. They include high Curie temperature ferromagnetism [120], with 100% spin. Hence, a timely review covering all kinds of aspects related to MXenes and its advancements in numerous research fields could offer considerable motivations for advanced multidisciplinary research.

2.1. Discovery of MXenes

Isolation of the first MXene (Ti_3C_2) from MAX powders was achieved after soaking Ti_3AlC_2 phase in a hydrofluoric acid solution. After that, a series of different kinds of MXenes were developed by adopting the same selective etching method [121]. The use of MXenes has been increased due to the strong curiosity in its structural characteristics, and recent theoretical investigations have brought about the invention of various kinds of new MXenes [122]. Generally, the boundary layer of MAX-bound is considerably more stable than A layers, and it displays comparatively weak interactions/contacts with the M−X layer. For the fabrication of M−X-layered structures, the continual out-diffusion and discriminatory reactions of layer atoms via extraneous species are considered to be most effective approaches (Fig. 4) [57,123,124]. Remarkably, the use of HF during the preparation of MXenes is regarded as the best choice owing to the well-established etchant [125]. The initial description suggested the different kinds of MAX phases during the existence of normal salts (Na_2SO) and the MAX phase is not effectively exfoliated by forming the MXene either from molten salts/molten metals. For that purpose, the dilute HF solution is regarded as the most effective strategy, in which the MAX phases immersion leads to the selective removal of A layers, which in turn brough about the successful development of M−X multilayer fragments. After that, the 2D-layered Ti_2C and Ti_3C_2 were formed by using the intercalation agents [126]. The as-prepared Ti_3C_2 nanosheets are found to be thick like few atomic layers, which could be further transformed into conical scrolls [127]. In addition to this, such kinds of nanosheets are found to be somehow similar to other 2D materials and graphene [128,129]. The MAX phase derivatives, such as 2D metal nitrides and carbides after the formation of A layer from MAX phases, are actually regarded as MXenes. Moreover, a series of functional groups (OH, O and F) also exist over the surface of MXene nanosheets (Fig. 4i), and such kind of various surface functional groups further leads to the development of functionalized semiconducting MXenes [$M_{n+1}X_nT_x$; e.g. $Ti_3C_2(OH)_2$], whereas the simple MXenes [Mn_{+1} Xn; e.g. Ti_3C_2] are found to be metallic (Fig. 4j).

2.2. Binary transition metal-based MXenes

Basically, MXenes consist of a single metal carbide, i.e. Ti_4C_3 and Ti_3C_2. But the binary metal-based compound is also found within M layers and these compounds are considered to be thermodynamically stable. Use of M_0 and M_{00} as two different metal sources for the preparation of both $M_0FM_{00}C_2$ and $M0_2M00_2C_3$ phases (Fig. 5a) could be easily achieved in the form of Mo_2TiC_2 and $Mo_2Ti_2C_3$ (Fig. 5b). Moreover, it was found that such kinds of binary MXenes usually exhibited analogous morphologies, atomic conformations and crystal structures, similar to other layered structures (Fig. 5c and d) [130]. After the invention of various surface functional groups over MXene surface sites, a wide variety of different MXene members, almost 250, were investigated through the combinations of different metal element M_0, M_{00} pairs, N C and N with different surface termination groups OH, F and O. Furthermore, the various kinds of binary transition metals ($Nb1_xV_x$, $Ti1_xV_x$, $Ti1_xTa_x$, $Ti1_xNb_x$, $Ti1_xMo_x$, $Ta1_xMo_x$, $Nb1_xMo_x$, $V1_xMo_x$) are extensively used to properly tune the compositional and morphological appearances of MXenes. Actually, the MXene family contains a wide variety of million members, which are different from each other depending upon their atomic ratios and configurations after combining with two alloyed metals at various preparation temperatures [131].

2.3. Computational approaches for MXenes

With the aid of the generalized gradient approximation (GGA) approach, the density functional theory (DFT) calculation was used to obtain deeper understanding regarding the use of MXenes in multiple applications. To achieve a deeper understanding regarding

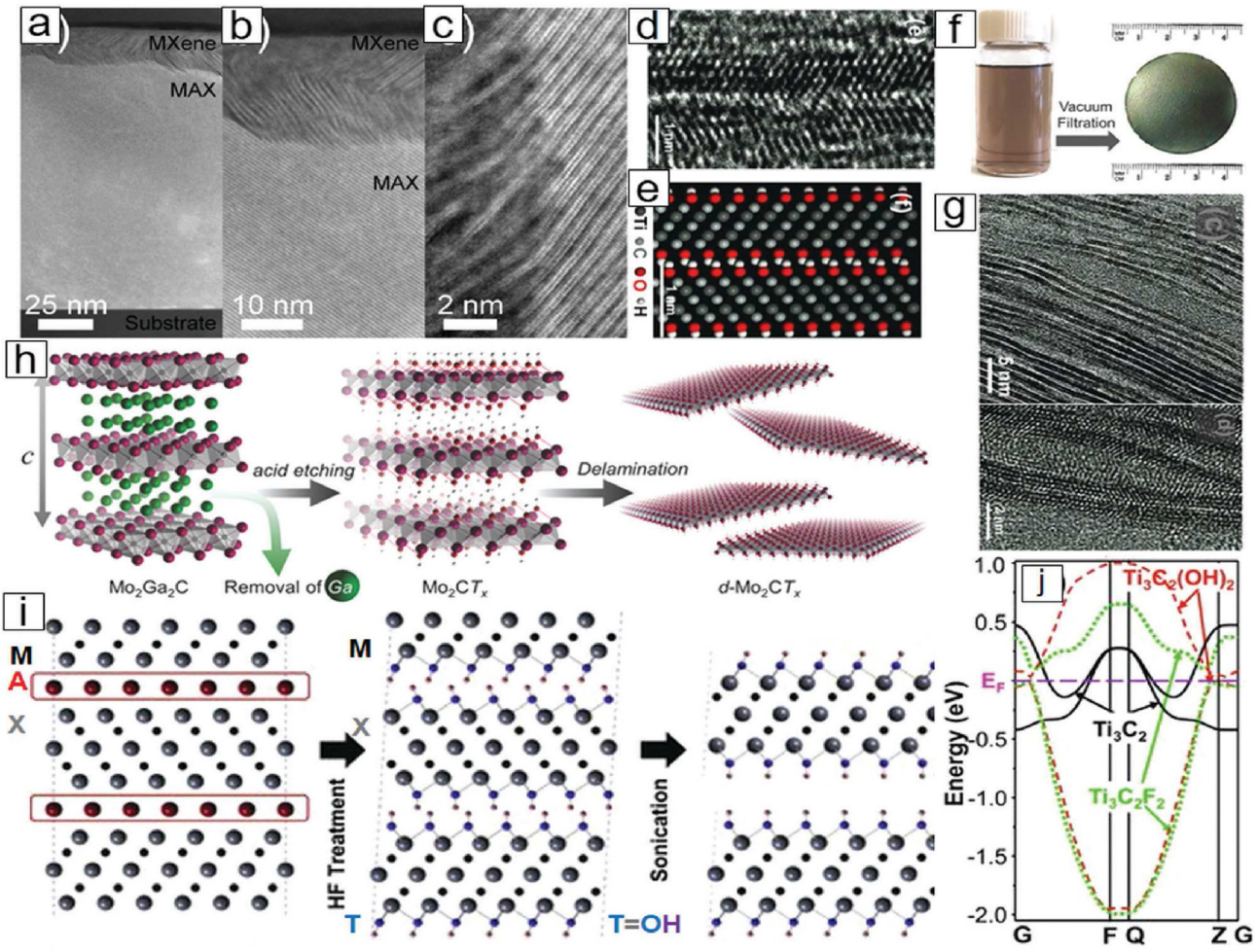

Fig. 4. Frameworks and TEM morphologies of the (a) MAX phases thinner film (b), MXene bonded to the MAX phases (c), and the MAX–MXene surface. (d) TEM image of an MXene with surface OH reactive units. (e) The simulated picture of atomic composition. (f) Images of MXene distribution and MXene sheet generated by screening MXene suspensions. (g) Transmission electron micrographs demonstrating the deformation of MXene layers. (h) Schematic representation of the synthesis of MXene after acid elimination in MAX. (i) Cross-sectional picture of the layered development of MXene. (j) Band configurations of virgin MXene and layered MXene with OH and F surfaces terminals units. (a–c) Reprinted with permission from Ref. [123], IOP Publishing. (d, e, g, i and j) from Ref. [57], by John Wiley & Sons, Inc. and Reprinted by permission of John Wiley & Sons, Inc. (f and h) [124].

the periodic structure of MXenes, the Perdew–Burke–Ernzerh of (PBE) exchange-correlation functional is considered to be a viable tool [132]. Moreover, this is an admitted reality that the PBE basically underrated the widths of actual bandgap. Therefore, the Heyd–Scuseria–Ernzerhof ($HSE0_6$) proposed a hybrid functional theory for the solid-state calculations, which has been extensively used to expand the bandgaps. Such kind of approaches usually made it more viable to deduce the overall trend and expected properties in MXenes, while the quasiparticle GW guesstimate [133,134] with the successive solution of Bethe-Salpeter equation (BSE) [135] is normally used to determine the optical spectra and the quantitative investigation of bandgaps. Occasionally, the experimental results of any research observation might be a challenging task and practically or economically are not feasible to obtain. To establish the structure-property relations, the first-principle methods are considered as the most viable tool. The thermodynamic stability of O-terminated MXenes was investigated by Ashton et al. using DFT-based first principle calculations. Except for Sc-based MXenes [135], these are highly stable compounds in F-terminated configurations, but, whenever these MXenes-based compounds are subjected to H_2O/HF solutions, then, these compounds are projected to be dynamically more promising at low hydrogen chemical potential [136]. Currently, in order to determine the prospect of MXenes exfoliation, the bond strengths, force constants and exfoliation energies, are significantly measured for MAX phases [137]. Amid all, different kinds of MXenes from their MAX phases have been reported as having effective exfoliation characteristics. The Pourbaix diagrams have already premeditated and presented that the higher amount of certain MXenes and the synthesis of metastable phases could be easily obtained by adjusting the synthesis conditions of MXenes during its preparation [138]. Amid hundreds to thousands of possible combinations, thousands of new potentially stable 2D materials have been extracted theoretically with the aid of highly developed up-to-date theoretical methods, which has the potential to efficiently curtain the multivariate chemical space of compounds [139]. However, it is the most viable tool to curtain the compounds, whose anticipated properties are highly determined. Currently, a lot of performance-based calculation about the composition and properties of MXenes has been reported due to its well-defined composition and general structural features [140,141]. Moreover, with the combination of cluster expansion and DFT approach, the structure-stability relationship of M_{1-x}-X_xC_2 alloys calculation were performed by Tan et al. to for searching MXenes alloys, where M = V/Nb/Ta/Ti and X = Mo/Nb/Ta/V with $0 \leq x \leq 1$ (Fig. 6a). According to their investigation, the surface layers in the Mo-rich MXenes

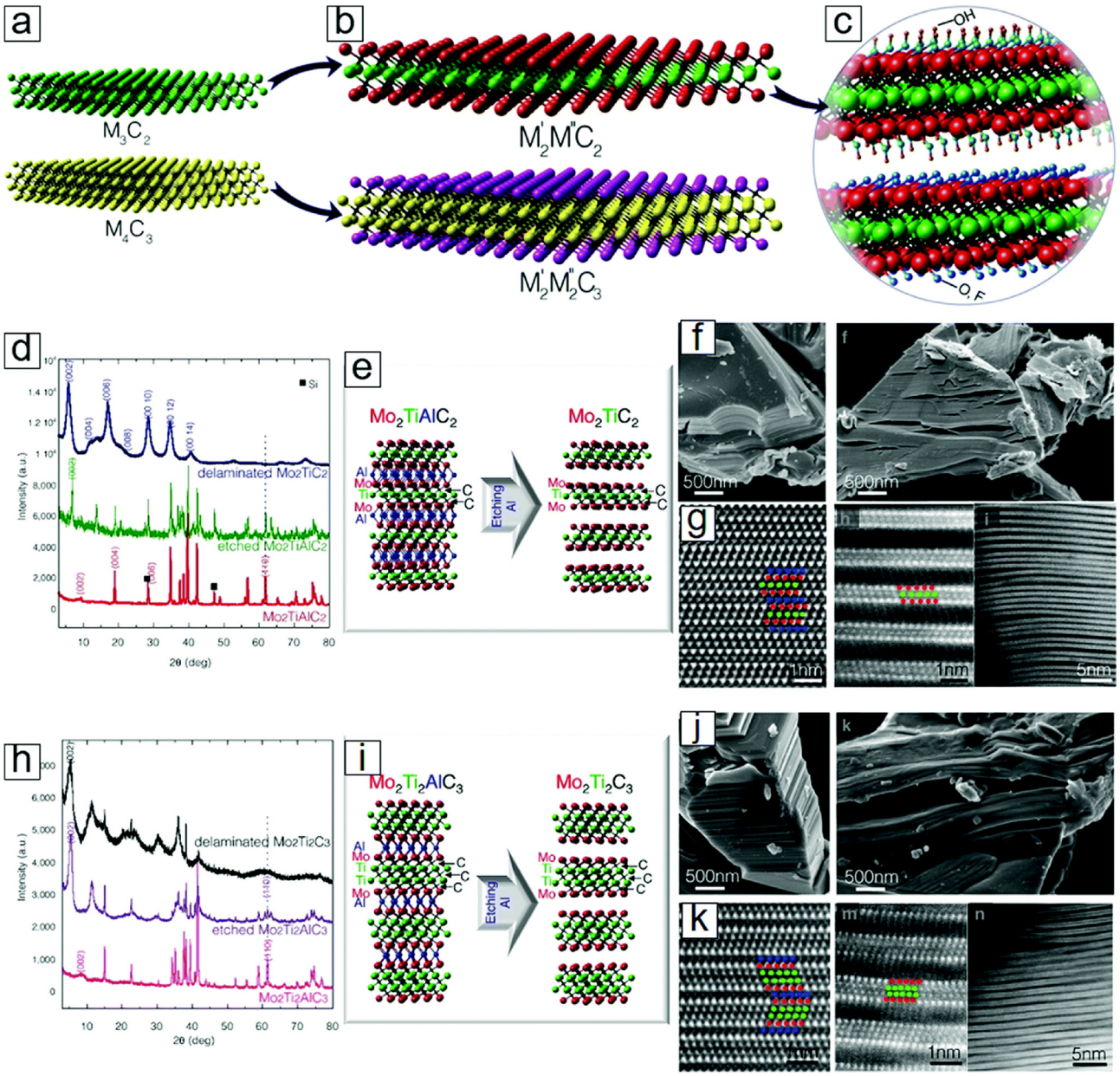

Fig. 5. MXene with two transition metals. (a) Structure of typical MXene including a single transition metal. (a) Configuration of the $M0_2M00_2C_2$ and $M0_2M00_2C_3$ double transition metal MXene. (c) Active units on the interfaces of MXene. (d) MXene XRD spectra. (e) Configuration atomic. (f) SEM images. (g) High-resolution transmission electron microscopy pictures. (h) X-ray diffraction. (i) Atomic Layout. (j) Scanning electron microscopy pictures. (k) High-resolution transmission electron microscopy pictures of MXene $M0_2M00_2C_2$ materials. Reproduced by permission of American Chemical Society [130].

$(M1-xMox)_3C_2$ are generally occupied by Mo atoms, while that of in Ti-containing MXenes, the position of Ti atoms mainly depends upon the alloying metals. For example, in the Nb- or Ta-rich MXenes, the Ti occupies only one surface layer [142]. Amid, transition metal carbides based MXenes, the O-terminated two-dimensional MXenes i.e. Ti_2CO_2 and W_2CO_2 could be extremely active HER catalysts during the screening procedure for the search of the most effective catalysts for hydrogen evolution reaction (HER). The efficiency of $TiVCO_2$ to enhance the catalytic activity has been proposed by a simple descriptor [140]. Later, a series of highly HER active partially modified M_2XO_2 were introduced, including Ag-Nb_2NO_2, W-Nb_2NO_2 Re-Nb_2NO_2, Ir-Sc_2CO_2, Os-Ta_2CO_2. The change in the reaction mechanism from Volmer–Heyrovsky to Volmer–Tafel is mainly due to the TM adatoms persuaded restructuring of electron density over the MXene surface [143]. It is well known that the thickness plays an important role, which further allows the proper tuning of desired MXenes. In consideration of this point, different kinds of MXenes have already been proposed as extremely active HER catalysts [144]. A series of models such as Gaussian process (GPR), bootstrap aggregating regression algorithms, support vector (SVR), kernel ridge (KRR), support vector (SVR), have already been developed to precisely envisage the bandgaps of functionalized MXenes. Amid all of these models, the improved correlation properties towards premeditated GW bandgap were observed. Basically, the initial MXenes were developed to provide a metal-semiconductor based classification model with an accuracy of about 94% (Fig. 6b) [145]. In addition, the mixed composition based MXenes compounds such as Ti_2CT_x, $Ti_3C_2T_x$, Nb_2CT_x, and $Nb_4C_3T_x$ (T = O, F, and OH) surface functionalization was studied in detail. In the category of decomposed and

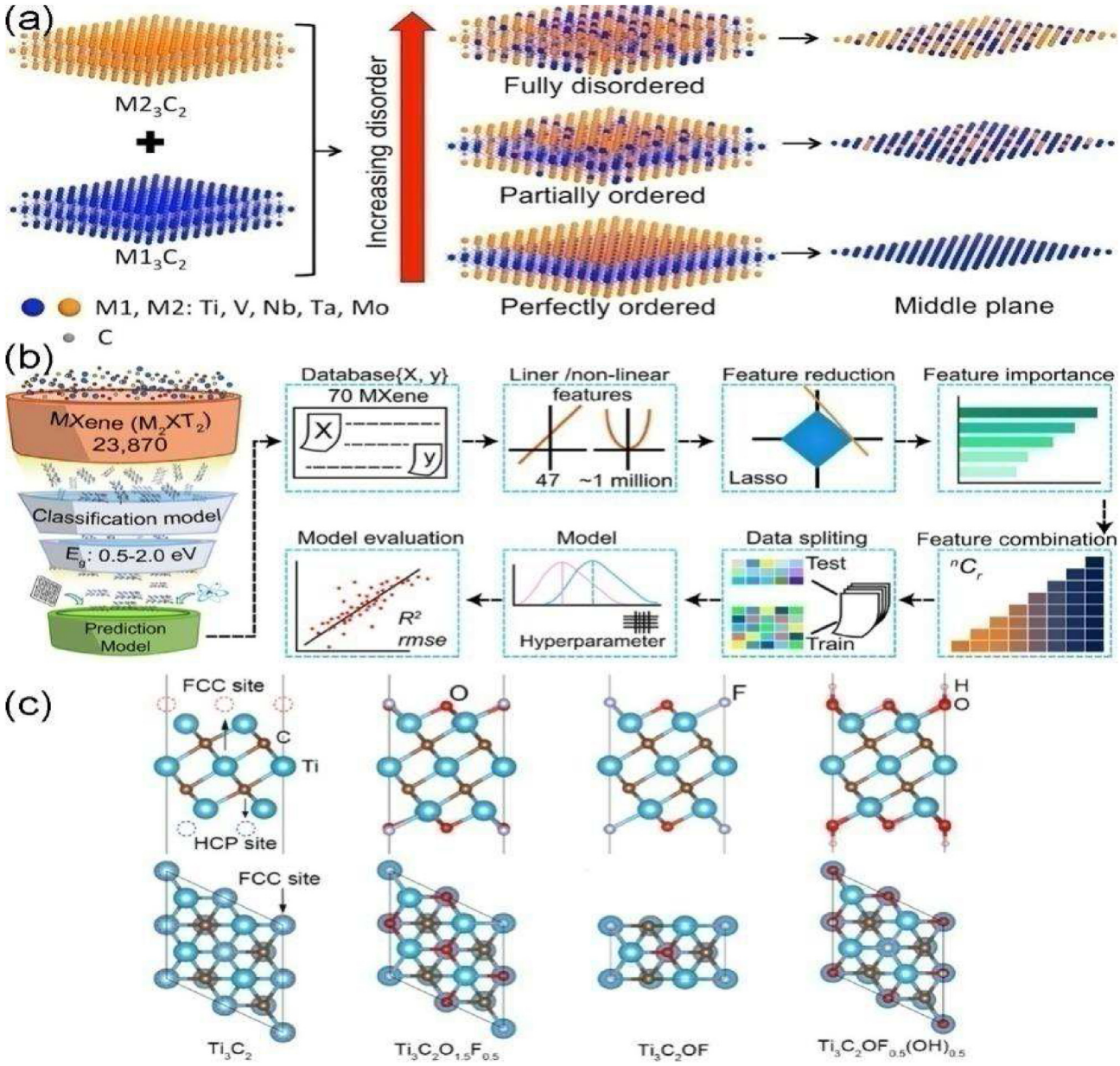

Fig. 6. (a) Diagram illustrating the production of MXene metals. M_1 and M_2 denote Ti, V, Nb, Ta, and Mo. M_3C_2 MXenes are composed of a single transition metal element. Right: answers to $(M_{11-x}M_2X)_3C_2$. Reprinted by permission of ref [141] Copy right, American Chemical Society. b) Graphical illustrates how machine technology is used to exclude semiconductors from the MXene databases. Reprinted by permission of ref [145]. Copy right 2018, American Chemical Society (c) The more robust O-containing $Ti_3C_2T_x$ MXene combinations Reprinted by permission of ref [142], Copy right, American Chemical Society.

most stable one MXenes, the O terminated MXenes (Fig. 6c), and OH-terminated MXenes were investigated, respectively [142]. For the proper detection and proper screening of the use of MXenes as an electrode material, different kinds of MXenes were categorized through computational screening of $M_{n+1}X_nT_x$ MXenes in a H_2SO_4 electrolyte. As compared to the carbide- based MXenes, the nitride-based MXenes usually reveal a better activity [146]. At the GW level of accuracy, the band edges of numerous MXenes were investigated by means of machine learning models [147].

2.4. Synthesis of MXenes

A wide range of synthesis strategies for the preparation of MXenes have already been reported and a concise description of all these methods have been critically evaluated in this part [111]. The synthesis of 2D (MXenes) is usually found to be possible via two different kinds of methods, namely, the top-down and bottom-up approaches [148]. But, the wet etching method via exfoliation is now getting immense attraction in recent years. The MAX phases are mostly used to produce most of the multilayered 2D MXenes via selectively etching the A layers with HF at room temperature [92]. During such a kind of chemical etching process, the slow-mode etching of Al layer is mainly started to react with HF solution, thereby producing the AF and hydrogen gas, which in turn brought about the exfoliation of MXene layers illustrated in Fig. 7a. During that process, the hydrophilic (−F,−O or −OH) groups replaced the A atoms, which brought about the weakness in the interaction between $M_{n+1}X_n$ layers, thus, leads to the development of loosely packed exfoliated graphite-like layered structures called MXenes [149]. The formation of stable dispersion is mainly attributed to

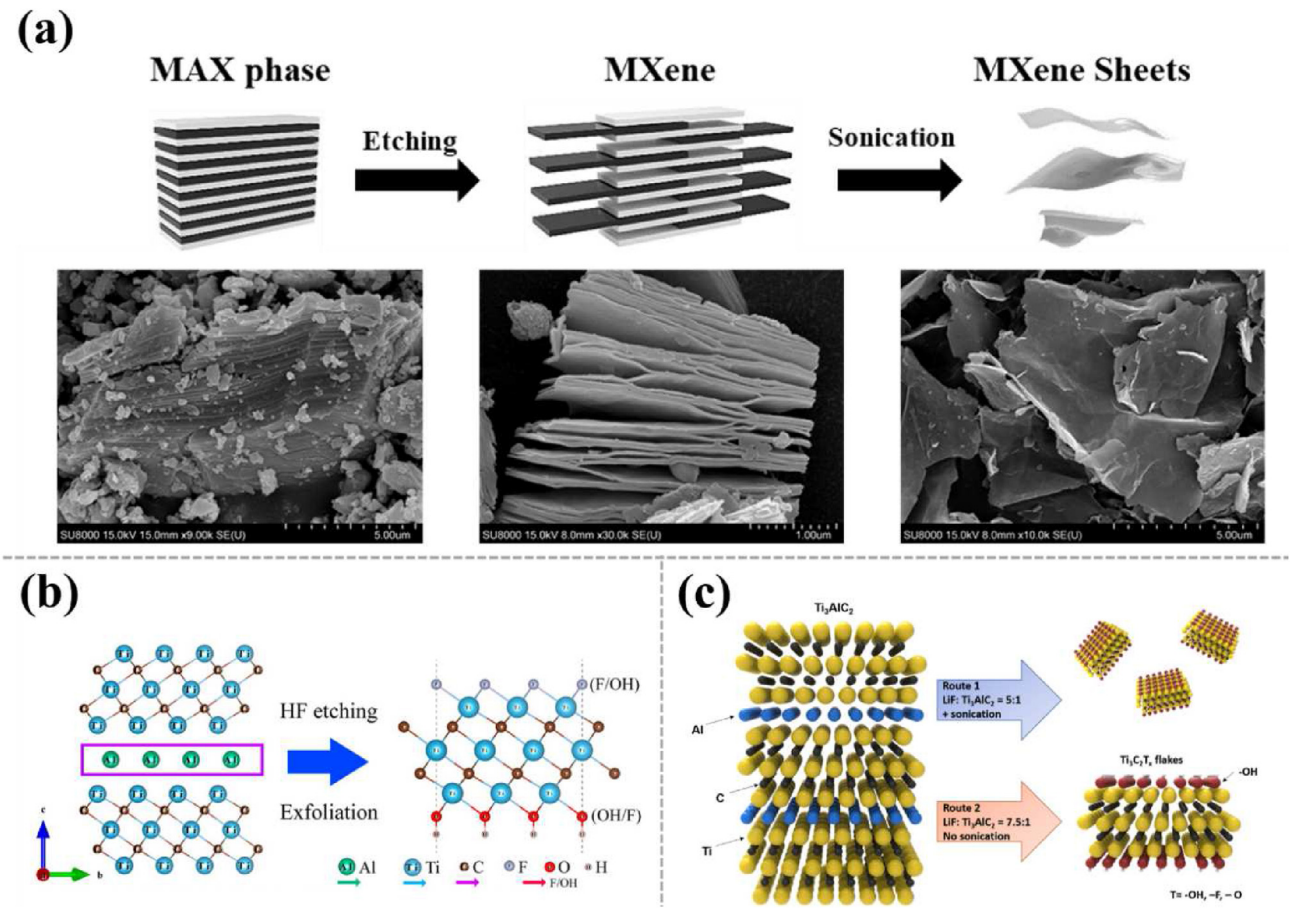

Fig. 7. (a) MXene fabrication. (b) The production of $Ti_3C_2T_x$ MXene is shown schematically. Reproduced with permission from Ref. [150], copy right, American Chemical Society (c) Synthetic flowchart of $Ti_3C_2T_x$ flakes via a multitude ways. Reproduced with permission from Ref. [156] Copyright John Wiley and Sons.

these functional groups [108]. As compared to simple MXenes, the surface functional group containing MXenes (−F, −OH or −O) known as terminated MXenes, mostly have superior thermodynamic stability (Fig. 7b) [150]. For the first time, the effective preparation of accordion-like well-exfoliated $Ti_3C_2T_x$ MXenes was accomplished by the Gogotsi and co-workers in 2011 [151]. According to their process, the selective etching of the raw Ti_3AlC_2 (MAX phase) was carried out via treating it with 50% concentrated HF solution for 2 h at room temperature. However, it is noted that in all kinds of as synthesized the $Ti_3C_2T_x$ MXenes is regarded as one of the best and extensively investigated MXenes among all the invented MXenes via various MAX phases-derived selective etching of atomic layers [67]. Thereafter, the HF etching method was further protracted to fabricate a wide variety of MXenes [83]. They include Ti_3SiC_2 [152], Cr_2TiC_2 [122], Mo_2C [153] and Ti_2C [154]. Moreover, the fabrication of stable nitride-based MXenes ($Ti_{n+1}N_n$) from MAX phases (Tin^{+1} AlC_n) via HF etching remains subtle, which is related to the low cohesion energy of their structure [90]. The dangerous nature and toxicity characteristic of concentrated HF during the preparation of MXenes further restricted its application, causing the use of less or somehow slighter etching method for the delamination and exfoliation process. A novel and single step pathway for the etching of AL from Ti_3AlC_2 was developed by Ghidiu et al. [155]. In this process, the lithium fluoride salts (LiF) and less harmful hydrochloric acid (HCl) is used. Furthermore, this process led to the production of water molecules and cation intercalation by providing higher yield of large interlayer space encompassing MXenes with negligible defects. The formation of well-defined clean edges and defect-free surfaces, high quality monolayer $Ti_3C_2T_x$ MXene flakes were fabricated as compared to pure MXenes derived from HF etching via various kinds of LIF to Ti_3AlC_2 molar ratios (5:1 and 7.5:1) by Lipatov et al. [156], as compared to the MXenes obtained via pure HF etching (Fig. 7c).

Generally, the formation of MXenes from inorganic ternary nitrides or carbides identified as the MAX phases, herein, the M indicates early transition metal. A signifies an A-group element (typically IIIA or IVA group), X denotes nitrogen/carbon atom and n value could 1−4 [157]. Because of the robust metallic properties M−A bond, the use of mechanical shearing for the isolation of $M_{n+1}X_n$ layers from MAX phases is quite difficult. Therefore, as compared to robust M−X bonds, more chemically active M−A bonds treatment stimuluses the selective etching of A layers, a major parameter for the efficient production of MXenes from parent MAX as shown in Fig. 8a and b [158]. After adjusting the proper HF concentration and reaction time, the various kinds of MXenes could be produced at room temperature and up to 55 °C (Fig. 8c−e) [122]. To prepare the multilayered $M_3C_2T_x$ MXenes, multilayered ternary carbide (M_3AC_2, MAX powder) was mixed in HF-based acid solution (i.e. HCl-LiF). The A layer (such as aluminum) in this process is etched selectively and the termination of surface groups is carried out via various oxygen, hydroxyl and fluorine groups. The single flake MXene dispersions could be produced due to the inclusion of tetrabutylammonium hydroxide (TBAOH), cations, dimethyl sulfoxide (DMSO) and water into the interlayer spacing via a sonochemical treatment. The Al-containing MAX phases etching conditions vary from metal to metal, mainly

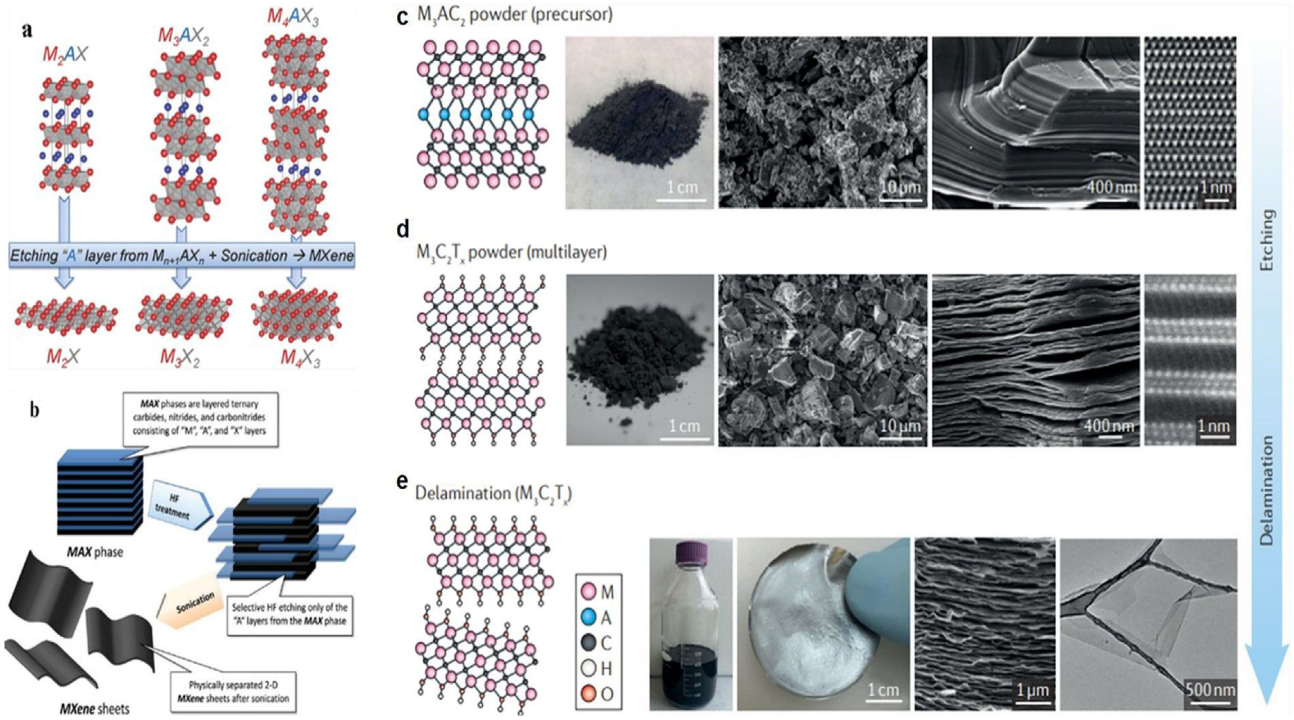

Fig. 8. MXenes are synthesized from basic MAX phases. (a) The various MAX aspects and their associated MXenes. Reproduced with permission from Ref. [121] Copyright, Wiley online library (b) MXene synthesized from MAX phases is shown schematically. (c–e) Synthesis and compositional characterization of MXenes. Reproduced with permission from Ref. [154] copyright, American Chemical Society (d) Pictures of stacked MXenes. (e) Graphs illustrating the resultant exfoliated MXenes. Reproduced with permission from Ref. [130] copyright, American Chemical Society.

depending upon the material bonding, size and structural characteristics. The ability of HF to selectively etch and remove the different SiC polytypes is very high [159]. From experimental results, it is well understood that the strong etching and a longer time are more suitable for the considerable rise in atomic number of M, which is mainly connected with M-Al metallic bonding. Due to the metallic nature of M-Al bonding, stouter etching is necessary to maximize the number of M valence electrons [108].

The development of alternate slighter etchant, (LiF/HCl solution) was accomplished due to the hazardous nature of hydrofluoric acid [160,161]. The reaction is mainly carried out by mixing the MAX Ti_3AlC_2 powders into HCL and LiF solutions (Fig. 9a) [162]. The as produced HF species act as etchant in reaction (4), and it is extremely manageable via regulating the concentration. The obtained product was rinsed with water for the removal of any side product (i.e. AlF_3) after the completion of reaction at 40 °C, e.g. in aqueous solution. Upon drying the final sample in the form of ($Ti_3C_2T_x$ MXenes) could be achieved. Remarkably, the as obtained MXenes was found to be highly shapeable and flexible by having clay-like structures.

$$LiF(aq) + HCl(aq) = HF(aq) + LiCl(aq) \quad (4)$$

The lateral sizes of the MXenes are found to be strongly influenced by the absence or presence of sonication treatments and the relative ratios of LiF in the reaction medium (Fig. 9b and c). For instance the sonicated sample shows an average width of 0.5 mm, while the average width of non-sonicated samples was found to be 3 mm (Fig. 9d and e) [162]. The electrochemical performance shows the highly volumetric capacitance of these compounds due to the proper intercalation of Li ions between MXene sheets. As compared to the pure HF-derived MXene sheets, the MXenes derived from such a kind of mild production scheme leads to the formation of bigger planar sizes with less atomic defects. The presence of some common salts (H_2SO_4 and HCl) suggests that this strategy could be adopted for the same fluoric salts. Indeed, cations such as Na, Ka, Cs, Mg, and Ca lead to the intercalation of the cations, applicable to one-step anion intercalation techniques for anode materials in rechargeable secondary ion batteries.

The production of MXenes without using acid could also be possible through selective etching method [164]. In the alkaline binary electrolyte solution (pH > 9), which contains tetramethylammonium hydroxide (TMA·OH) and ammonium chloride (NH_4Cl), the production of Ti_3C_2 MXenes could be possible through anodic etching, where the Ti_3AlC_2 sticks act as electrodes. The electric current mainly produced the required proton during etching process [164]. In biomedical field, most of the fluoride termination free MXenes are used [118]. The molten salt etching method at 550 °C was used to produce the first two-dimensional transition metal nitride, Ti_4N_3 [64], while that of traditional wet acid etching method has been reported to produce the carbon nitride based MXenes (Fig. 10) [154]. The primary reasons for the stringent preparation conditions for nitride MXenes might be instigated from more energies of nitrides than their carbide corresponding parts and lower cohesive energies [165]. The combination of solution-based nanolamination and plasma etching processes are responsible for the production of Large-scale (~4 cm) Ti_2C films [166]. The in situ chemical transformations method has been regarded as one of the most effective processess for termination free MXenes production beside extensively used selective etching methods, particularly high-activity heterostructures [167]. The carburization and oxygenation of H_2MoO_5 on

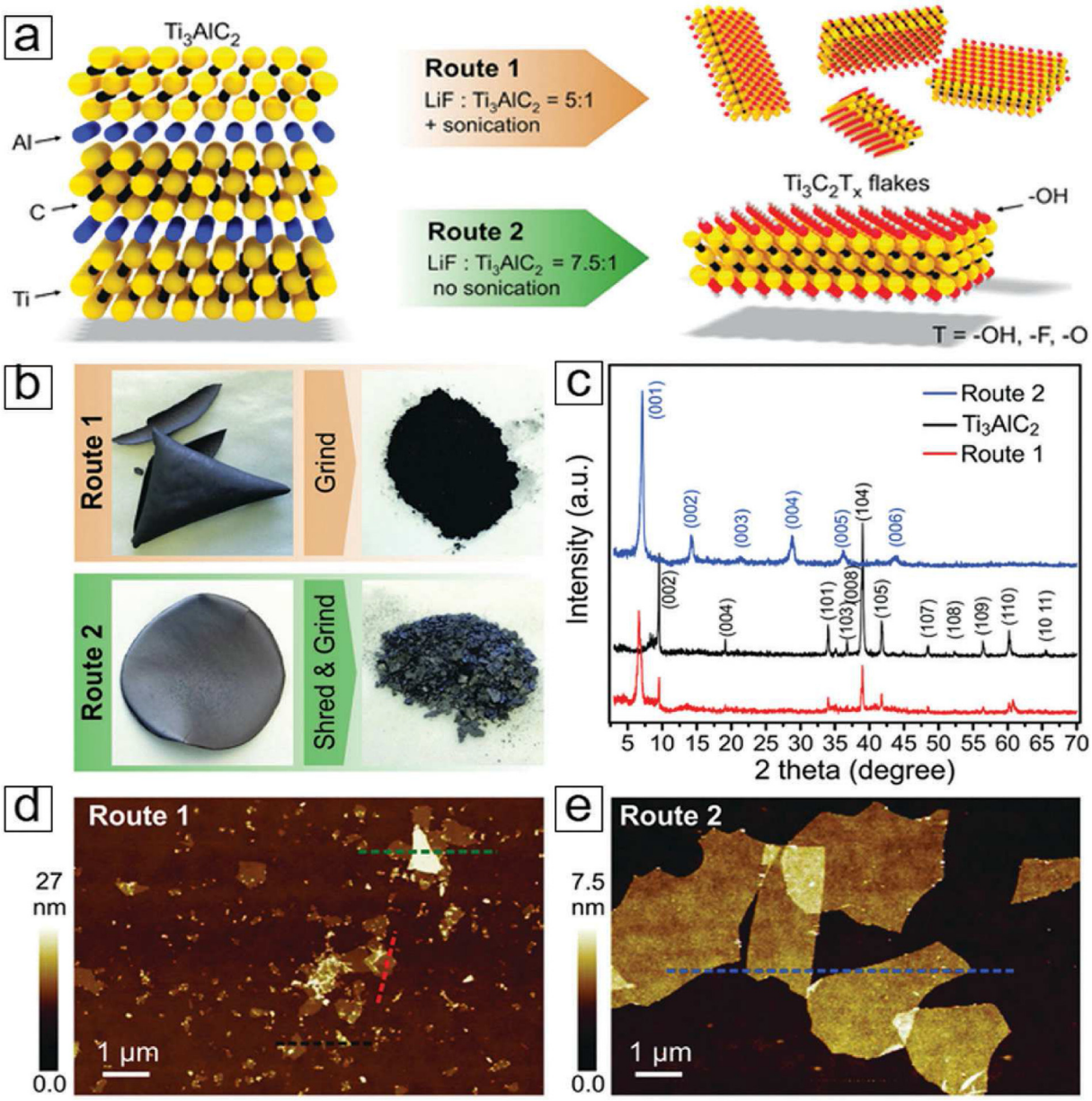

Fig. 9. Exfoliation of Ti_3C_2 MXene using LiF etched techniques. (a) Exfoliation process diagram. (b) Photos of an MXene sheet that was created by filtrating an MXene emulsion over a polyvinylidene difluoride membrane. (c) MAX and MXene X-ray diffraction (XRD) patterns. (d-e) Microstructures of MXene flakes taken using atomic force microscopy (AFM). Reproduced with permission from Ref. [163] Copyright, John Wiley and Sons online library.

a carbon film leads to the formation of Hexagon Mo_2C nanosheet films. This is also noteworthy that the inactive carbon precursor from carbon film mainly acquires low reduction atmosphere, which in turn brough about the difficulty in the occupy of the interstitial sites for carbon atoms and thus hcp-Mo_2C formation occurred instead of fcc-MoC [167]. With the aid of carbide conversion and fractional consecutive hydrodesulfurization of the semiconducting 2D material, an atomically sharp metallic/semiconducting hybrid structure (Mo_2C/Mo_2S) can be formed. From this hybrid junction, the low Schottky barrier height (26 meV) and low contact resistance (1.2 kΩ μm) was observed [168]. Through the process of ammonization of their parent carbides, the production of Transition metal nitrides MXenes having enhanced electrical conductivity could be achieved. After the ammonization of V_2C and Mo_2C MXenes at 600 °C, the vanadium and molybdenum nitrides (V_2N and Mo_2N) are produced. Moreover, the mixed layered structure of trigonal V_2N and cubic VN was obtained after the transformation of V_2C , while that of Mo_2N retains the hexagon structure [169]. The synthesis of MXenes through ion exchange mechanism has also been reported [170].

2.4.1. Intercalation and delamination of MXenes

To obtain the separate 2D sheets, increasing the interlayer spacing of multilayer MXene flakes through the delamination and intercalation process is an important strategy (Fig. 11a) [173]. Mainly, the different intercalating compounds are used to start the process of intercalation. They include metal cations (Na^+, K^+, NH^{4+}, and Mg^{2+}), $N_2H_4•H_2O$ [174], tetrapropylammonium hydroxide [175], urea, isopropyl alcohol, alkylamines, (Fig. 11c), CTAB [176], DMSO [177] (Fig. 11b), as well as metal hydroxides in solutions. The

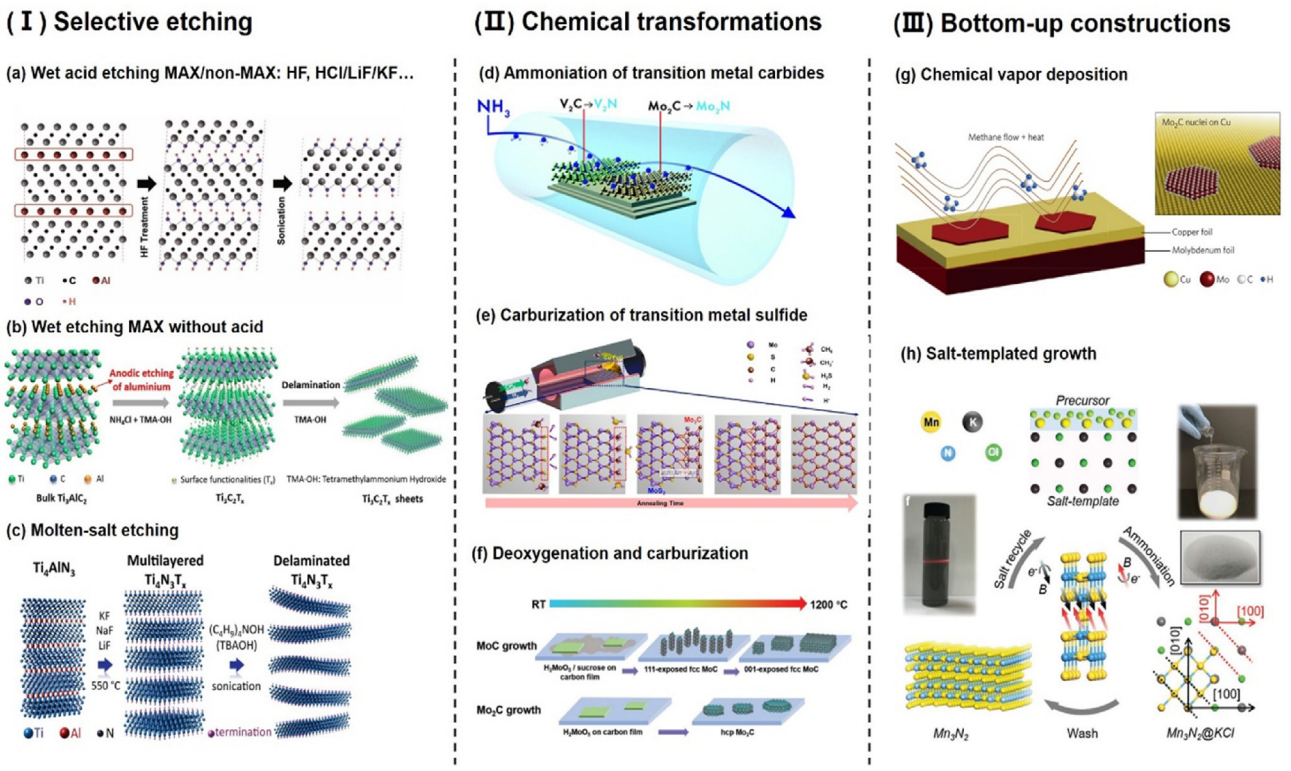

Fig. 10. Strategies for synthesizing MXenes. (i) Techniques for selected etching fabrication, such as (a) wet acid etching MAX/non-MAX through HCl, HCl + LiF/KF, etc. Reproduced with permission from Ref. [107]. Copyright, John Wiley and Sons online library (b) MXene synthesis through anodic etching in electrolyte solution (NH_4Cl + TMAOH) without acid. Reproduced with permission from Ref. [164] Copyright, John Wiley and Sons online library (c) molten salt etching of $Ti_4N_3T_x$ MXenes at 550 °C. Reproduced with permission from Ref. [64]. (ii) Chemical transformation methods. (d) Ammoniation of Mo_2C and V_2C [169]. (e) Carburization of MoS_2 to Mo_2C. Reproduced with permission from Ref. [168] Copyright, American chemical society (f) De-oxygenation and carburization of MoC to Mo_2C [167]. (iii) Bottom-up synthesis. (g) Chemical vapor deposition growth of α-Mo_2C sheet on Cu surface. Reproduced with permission from Ref. [171]. (h) Sodium templating for Mn_3N_2 MXenes. Reproduced with permission from Ref. [172].

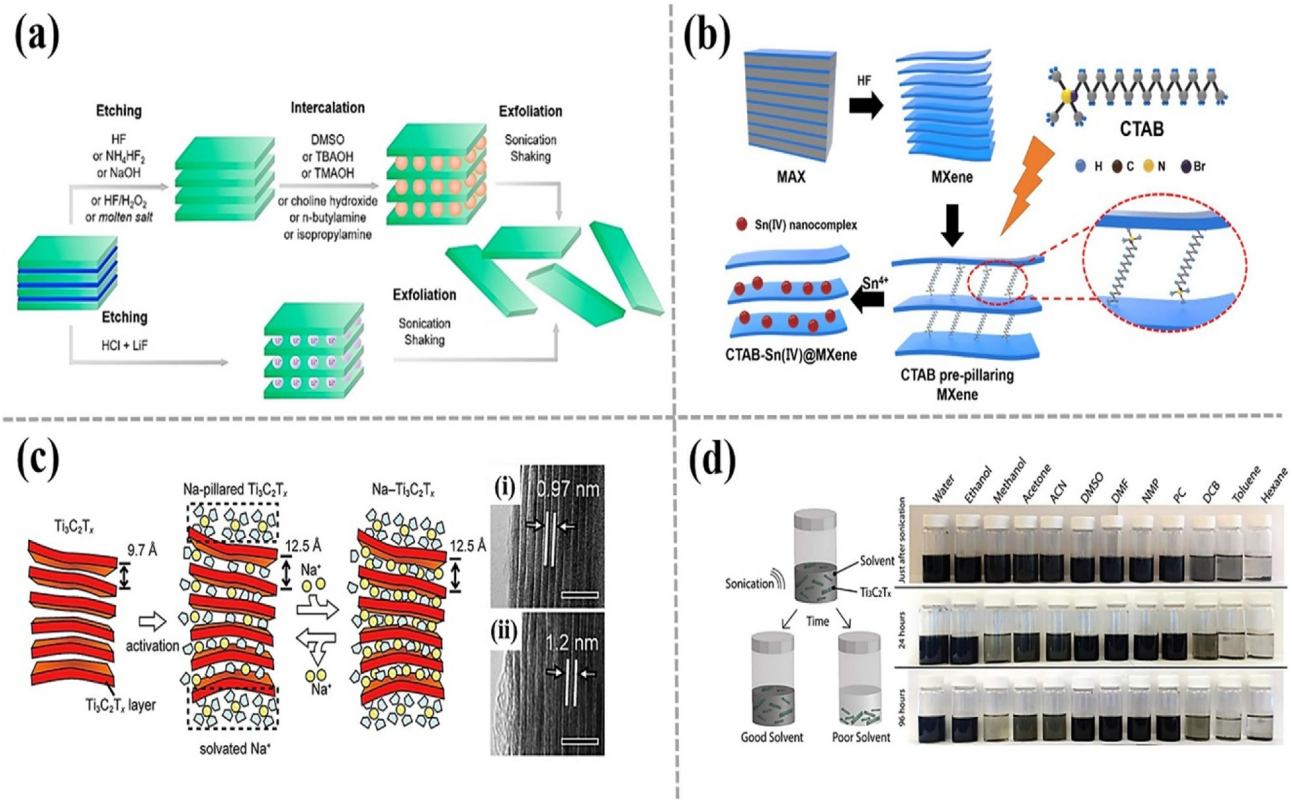

Fig. 11. (a) MXene nanosheets upon etching process. Reproduced with permission from Ref. [173] Copyright, Elsevier (b) synthesis of CTAB-Sn(IV)@Ti_3C_2 [176]. Need permission (c) integration of Na^+ ion within $Ti_3C_2T_x$ Reproduced with permission from Ref. [174]. Copyright, American Chemical Society (d) Dilution of $Ti_3C_2T_x$. Reproduced with permission from Ref. [179]

single layer or few layers-based MXene is mainly produced by the guest molecule intercalation process, which weakens the van der Waals and hydrogen forces. Thereby enhancing the c-lattice parameters between the 2D MXene layers. After filtration, the free-standing paper-like MXene could be achieved from the dispersion-derived steady colloidal solution of delaminated MXene layers [178]. According to the nature of intercalant and MXenes, the selection of a suitable solvent is highly needed in this process. As compared to multilayered MXene stacks, the delaminated MXene layers shows superior su';rface area by having negative charged with −OH, −F and C atoms, which are favorable for the efficient adsorption and removal of radionuclides, dyes and heavy metal ions [84]. The proper selection of intercalation is important for the adjustment of the c-lattice parameter of the MXenes, which in turn enhances the capability of MXenes to capture the radionuclides more efficiently [84]. In organic solvents, the dispersions of Ti_3C_2Tx nanosheets by Maleski et al. [179] was studied and found that the delaminated $Ti_3C_2T_x$ is well dispersed in polar solvents (i.e. DMSO, N,N-dimethylformamide, propylene carbonate, N-methyl-2-pyrrolidone, ethanol and H_2O) (Fig. 11d). It is due to the similar chemistry of both $Ti_3C_2T_x$ and organic solvents. Due to less polar and hydrophobic characteristics, the hexane, toluene and 1,2-dichlorobenzene cause showed slight dispersions. During the preparation of MXenes, the chemical exfoliation of MAX phases is regarded as a very common strategy [67]. To enhance the adsorption capacity and improve the surface accessibility of adsorbent, the intercalation and delamination of MXenes into smaller nanosheets is considered as a more probable approach nowadays [177].

2.5. Properties of MXenes

Due to the close association of free electrons with transition metals, the MXenes show tunable and ridiculous surface chemistry [115]. There are various factors, which can strongly influence the MXene surface, chemical, magnetic and intriguing structural properties, along with oxidation-reduction and environmental stability. These factors include intercalation strategy, etchant, etching methodology, and MXene precursor. In addition, the MXene properties could be further tuned according to certain applications by changing either surface terminations or MXene composition (different M and X) [83]. To further determine the properties of MXenes, various experimental and theoretical investigations have been conducted. Herein, we will discuss the utmost attractive characteristics of MXenes in all aspects.

2.5.1. Mechanical stability

The mechanical stability of MXenes materials is strongly influenced by the robust M−X bond and surface terminations (−F, −OH, and −O). The surface functionalization greatly enhanced the mechanical elasticity of MXenes; the improvement reduces the atomic layer breakage [180]. The DFT calculations show that MXenes stretched along basal planes display higher elastic moduli as compared to parental MAX counterparts (i.e. bonding in the ab plane is more robust than in the c-direction) [83]. According to Gogotsi and co-workers, through the process of the overlying of the corners of cylinder-shaped $Ti_3C_2T_2$-based MXenes films with electrically neutral polyvinyl alcohol, the as obtained mechanical robustness of a polymer composite might culminate in a mass that was around 15,000 times of its personal weight (Fig. 12a) [181]. A strain sensor was designed by the Cai et al. (2017), which has the highly stretchable (130%) $Ti_3C_2T_x$ MXene/carbon nanotube composite and its tensile strength was found to be more than 5000 cycles [182].

2.5.2. Oxidative and thermal stabilities of MXenes

If water and O_2 are used for the preparation of MXenes, the stability is considered as an important index. Enyashin and Ivanovskii [183] investigated through the density functional tight-binding approximations and found that hydroxylated carbonitrides having considerable C and N atoms are extremely thermodynamically stable and promising. Therefore, the simple MXene usually degrades due to severe oxygen exposure during the real time synthesis process at elevated temperature in the presence of water [115]. For instance, owing to the oxygen that triggers the nucleation process, the layered structure depreciates, in the form of colloidal $Ti_3C_2T_x$ MXenes solution in air. Therefore, MXene converts into TiO_2 over carbon sheets, as evidenced by the color change of TiO_2 precipitates from greenish/black to cloudy white (Fig. 12b) [184]. Li et al. found that at higher temperatures, the rutile TiO_2 was formed from the anatase TiO_2 in Ti_2C nanosheets at 500 K [185]. The MXene is found to be highly stable up to 1200 °C under argon environment [186]. To retain the original structure and properties, under the oxidizing environments, a wide range of stabilization methods such as high-energy mechanical milling in dimethyl

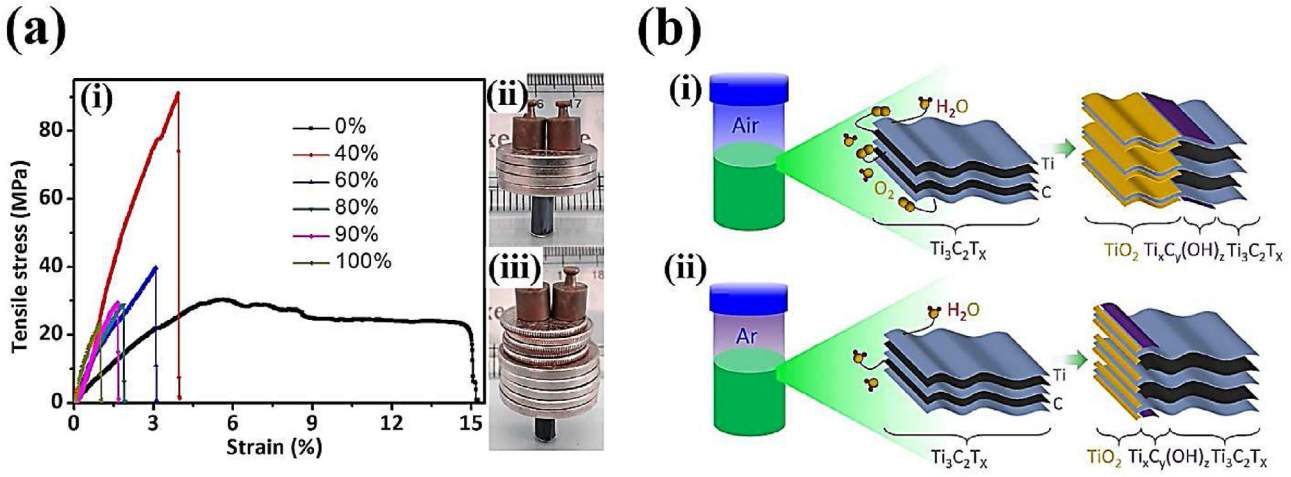

Fig. 12. (a) Mechanical characteristics of $Ti_3C_2T_x$, $Ti_3C_2T_x$/PVA, and cast PVA films. (i) A comparison of $Ti_3C_2T_x$/PVA films with varying $Ti_3C_2T_x$ composition. (ii) The 6-mm $Ti_3C_2T_x$ can bear 4000 times its own mass. (iii) A 6-mm $Ti_3C_2T_x$/PVA can sustain 15,000 times its own mass [181]. (b) Illustrations of d-$Ti_3C_2T_x$ MXenes degeneration in (i) Air/RT and (ii) Ar/RT [184].

sulfoxide (DMSO) [187] and carbon nano-plating method [188] have been used. The stability of MXenes could normally extend through the proper storage of MXenes in dry air or degassed oxygen-free water. In addition, after putting the colloidal MXenes under dry conditions in vacuum or dark refrigerated environment, the oxidation rate of colloidal MXene solution started [115].

2.5.3. Electronic properties

Typically, owing to the outer layer of transition metal elements, the non-terminated MXenes at the Fermi surface are found to be more metallic with high density of states (DOS). Usually, near the Fermi surface, the DOS is mainly conquered by transition metal-based d-electrons, while X atoms derive p-electrons paradigm energy bands at around −3 to −5 eV lower the Fermi surface [183]. As compared to the inner transition metal layers, the outer layers of transition metal on MXenes are proposed to perform a major role in their electronic properties [189]. Consequently, the electronic band structures are strongly influenced by the surface terminations, those are strongly bonded with the outer layer of the transition metal atoms. As, the new energy band under fermi surface is formed due to the entrapment of one or two electrons by the electronegative termination from the outer layer of transition metal, which in turn brought about the reduction of DOS density at or lowers the Fermi surface instinctively. It is due to the entrapment of only one electron by OH- and F- groups, and these groups in turn exhibiting a comparable effect onto the electronic structure of MXenes, while that of O-group have the ability to receive two electrons thereby, leaving or demonstrating the diverse effects. During the first MXene synthesis experiment by Naguib et al. [107] the simple Ti_3C_2 was found to have zero bandgap metal having limited density of states over Fermi level, while that of F and OH based surface functionalization breakdowns the bandgap at 0.05 eV and 0.1 eV, correspondingly (Fig. 13a). Moreover, the electric fields [190], and external strain [191], are commonly used to adjust the bandgaps of Sc_2CO_2 and Ti_2CO_2. In MXenes, the thermal [192] and electronic [193] transport are greatly influenced by the surface functional groups of MXenes. Predominantly, the O atoms-based surface functionalization reveals the substantial reduction in the electronic transmission, while that of F-terminated MXenes leads towards the higher electronic transmission [193]. Furthermore, in various MXenes, the nearly free electron (NFE) states are strongly induced by the surface terminations near Fermi level. They include e.g. $Hf_2N(OH)_2$, $Hf_2C(OH)_2$, $Ti_2C(OH)_2$, $Ta_2C(OH)_2$, $Zr_2C(OH)_2$, $Nb_2C(OH)_2$ and $Zr_2N(OH)_2$. The easy transport of electrons via scatter-free channels in MXenes is mainly attributed to the NFE states in MXenes (Fig. 13e) [113,194]. A wide range of terminated MXenes electronic properties have been demonstrated from both partly experimentally and theoretically point of view until now. Most of the MXenes are mainly derived from topologically insulating and highly insulating states [195], semiconducting [196], half-metallic [197], conductive metallic [198], Particularly in the applications of valley-spintronics and ferromagnetic devices, the half-metallic MXenes with 100% spin polarization at Fermi level and the topologically insulating MXenes with non-trivial edge states are found to be most favorable and thereby, attaining the considerable attention in this current era. The energy structure of

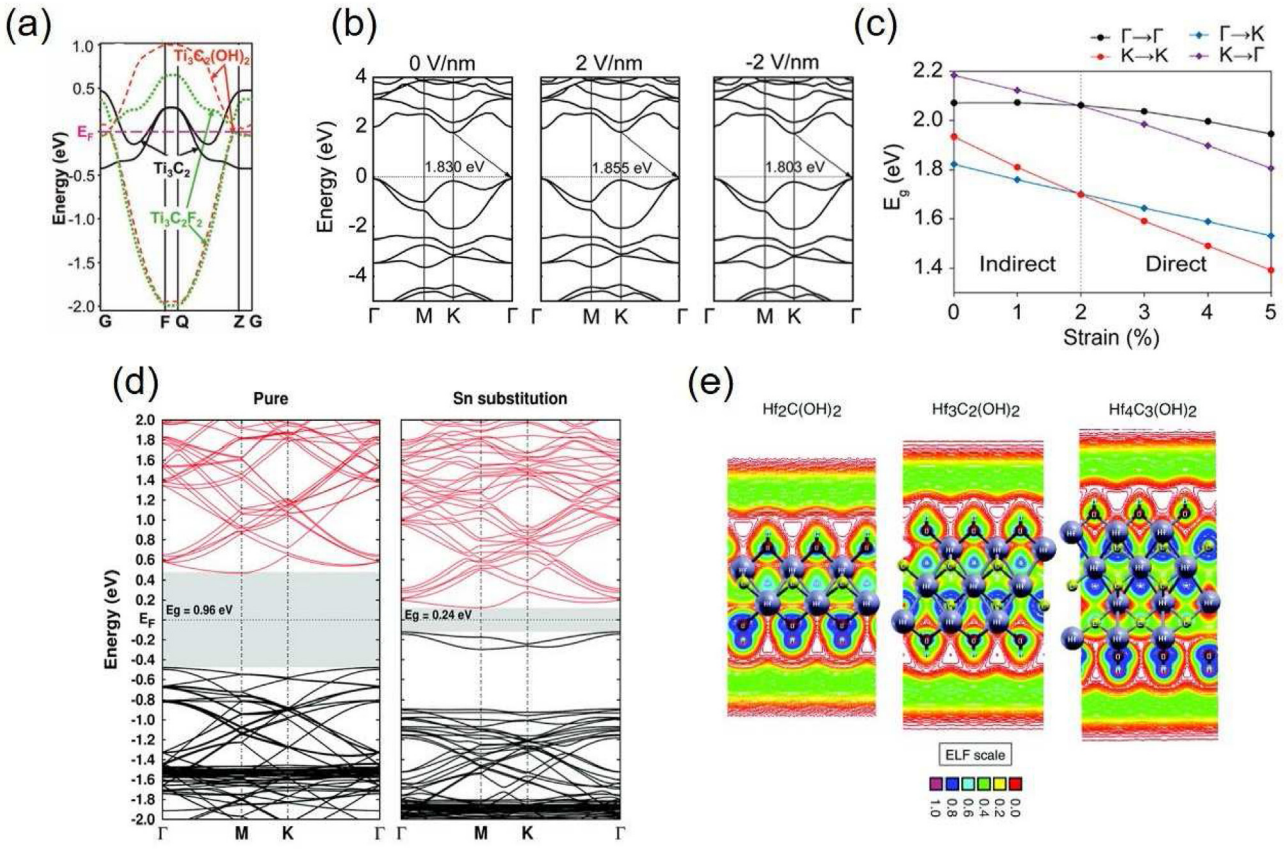

Fig. 13. MXene configuration characteristics (a) $Ti_3C_2T_x$ MXenes band design Adapted from Ref. [107], with the permission of John Wiley and Sons (b) Band structure of Sc_2CO_2 Adapted from Ref. [190] with the permission of the Royal Society of Chemistry. (c) Direct-indirect bandgap transformation of Sc_2CO_2 Adapted from Ref. [191], with the permission of the American Chemical Society (d) electronics topologies of Sc_2CF_2 with Sn substitution. Adapted from Ref. [203] with the permission of the Royal Society of Chemistry. (e) For $Hf_{n+1}Cn(OH)_2$ (n = 1, 2, and 3) MXenes with varied folds. Adapted from Ref. [113]. with the permission of the Royal Society of Chemistry.

MXenes could be efficiently changed by crystal lattice symmetry [199], strains [191], doping [200], via stoichiometry engineering [201], and external electric field (Fig. 13) [202]. But, still there is needed a strong experimental confirmation needed to support the idea about the exact electronic properties of MXenes.

2.5.4. Optical properties

The Random Phase approximation (RPA) method was used to study the optical properties of sample Ti_2C, Ti_2N, Ti_3C_2, and Ti_3N_2 [204]. Such kinds of compounds basically hold the metallic kinds of conductivity, and no other optical gaps further exist in the imaginary side of dielectric function. The plasmon energy for Ti_2C, Ti_2N, Ti_3C_2, and Ti_3N_2 was projected to be 10.00, 11.63, 10.81, and 11.38 eV with the continuous application of the electric field in parallel to the surface. Under the photon energy of 1 eV, the reflectivity ranges up to 100%, along with indicating the considerable aptitude of such kinds of compounds for the effective transmission of electromagnetic waves. The need and the importance of optical characteristics for a series of MXene layers have also been investigated. Hence, it is well known that the electronic structure [193], during the process of MXene preparation is greatly influenced by the surface termination, which has the greater impact on modifying the optical characteristics of MXenes [205], However, this is also well understood that compared to that of O terminated and pristine MXenes, the OH and F terminated surfaces of Ti_3C_2 exhibit smaller absorption coefficients. (Fig. 14a), thereby demonstrating the appropriate properties of the application of transparent electrodes [206]. Thus, this kind of information clearly indicates the importance of controlling the surface functional groups or termination to properly tune the optical properties of compounds [207]. Additional outcomes show that O-functionalized M_2C (M = Ti, Zr, Hf) encompasses the visible-light absorption by comparatively huge area below the $\varepsilon 2(\omega)$ curve. Normally, the absorption coefficients are found to be in this subsequent direction: $Ti_2CO_2 > Zr_2CO_2 > Hf_2CO_2$ (Fig. 14b) [208]. Likewise, the diluted $ScNbCO_2$ and Sc_2CO_2, absorption coefficients with and without strain have also been stated in detail. The B9%-$ScNbCO_2$, $ScNbCO_2$ and U3%-$ScNbCO_2$, demonstrate the main absorption peak in the visible region about 20 times higher than Sc_2CO_2, while that of Sc_2CO_2 absorption peaks are positioned in the deep UV region [209]. Moreover, the strain could properly tune the bandgap, which has the significant impact on the absorption coefficient of Zr_2CO_2 [210]. Nevertheless, there are still fundamental weaknesses in the above listed calculations [211]. Like other low-dimensional materials the MXenes should be affected by a large excitonic effect caused by 2D screening, where requirement of electron hole interactions should be taken into account to quantitatively demonstrate the absorption profiles [212]. Currently, with the aid of GW + PRA/BSE calculations for the determination of both light absorbance and the quasiparticle bandgap, Zhou et al. theoretically examined the absorbance spectra of 2D Sc_2CCl_2 (Fig. 14c). For 1L, 2L and 3L Sc_2CCl_2, optical bandgaps were found to be about 1.52 eV, with average exciton binding energies of 0.75, 0.67, 0.63 eV, individually. The promising light-harvesting ability could be further determined by the calculated absorbed photon flux of 1L, 2L and 3L Sc_2CCl_2, which was found to be 1.32, 4.51 and 7.80 mA/cm^2, respectively [213]. In the absorption spectra of the Mo_2CO_2/W_2CO_2 heterojunction that exhibit Type II band orientation, the corners of one material's conduction and valence bands are situated lesser than the corners of another material's respective bands. They further demonstrate a blue transition in comparison to the secluded layers due to interatomic charge transition [214].

2.5.5. Magnetic properties and theoretical investigation

To determinate the magnetic nature of MXenes, the surface terminations play a vital role in this regard. Most of the MXenes are found to be non-magnetic in nature due to the strong covalent bonding between M, X, and surface functional groups. MXenes, on

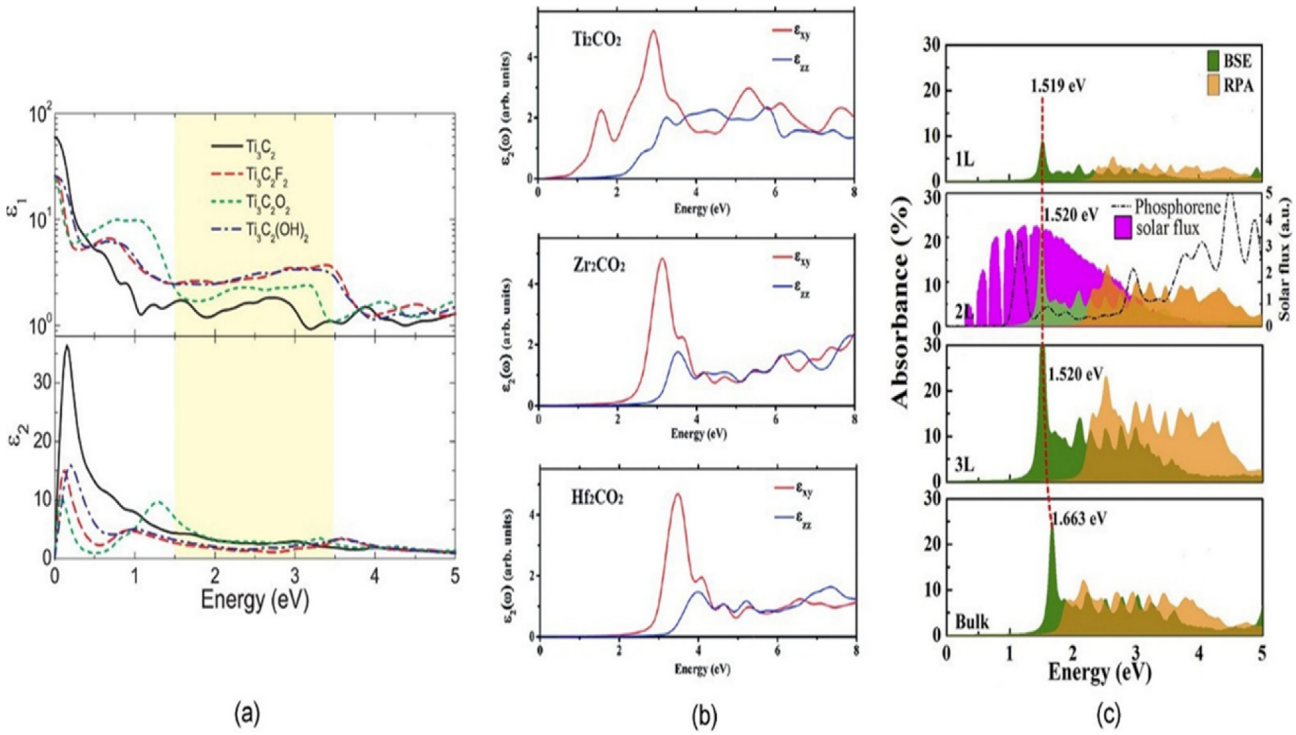

Fig. 14. (a) Realistic (ε1) and hypothetical (ε2) dielectric functions for Ti_3C_2, $Ti_3C_2F_2$, $Ti_3C_2O_2$, and $Ti_3C_2(OH)_2$ Adapted from Ref. [206], with the permission of AIP Publishing (b) hypothetical dielectric values of M_2CO_2 Adapted from Ref. [208] with the permission of the Royal Society of Chemistry (c) Estimated optically absorption bands of 1, 2, 3 sheets and pristine Sc_2CCl_2 for z-direction incident illumination and oriented in-plane. Adapted from Ref. [213]. with the permission of the American Chemical Society.

the other hand, could exhibit the magnetic properties owing to external in-plane strain that breakdown the robust covalent bonds such as M–A and M–M bonds or rise in electron density near Fermi level associated with transition metal (M) d orbitals [215]. Moreover, it is well known that 2D Ti_3N_2 and Ti_3C_2 are antiferromagnetic in nature, while that of 2D Cr_2C and Cr_2N are found to be ferromagnetic [216]. The introduction of surface terminations via functionalization, leads to the reduction of electron density near Fermi energy level, which further brought about the diminishing of the magnetic properties. The wide variety of magnetic properties are observed in the family of MXenes-based materials in the form of especially two-dimensional layers materials [216]. As, the 2D based MXenes are considered to be ferromagnetic in nature and they can be easily exfoliated from their MAX phases [217]. They include 2D Cr_3C_2, Ta_3C_2, Cr_2N, and Cr_2C [216]. Moreover, other 2D based MXenes compounds Ti_3N_2 and Ti_3C_2 are considered to be antiferromagnetic in nature, while that of Ti_2N and Ti_2C are perceived to have half-metallic ferromagnetism properties in nature [218]. In addition to that, the high Neel temperature of 720 K the Mn_2C monolayer nature as predicted by the theoretical calculations is considered to have antiferromagnetic properties [219]. Because, over the higher Curie temperature of (520 K), the appropriate surface functional groups (OH, Cl and F) directly convert into a ferromagnetic state [220]. Though the some bare MXenes that are experimentally confirmed along with terminated by the OH, O and F and other atoms, are basically projected to be ferromagnetic in nature [221]. Consequently, this is relatively a difficult task to fabricate the simple MXenes such as Cr_2C. Therefore, the current research progress in MXenes-based materials shows the enhanced electrical conductivity of MXenes after partially removed surface termination process [222]. However, this is understood that Cr_2N and Cr_2C MXenes functionalized by the (OH, Cl, O, F, and H) groups are magnetic in nature [223], while few of the MXenes shows ferromagnetic-to-antiferromagnetic (FM-AFM) shifts Because, the d-orbitals of Cr atoms basically instigate the magnetic properties of these MXenes. As, the energy difference of Cr-based MXenes AFM and FM and configurations are quite big, and it may be sustaining the magnetic properties of Cr based MXenes approximately near to room temperature. Moreover, the ferromagnetic nature of non-terminated Cr_2C has also been investigated by Si et al. [224] which has an average half-metallic gap of 2.85 eV (Fig. 15d). Similarly, his research pointed out that the peripatetic Cr d-orbital electrons are responsible only for the ferromagnetism behavior while that of ferromagnetic-antiferromagnetic (FM-AFM) behavior is only induced by the localization of d electrons localization, which is initiated through the surface terminations (Cl, H, OH or F) thus, leads to the transitions of metal-into-insulator. The well-equipped (100%) spin polarization of electrons around the Fermi level of Ferrimagnetic half-metals further makes them more viable material in the spintronic applications. In addition, it has been determined that the oxygen-terminated Cr_2NO_2 shows ferromagnetic properties, while that of OH and F passivated Cr_2N MXenes has antiferromagnetic properties, has antiferromagnetic properties by having enhanced half-metal gap of 2.79 eV [225]. The simple Cr_3C_2

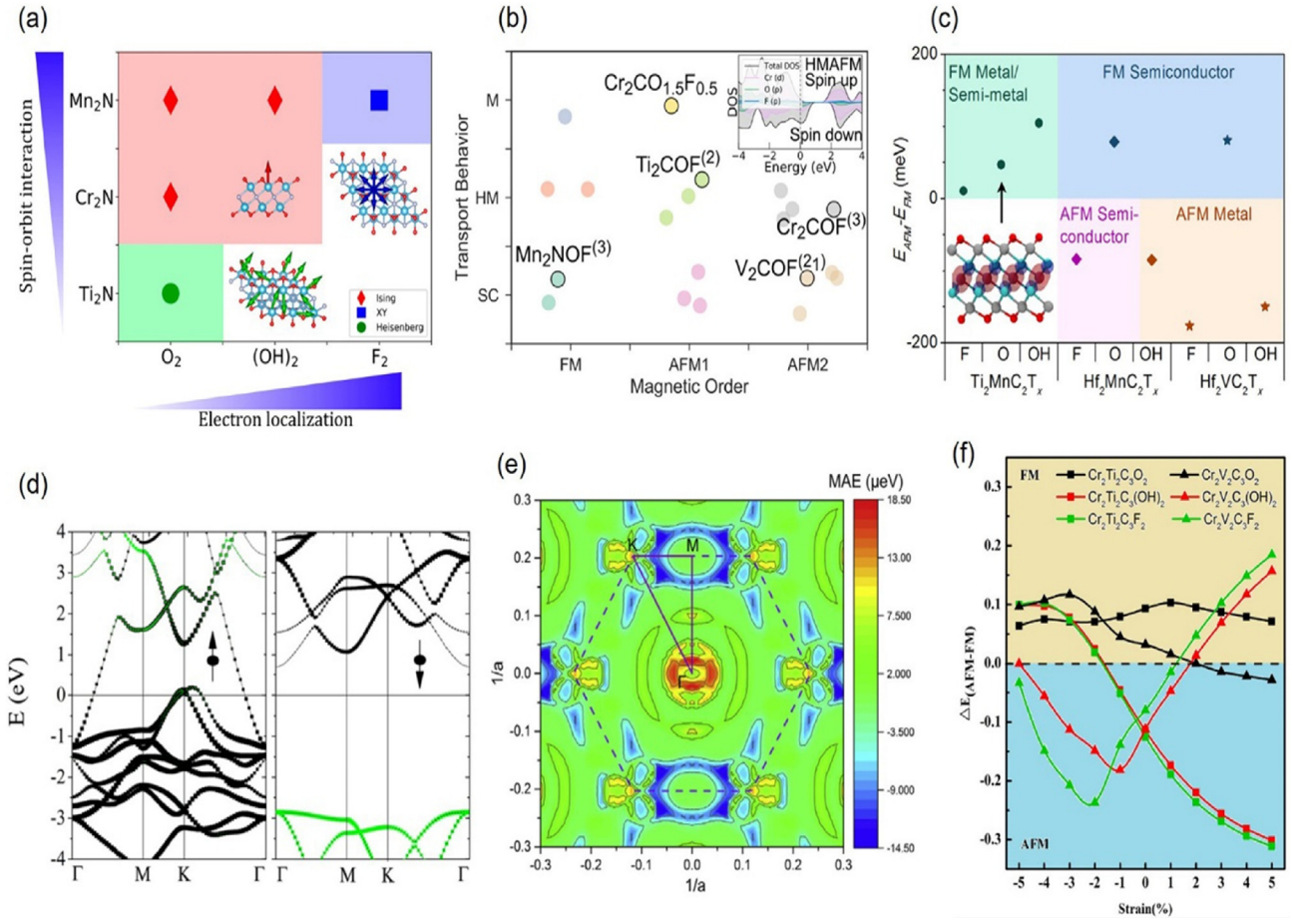

Fig. 15. (a) M_2N (M = Ti, Cr, Mn) magnetic modes Adopted from Ref. [228], American Chemical Society. (b) Janus MXenes have a wide range of mobility and dielectric properties. Adopted from Ref. [232], American Chemical Society. (c) Interchange potential and electromagnetic modes in hybrid Ti and Hf-based MXene. Adopted from Ref. [230], American Chemical Society (d) Bands configuration of Cr_2C MXene [224] American Chemical Society. (e) The hexagon shaped Brillouin region of Fe_2C MXene has large negative magnetic anisotropy potential. Adopted from Ref. [231], Elsevier. (f) Electrostatic attributes of $Cr_2M_2C_3T_2$ (M = Ti and V, T = OH, O, and F). Adopted from Ref. [226], Elsevier.

monolayer by having an average magnetic moment of 3.9 μB per formula unit was found to be highly ferromagnetic and metallic in nature. On the other hand, the half metallic nature of Cr_3C_2 was observed due to constant increase of strains up to 3%, by having an average half-metallic gap of 1.2 eV, thus such behavior is only sustained towards larger strains [197]. Hence, the Cr-based carbides ($Cr_2M_2C_3T_2$; M = Ti, V Nb, and Ta; T = OH, O, and F) materials magnetic properties have also been determined by Yang et al. [226]. According to the results of theoretical calculation, the anti-ferromagnetic arrangement is suitable for the most of the materials having the magnetic moment of Cr atoms more than that of 1.9 μB, whereas the $Cr_2Ti_2C_3O_2$ and $Cr_2V_2C_3O_2$ have energetically favorable anti-ferromagnetic properties. Apart from $Cr_2Ti_2C_3O_2$, where only FM is constantly energetically viable, as the extensile strain changing from −5% to 5%, then, a possible transition of FM-to-AFM is usually observed for $Cr_2V_2C_3T_2$ and $Cr_2Ti_2C_3T_2$ (Fig. 15f). The Cr_2NO_2, Ti_2NO_2 and Mn_2NT_x with diverse range of surface terminations (T = F, OH and O), exhibited strong half-metallic ferromagnetism owing to high Curie temperatures and magnetic moments (up to 9 μB per unit cell), whereas the intralayer AFM nature was observed for $Cr_2N(OH)_2$, Cr_2NF_2, $V_2N(OH)_2$, V_2NO_2, V_2NF_2, $Ti_2N(OH)_2$ and Ti_2NF_2 [120]. In oxygen terminated MXenes during the process of electron delocalization, the double exchange interaction usually occurred, which further results into FM ground state. The superexchange interaction is mainly accelerated due to the electron localization induced by the F termination and thus in turn leads to the AFM ground state. During the $Sc_2C(OH)_2$ conversion into Sc_2CO_2 MXenes, the maximum magnetic moment was observed to be 1.00 μB [227]. According to Frey et al. investigation, the manipulation of the chemical compositions of MXenes nitrides leads to the desired spin symmetry in M_2NT_x nitrides (M = Ti, Cr, Mn [228]. To obtain the various magnetic interactions (Ising, XY, or Heisenberg), the careful controlling of the spin symmetries through spin-orbit coupling mechanism is considered to be an important factor, which is presented in Fig. 15a. So far, the magnetic properties of a wide range of mixed MXenes such as $Cr_2M\ C_2T_2$ (M = Ti and V, T = F, OH, and O) have been reported. On the basis of surface termination, the MXene properties could be varied from ferro-magnetic ($Cr_2VC_2(OH)_2$, $Cr_2VC_2F_2$, and $Cr_2VC_2O_2$), to antiferro-magnetic ($Cr_2TiC_2F_2$ and $Cr_2TiC_2(OH)_2$) and non-magnetic ($Cr_2TiC_2O_2$), or metallic to semiconducting nature [229]. With the aid of small electric fields, the magnetism in Janus MXenes M_2XOxF_{2-x} (M = initial transition metal, X = nitrogen or carbon, and x = 0.5, 1, or 1.5) with asymmetric surface functionalization can be easily controlled (Fig. 15b) The high curie temperatures (495–1133 K) and strong ferromagnetism in a recent study has been investigated for F, OH and O terminated Ti_2MnC_2Tx monolayers (Fig. 17c) and it is found to be higher than already reported 2D ferromagnetic compounds [230]. The ferromagnetism of $Hf_2VC_2O_2$ and $Hf_2MnC_2O_2$ has also been reported in the similar research investigation. The in-plane magnetization of Fe_2C is ascribed to more negative magnetic anisotropy energy around hexagonal Brillouin zone sides (Fig. 15e) [231].

2.5.6. Topological properties

The sum of surface terminated MXenes are observed to be 2D topological insulators (TI) in nature [233] where electrons proliferate towards the edge position, and thus, leads to the indulgence of slow transference, which is appropriate for low power electronic devices. Even though most of the MXenes are found to be semiconductors and pure metallic, where electrons proliferate towards the edge states by following the less transference [234]. The relativistic spin-orbit coupling (SOC) actually induced the 2D topological insulating phase and it has a significant impact on the

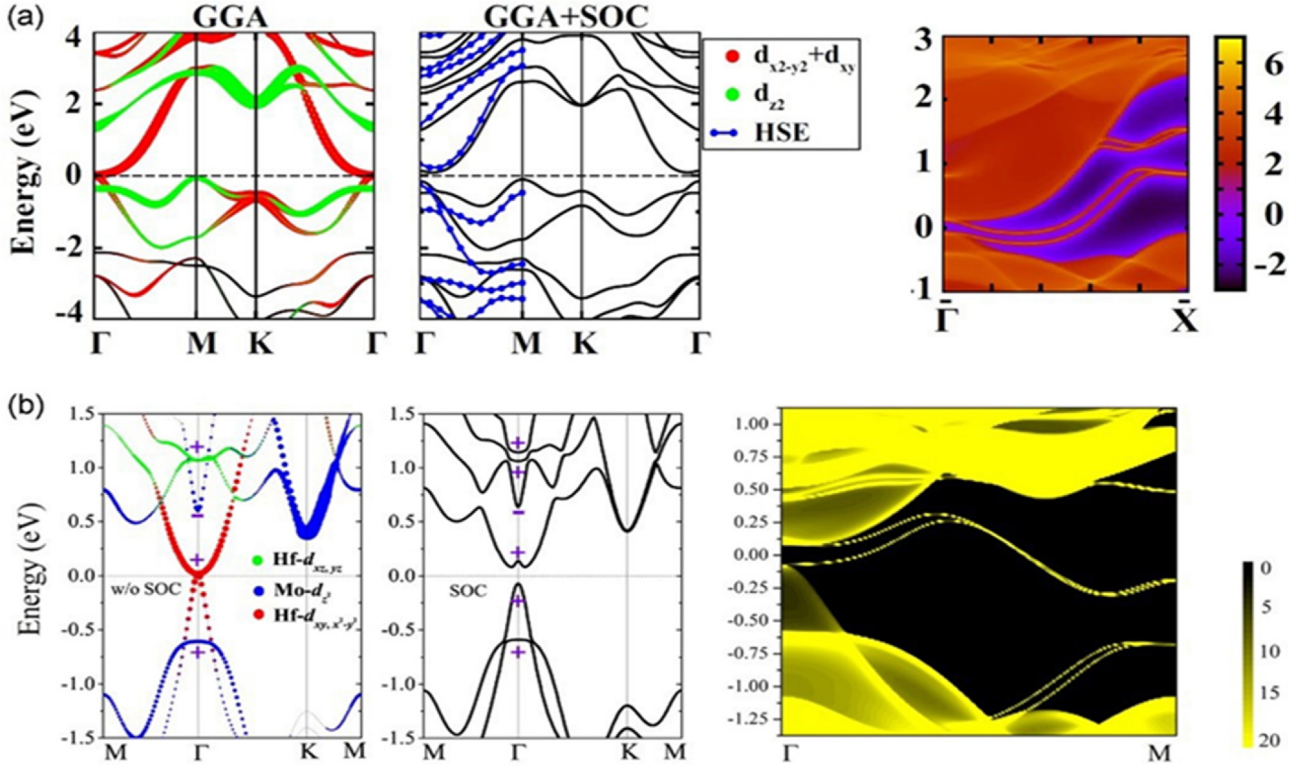

Fig. 16. Band configurations of (a) W_2CO_2 and (b) $Mo_2HfC_2O_2$, and their boundary energies. Adopted from ref. (a,b) [236,237]. with the permission of the American Physical Society.

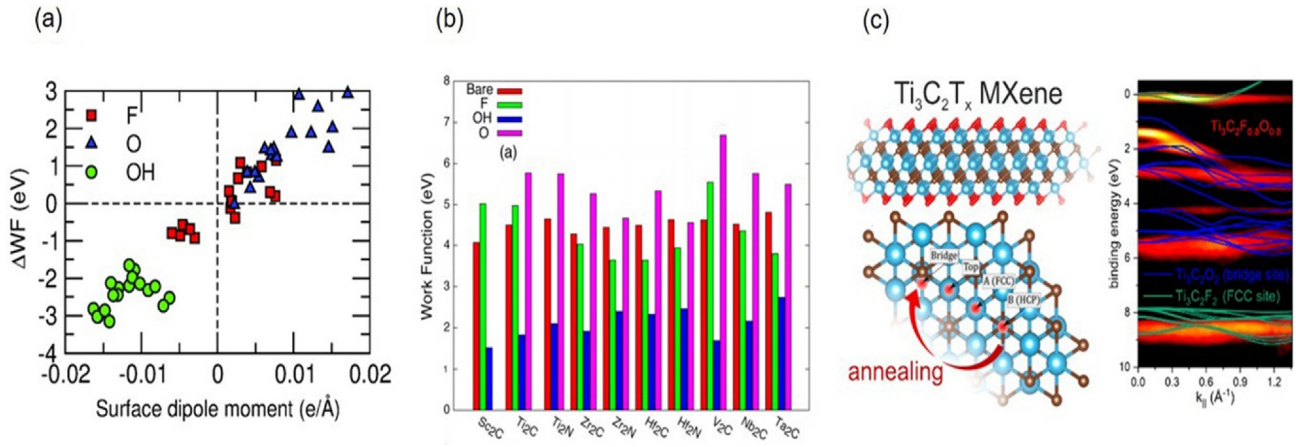

Fig. 17. (a) Work function changes. Adopted from Ref. [240], with the permission of the Royal Society of Chemistry (b) The work functions of M2C and M′2 N. Adopted from Ref. [241], with the permission of the American Physical Society (c) Thermal depiction of $Ti_3C_2T_x$ MXenes. The illustration on the right demonstrates the curvature spectral range of $Ti_3C_2F_{0.8}O_{0.8}$ (yellow-red), as well as two energy configurations of $Ti_3C_2O_2$ (blue) and $Ti_3C_2F_2$ (red) (green). Adopted from Ref. [243], with the permission of American Chemical Society.

electronic structure of materials, which are mainly derived from heavy elements [235]. The recent literature shows the topological insulating MXenes, which are mainly composed of Hf, Zr, Mo, Ti and W, atoms. By means of GGA (HSE06) functional calculations, the large SOC-induced bandgaps ranging 0.194 (0.472) eV in W_2CO_2 based O-functionalized M_2CO_2 (M = W, Mo, and Cr) are found to be 2D TIs (Fig. 16a) [236]. Moreover, in the Ti_2CF_2 phase, a wide variety of giant spin-orbit splitting and Dirac cones are observed [195]. In addition, it is well known that the 2D band structure of MXenes is not destroyed by the peripheral trepidations and multilayer phases. Independently, along with double transition metal elements $Mo_2MC_2O_2$ (M = Ti, Zr, or Hf), the Khazaei et al. and Si et al. noticed the presence of 2D topological insulating phase in MXenes presented in (Fig. 16b) [237]. The $W_2HfC_2O_2$ are projected to have largest bandgap of 0.285 eV (0.409 eV at the HSE06 level), while that of $Mo_2MC_2O_2$ predicted to have sizeable gaps of 0.1–0.2 eV, which is mainly depends upon the M atoms. In $Mo_2M_2C_3O_2$ (M = Ti, Zr, or Hf), the presence of Quantum Spin Hall (QSH) phase was also observed where various kinds of M atoms are found to be considerably participate towards the SOC-induced gap from 38 to 152 meV [233]. According to Liang et al. investigation, the nitride based MXenes ($Ti_3N_2F_2$) are perceived to be 2D TI in nature, while that of the transformation of $Hf_3N_2F_2$ and $Zr_3N_2F_2$ into 2D TI materials is possible by the application of lattice strain [238]. Due to substitutional doping [200], proximity induced effects [239], and charge transfer [202], due to applying the electric field, the $Sc_2C(OH)_2$ based MXenes, which is regarded as innovative kind of s-pd band inversion topological insulator could be further turn into

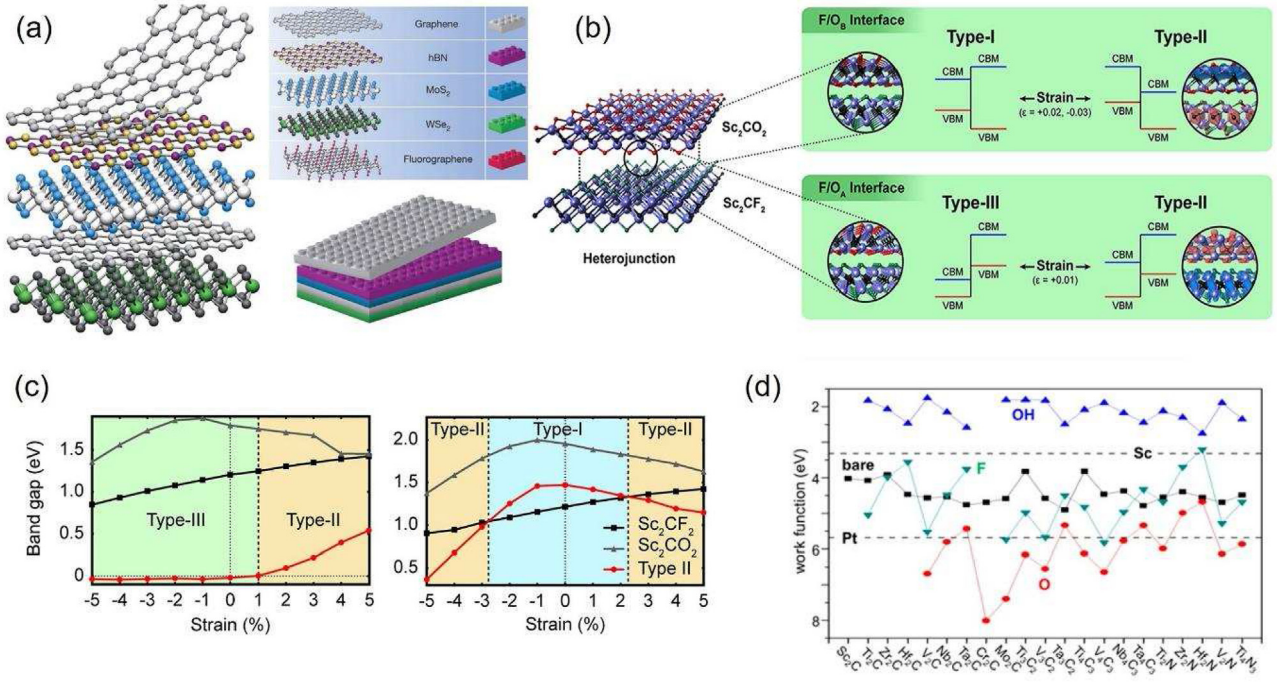

Fig. 18. (a) Description of the synthesis of heterojunctions schematically. Adopted form Ref. [247], with the permission of springer nature (b) Multiple heterostructures of MXenes. (c) Bandgap illustration for (black) Sc_2CF_2, (gray) Sc_2CO_2, and (red) type-II heterostructures. Adopted from Ref. [253]· with the permission of the American chemical society (d) MXene work functions based on terminating sort. Adopted from Ref. [246], with the permission of the American Chemical Society.

the topological insulating phase. According to the parabolic energy dispersion in $Sc_2C(OH)_2$, the high carrier mobility is mainly induced by the free electron states, which are considered to be superlative surface transportation networks [194]. However, such kinds of states do not consist of any element and mainly exist near and above the Fermi level.

2.5.7. Electronic work functions

Actually, the electronic work function (WF) is referring to the energy difference between vacuum level and Fermi level, which further determines the minimum amount of energy which is mandatory for removing the electron from the MXene surface. The alteration of work function than that of simple MXenes is mainly related with the persuaded surface dipoles that are being produced via surface functional groups and further moves in the material Fermi level owing to electronic restructuring [240]. Thus, the altered work function (ΔWF) could be merely articulated as $\Delta WF = -(e/\varepsilon_0)\ \Delta P$, where ΔP is the variation in the total dipole moment. Typically, the work function of MXenes follows this trend: O–> F–> bare > OH- functionalized MXenes (Fig. 17a). After studying a wide range of terminated MXenes (Ta_2X, Hf_2X, Nb_2X, Zr_2X, Cr_2X, Mo_2X, V_2X, Ti_2X and Sc_2X, X = C or N), the projected lowermost work function is 1.2 eV in the OH-functionalized MXenes (Fig. 17b) [241], which is due to the metal O2p orbitals and d orbitals hybridization [242]. The lowermost work function has also been reported for the methoxylat-ionized niobium carbide $Nb_3C_2(OCH_3)_2$ MXenes with average value of 0.9 eV. For thermionic devices and field emitter cathodes, the lowest work function of MXenes is considered to be the most auspicious in this regard. But experimental investigation still didn't confirm such a kind of ultralow work function. Thus, depending upon the annealing treatment temperature, Schultz et al. [243] investigated that the WF of $Ti_3C_2T_x$ MXenes could be easily shifted in the range of 3.9–4.8 eV, and it further adjust the surface functional groups (Fig. 17c). By using a Kelvin probe equipped with an atomic force microscope, the terminated Ti_3C_2 MXenes thin film work function was measured to be 5.28 eV. Especially, in the presence of water, the OH termination might be deprotonated thereby, leading to the ending of the layer with O^- as a substitute, and it further brought about the high work function. The work function of O^- terminated Ti_3C_2 MXenes, which could be low up to 4.6 eV, by producing a better electrical interaction with equally tin monoxide (SnO) and zinc oxide (ZnO) semiconductors, has been reported in another study by showing negligible band offsets [244]. In addition to that, the van der Waals forces play an important role at room temperature by making $Ti_3C_2T_X$ MXene with a work function of 4.37 eV to form a good Schottky contact with n-Si, which further could perform as a transparent electrode, while contributing in the parting and transportation of photo-induced carriers in the self-driven photodetectors [245]. The role of surface termination has also been reported in terms of their contribution for producing the Schottky-barrier-free contacts with 2D semiconductors [246].

2.5.8. MXenes heterostructures and interfaces

On the basis of MXenes and other different kinds of 2D materials, the proper construction of Layer-by-layer van der Waals (vdW) heterostructures could also be possible, by showing fascinating electrical features, which are presented in Fig. 18a [247]. With the aid of interface induced strain, the proximity effect and the direct charge transfer phenomenon, the proper manipulation and tuning of electronic properties of such kinds of heterostructures is easier. Moreover, it has been predicted by the theoretical investigation that the electronic structure of MXenes is strongly influenced by the formation of heterostructure compounds [248]. Due to the considerable presence of a wide range of transition metal dichalcogenides and MXenes, the formation of appropriate heterostructures could be possible via slight lattice divergence, thereby, consenting to fabricate and further studied the different kind of interfaces [249]. The vdW-type compound shows non-covalent interaction in $MoS_2/Ti_2C(OH)_2$ and MoS_2/Ti_2CF_2 interface owing to the unsaturated nature of surface states, while that of MoS_2/Ti_2C revealed strong chemical bonding (as observed later in graphene/Ti_2C) [250]. The conversion of electronic structure of MoS_2 into metallic type structure is due to the distinct metallic properties of Ti_2C, whereas two further heterostructures reserve their semiconductor type characteristics [251]. Furthermore, the alteration of some TMD/Sc_2CF_2 hetero-bilayers into type-II (0.13–1.18 eV) indirect bandgap semiconductors is also possible [252]. Similarly, the MoS_2/TM_2CO_2 (TM = Ti, Zr, or Hf) composites also exhibit type-II semiconducting properties [248]. By combining various kinds of MXene layers, the wide variety of types (I, II, and III) of heterostructures could be easily fabricated via (2D $Sc_2C(OH)_2$, Sc_2CO_2 and Sc_2CF_2) (Fig. 18b). In the as-synthesized heterostructure, the mutual band configurations of specific materials basically predicted the Type I, Type II and Type III based heterostructures. The complete overlap of one bandgap with other, is mainly found in Type I heterostructure, which in turn constructing the ostensible straddling gap, while both valence band and conduction band edges are found to be lower than other second semiconductor band edges in the Type II heterostructure (staggered gap). The overlapping of valence and conduction bands from other semiconductors was observed in Type III heterostructure, to construct a semimetal-like gap over interface sites (broken gap). For example, the type-III heterostructure formation mainly depends upon the O/OH and F/OH system, but whenever the O- and functionalized MXenes are slanted, the type-I band arrangement is obviously developed. The formation of type-II hetero-bilayers is mainly accomplished by the applied Equibiaxial strain, which is presented in Fig. 18c [253]. Machine learning with GW level precision, was used to investigate the band positions of different kinds of MXenes [68]. For the obvious Ohmic contacts, the electrode materials were invented by means of calculating the transportation properties of $Ta_2C(OH)_2$, Ta_2CF_2, Ta_2C and MoS_2 MXenes. Obtained findings clearly indicate that Ohmic contacts exist between $Ta_2C(OH)_2$, Ta_2CF_2 and MoS_2 electrodes, thereby demonstrating the two-fold superior activity of the latter one [249]. The n-type Schottky barrier of 0.85 eV and 0.26 eV is mainly found in $MoS_2/Ti_2C(OH)_2$ and MoS_2/Ti_2CF_2 and heterojunctions, respectively [251]. The two major factors including applied electric fields and desired surface functionalization can easily control the Schottky barriers in metal/semiconductor/heterostructures [246]. The work function of MXenes, which mainly depends upon the specific functional group, actually governs the Schottky barriers (Fig. 18d). According to First-principle calculations the OH-terminated MXenes could make an electron barrier-free interaction with 2D semiconductors, while that of O-terminated MXenes i.e. $Ti_4N_3O_2$, $Ti_3C_2O_2$, Ti_2NO_2, $Ti_4C_3O_2$, V_2NO_2, $V_4C_3O_2$, $V_3C_2O_2$, V_2CO_2, Mo_2CO_2, Cr_2CO_2 and Nb_2CO_2, could produce a hole barrier-free interaction with WSe_2. The possibility of the formation of Mo_2C/MoS_2 heterostructure during an epitaxial synthesis of MoS_2 with a low Schottky barrier height (26 meV) has also been confirmed by the new combined experimental/theoretical calculation [168]. With TMD, the as-predicted heterostructure MXenes M_2CO_2 (M: Ti, Zr, Hf), the thermal conductivity was not reduced [254].

After preserving the energy dispersion and n-doping, the graphene/$Hf_2C(OH)_2$ heterostructure moves the Dirac cone of graphene into −1.1 eV [194]. Similar kind of doping was observed for $Ti_3C_2(OH)_2$ interface, whereas F^- and O^- terminated surfaces are controlling the p-doping, which is basically due to the better work function principles as compared to graphene (Fig. 19) [255]. With

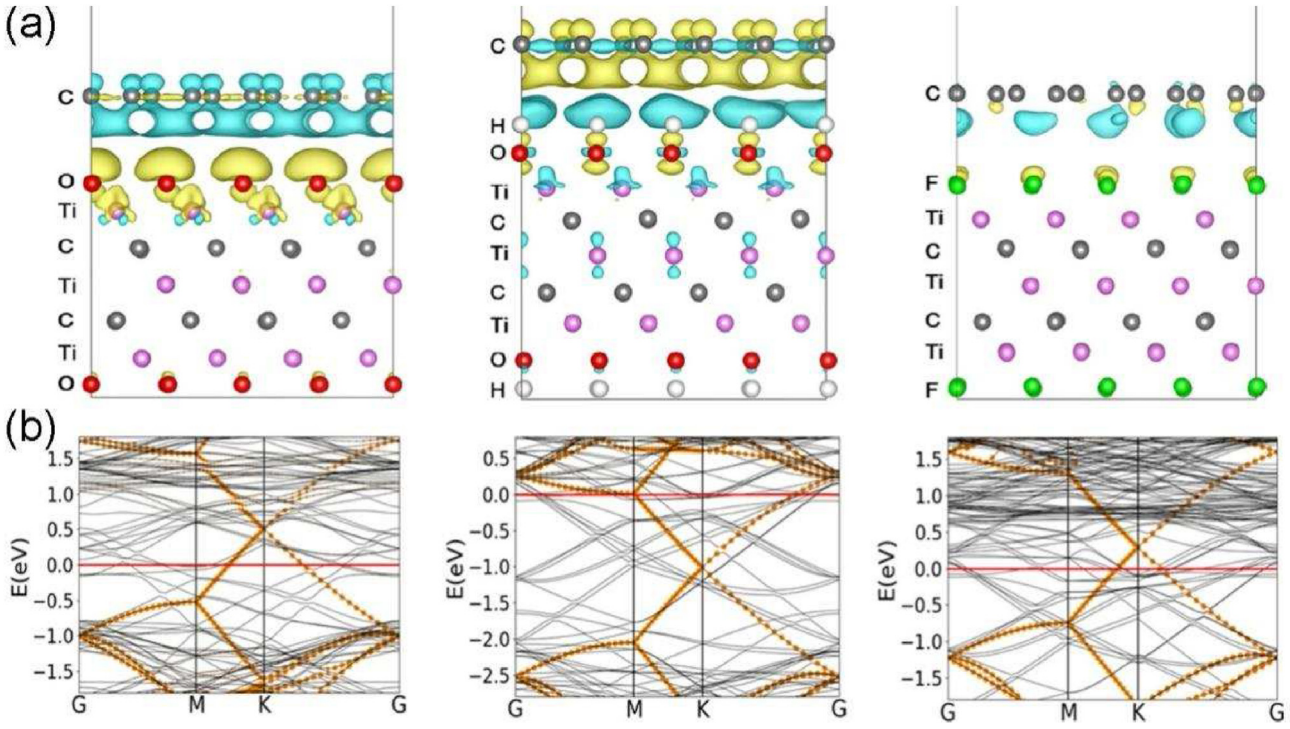

Fig. 19. (a) Electron density variation between $Ti_3C_2O_2$/graphene, $Ti_3C_2(OH)_2$/graphene, $Ti_3C_2F_2$/graphene and (b) their band configuration. Adopted from Ref. [255], with the permission of the American Physical Society.

the aim of finding the constructive impact of graphene [256], the F^- and OH^- functionalized MXenes [257], and the MXenes/graphene heterostructures application has also been studied for Li-ion batteries. The small opening of the Dirac cone was observed in silicene/Sc_2CF_2 heterojunctions, whereas the band distribution is well-maintained, which is escorted by an actual mass of small electrons [258].

2.6. Interfacial and morphological characteristics of MXenes

2.6.1. Atomic lattice to mesoscale

MXenes, which are prepared via selective etching method are usually inherit the hexagonal atomic lattice P63/mmc from their MAX parents' crystal structure. The M atoms are hexagonally close-packed, where the X atoms covers the octahedral interstitial sites. The MXenes's atom filling arrangements are MXM, MXM'XM, MXM'X'M'XM for $M_{n+1}X_n$ (n = 1, 2, 3), respectively [165] wherein, M and M' (X and X′) specify diverse equilibrium positions intended for transition metal atoms (carbon or nitride atoms). The M and M′ sites could be engaged via one or two types of transition metal elements, which in turn makes the mono-M element, solid-solution M elements and ordered double-M elements MXenes [154]. Therefore, the transition metal (carbides/nitrides/carbonitrides) atomic lattice depending upon the fabrication route could be further changed among a wide range of MXenes. For example, the ultra-thin α-Mo_2C film, which was synthesized via CVD bottom-up technique in turn shows the features of orthorhombic lattice type film [259]. Therefore, following the various chemical transformation temperatures, the structure of transition metal nitrides, which was attained via ammoniation of their carbide precursors, obviously shows the various kinds of lattice alteration, which in turn brought about the trigonal V_2N formations [169]. The transition metal nitrides Mn_3N_2 fabricated thru salt-templated preparation route also showed the alike square symmetry along the (001) direction (c axis) with its prototype fcc-KCl, as well as exhibiting a hexagonal-like symmetry in the [010] (b axis) plane [172]. The ordered metal di-vacancies encompassing MXenes (Mo/Nb/W1.33C) shows lattice with hexagonal symmetry, and various kinds of atomic lattices could co-exist there [260]. The surface terminations, Fermi energies, cohesive energies, lattice parameters, and transition metal elements, could also possibly change the phase transition between honeycomb (H) and centered honeycomb (T) lattices [261]. The atomic piling arrangement of M atoms is the major difference between H and T. However during the carburization process the lattice of an MXenes by changing the annealing temperature could be easily reformed [167]. According to Zhang et al. investigation, both a and c axes of Ti_3C_2 MXenes at high peripheral pressure could be clasped, while that of no phase alteration was detected at the pressure range of 26.7 GPa, [262]. The distinct mesoscopic morphologies have been reported as a result of different crystal lattices of MXenes, resulting from different techniques subsequent to treatment and synthesis techniques. The MXenes showed a diverse range of microscopic properties mainly depending upon their preparation source, such as different strategies adopted subsequent to treatment and synthetic strategies. Moreover, it has been reported that the MXenes produced via selective etching process primarily shows accordion-like multilayer structure morphology (Fig. 20a, d) [107]. The formation of ultrasmall MXenes quantum dots is possible by the long-time ultrasonication of a MXenes colloid during the delamination process (Fig. 20l). In addition to this, it is well known that the homogenous MXenes without surface termination with large surface area are mainly produced through bottom-up CVD construction strategy (Fig. 20c), and it is considered as a promising to further investigate their chemical and physical properties [263]. The high specific surface area containing three-dimensional interconnected porous frameworks of MXenes nanoribbons is considered to be the most promising material in the field of EMI, catalysis and energy storage. According to Natu et al. [264] investigation, the highly porous crumpled MXenes sediments could be produced only

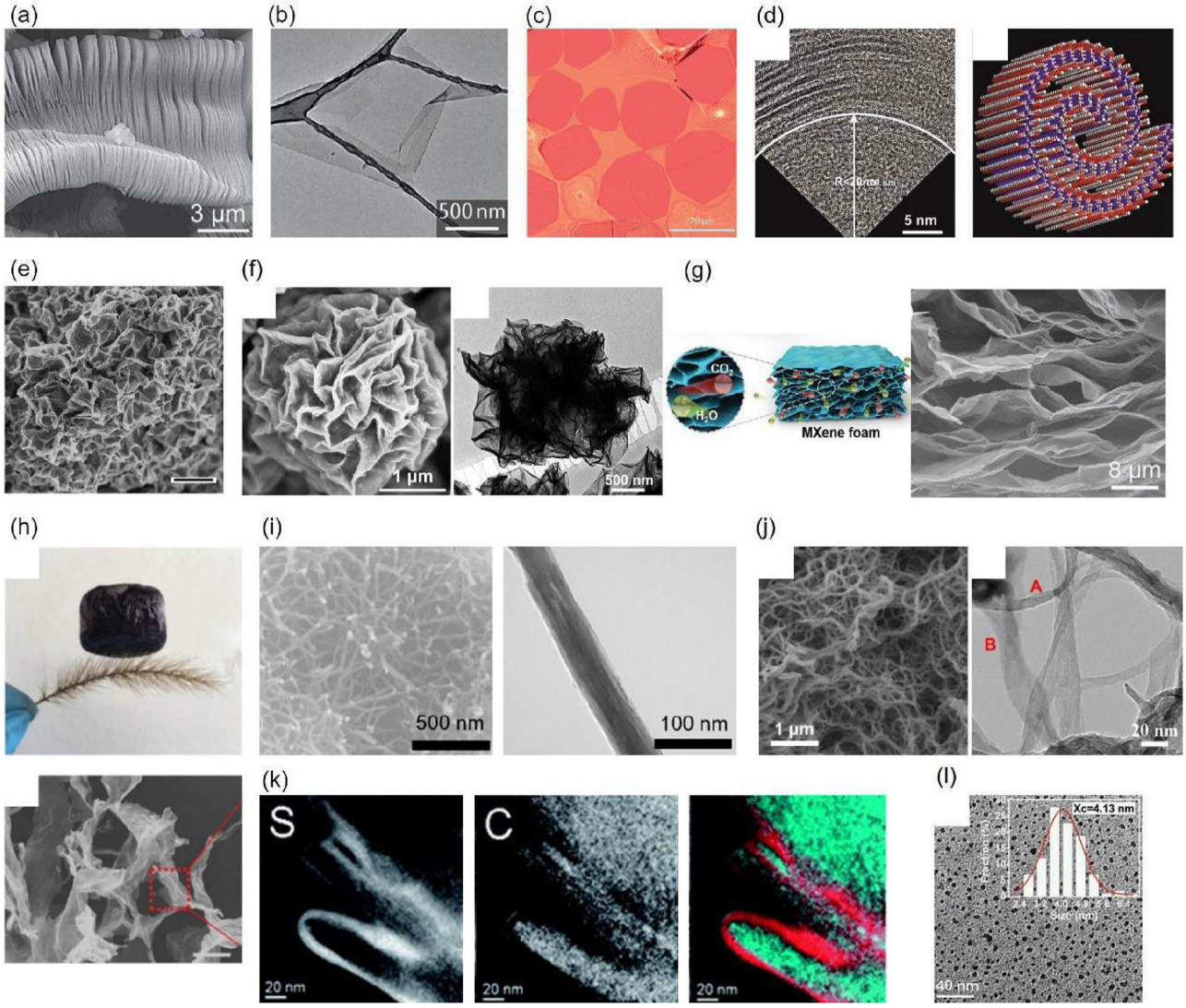

Fig. 20. Morphology of MXenes. (a) MXene fabrication through acid etching. Adopted from Ref. [107], with the permission of the American Chemical Society (b) MXenes with delaminated flakes. Adopted from Ref. [108], with the permission of Springer Nature (c) Optical view of nanostructures Mo_2C MXene nanoparticles on Cu/Mo. Adopted from Ref. [263], with the permission of Springer Nature. (d) TEM of Ti_3C_2 MXenes. Adopted from Ref. [107]. with the permission of John Wiley and Sons. (e) SEM of $Ti_3C_2T_x$. Adopted from Ref. [264], with the permission of the American Chemical Society (f) SEM (left) and TEM (right) of 3D $Ti_3C_2T_x$ MXene. Adopted from Ref. [265], with the permission of the American Chemical Society. (g) SEM of $Ti_3C_2T_x$ MXene foam. Adopted from Ref. [266], with the permission of John Wiley and Sons (h) A MXene aerogel. Adopted from Ref. [267], with the permission of permission of the Royal Society of Chemistry. (i) SEM (left) and TEM (right) of $Ti_3C_2T_x$ MXene nanofiber. Adopted from Ref. [269], with the permission of the American Chemical Society (j) SEM (left) and TEM (right) of Ti_3C_2 MXene nanoribbons. Adopted from Ref. [270], with the permission of Elsevier. (k) TEM of Mo_2C MXene nanorods. Adopted from Ref. [272], with the permission of the Royal Society of Chemistry. (l) TEM of V_2C MXene quantum dots. Adopted from Ref. [271], with the permission of John Wiley and Sons.

through the colloidal MXenes suspensions by the addition of high pH alkali M'OH (M' = Na^+, Li^+, K^+ or tetrabutylammonium, TBA^+), neutral salt (NaCl) and low pH acid (HCl) (Fig. 20e). It is because of the positive cation's passivation towards MXenes edges at neutral and high pH and the reduction of electronic repulsion at low pH. During the process of fast evaporation of MXenes aerosol droplets, the highly porous MXenes could also be synthesized due to capillary force action. The isotropic inward capillary compression force results in the formation of nano-flower like MXenes 3D architectures (Fig. 20f) [265]. The infiltration of small molecules such as the penetration of hydrazine into MXenes multilayer interior side, which in turn causes the inflation and synergistic hydrophobic behavior of the MXenes film, further leads to the formation of highly porous MXenes [266]. Use of facile freeze-casting approach without external supporters ultralight ($\rho < 10$ mg/cm^3), the fabrication of MXenes aerogels have also been proposed Fig. 20h [267]. According to theoretical investigation, the MXenes nanotubes have been proposed to have a diverse range of physical and chemical properties along with thermally stable characteristics [268]. The experimental investigation still didn't succeed to produce any kind of MXenes nanotubes. In the hydrolyzation process of Ti_3AlC_2 MAX nanofibers during acid etching in KOH solution, the formation of $Ti_3C_2T_x$ MXene nanofibers was observed (Fig. 20i). The function of OH- ions was as scissors by making cracks in Ti_3AlC_2 MAX, and further shearing force via string, which in turn brought about the proliferation of cracks till approaching the corners [269]. Similarly, the constant stirring of as-synthesized $Ti_3C_2T_x$ MXenes in KOH solution further leads to the formation of $Ti_3C_2T_x$ MXenes nanoribbons (Fig. 20j) [270]. Notably, the encapsulated MO_2C nanorods are prepared via chemical transformation of Mo_2S through carbothermal reaction at 1200–1300 °C [271,272]. Hence, due to diverse range of microscopic morphological features of pure MXenes, a

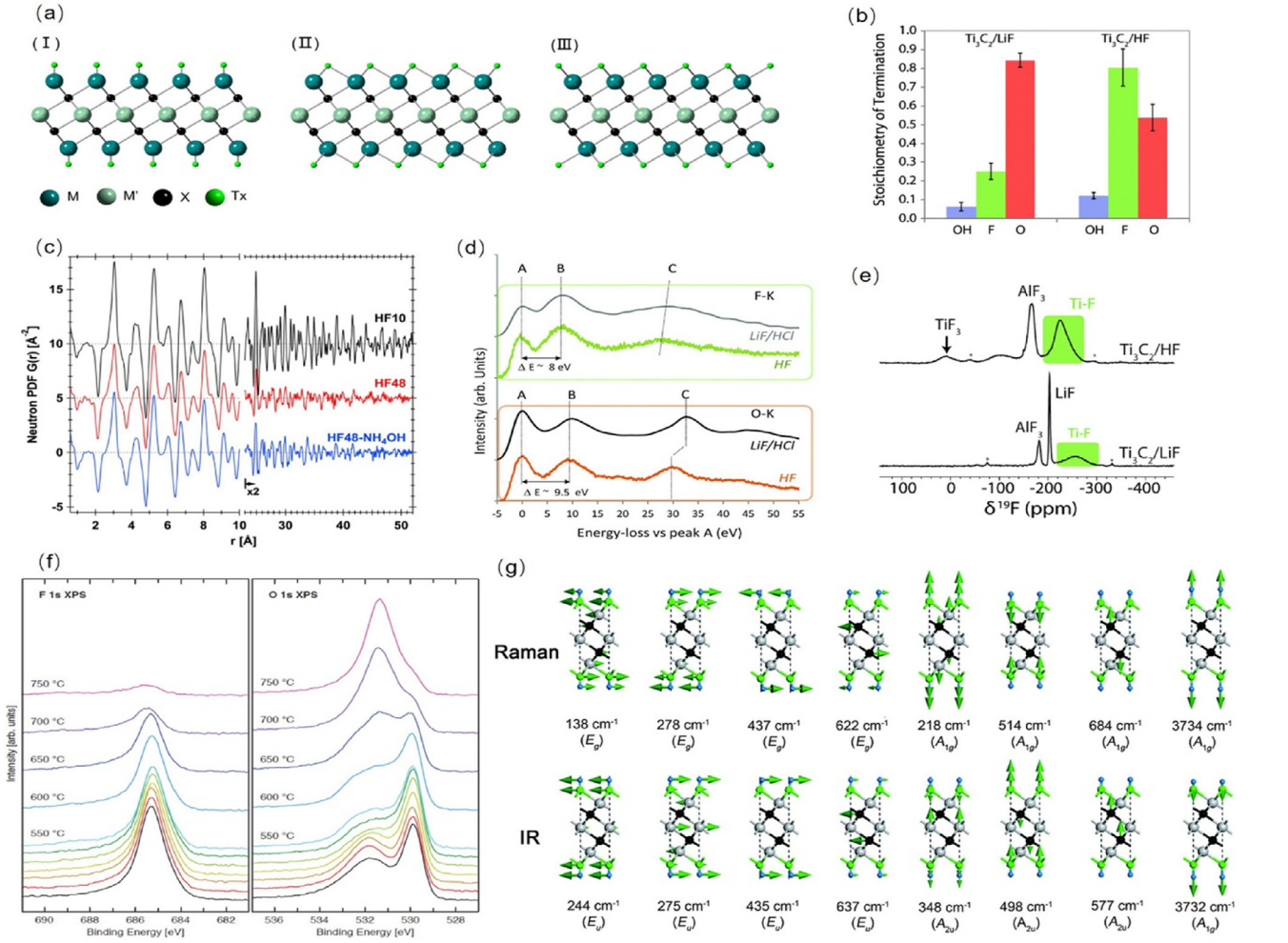

Fig. 21. Analysis schemes. (a) surface depiction of MXenes. (b) Surface functionality generated via etched Ti_3AlC_2 in HF and LiF−HCl. Adopted from Ref. [281], with the permission of the Royal Society of Chemistry. (c) Neutron scattering spectra of $Ti_3C_2T_x$ MXene [283] (d) EELS spectrum of HF and LiF/HCl based Ti_3C_2T [284]. (e)19F NMR (11.7 T) spectrum of HF and LiF−HCl synthesized Ti_3C_2 MXene. Adopted from Ref. [281], the permission of the Royal Society of Chemistry (f) TP-XPS depicting the thermal properties of F1s and O1s. Adopted from ref. [288], with permission of IOP Publishing Ltd. (g) The Raman and IR spectrum for $Ti_3C_2T_x$ MXene. Adopted from Ref. [276], the permission of the Royal Society of Chemistry. with permission of IOP Publishing Ltd.

wide variety of MXenes-based hybrid structures have already been proposed with the aim of improving overall activity of MXenes for a certain application [273–275].

2.6.2. Surface terminations

According to density functional theory (DFT) calculations, the MXenes are, indeed, projected to be completely terminated, owing to high negative foundation energy, as it in turn proposes robust bonding between surface termination moieties and transition metals [276]. Consequently, the inherit electronegative surface terminations i.e. O, OH and F, those are hydrophilic in nature, are usually observed in the MXenes, which is synthesized via aqueous fluoride-containing acid etching i.e. −F. In various kinds of MXenes, the existence of a comparatively strong bonding with H_2O molecules was observed more clearly [277]. Due to higher bonding energy, the existence of anionic terminations like −Cl, −S could be similarly fastened over the surface of MXenes [278]. In a binary aqueous method, the fluoride terminated free MXenes could also be fabricated [164]. The surface terminations could be possible via three routes: (i) in a deep point in top metal atoms, (ii) a deep location between subsequent stacking layer of X atoms (iii) directly positioned over the surface of transition metal atoms [276], which is presented in Fig. 21a(i, ii, iii). The intended bond dimensions of O−H, Ti−O and Ti−F are found to be almost 1.9 Å, 0.97 Å and 2.1 Å individually. The oxygen termination (-O) exhibits the highest adsorption energy of 7.7 eV, in the order of −O, −F, −OH, −Cl and −H [279]. That is yet incredible to achieve MXenes with no or pure surface termination because of the random distribution of the termination's points, according to the information from the theoretical calculation regarding the considerable impact of specific surface terminations [280]. Therefore, it is a challenging task to predict the surface termination on MXene surfaces. To investigate their properties up to a specific point, the different kinds of characterization techniques, e.g. surface acoustic, neutron scattering, NMR, Raman, X-ray photoelectron spectroscopy (XPS), neutron scattering were used. The surface termination could be possible via three routes: (i) one surface metal based single bonding, (ii) two surface metals based dual bonding with middle symmetry, and (iii) reflecting symmetry with respect to the central metal layer Fig. 21a. However, with respect to one electron based −F and −OH terminations, the two electrons are needed to the Oxygen termination (−O) for its stable states; therefore, −O terminations are further probable to reside in the interstitial resonating positions, which confined with two metal atoms. Furthermore, the −O terminations were observed to be thermodynamically indulgence the sites as predicted by the corroborating STEM image and high-resolution

STEM imaging (iii), i.e. on over topmost of Ti atoms of mid layer (Fig. 21a). The −OH and −F terminations are proposed to be closely collapsed at the position (i) −OH termination amounts could be suggestively lower than −O and −F [281]. The variation in the layers numbers n, or the X element, in Ti-based MXenes, had minute impact on F-terminations fraction, while that of surface termination are observed to be highly affected in Nb-based MXenes [282,283]. The ratio of terminations is strongly influenced by the selective etching method. According to NMR results, the −F terminations ratio via HF etching process could be four times higher than the MXenes synthesized via LiF−HCl, which were further confirmed via electron energy-loss near-edge structures (ELNES) [284] (Fig. 21d and e). However, the strong oxidizing environment and higher temperatures might endorse the oxidation progressions, for instance, the oxidation degree found to be H_2O_2> wet air > dry air. Notably, the formation of carbon-supported titania is possible via e Ti atoms diffusion process over layer structures of surface sites throughout the topotactic transformation of MXenes at high-temperature (e.g. Ti_3C_2), which in turn further brought about the synthesis of cubic TiC under vacuum conditions [285]. Normally, the fewer oxygen terminations could be formed under a milder etching environment. The evolution of monohydrated to bi-hydrated MXenes of different hydration states is significantly increased with an increase in relative humidity thereby, showing partial segregation and interstratification of layers [286]. Nevertheless, the O atom is sturdily bound to Ti surface, the relocation and cleaving of surface groups over the surface of MXenes was also detected [287]. According to temperature automated X-ray photoelectron spectroscopy (TP-XPS) results, the functional F atoms were found to be slowly desorbed at 550 °C, and were found to be principally detached at 750 °C. After the desorption of F atoms, the O surface atoms were roamed to the exact direction, which was evacuated by F atom desorption (Fig. 21f) [288]. In $Ti_3C_2T_x$ MXenes, the termination desorption phenomenon was also cleared under both argon and hydrogen atmospheres as predicted by the Raman spectroscopy (Fig. 21g) [276,289]. Under normal oxidation condition in air at same temperature, the transformation of $Ti_3C_2T_x$ MXenes was converted into TiO_2/carbon hybrid material, but the lower temperature of 450 °C for 2 h is suitable for the slow oxidation [290].

2.6.3. Photoluminescence

Both kinds of MXenes including nanosheets and quantum dots (QDs) have revealed virtuous photoluminescence (PL) properties

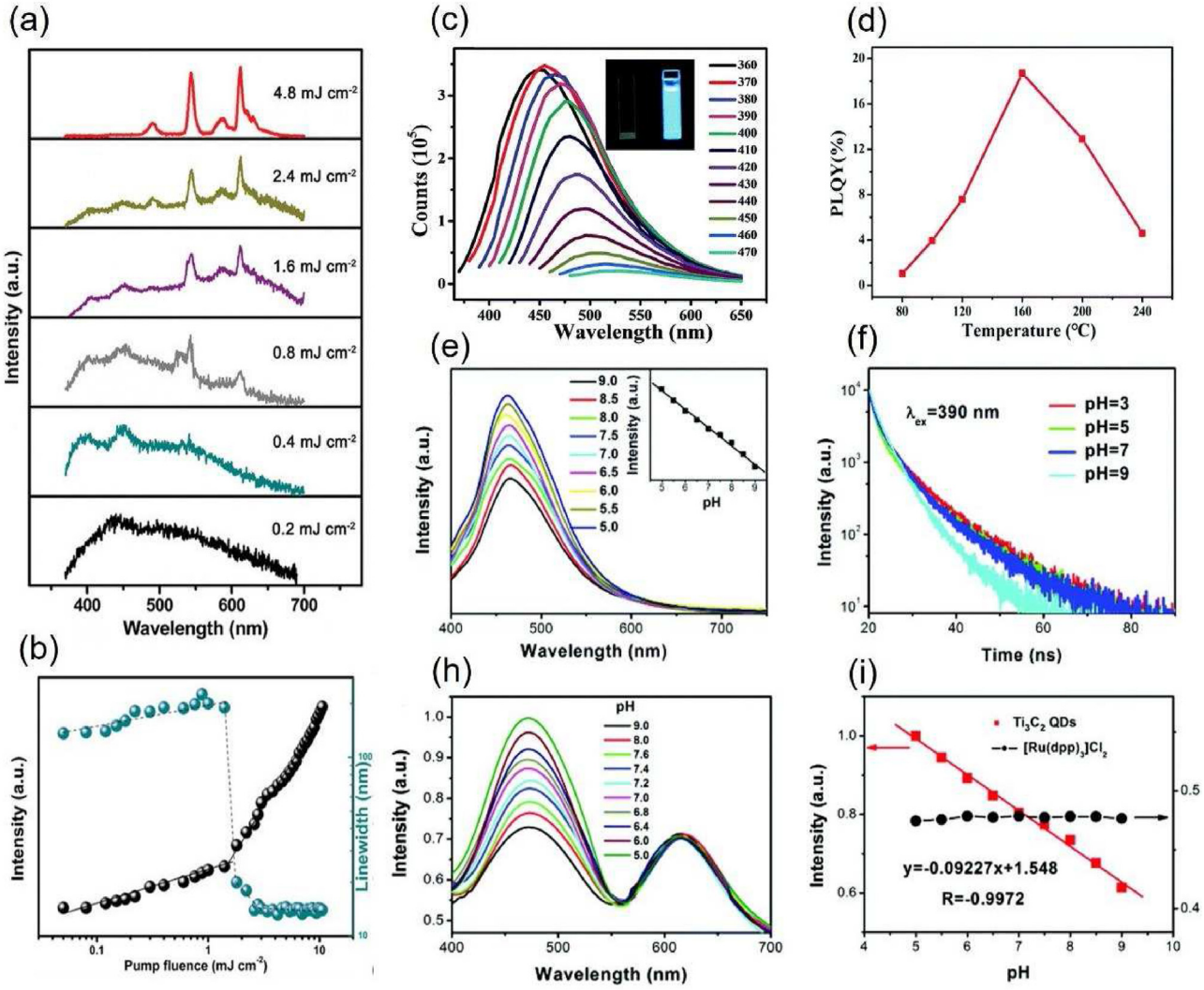

Fig. 22. PL of MXene QDs. (a) V2C MXene QDs PL spectrum. (b) 490 nm emitted rate and spectrum linewidth. Adopted from Ref. [271], with the permission of John Wiley and Sons (c) PL of Ti_3C_2 QDs. (d) Ti_3C_2 QDs' PL quantum yields efficiency. Adopted from Ref. [296], with the permission of the Royal Society of Chemistry (e) emitted rate of Ti_3C_2 QDs. (f) Emission lifetimes of. (h) Emitted spectra between 490 and 615 nm for Ti_3C_2 QDs. (i) Emitted spectra between 490 and 615 nm for Ti_3C_2 QDs at pH gradients. Adopted from Ref. [297], with the permission of the Royal Society of Chemistry.

[291]. It is due to the decrease in system size owing to establishment of direct bandgap energy, which in turn permits the radiative electronic transitions. Usually, considering composition and the particle size, the three intense absorption lines at (260 nm, 310 nm and 350 nm) could be seen in MXenes QDs. The excitation wavelengths are the major feature to express the PL spectral band. The PL spectra lies from 400 to 600 nm, after the shifting of the excitation wavelengths from 340 to 440 nm (Fig. 22c). By means of hydrothermal approach with the aid of changing the temperature, Xue et al. [292] fabricated a wide range of $Ti_3C_2T_x$ MXenes quantum dots having average particle size of 2.9, 3.7, and 6.2 nm. The highest quantum yield was found to be up to 9.9% under the excitation wavelength of 320 nm. The MXenes QDs PL properties could be further employed for labeling and bioimaging purposes. The independent nature of PL intensities on solution pH were also investigated by the same researchers, which might be instigated from the extensive passivation of MXenes QDs surface site via −NH groups [293]. Moreover, Xu et al. [294] investigated that the solvent plays an important role to extensively affect the fluorescence lifetime and quantum yield of $Ti_3C_2T_x$ MXenes QDs. Among the ethanol, DMSO and DMF solvents, the dimethylformamide (DMF) causes high quantum yield of 10.7% for MXenes QDs, while that of dimethyl sulfoxide (DMSO) provides a higher lifetime of 4.7 ns. The comparatively extended lifetime in DMSO is due to the stronger oxidative ability of DMSO and the reduced particle size from the higher polarity. As compared to other two solvents, the Fe^{3+} leaves a certain quenching impact over the MXenes QDs photoluminescence in DMF. Huang et al. [271] reported the highest PL yield of 15.9% for the V_2C MXenes QDs via employing similar hydrothermal method in ammonia aqueous solution, and it was found to be higher than other non-passivated quantum dots (QDs). In addition, after ammonia passivation, the emission lifetime (6.57 ns) was found to be longer and emission band was observed to be wider. The strong excitation in the solution could cause non-linear scattering and localization of bubbles, which could be further employed to create the random lasing cavity. The four laser-like emission peaks at (490 nm, 545 nm, 587 nm, and 613 nm) were realized, when the excitation energy was increased to 4.8 mJ/cm^2 at 355 nm. (Fig. 22a and b). The MXenes QDs concentrations could be directly enhanced by lowering the random lasing threshold [295]. The as-prepared nitrogen doped Ti_3C_2 quantum dots, through the process of ethane-diamine Ti_3C_2 quantum dots mixing in autoclave for 12 h at 160° Celsius, had the highest photoluminescence quantum yield of 18.7% [296]. The attained emission lifetime is 7.06 ns, which could be changed by altering the doping temperatures (Fig. 22d). Among Ni^{2+}, Cu^{+}, Ce^{3+}, Al^{3+}, Ca^{2+}, Zn^{2+}, Mn^{2+}, K^{+}, Cu^{2+}, Mg^{2+} and Na^{+}, the nitrogen-doped Ti_3C_2 QDs exhibit selective emission quenching characteristics via Fe^{3+} ions. The as-synthesized nitrogen-doped Ti_3C_2 QDs show discerning emanation quenching properties by Fe^{3+} ions among (Na^{+}, Mg^{2+}, Cu^{2+}, K^{+}, Mn^{2+}, Zn^{2+}, Ca^{2+}, Al^{3+}, Ce^{3+}, Cu^{+}, and Ni^{2+} ions), as a result, it could be used as a high-sensitivity Fe^{3+} probe with a detection limit of up to 100 M, and thus, could be further employed as an ultrasensitive Fe^{3+} probe, which have the maximum detection limit of 100 μM. Using $Ti_3C_2T_x$ QDs, Chen et al. [297] found that the PL intensity changes when the surface defects deprotonate. The zeta-potential, absorbance, PL emission intensity, and lifetime at 460 nm decrease as the pH value of the MXenes QDs solution increases (Fig. 22e and f). The ratio metric pH sensor of $Ti_3C_2T_x$ QDs is capable of being used as a pH sensor quantitatively monitoring intracellular pH levels by using pH insensitive $[Ru(dpp)_3]Cl_2$. (Fig. 22g and h). At pH values above 6, Wang et al. [298] investigated that neither the wavelength nor the intensity of the photoluminescence increased significantly for $Ti_3C_2T_x$ QDs, while intensity was found to be declined at low pH values.

2.6.4. Non-linear optical properties

An intense light source manifests non-linear optical effect. As a result of a strong electric field oscillating in the medium, macroscopic polarization is induced that doesn't only oscillate with the applied frequency but also at higher harmonics and even contains a DC component. Comparatively to other 2D materials, the MXenes have seen very few studies on their non-linear optical properties, with a main focus on their saturable absorption effects, rather than their second-order effects. When a collimated laser beam is focused, it produces a simple high-intensity condition that can be used to study the non-linear optical refraction or absorption (Fig. 23a). The Z-scan method is an extremely viable method, which consists of translating the MXenes sample along the optical axis (Z) across the laser beam focal points, where mostly the sample receives various kinds of light intensity at diverse points in the laser beam. The information on the sample's non-linear refractive responses and optical absorption could be revealed by measuring the transmittance under close and open orifice conditions as a function of laser intensity [299]. Jiang et al. [300] used the Z-scan method to scientifically examine the broadband non-linear optical retort of $Ti_3C_2T_x$ from 800 nm to 1800 nm. They observed that similar to other 2D material-based saturable absorbers such as black phosphorus and topological insulators, the MXenes's samples saturable absorption modulation depth rises with the illumination intensity along with highest modulation depth of 40% [301]. According to the earlier debate, the linear optical reduction could be as low as 2%, which is the modulation depth limit. At the expense of increased saturation intensity, the modulation limits could be effectively increased with an increased quantity of the MXenes materials for saturable absorption. At low pulse energies, there appears to be a significant difference in the non-linear absorption coefficient for a specified wavelength, thereby suggesting the direction of the non-linear absorption by photon saturable absorption process. Therefore, the increase in the pulse energy, in turn brought about the occurrence of two-photon absorption process (Fig. 23e and f) [300]. This phenomenon is mainly characterized by a simple two-level model, which occurs after the ground and excited state populations equalize, and after the decoupling of the incident field from the absorbing medium, that in turn shows that no more photons could be further absorbed by it. In experimental tests, it is observed that an incremental increase in illumination intensity in turn brought about the constant increase of the transmittance (Fig. 23b). For ultrafast mode-locked and Q-switched operations at 1.55, 1.88 m, and 1.55 cm, the use of MXenes has been reported in place of a saturable absorber with 1.7% modulation depth [302]. Moreover, to generate the ultrafast laser from near-infrared to mid-infrared by having average pulse duration as short as 100 fs, [303], the various laser resonators were combined with multipurpose based MXenes's, which have the merits of high transparency and broad spectrum saturable absorption properties indeed. Currently, the ceramic laser and solid-state system are constantly using the MXenes-based saturable absorbers [304]. Beside generating ultrafast lasers, owing to C60's reverse saturable absorption properties, a non-reciprocal transmission photonic diode could be obtained by combining the MXenes with C60 [305]. A number of non-linear refractive indices of 2D materials have been characterized recently using solution-based spatial self-phase modulation (SSPM) technique [306]. Using closed aperture Z-scan methods, Wu et al. [307], determine that the non-linear refractive index of $Ti_3C_2T_x$ MXenes ($10-4$ cm^2/W^{-1}) could be significantly larger than previously reported values in the optical regime. Differences in sample preparation and characterization methods may be a possible explanation and major cause for this discrepancy. In spite of this, all-optical switching dispersion $Ti_3C_2T_x$ MXenes nanosheet, has been demonstrated in this regard by using intensity-dependent

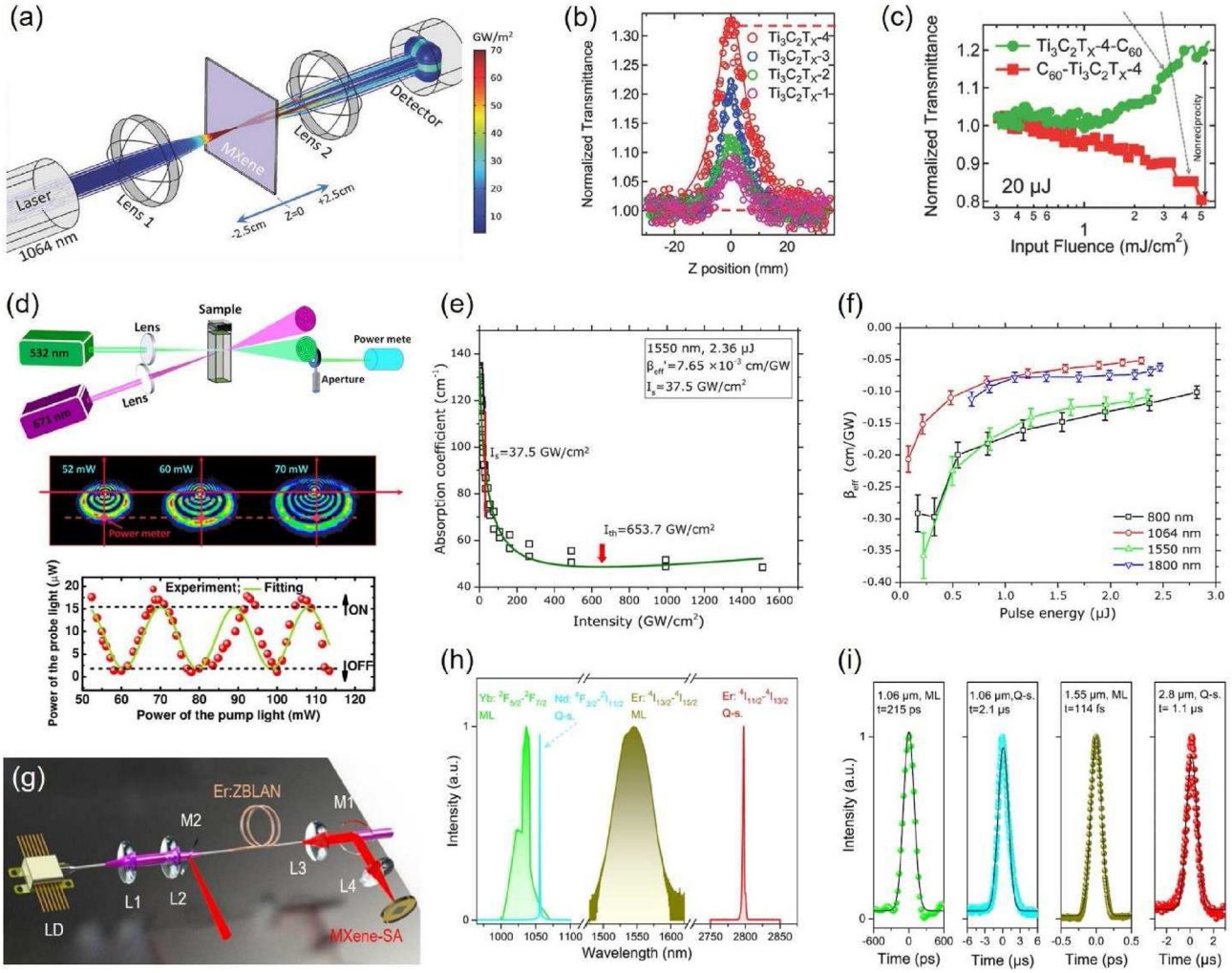

Fig. 23. (a) Non-linear optical characteristics using Z-scan. (b) Position-dependent variations in the non-linear transparency of $Ti_3C_2T_x$ sheets. (c) Operation of an optical diode in a $Ti_3C_2T_x/C_{60}$ layer [308]. (d) Optical switching of $Ti_3C_2T_x$ sheets [307]. (e) Intensity of $Ti_3C_2T_x$ at 1550 nm. (f) Optimal non-linear absorptivity is proportion of pulse energy (Ep) [300]. (g) Mid-infrared Er:ZBLAN light oscillator. (h) Employing inkjet-printed MXene pulsed absorbance at various wavelengths. (i) Four wavelengths pulse rates [303].

refractive index exceptional optical Kerr effect (Fig. 23d). The all-fiber setup has currently been established with four-wave mixing having average conversion efficiency of −59 dB and modulation speed of 10 GHz owing to the exceptional third-order non-linear optical characteristics [308].

2.6.5. Surface plasmonics

The 2D layered MXenes' metallic characteristics indeed provide an ideal substrate to photon-electron interaction over their surface. Excitation of surface plasmons (SP) induced high constricted light internment has found interesting applications in a wide variety of fields. They include surface-enhanced Raman spectroscopy (SERS), optical sensors, chemical and biological fields [309]. According to Mauchamp et al. investigation, the surface plasmon frequency of Ti_3C_2 MXene sheets can be controlled in the mid-infrared region via altering the functionalization and sheet thickness by using high-resolution transmission electron energy-loss spectroscopy (EELS) [310]. The number of MXene sheets in a stack form has a little effect on the probability of bulk plasmon excitations (Fig. 24c), which is normally attributed to weedy interaction between the $Ti_3C_2T_x$ sheets in the stack, which accounts for their outstanding ability to be interpolated with various kinds of tiny organic molecules and cations. In $Ti_3C_2T_x$ flakes, ultra-high-resolution EELS revealed the presence of edge and central longitudinal multipolar modes, escorted via transversal mode. The existence of edge and central longitudinal multipolar modes, escorted by a transversal mode, have been observed via ultra-high-resolution EELS in $Ti_3C_2T_x$ flakes (Fig. 24a) [311]. Throughout the mono- and multilayer flakes, the transverse surface plasmon mode and inter-band transition were evenly distributed, while that of longitudinal multipolar modes (both sub-radiant and super-radiant) showed robust energy and longitudinal dependence over morphological features of the fragment, e.g. thickness, size and shape. The metallic free electron density of $Ti_3C_2T_x$ flakes is multiplied by the desorption of fluorine (F) termination at annealing temperatures above 550 °C, thereby resulting in a monotonic blueshift of the SP energy in all modes. However, the MXenes are shown to have outstanding plasmonic characteristics in several tests. The surface-enhanced Raman spectroscopy (SERS) has the development factor of 105 for the methylene blue dye by mixing MXenes $Ti_3C_2T_x$ nanosheets with noble metals such as Pd, Ag and Au [309]. In addition, the detection of Acid blue, Crystal violet, Methylene blue and Rhodamine 6G, with development factors of Raman signal up to 106, was accomplished by using the spray-coated MXenes substrates without noble metals. Followed by a charge transfer to the adsorbed molecule, the inter-band transitions to the unoccupied energy states of

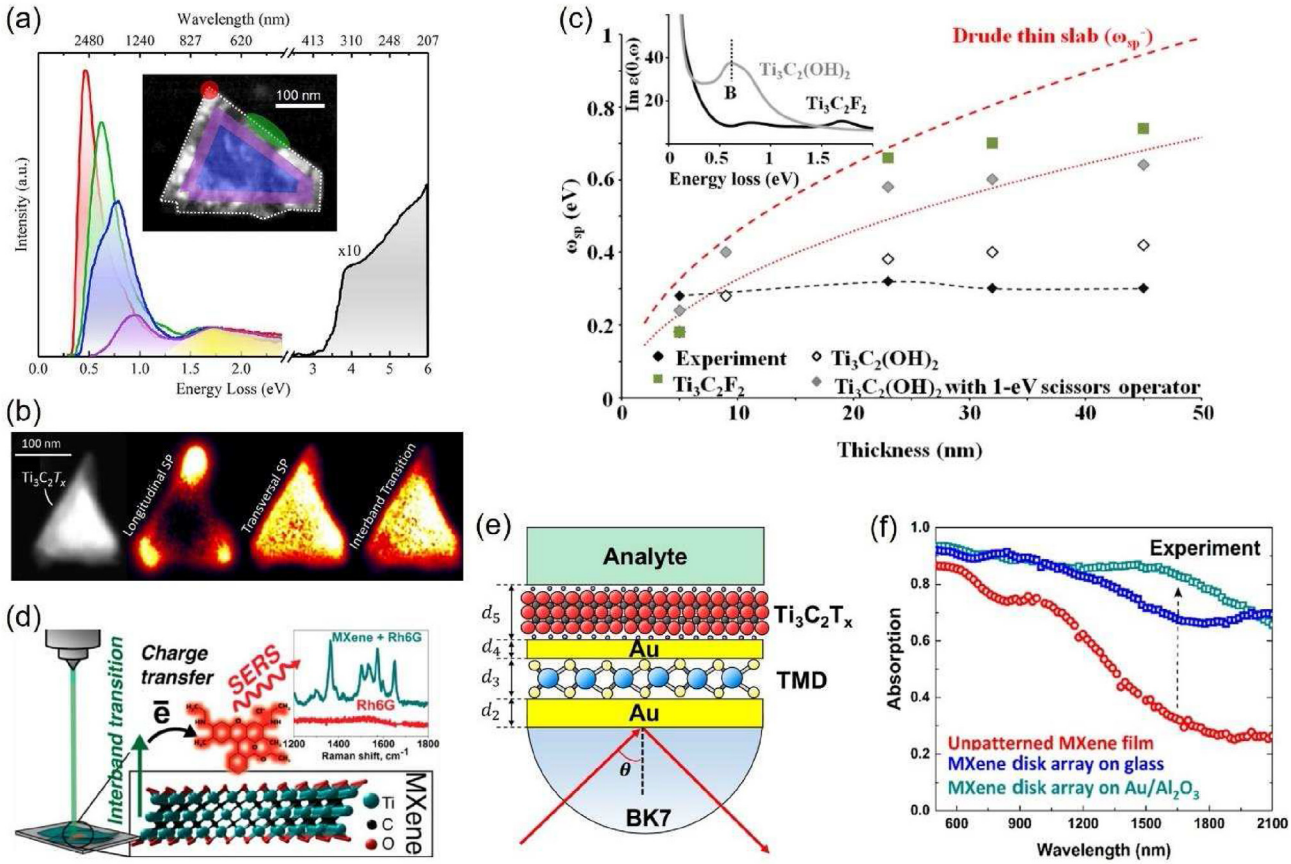

Fig. 24. (a) The minimal energy loss EEL spectrum of a triangular $Ti_3C_2T_x$ flakes. (b) $T_3C_2T_x$ flake activated longitudinally. Adopted from ref. [311], with the permission of the American Chemical Society (c) ωSP as a proportion of MXene thicknesses. Adopted from ref. [310], with the permission of the American Physical Society (d) Spray-coated MXene SERS surfaces for dye sensing. Adopted from ref. [292], with the permission of the American Chemical Society (e) Designed SPR detector with Au-$Ti_3C_2T_x$-Au-TMD heterojunction. Adopted from ref. [314], with the permission of MDPI (f) MXene plasmonic wide-bandgap. Adopted from ref. [316], with the permission of the American Chemical Society.

MXenes's functional groups were due to the increased process (Fig. 24d) [292]. As an effective optical sensor for a chemical or biological analyte, the Kretschmann configuration prism-coupled surface plasmon resonance (SPR) sensor was established [312]. In which, the plasmonic metal film and thickness of MXenes were found to have strongly influenced the sensitivity. The Al metal film with 12 atomic layers of $Ti_3C_2T_x$ provides the maximum sensitivity enhancement of 46% [313]. As compared to the conventional Au film SPR sensors, the SPR sensor based on a hybrid structure of Au-$Ti_3C_2T_x$-Au-TMDs have proposed with an average enhancement of 41% (Fig. 24e) [314]. As an alternative plasmonic materials towards the synthesis of meta-surfaces especially, phase gradient meta-surfaces, the simple non-terminated MXenes has currently been ongoing to get more awareness. Based on nano-engineered scatters, the metal-surfaces are usually considered to be the flat photonics or planar devices. According to Chaudhuri et al. [315] investigation the effect of photon spin Hall had recently been observed by using ZrN and TiN based optical metasurfaces. A strong localized surface plasmon resonance at near-infrared frequencies, introducing inter-band shifts in the visible range, was also examined by using meta-surface having $Ti_3C_2T_x$ nano disk arrangement over Au/Al_2O_3 substrate. Such kind of meta-surface in turn shows a highly efficient absorption (~90%) in wide range of wavelength window of 1.55 μm, thereby, making their broad applications in sensing, biomedical imaging and collecting the energy from light and biomedical imaging, and sensing [316].

2.6.6. Photon-phonon conversion

Depending upon the material morphologies and concentrations, material absorption coefficients (i.e. plasmonic absorptions, non-linear, linear absorptions), incident light (i.e. intensity, pulse duration, wavelength), the photon-phonon conversion properties of MXenes are characterized by the photothermal effect. Explicitly, the diverse energies encompassing photos are usually facing various diminutions of the flux, thereby, reliant on whether photon energy contests with energy bandgap or not; light rhythms with smaller duration as compared to 1 ps result into the thermal regime, where photons could not be combined with other phonons for the effective transfer of energy [317] non-linear optical phenomena owing to strong incident light ensures, which might suggestively distress the absorption coefficient of higher photothermal efficiency induced by the multireflection and absorption in porous MXenes than non-delaminated MXenes; and little non-radiative photothermal proficiency [300]. The phonon indulgence characteristics and environments strongly affect the experimentally characterized photothermal effectiveness [318]. In droplet-based water evaporation experiments, the markedly, 100% light-to-heat conversion efficiency was observed (Fig. 25d–f) [319]. The light-to-water evaporation efficiency as much as 84% beneath sunlight was obtained through heat barrier and vacuum filtrated MXenes films. All of these activities are considered to be the best efficacies than hybrid foams or meshes [320], and noble metals [321]. Remarkably, by means of diverse irradiation positions and coherent

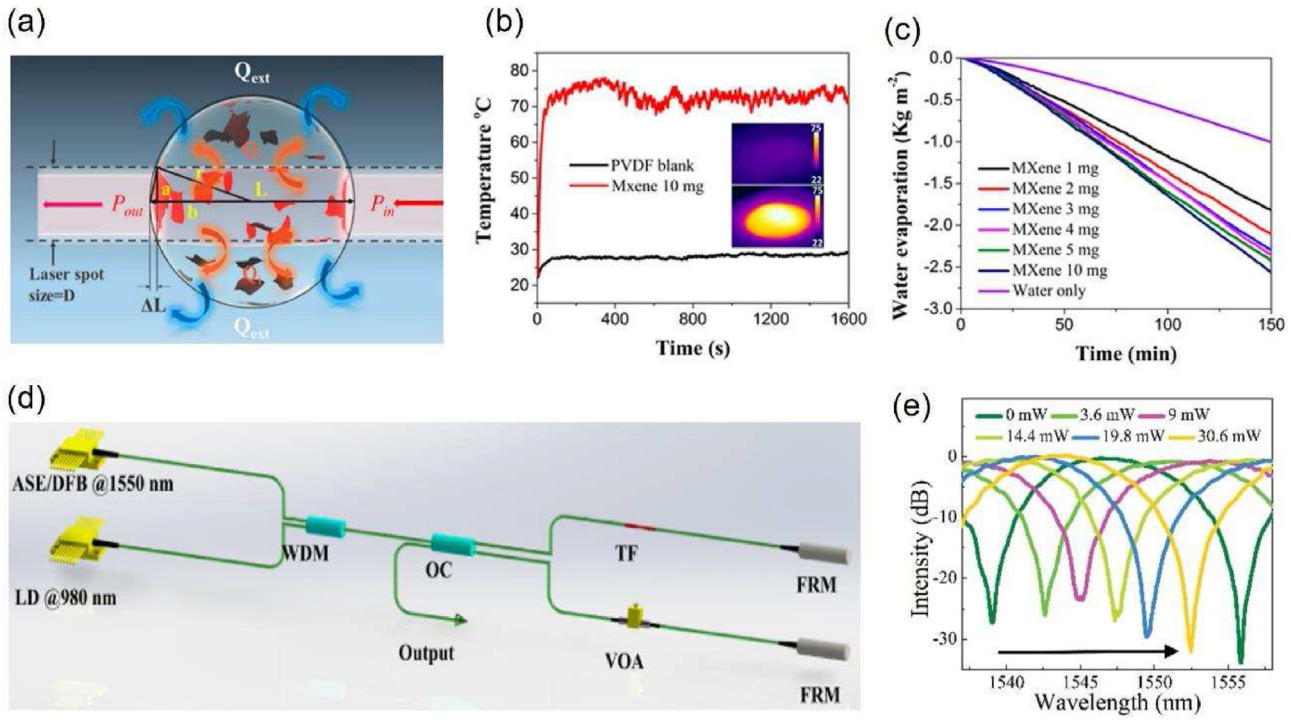

Fig. 25. (a) Photodynamic desalination. (b) Thermal differences between MXene and PVDF. (c) Evaporating rate vs MXene content [319]. (d) All-light photodynamic modification. (e) Variations in interfering wavelengths [324].

combination of an asymmetric assembly, light-driven object motions were detected [322]. The results of the Marangoni micro-fluid effect confirmed the formation of local thermal surface tension gradients in the presence of light irradiation, which in turn produce the recoil force for the motion [323]. According to Lao et al. [345] investigation, the photothermal effect could reversibly control the nano-fluidic transport of $Ti_3C_2T_x$ membrane. The local MXenes quickly warms up after the laser irradiation, thereby evaporating the interlayer water, which leads to the blockage of the transport of ions in a time period of 0.34 s. The solvent (water) only rehydrates the MXenes membrane as the laser is turned off, thereby, permitting the ions to move freely. In a Michelson interferometer, the all-optical modulator based on effective photothermal conversion of MXenes was recently shown. A Michelson interferometer-based all-optical modulator based on effective photothermal alteration of MXenes has recently been shown in (Fig. 25g and h). The photothermal action of the MXenes nanosheet in MXenes clad microfiber in one armrest of the interferometer modifies the actual refractive catalogue of this arm, thereby, leads to the alteration of the interfering peripherals. A free spectrum range of 16.8 nm, varied deepness of >27 dB, has been obtained with a pump-tempted phase shift angle of 0.043/mW [324].

2.7. Advantages and disadvantages of MXenes in comparison with 2D materials

Graphene, hexagonal boron nitride, transitional metal dichalcogenides, and other fascinating materials have received much research owing to their fascinating features including as exceptional conductance, inertness, big surface area, and so on [2–4,7,8,24–27,88,325–328]. MXenes also had some favorable circumstances over such 2D composites due to their variable electromagnetism attributes. For example, simple 2D graphene does have outstanding electronic permeability and though poor physical assets, making it unsuitable for electrostatic interference (EMI) sheltering implementations that necessitate modest permeability and magnetostrictive polarizability to converse with electromagnetic (EM) signals. The hydrophobicity and expensive demand of fabrication of carbon allotrope-based nanocomposite (including carbon nanotubes (CNTs), carbon nanofibres (CNFs)) limit their consumption as EMI isolating objects [23,329,330]. Molybdenum disulfide (MoS_2), on the other side, is a faceted 2D transition metal dichalcogenide. The MoS_2 sample is a nanomaterial with a hyperbolic fuel dissipation connection (band structure of 1.2 eV). Because the quantum restraint impact caused by distinct interfacial morphological features could optimize the band structure, therefore MoS_2 is an applicant for EMI sheltering functionalities [331,332]. Pure MoS_2 has reduced charge carrier permeability and transmittance than 2D graphene due to poor charge transport. Another issue with TMDs is that feeble van der Waals dynamics induce compaction of specific lateral strands of MoS_2, that could be results in impedance unmatching among the EM waves and the scattering content [333]. MXenes, on the other hand, have configurable transmittance varying from metal oxides to semiconductor, as well as cost-effective fabrication and lipophilicity. Numerous MXenes have an inherent magnetic property, making them suitable for EMI insulation and thermophysical implementations. An abundance of peripheral clusters (oxygen and fluorine based) in the MXene sheet, on the other hand, can induce the imperative lamination to implode or texture ladling in the fibrous MXenes. The stacked configuration could impede the formation of holes inside the MXenes ranging from micro to micrometer dimension, altering its electrical and magnetic properties and therefore negatively impacting the EMI achievement of MXenes-based nanocomposite. This is a disadvantage of MXenes that can be overcome by combining MXenes with magnetic/conductive polymers such as metal alloys or ceramic materials, organic polymers, and carbon allotropic forms. Pure 2D graphene is a semimetal with a negligible electronic structure. Whereas lowered graphene oxide and graphene oxide are both semiconductors and insulators [330]. Two-dimensional TMDs exhibit semiconductor attitude. MXenes' appearance lies in their configurable

electrical characteristics, which allow them to function as metallic materials, semi - conductor, superconductivity, topographic insulators, and, most interestingly, half metal alloys [334,335]. Tuning the semi-metal of MXenes is possible through manipulation of the termination ring, loading, or the application of an electrostatic potential and stress. The semi metallicity of MXenes nature signals the significant possibilities in the field of superconductors [336]. Due to their distinctive 2D structure, GO analog-based substrates were identified as interesting coating materials for gas and liquid isolation. The narrow interfacial separation of GO moiety, however, results in a comparatively modest flux under pressures [337]. Using vapor circumstances, Huang et al. observed a flow of 1702 g m^2 h^1 for the GO membranes [338]. Due to the hydrating impact which can enhance the multilayer gap of the GO membranes, hydrogen connections can be broken inside the membrane, resulting in unstable segregation efficiency. Compared to GO walls, MXenes-based nanomaterials provide greater thermal endurance and physical and chemical stability. Through the incorporation of nanostructure between the surfaces of the MXenes membranes, rapid water permeability could be obtained. 27 The MXenes membranes had a significant water permeability and rejected ratio (1000 L m^2 h^1 and 90%, correspondingly) due to its exceptionally brief transportation route and vast number of nanopores. MXenes membranes are accessible to both organic solvents, whereas GO barriers are nearly resistant to organic solvents [339]. The flexible lamellar composition of MXenes provides a suitable flow route for the solutions, resulting in a significant flux. Consequently, it is projected that MXenes will have a significant impact on membrane materials. Furthermore, MXenes exhibit reduced rejection of dye molecules; this is the primary issue that may be addressed by mixing MXenes with other polymers [339,340]. Conservation and transmission of energy are becoming crucial challenges in the modern era. Prominent electrocatalytic energy storing (EES) technologies include electrode materials and batteries, including lithium metal, potassium ions, and sodium batteries. Fast-growing energy storage systems are preferable due to their shared characteristics, which include a prolonged lifetime, specific strength, fast response, and environmentally friendliness [341]. High surface area, excellent conductance, and great dynamic durability are all advantages of 2D graphene or 1D carbon nanotube (CNT)-based electrode composites. In addition, carbon-based nanomaterials retain charges by the adsorbed of particles in the electrolytes, releasing reduced energy intensities. To obtain substantial energy efficiencies in this situation, pseudo-capacitive polymers (such as transition-metal oxides (RuO_2, MnO_2), conductive materials, and TMDs) are utilized. The poor conductance of metal oxides and hydroxides leads to low cycle efficiency and energy yields. Due to their substantial interface potential, 2D TMDs including $MoSe_2$ nanostructure prefer to aggregate. In addition, 2D TMDs (e.g. $MoSe_2$) do have greater resistivity whenever employed as electrocatalysts, and aggregation leads to fast capability decreasing, preventing their widespread application in EES. MXenes are advantageous as electrocatalysts for EES due to their unusual configuration, which consists of an interfacial resembling transition-metal oxide and an interior conducting transition metal carbide layers that offers reactive groups for rapid oxidation reaction and facilitates adequate charge separation. Despite the fact that conventionally generated MXenes include termination interface clusters, a number of MXenes retain metal conductance (e.g. $Ti_3C_2T_x$), that promotes quick faradaic processes and results in enhanced energy capabilities (i.e. pseudocapacitance) [336]. The nano-configuration of stacking MXenes has the shortcomings of insufficient permeability and poor performance capabilities, which limit its broad usage in EES devices. However, these drawbacks can be mitigated by the beneficial action of MXenes and other substances, a regulated production technique, etc. Using groups terminating MXenes foundation with MoS_2 nanostructure, for example, inhibits the agglomeration of nanostructure, hence enhancing the conductance of TMD/MXenes-based electrocatalyst [342]. Thus, it can be argued that MXenes are superior to other 2D polymers due to their distinct features. The main disadvantages of MXenes are their conventional fabrication processes and a lack of knowledge of their physiochemical properties, that also demands more research but offers significant potential for potential advanced materials. Considering, chemical etching and deformation leaving peripheral substituents and deformities on the surface of MXenes, and the variety of layers could really affect their physicochemical characteristics. Configurable interfacial completion must thus be investigated. On either side, bottom-up strategies make it hard to make them in massive quantities and lead to properties that depend on the substrate, which limits how widely they can be used. Because of this, it's essential to find the best way to make MXenes and to comprehend how their surfaces work. For example, in photocatalytic functionalities, pure MXenes don't absorb light well and have an elevated rate of charge transport replication. In the same way, pure MXenes have good capacitance, and also some of them are not magnetic, which makes it hard to use them to block EMI. In this situation, knowing the surface properties of MXenes opens up a lot of potentials for their application in EMI insulation, photocatalysis, and many other things. It could also assist scientists to make smart MXenes-based equipment as early as possible [343,344].

3. Application of MXenes

3.1. Photo-electrochemical catalysis

Use of MXenes in a wide variety of research applications including carbon dioxide (CO_2) reduction [273,345,346], carbon monoxide (CO) oxidation [347,348], ammonization of N_2 [349,350], oxygen evolution reaction (OER) [351,352], ORR [353,354], water splitting [355,356], hydrogen evolution (HER) [357,358] and other material degradation and decomposition [359–363], are considered as a robust material owing to their rich surface terminations, low-cost, high accessibility towards active sites, hydrophilic surface, tunable bandgap, large surface area and fast charge transfer. Herein, we will provide a concise description regarding the use of MXenes-based catalyst. Usually, three kinds of reaction are needed to accelerate the HER process: (1) occurrence of negative electron and positive protons; (2) protons adsorption phenomenon (H*) via electrode; (3) and protons reduction for $1/2H_2$ gas generation. The most efficient catalyst for HER is the noble metal-based platinum (Pt) metal. To examine the HER activity of various kinds of different catalysts, the intermediate state Gibbs free energy, ΔGH*, is considered as main indicator. The Δ_{GH*} value of zero is considered to be the most desirable value [364]. The well-known, highly active Pt catalyst displays $\Delta_{GH*} = -0.09$ eV near to zero [365]. To accelerate HER dynamics, the high carrier conductivity is highly needed beside the extraordinary HER activity. According to density functional theory (DFT) calculations, the Gibbs free energy of oxygen terminated MXenes is near to zero for the adsorption of hydrogen atoms, and it is considered to be more desirable towards the effective HER than that of surface functional groups [358]. By having desirable Fermi level (1.88 V vs. standard hydrogen electrode (SHE), the oxygen terminated (Ti_3C_2) MXenes) metallic conductivity and nearly-zero approaching Gibbs free energy change ($\Delta_{GH*} = 0.00283$ eV), is regarded as extremely effective co-catalyst over metal sulfide photo-absorbers towards highly improved efficiency of photocatalytic hydrogen production (Fig. 26d–f) [274,366]. At

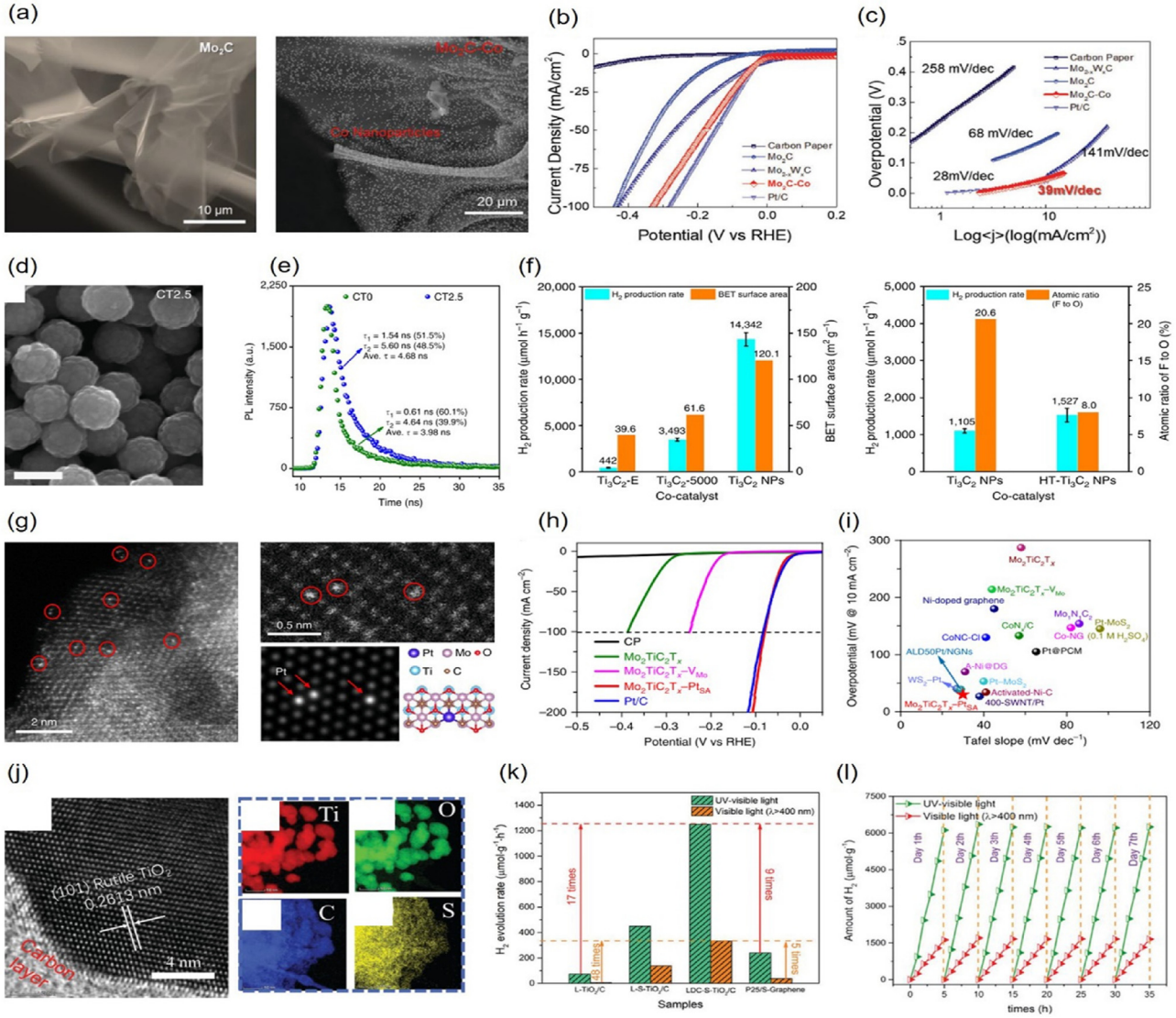

Fig. 26. HER performance. (a) SEM depiction for 2D Mo_2C sheets. (b) Different metal carbide materials CV for HER. (c) Analyzed stoichiometric overpotentials and Tafel gradients. Adopted from ref. [368], with the permission of John Wiley and Sons (d) MXene Heterojunction. (e) Life-time plot for CdS and MXenes-based CdS. (f) Photocatalytic efficiency based on interface termination. Adopted from ref. [366], with the permission of Springer Nature (g) SEM of Mo_2TiC_2Tx−PtSA. (h) HER of $Mo_2TiC_2T_x$−PtSA for different phases. (i) HER overpotential and Tafel slope assessment. Adopted from ref. [370], with the permission of Springer Nature. (j) TEM for S/Ti_3C_2 based TiO_2/C composites. (k) Overall photocatalytic HER for as-synthesized samples. (l) HER performance for S/TiO_2/C materials. Adopted from ref. [371], with the permission of John Wiley and Sons.

wavelength of 420 nm, the hydrothermally synthesized O terminated Ti_3C_2 nanoparticles with cadmium sulfide shows superior H_2 production activity of (14,342 μmol/(h*g)) along with average quantum efficiency of (40.1%). Under the Ar environment, the heat treatment strategy (~450°) is also considered a proficient mode for increasing the HER activity of simple material by means of producing O-terminated Ti_3C_2 MXenes [367]. Through the strategy of carbon-coated few-layered MoS_2 nanoplates assembling over carbon-stabilized Ti_3C_2-MXenes/C, a new type of hierarchical nanohybrid (MoS_2/Ti_3C_2-MXenes/C) was produced, which in turn become the robust material in enhancing the electrochemical reaction with superb structural, electrical and stability characteristics [188,368]. In the 0.5 M H_2SO_4 solution, onset potential of the MoS_2/Ti_3C_2-MXenes/C nanohybrids was found to be almost (−20 mV) and it is a little higher as compared to Pt catalyst, while that of considerably lower as compared to standard MoS_2/oxidized MXenes (−210 mV) and MoS_2/Rgo/C (−260 mV). With the aim of obtaining higher hydrogen generation from water, the synthesis of highly active electrocatalyst with small overpotential demand is most important for its potential practical application. An efficient HER activity by following Volmer-Heyrovsky mechanism due to low Tafel slope (45 mV/dec) was obtained by using MoS_2/Ti_3C_2-MXenes/C electrocatalyst [369]. After 2000 cycles, the negligible shift in polarization curves approves the long-lasting constancy of MoS_2/Ti_3C_2-MXenes/C catalyst. The transition metal modified M_2XO_2 MXenes was used by Li et al. [143] to examine the kinetics (e.g. reaction rate and energy barrier) and thermodynamics (e.g. hydrogen adsorption energy) of reaction by means of high-throughput computational methods. They discovered that the transition metal could also have the ability to reduce the H_2 generation barrier along with changing the hydrogen adsorption Gibbs free energy. Furthermore, they found that the HER mechanism on simple MXenes automatically convert into Volmer−Tafel from Volmer−Heyrovsky after the modification with transition metal adatoms. Moreover, Yuan

et al. [269] used hydrolysis of bulk MAX ceramics by following the HF etching method to develop robust MXene nanofiber having a large specific surface area characteristic. At a current density (10 mA/cm^2), the Ti_3C_2 nanofibers produced a low overpotential of (169 mV), a lowest Tafel slope (97 mV/dec), along with ultra-low electrochemical confrontation. Furthermore, substantial transfer of charge carriers from corner metal atoms towards (H*) reactants in transition state, the nanoribbons of Ti_3C_2 are projected to have a small Tafel barrier under 0.42 eV [268]. The electrochemical deposition method was used by Zhang et al. [370], for the immobilization of the single Pt atoms over Mo vacancies of MXenes/$Mo_2TiC_2T_x$. The as-obtained single Pt immobilized MXenes $Mo_2TiC_2T_x$ was found to have the platinum-like kinetics for HER in both neutral and acidic solutions at a higher overpotential, thereby, suggesting the superior catalytic performance as compared to innovative purchased HER Pt/C catalyst. Because of robust covalent interaction amid $Mo_2TiC_2T_x$ and the Pt atoms, the catalyst has a high degree of stability (Fig. 26g–i) [370]**.** The carbon substrate and properly coated hybrid connection of sulfur-doped TiO_2 could be obtained from the Ti_3C_2 MXenes due to the oxidation of MXenes in the ambient environment. The carriers could be normally excited via UV photons in carbon substratum and TiO_2 due to the energy bandgap's location of TiO_2 in the UV region (400 nm), thereby, making the photocatalysis more efficient than visible light illuminations because of its wavelength sensitivity (Fig. 26j-l). [371]. The MXenes could produce the heterostructures with other two-dimensional materials (like MoS_2), or it can make TiO_2 via in situ strategy for better HER, in addition to the elemental doping (e.g. P, Co, Pt), morphology engineering, and surface termination [372].

The Oxygen Reduction Reaction (ORR) and Oxygen Evolution Reaction (OER) are equally important in the energy conversion process. The catalysts needed for the OER and ORR are basically distinct. Generally, the OER occurs near high-voltage anode material, and OH normally loses the proton along with electron to O_2 molecules.; while that of ORR normally occurs at the low potential cathode site, where O_2 acquire proton and electrons to further produce (water) (H_2O) or hydrogen peroxide (H_2O_2) . The Ma et al. [373] used Ti_3C_2MXenes nanosheets and graphitic carbon nitride (g-C_3N_4) to construct the free-standing, flexible films with a conductive framework and hydrophilic surface (Fig. 27a–d). The as-synthesized film displays the lower Tafel of (74.6 mV/dec), as compared to Ti_3C_2 (119.7 Mv/dec), g-C_3N_4 (136.2 mV/dec) and IrO_2/C (93.2 mV/dec), thereby, showing its ability to accelerate the OER reaction kinetics. Proposed mechanism due to Ti interaction with g-C_3N_4, which actually reduces the Ti atoms electron density, by making the OH- adsorption easier in alkaline solution, which in turn speed up the electron transfer for quick evolution of O_2 [374]. Using an in situ inter-diffusion reaction-assisted method, the cobalt 1,4-benzenedicarboxylate (CoBDC) based metal-organic-framework (MOF) was combined with hydrophilic and conductive $Ti_3C_2T_x$ nanosheets. According to Zhao et al. [352] the as -synthesized catalyst shows the Tafel slope of (48.2 mV/dec) in 0.1 M KOH along with average current density (10 mA/cm^2) at 1.64 V potential for OER. This is better than the typical iridium dioxide (IrO_2)-based catalyst as well as other similar catalysts derived from various transition-metals, which have been previously reported. The MXenes nanosheets synthesized with metal-organic-framework (MOF)-derived nickel-cobalt sulfide on ultrathin at lower onset potential showed higher current densities for OER than those made with just NiCOS and nickel cobalt layered double hydroxide (NiCo-LDH). Markedly, the NiCoS/$Ti_3C_2T_x$ showed high current density of (10 mA/cm^2), at lower overpotential (η) of 365 mV and it is lower as compared to commercial ruthenium(IV) oxide [RuO_2] (397 mV). The NiCoS/$Ti_3C_2T_x$ has a Tafel slope of (58.2 mV/dec), thereby, indicating a good kinetics and strong OER rate [375]. To improve the OER performance, the highly porous MXenes-based hierarchical structures have also been proposed [376]. To tackle the problem of overpotential in proton exchange membrane fuel cells, the low-cost and highly efficient (ORR) catalysts are required. The Metal–nitrogen–carbon compounds (Me–N–Cs) are undergoing extensive research and show promise as a potential replacement for costly metal catalysts [377]. When $Ti_3C_2T_x$ MXenes is combined with iron phthalocyanine (FePc), then a spin configuration modifications and dramatic delocalization and Fe 3d electron occur. Actually, the enhanced ORR catalysis is a result of the strong contacts between active FeN_4 sites and reaction species. Compared to the simple and Pt/C catalyst, the improved catalyst has a two- and five-fold greater ORR performance, more than that of mostly reported Fe–N–C catalysts (Fig. 27e–h) [349,378]. Because of the improved charge separation and oxygen adsorption capacity, the MXenes nanoparticle with average loading of (2 wt %) decorated g-C_3N_4 nanosheets have a noteworthy higher ORR than pure g-C_3N_4 nanosheets [379]. The Zhang et al. investigate the oxygen evolution reaction (OER) and oxygen reduction reaction (ORR) by using bifunctional electrocatalyst (Co/N-CNTs@$Ti_3C_2T_x$) on the $Ti_3C_2T_x$(MXenes) matrix [353]. Liu et al. first principles calculations results indicated that F-terminated Pt-Ti $_{n+1}$ C_nT_x, which has the Pt atoms in the surface vacancy, could be better than that of O-terminated counterparts. Owing to the limited density of states (DOS) intersection of Ti and F, the F-terminated MXenes are found to be highly unstable, thereby, leading to the poor bonding between F and the surface sites [354]. According to Cheng et al. a higher electronic trepidation in the Au monolayer could enhance the oxygen-containing species adsorption, thereby, enhancing the catalytic activity [380]. The reduction of CO_2 to methanol, SEM images and Nyquist plots from electrochemical impedance spectroscopy (EIS) of Ti_3C_2 QDs/Cu_2O NWs/Cu heterostructure has been manifested in Fig. 27m–o [273].

The Mo_2CTx MXenes is regarded as a conductive and active support for electron transport during hydrogen evolution reaction (HER) catalysis [381,382]. Yu et al. [383] investigated the hydrothermal synthesis via combining MoS_2@Mo_2CTx hybrids and its extensive structural characteristic to boost the HER activity in alkaline medium (Fig. 28a–c). Obtained results indicate the higher HER activity of MoS_2@Mo_2CTx nanohybrids with average current density of (10 mA/cm^2) at low overpotential (176 mV). Moreover, the very low transfer resistance of 26 Ω was observed than simple Mo_2CTx, MoS_2 and Mo_2Ga_2C catalysts, which showed greater overpotentials of 533 mV, 394, 897, respectively in alkaline solution. This preparation method indicates that tailoring the surface characteristics of MXenes for required application is necessary to prepare the organ-like molybdenum carbide mutual with MoS_2 nanoflowers. The catalytic efficiency and stability of MXenes are greatly improved by substituting mid-to-late transition metals of group III-VI within the host matrix [384]. For the first time, intercalation of gallium yielding Mo_2Ga_2C (Co insulated by Ga removal via HF treatment), the Kuznetsov et al. [385] prepared a cobalt-intense molybdenum carbide (Mo_2CTx: Co) MXenes (Mo_2CTx: Co). In DFT simulations, it was found that even a little amount of Co in the Mo_2CTx host lattice had a significant effect on the electronic structure of Mo_2CTx: Co (Fig. 28d and e). In oxygen-terminated Mo_2CO_2: Co surfaces, replacing Mo with Co significantly changes the adsorption energies of hydrogen on the neighboring oxygen atoms, thereby, in turn making all of those sites more favorable for HER catalysis. As shown in Fig. 28f, the first form of 2D MXenes transition metal nitride was discovered by Urbankowski et al. ($Ti_4N_3T_x$) [64]. Rather than etching the MAX phase in an acidic solution, they employed a melted fluoride salt to remove the Al

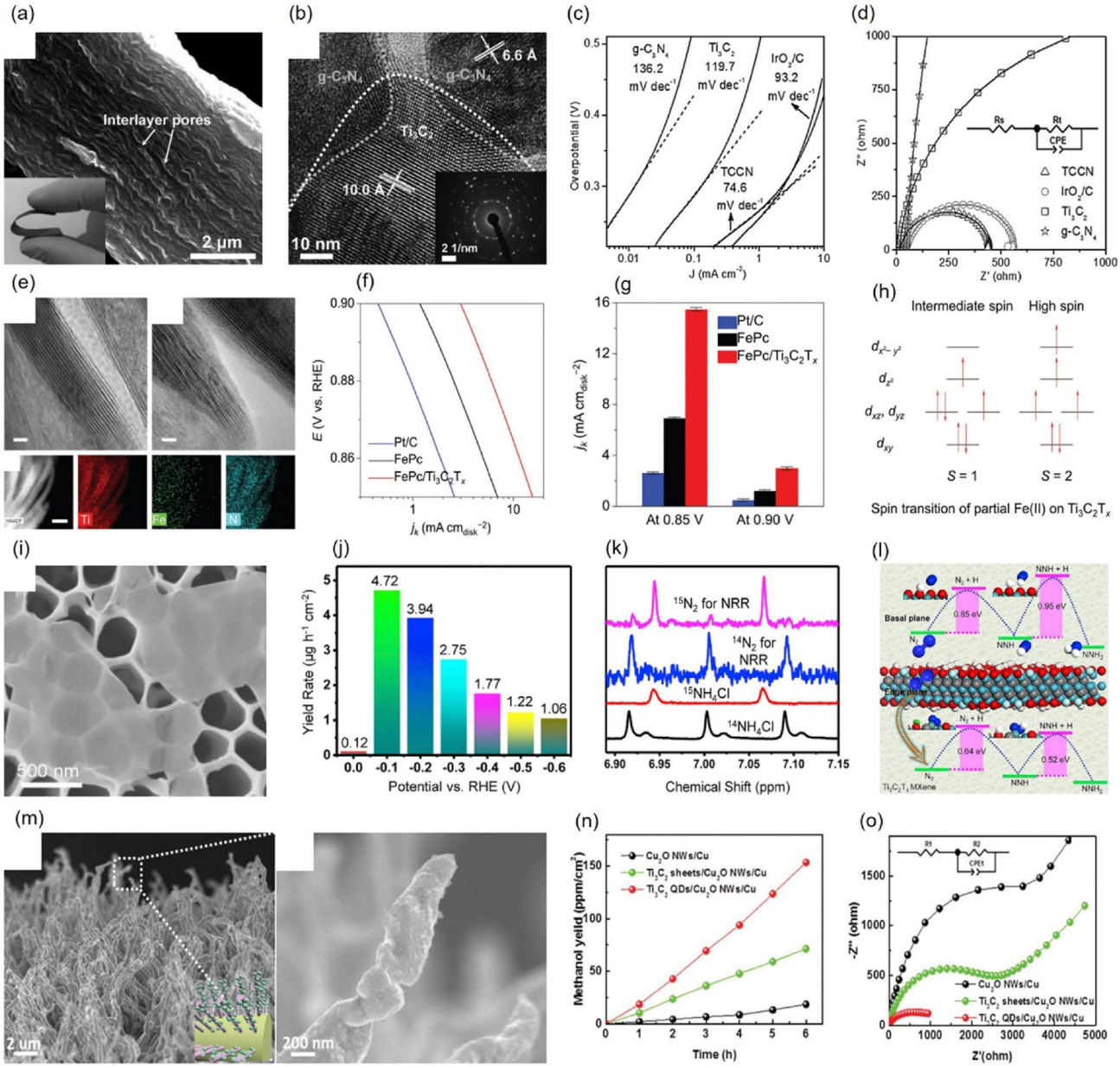

Fig. 27. OER) output for g-C_3N_4/$Ti_3C_2T_x$ (TCCN). Adopted from ref. [373], with the permission of John Wiley and Sons. (a) SEM and (b) TEM of TCCN. (c) Tafel depiction, (d) Electrochemical impedance spectroscopy (EIS) of TCCN, iridium dioxide (IrO_2) materials. Oxygen reduction reaction (ORR) output of iron phthalocyanine (FePc)/$Ti_3C_2T_x$ Adopted from ref. [378], with the permission of John Wiley and Sons. (e) TEM of $Ti_3C_2T_x$ and FePc/$Ti_3C_2T_x$. (f) Tafel illustration. (g) Kinetic current density (jk) of FePc, FePc/$Ti_3C_2T_x$, and Pt/C. (h) Graphical designation of spin transition for Fe(II) on $Ti_3C_2T_x$. Process of N_2 to NH_3 using $Ti_3C_2T_x$ MXene. Adopted from ref. [349], with the permission of Elsevier (i) SEM of $Ti_3C_2T_x$. (j) NH_3 products performance. (k) NMR illustration. (l) Transformation process efficiency of nitrogen to ammonia for $Ti_3C_2T_x$. CO_2 reduction into CH_4 via MXene quantum dots (QDs) as a co-catalyst. Adopted from ref. [273], with the permission of John Wiley and Sons. (m) SEM of Ti_3C_2QDs/Cu_2O NWs/Cu composites. (n) Methanol productivity. (o) EIS plots.

from a Ti_4AlN_3 powder under Argon environment at 550°C. Delamination of the succeeding MXenes with tetrabutylammonium hydroxide (TBAOH) consequently produced the monolayers and few-layered $Ti_4N_3T_x$, where T is the surface termination (F, O, or OH). The as-synthesized two-dimensional titanium nitride (Ti_4N_3) MXenes was expected to be metallic. According to the results of a DFT simulation study on the material, the greater density of states of non-terminated and simple $Ti_4N_3T_x$ was observed with a magnetic moment of 7.0 B per unit cell. Two-dimensional (2D) $Ti_4N_3T_x$ MXenes exhibits both metallic and semiconducting characteristics, as later investigated by the Djire et al. [386]. Exfoliated $Ti_4N_3T_x$ showed an overpotential of 300 mV at 10 mA/cm^2 and a Tafel slope of 190 mV dec1 after being evaluated as an efficient electrocatalyst for the hydrogen evolution reaction. According to these prospective results, for example, the $Ti_4N_3T_x$ MXenes has fascinating electrical, electrocatalytic and optical properties that could be used in both electrocatalysis and optoelectronic applications. According to Xie et al. investigation, the self-assembly of metallic $Ti_3C_2T_x$ MXene flakes with positively charged CNTs as spacers results into the formation of 2D/1D combination see in Fig. 28g and h, which in turn provide highly porous structure by making MXenes to easily contact with electrolyte due to intruding order stacking of MXenes/graphene-2D/2D films. Due to the development of the conductive net with excellent restacking, the MXenes/CNT sheets displayed

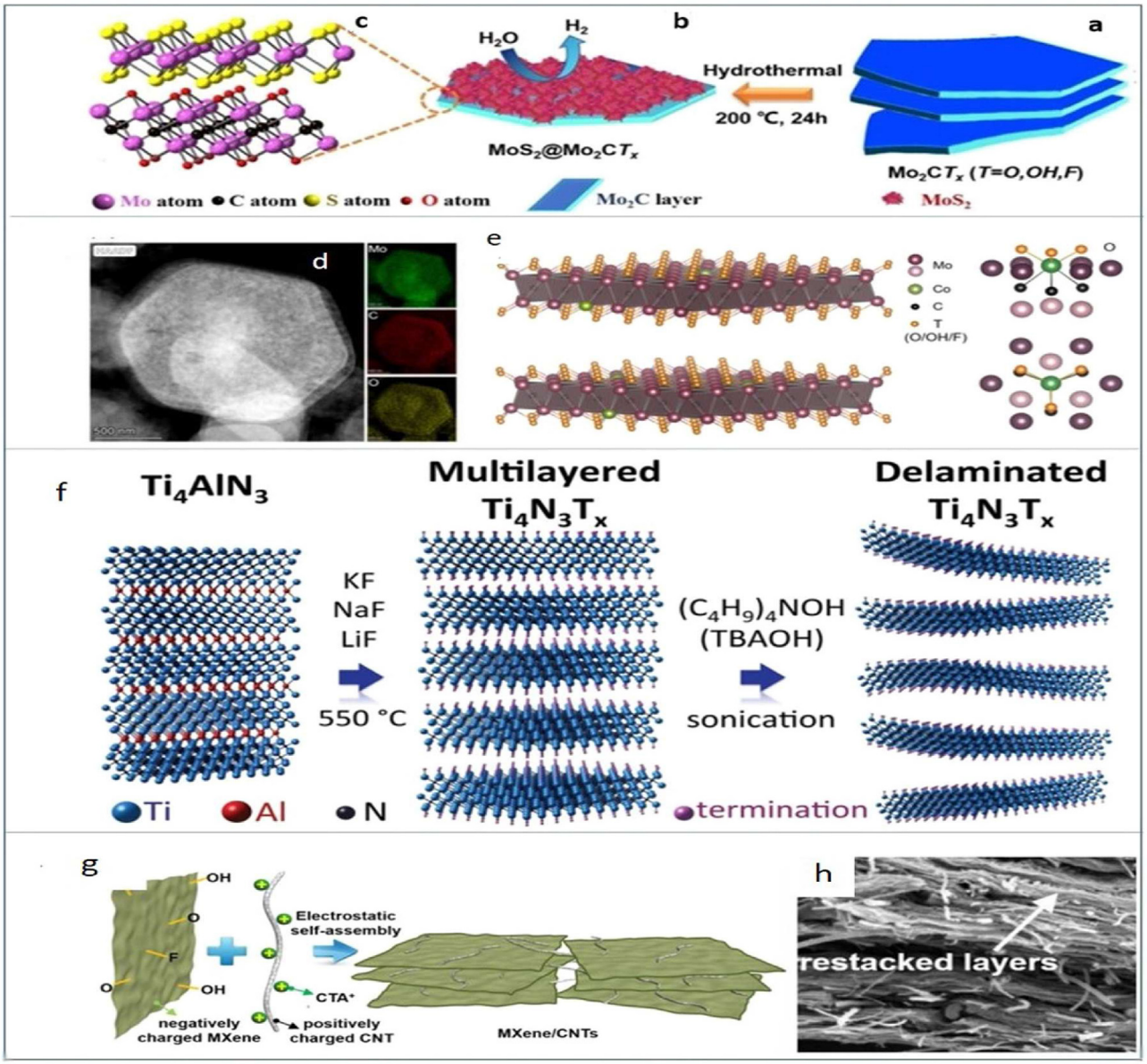

Fig. 28. MXenes as conductors. (a–c) Fabrication of MoS_2/Mo_2CT_x composites. Adopted from Ref. [383], with the permission of ROYAL SOCIETY OF CHEMISTRY. (d) TEM and mapping of Mo_2CT_x:Co, (e) graphical illustration of Mo_2CT_x:Co. Adopted from Ref. [385], with the permission of American Chemical Society (f) Fabrication of $Ti_4N_3T_x$ [64]. (g) Fabrication of MXene/CNT, (h) SEM of $Ti_3C_2T_x$/CNT composites. Adopted from ref. [387], with the permission of Elsevier.

stretched cyclic performance, high volumetric ability, good rate capability [387]. All of these nitrides and carbides have been used in a diverse range of research fields. They include overall water splitting, hydrogen evolution, electrode materials, batteries. A lot of work has been done on the use of MXenes and related nanocomposites and heterostructures in relation to its application for HER. The pristine MXenes, on the other hand, has not yet been approved as a viable OER electrocatalyst owing to its rapid oxidation in an aquatic medium. A considerable increase in the OER performance of MXenes has been observed when it is being used in conjunction with other OER active layered double hydroxide catalyst materials. They include CoFe [388], black phosphorus quantum dots [389], Ni_{1-x} $FexPS_3$ [390]. Synergistic results of active catalyst materials and 2D MXenes's metallic conductivity were attributed to the increased OER performance. Because of its wide surface area and more functional group, the MXenes is commonly employed as a support in various OER active hybrid composites [391].

Additionally, the MXenes are being used in the development of new sustainable energy systems. After eliminating the Ga and Al atoms from the parental ternary carbides Ti_2AlC and Mo_2Ga_2C, the HF etching in turn yields MXenes such as Ti_2CT_x and Mo_2CT_x [357]. The electrochemical cells with three electrodes by having MXenes droplets on the glassy carbon electrode were used to exhibit the electrochemical activities. With an overpotential of 283 mV, the Mo2CTx was found to have the highest HER current density of around (10 mA/cm^2), which is shown in Fig. 29a [357]. The Ti_2CT_x MXenes, on the other hand, had a lower current density of 10 mA/cm^2 at an overpotential of 609 mV. As compared to HER activity of Mo_2CT_x, which decreases slightly at the initial stage but later maintain by showing maximum of current density (10 mA/cm^2), at

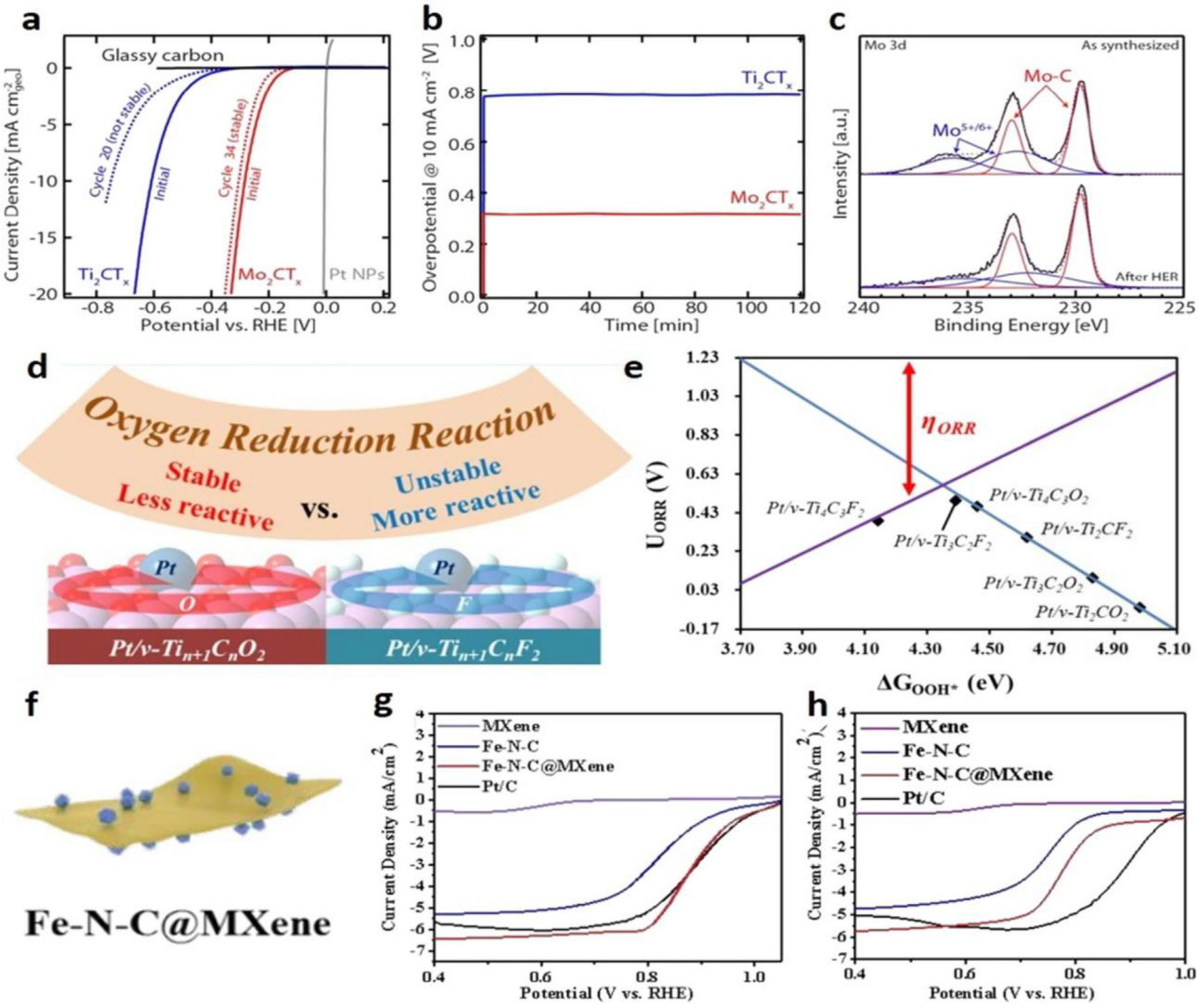

Fig. 29. HER and ORR performance. (a) LSVs of Mo_2CT_x and Ti_2CT_x. (b) Current density plot. (c) XPS spectra. Adopted from Ref. [357], with the permission of American chemical society (d) Illustration of Pt/v-$Ti_{n+1}C_nT_2$ for ORR output. (e) Volcano plot for the ORR. Adopted from ref. [354], with the permission of American chemical society (f) Fe—N—C/$Ti_3C_2T_x$ material through pyrolysis method. (g) LSV plots in KOH. (h) LSV plots in M $HClO_4$. Adopted from Ref. [393], Royal Society of Chemistry.

onset potential of 305 mV, the Ti_2CT_x HER activity reduces initially thereby showing its instability. There was no any significant variation in Ti_2CT_x or Mo_2CT_x onset potential, which is shown in Fig. 29b, while that of before and after HER performance the significant difference in the chemical states of the Mo_2CT_x was observed, which is shown in XPS (Fig. 29c). Energy conversion devices totally rely on the oxygen reduction reaction (ORR). In the case of proton exchange membrane fuel cells, the ORR is a rate limiting step in determining the cell's performance by generating the electricity in turn. Although Pt-based alloys have excellent catalytic activity as an ideal ORR catalyst, they are highly susceptible to instability and carbon monoxide (CO) poisoning. To overcome this issue, the Regmi et al. [392] proposed that as a cost-effective replacement, there are a lot of materials like vanadium carbide (V_8C_7), chromium carbide (Cr_3C_2) and molybdenum carbide (Mo_2C), by having greater activity, while that of nano dimensional carbides such as WC, V8C and Mo_2C exhibit superior HER performance. According to theoretical investigation based on first-principles calculations, Liu et al. [354] examined the considerable effects of surface termination groups of MXenes, which are known to have a significant impact on ORR activity. The detailed computational investigations of the charges, electronic structures and geometries of diverse surface sites are used to describe their properties. Compared to their O-ended counterparts, the F-ended surfaces are expected to be more active for ORR but less stable (Fig. 29d). [354]. The Fig. 29e shows the calculated ORR activity over various surface sites, as depicted by the volcano plot. The equation ηORR = 1.23 − min (UORR) (in V), is used to characterize the expected theoretical overpotential (ηORR), where the equilibrium potential of ORR is 1.23 V, and the min (UORR) is the lowest ORR potential in four electrochemical steps. As compared to O-terminated counterparts, the ORR activity of all F-terminated surfaces is found to be superior. With an ηORR of 0.74 V, the Pt/v-$Ti_3C_2F_2$ surface showed the lowest overpotential. The termination groups' electronic impact was thoroughly explored in this study, which may lead to the development of more viable MXenes frameworks for ORR catalysis. The Yang et al. used a separate pyrolysis preparation method to fabricate a non-noble metal composited Fe-N-C/$Ti_3C_2T_x$ catalyst and according to experimental results, the performance of $Ti_3C_2T_x$ MXenes was not only found to be satisfactorily as conductive substrate, while its addition could also significantly reduce the accumulation and breakdown of Fe—N—C catalyst

following carbonization, while enhancing the ORR activity and the Fe–N–C catalyst stability [393]. The linear sweep voltammetry (LSV) curves of MXenes, Pt/C, Fe–N–C/MXenes and Fe–N–C, in 0.1 M perchloric acid ($HClO_4$) and 0.1 M KOH are shown in Fig. 29g and h, respectively. A half-wave potential of 0.887 V and a current density limit of 6.4 mA/cm^2 of Fe–N–C/MXenes were found to have higher electrocatalytic ORR activity than Fe–N–C with current density of 5.3 mA/cm^2 and half-wave potential of 0.809 V, which is even capable of competing with the commercial Pt/C. Consequently, the bare MXenes almost showed little ORR activity due to the lack of active sites. With a half-wave potential of 0.777 V, the Fe–N–C/MXenes demonstrated an astonishing increase in electrocatalytic ORR activity in the acidic medium, as well as a limited current density of 5.7 mA/cm^2.

According to liu et al. [394], the in situ TiO_2 conversion on the surface of two-dimensional titanium carbide MXene/ruthenium (Ti_3C_2/Ru) resulted into the synthesis of TiO_2–Ti_3C_2/Ru, via direct reduction of Ru^{3+} ions over nanoconfined cocatalyst of Ti_3C_2/Ru (Fig. 30a). Compared to the conventional Ru-TiO_2–Ti_3C_2 catalyst, such a constructed catalyst usually showed more proficient charge buildup and transport. It was observed that the electron–hole recombination is prevented by increasing the distance between the oxidation reduction active sites, which increases photocatalytic performance [345,395]. For the optimized TiO_2–Ti_3C_2/Ru 20 catalyst, the average H_2 evolution rate reached 235.3 mol(/g*h) (Fig. 30b). The quick transfer of photo-induced electrons to the Ti_3C_2/Ru cocatalyst due to lower fermi energy level induced by the increased work function of Ti_3C_2/Ru cocatalyst in turn eliminates the need for cycle in the photocatalytic H_2 production (Fig. 30c) [396]. The Ti_3C_2 MXenes played a crucial part in this unique design technique for separating the semiconductor from the cocatalyst. In terms of surface and structural stability, the newly synthesized material is found to be highly promising in this regard. The heterojunction of 1D CdS nanorod/2D Ti_3C_2 MXenes NSs were synthesized by Xiao et al. [397] by joining solvothermal-generated CdS nanorods with 2D Ti_3C_2 sheets (Fig. 30d). For the solar-driven hydrogen evolution, a composite photocatalyst comprising 1D CdS/2D Ti_3C_2 MXenes photocatalyst was seven times more active than CdS nanorods (Fig. 30e). [274]. The 1D cadmium sulfide (CdS)/2D Ti_3C_2 catalysts fabricated via utilizing the varying proportions of ultrathin exfoliated Ti_3C_2 MXene sheets could be systematically identified using the notation CM-10, CM-20, CM-30, CM-40, CM-60. The enhanced performance is ascribed to the 1D/2D Schottky heterojunction, which facilitated low Schottky barrier height and quick charge separation for the photocatalytic production of H_2 energy (Fig. 30f). [398]. By means of hydrothermal oxidation of Ti_3C_2 MXenes via in situ TiO_2 NSs growth, Meng et al. synthesized a hierarchical Ti_3C_2 MXenes@TiO_2/$ZnIn_2S_4$ nanostructures, which was further deposited by through fixing of the proper quantity of appropriate precursors (Fig. 30g) [399]. As compared to M@TiO_2 and bare ZIS, the properly tuned M@T/ZIS mesoporous hybrid-photocatalyst displayed incredible visible-light absorption activity, effective photogenerated charges separation and transportation, as well as superior efficiency efficiencyfor photocatalytic H_2 evolution at rate of (1185.8 μmol/(g*h)) (Fig. 30h). It is due to the favorable light-harvesting, excellent conductivity appropriate TiO_2 nanosheet band location 100, abundant Ti_3C_2 active sites 101 synergistic effect of ZIS visible-light absorption and, as well as

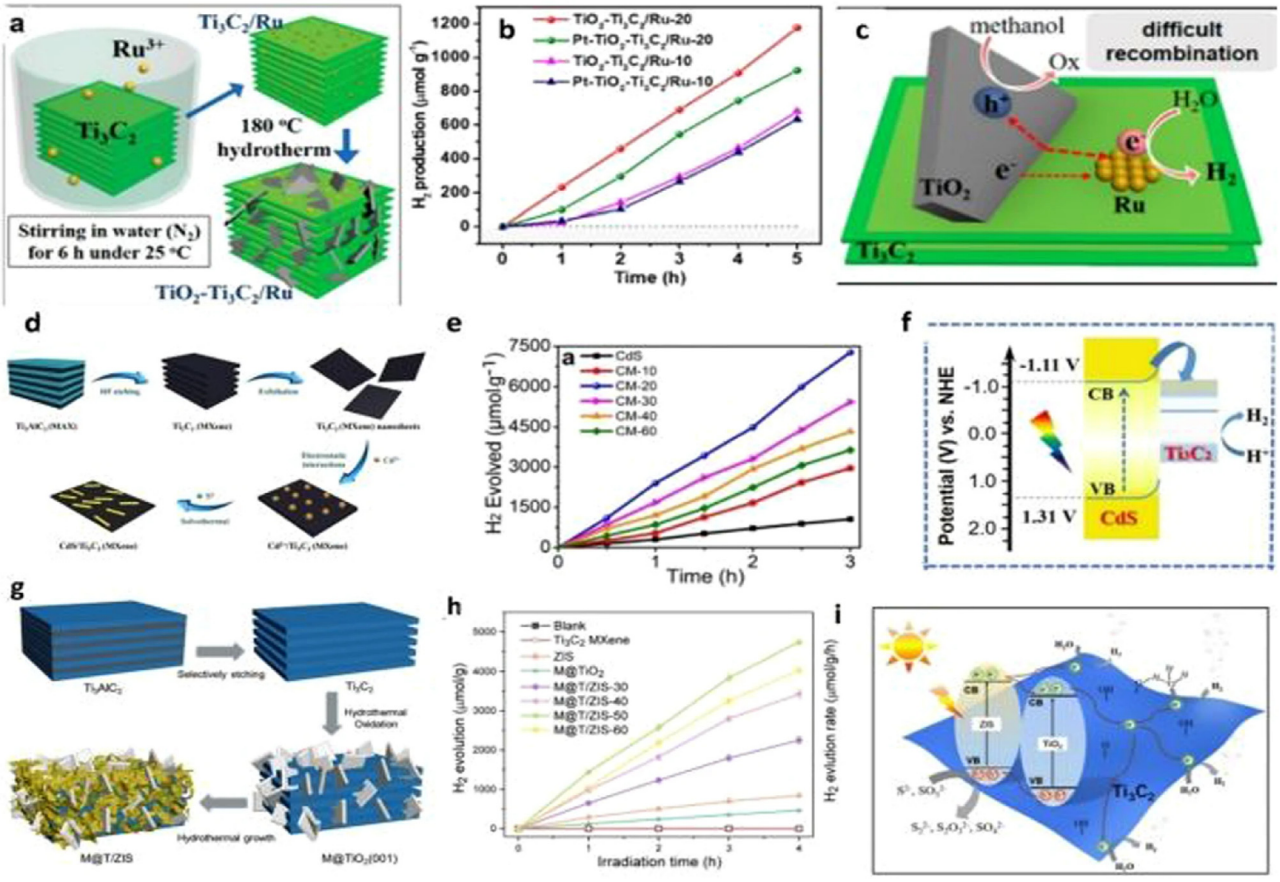

Fig. 30. Photocatalysis of MXene. (a) Fabrication steps of TiO_2–Ti_3C_2/Ru, (b) HER, (c) Electrons/holes mechanism in TiO_2–Ti_3C_2/Ru composite catalyst. Adopted from ref. [394,396], with the permission of (d) Fabrication of CdS/MXenes, (e) HER of as-prepared materials, (f) Scheme of CdS/2D MXenes. Adopted from Refs. [274,397], with the permission of Elsevier. (g) Fabrication of M@T/ZIS, (h) HER of M@T/ZIS photocatalyst, (i) HER of M@T/ZIS material. Adopted from ref. [398–400], with the permission of Elsevier.

specifically allowing the interfacial connection between three components (Fig. 30i) [400]. The engineered ternary heterojunction provided selective separation and transfer of photogenerated charges via quick transfer channels comprising of a well-designed type II heterojunction between ZIS and TiO_2, and a Ti_3C_2/ semiconductor interfacial Schottky junction [401]. In conclusion, it is found that the MXenes based hybrid nanocomposite photocatalysts are considered to effectively enhance the stability and photo-activity of these compounds towards the photocatalytic applications by encouraging the articulate manipulation of MXenes in the field of photocatalysis.

3.2. Environmental detoxification

3.2.1. Nuclear waste treatment

Recently the treatment of nuclear waste has been included in the effective removal of long-half-life radionuclides i.e. $^{133,\ 140}$Ba (barium isotopes), cesium isotopes ^{137}Cs [402–404], $^{152,\ 154}$Eu (europium isotopes), $^{105,\ 107}$Pd (palladium isotopes), ^{90}Sr (strontium isotopes), ^{99}Tc (technetium isotopes), ^{232}Th (thorium isotopes), and $^{235,\ 238}$U (uranium isotopes) from the environment. Due to the toxic effect of nuclides on human's health and the environment, its removal has become a subject of utmost interest. The adsorption techniques have gained much interest to remove radionuclide from wastewater owing to their promising characteristics of low cost, ease in operation, no sludge production and environmentally friendly process [405–409]. For that purpose, a wide variety of adsorbents such as inorganic, organic and combination of both has been extensively investigated for the management of nuclear waste management [36,410–414]. Due to the disadvantage of slow dynamics, poor selectivity and low adsorption capacities, the adsorption techniques have been of limited use for large scale application [415–420]. Nevertheless, the use of 2D layered materials i.e. graphene and transition metal dichalcogenides (TMDs) have already been investigated [421,422]. But these kinds of materials showed low adsorption capacity, which is attributed to the development of weak van der Waals forces between the adsorbent and adsorbate. The 2D layered MXenes owing to the advantage of admirable resistance to acids, good thermal stability, superior specific surface area tunable interlayer spacing and structures, higher ion-exchange capacity, high hydrophilicity, ample surface functional groups ($^{-}$OH, $^{-}$O, and $^{-}$F), have received tremendous research interest in the field of nuclear waste management and overall environmental pollution reduction [66,423,424]. Due to the existence of hydrophilic groups, the MXenes showed good activity by creating ultrafast water flux inside the MXenes galleries, which is attributed to the large interlayer spaces and in turn brought about the higher pollutant's removal capacity from wastewater with fast kinetics [1]. The adsorption of radionuclide over the surface of MXenes has been demonstrated to follow different mechanism such as d-layer manipulation, ion-exchange [425], inner-sphere and complexation [426]. The metal ions adsorption onto MXene surface sites is mainly attributed to the involvement of ion-exchange. The surface sites of metal, which are etched with surface ($^{-}$OH, $^{-}$F and $^{-}$O), terminations help to effectively adsorb the radionuclides. To capture the radionuclides more efficiently, the proper adjustment of the layer d-spacing of MXenes suitable intercalants is considered to be an important parameter in this regard. Moreover, it is well known that the thinner nanosheets formation of multilayered MXenes delamination process could significantly enhance the surface-active sites, which in turn enhance the adsorption of radionuclide coordination [90]. Moreover, the MXenes material has been regarded as the most multifunctional material in the field of nuclear wastewater treatment owing to the advantage of enhanced chemical compatibility with molten salt exacting conditions and superior ability to resist strong radiations [56,90]. That's why, owing to the most promising environmental compatibility characteristics of MXenes such as high thermal stability, exceptional chemical compatibility, strong resistance to radiation further promotes the synthesis of low cost MXenes on large scale with the aim of removing toxic radionuclides from nuclear waste.

3.2.2. Barium and strontium removal

The presence of toxic fission products strontium (^{90}Sr) and barium (^{133}Ba and ^{140}Ba) due to release and inadequate management and disposal of radioactive wastes are present in massive amount in the radioactive liquid wastes [425,427]. Severe kidney, heart and liver problems with intense breathing issues have been reported by the radioactive barium isotopes [425]. Similarly, the oxygen shortage and anemia disease has been reported in literature mainly driven by the and Sr^{2+} isotopes [428]. However, it has become a hot topic to urgently remove the Sr^{2+} and Ba^{2+} from wastes [428]. The ^{140}Ba and ^{133}Ba are considered to be the major radioactive barium isotopes as fission products, which are found to be in large quantities in the radioactive liquid waste. For the first time, the removal of barium was investigated by Fard et al. by means of titanium (III) carbide (II) ($Ti_3C_2T_x$) MXenes, which was prepared by the intercalation and exfoliation of Ti_3AlC_2 in HF solution [425]. The obtained results indicate the 100% removal efficiency of Ba ions within the first 10 min with superior selectivity that other coexisting ions with optimum adsorption capacity (9.3 mg/g) from waste stream. The responsible mechanism for the efficient adsorption of Ba ions onto MXene surface sites appeared as physisorption mode. (Fig. 31a), The improvement in Ba adsorption capacity was carried out by Mu et al. [429], by metal basic intercalation and surface activation of $Ti_3C_2T_x$ in NaOH solution (Fig. 31b). After proper intercalation, the Na^{+} ions are readily interpolated into $Ti_3C_2T_x$ layered structure, thereby, enhancing the overall c-lattice parameter (2.09 nm) of MXenes, which in turn increase the interface attractions of surface-anchored functional groups over the MXene surface sites. Such treatment shows the outstanding ability of MXenes by adsorbing barium ions from wastewater. Mu et al. found the extraordinary Ba^{2+} ions adsorption capacity (46.46 mg/g^{1}) of alkali-treated $Ti_3C_2T_x$ (Alk-$Ti_3C_2T_x$). Therefore, the activation of the MXene surface site via sodium hydroxide (NaOH) was considered to be an effective treatment strategy to enhance the ability of MXenes to effectively capture the toxic ions from the environment. Recently, Jun et al. [428] investigated that the adsorption of Sr^{2+} and Ba^{2+} from fracking wastewater was found to be 225 and 180 mg/g^{1} over $Ti_3C_2T_x$ MXene surface sites, which was mainly attributed to the electrostatic attraction force due to the negative MXene surface sites and positive toxic ions interaction (Fig. 31c(i-ii)). Furthermore, the different mathematical model and characterization techniques (X-ray photoelectron spectroscopy [XPS] and Fourier transform infrared [FTIR] spectroscopy) showed various adsorption mechanisms during Sr^{2+} and Ba^{2+} over MXene surface sites. These mechanisms include chemical ion exchange, inner-sphere complexation and chemisorption mechanisms. Interestingly, they reported the reuse of MXenes up to four regeneration cycles, which is an important parameter in the field of toxic radionuclides removal from fracking wastewater.

3.2.3. Palladium removal

Th high level radioactive waste (HLV) consists of a wide variety of pollutants and among them the radioactive palladium (^{107}Pd) is considered as most toxic element owing to a long-lived fission characteristic, which has the average half-life of about 6.5 million years; [430]. Usually, the discharge wastewater after the fission of

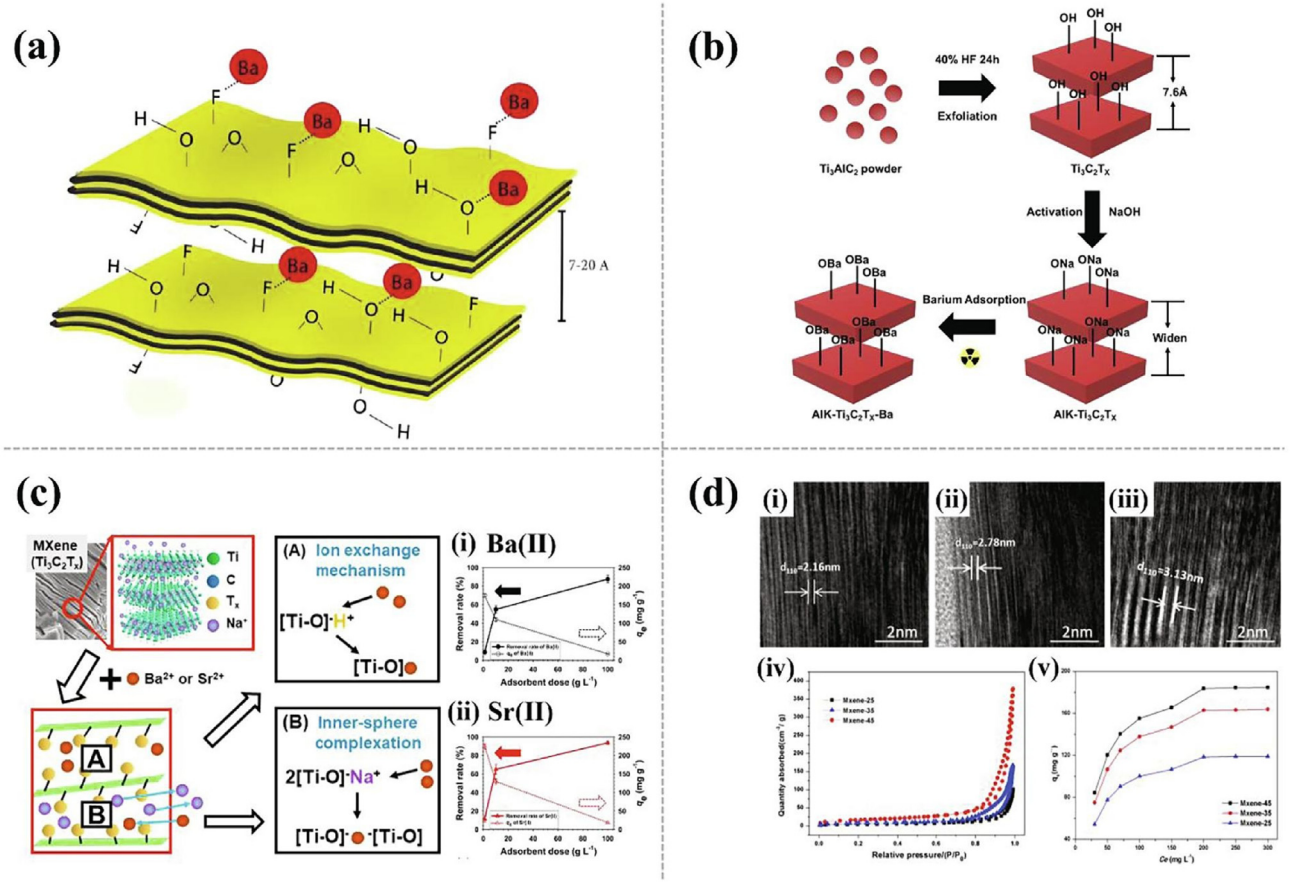

Fig. 31. (a) Adsorption of Ba^{2+} over $Ti_3C_2T_x$ MXene. Adopted from Ref. [425], with the permission of Elsevier (b) Adsorption of radioactive Ba^{2+} ions. Adopted from Ref. [429], with the permission of Royal society of chemistry. (c) (i,ii) Adsorption of Ba^{2+}/Sr^{2+} by MXene. Adopted from Ref. [428], with the permission of Elsevier (d) (i-iii) TEM, (iv) Brunauer-Emmett-Teller (BET) analysis, and (v) pH influence over adsorption. Adopted from Ref. [431], with the permission of Elsevier.

uranium contains different palladium isotopes i.e. ^{105}Pd and ^{107}Pd and these isotopes need to be efficiently removed from nuclear waste stream. By treating the MAX (Ti_3AlC_2) with HF at different temperatures, the Mu et al. (2019) [431] fabricated the MXenes ($Ti_3C_2T_x$) materials to remove the radioactive Pd^{2+} from the HNO_3 medium. The d-spacing values were found to be (0.216, 0.278, and 0.313 nm), for the MXenes prepared at different temperatures (i.e. 25, 35, and 45°C), respectively (Fig. 31d). The superior adsorption capacity of Pd^{2+} (184.56 mg/g^1), was achieved by the MXenes prepared at 45°C owing to high surface area and large d-spacing. Such a superior adsorption capacity was found to be higher as compared to many other reported inorganic materials. Therefore, the obtained finding indicates the considerable effect of exfoliation temperature, which play an important role to enhance the adsorption of Pd^{2+} via larger d-spacing and superior surface area characteristics. All in all, such a treatment strategy shows the MXenes as a promising candidate in the field of Pd^{2+} contaminated wastewater treatment.

3.2.4. Thorium removal

Thorium (Th) is also on the other hand, considered to be a probable productive material as the superlative nuclear fuel substitute to ^{233}U (uranium). Even its negligible amount could cause severe health (cancer) and environmental consequences owing to its radioactive nature [432]. Therefore, the adsorption of thorium is also considered as an important environmental issue to humans [426]. The removal of thorium (IV) was investigated by Li et al. [426] using lightest MXenes Ti_2CT_x owing to their good dispersibility in water, and abundant functional groups. The Ti_2CT_x was prepared through a lithium salt approach by keeping it in dry (denoted as Ti_2CT_x dry) and hydrated conditions (labeled as Ti_2CT_x hydrated). The higher Th(IV) adsorption capacity (213.2 mg/g^1) was achieved onto the surface of Ti_2CT_x-hydrated MXenes by following inner-sphere complexation as compared to the Ti_2CT_x dry MXenes Ti_2CT_x-which is attributed to its larger interlayer space, which in turn makes the easy entrance and distribution of Th(IV) ions into the pores of Ti_2CT_x hydrated MXenes thereby, showing the suitability of lightest Ti_2CT_x material for efficient Th(IV) removal from nuclear waste stream (Fig. 32a(i).

3.2.5. Europium removal

Europium (^{152}Eu and ^{154}Eu radioisotopes), a representative of trivalent lanthanides and a trivalent actinide analog, is one of the principal fission products inevitably discharged into the natural environment from nuclear reactors, posing a public health risk owing to its toxicity even at trace levels [433]. As a result, research into the adsorption of europium from the environment is crucial [434]. Zhang et al. [435] used a moderate (1 M sodium hydroxide/potassium hydroxide (NaOH/KOH), 150°C) in situ oxidation conversion method to make two types of stable hierarchical titanate

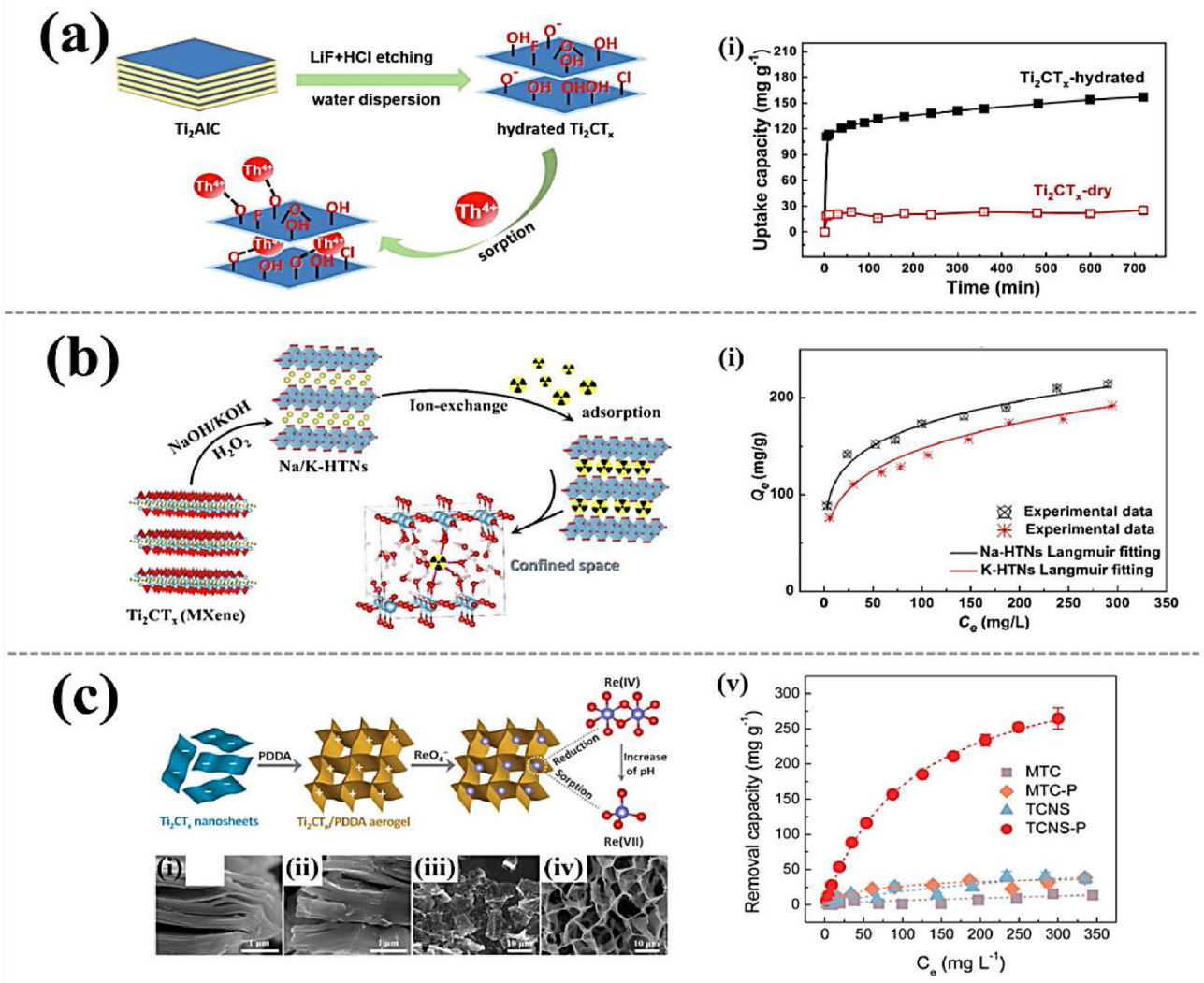

Fig. 32. (a) (i)T horium adsorption over Ti_2CT_x. Adopted from ref. [426], with the permission of Elsevier (b) (i)Fabrication of MXene-based titanate microstructures (HTNs) Adopted from Ref. [435], with the permission of Elsevier. (c) (i-v) Re(VII) elimination by Ti_2CT_x/PDDA hydrogel. Adopted from Ref. [436], with the permission of a American Chemical society.

nanostructures (HTNs; Na-HTN and K-HTN) from a 2D Ti_2CT_x MXenes precursor. The HTNs produced have high adsorption capabilities for Eu (>200 mg/g^1) (III). The ion-exchange process, in which $H^+/Na^+/K^+$ were replaced by stronger hydrogen bonds and electrostatic attraction, resulted in the adsorption of Eu(III). The Eu(III) was trapped in the HTN's nanoscale interlayers and immobilized (Fig. 32b (i)). The Eu(III) was chosen as a chemical equivalent of trivalent lanthanides and actinides by the author. The Na-HTN had a greater adsorption capacity (221.7 mg^1/g^1) than K-HTN (202.8 mg^1/g^1), which might be attributable to its broad interlayer space and high hydration energy of Na^+; these properties could facilitate Eu transport and exchange (III). The presence of a significant number of interlayer water molecules might aid in the rapid transit and diffusion of exchangeable cations within Na-HTNs, resulting in improved ion-exchange performance.

3.2.6. Rhenium and technetium sequestration

The Wang et al. [436] described a new MXenes-polyelectrolyte nanocomposite with three-dimensional networks for improved removal of perrhenate, a pertechnetate mimic. The addition of poly(diallyldimethylammonium chloride) (PDDA) to a Ti_2CT_x nanosheet reduced the surface charge and enhanced the stability, resulting in a Re(VII) removal capacity of up to 363 mg^1/g^1 and rapid sorption kinetics. When competing anions (such as Cl and SO_4^{2}) coexisted at a concentration of 1800 times, the Ti_2CT_x/PDDA nanocomposite showed high selectivity for ReO_4 (Fig. 32c). Overall, the Ti_2CT_x/PDDA nanocomposite appeared as a good option for the effective eradication of Tc contamination. The disclosed surface modification method might make it easier to use MXenes-based materials to treat additional oxidized anion contaminants in the environment.

3.3. MXenes-based electrochemical capacitors

The Polar organic molecules [177] and metal ions [437] can spontaneously intercalate MXenes. For instance, a variety of monovalent and multivalent cations (such as Li^+, Na^+, K^+, NH^{4+}, and Mg^{2+}) could chemically or electrochemically intercalate MXenes, occupying electrochemically active sites on the MXene surfaces, and engage in energy storage [437,438] (Fig. 33a). For electrochemical capacitors, $Ti_3C_2T_x$ is the most investigated MXenes. The volumetric capacitance of freestanding $Ti_3C_2T_x$ paper electrodes in neutral and basic electrolytes has been demonstrated to be 300–400 F/cm^3; these outstanding values are comparable to recently reported activated graphene-based electrodes (350Fcm^3) and exceed the best all-carbon electrical double-layer capacitors

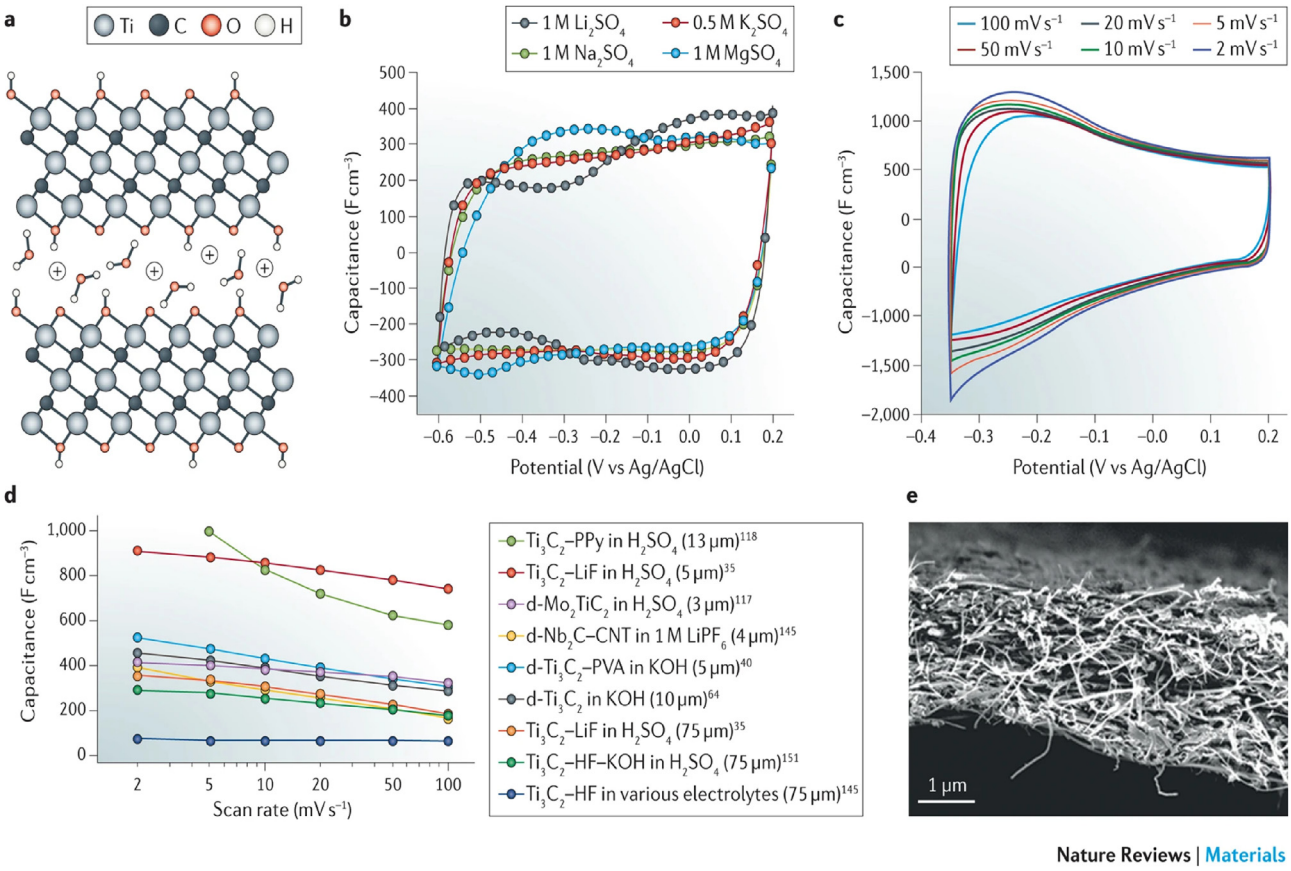

Fig. 33. MXene capacitance efficiency (a) Cation interaction among $Ti_3C_2T_x$ sheets. (b) CV of $Ti_3C_2T_x$ sheet electrodes in sulfate electrolytes. Adopted from ref. [438], with the permission of Elsevier (c) CV of $Ti_3C_2T_x$ sheet electrodes in H_2SO_4. Adopted from Ref. [155], with the permission of Nature (d) Differentiation between activity. Adopted from ref. [155,437], with the permission of Nature. (e) SEM of Nb_2CT_x—CNT sheets [445], with the permission of Wiley-VCH.

[155]. The cyclic voltammetry curves change somewhat depending on the cation (Fig. 33b) [437], but there are no prominent peaks and the cyclic voltammetry profiles resemble 'capacitor-like.' A rolled pure $Ti_3C_2T_x$ clay electrode achieved a volumetric capacitance of over 900 F/cm^3 in 1 MH_2SO_4, presumably as protons are the smallest cations and thus, could easily access the greater number of electrochemically active sites, especially when Li^+ ions with water molecules intercalated during the synthesis and prevent MXene sheets from stacking again. Furthermore, as shown in Fig. 33c (i-v), the $Ti_3C_2T_x$ exhibits excellent capacitive behavior even at relatively high charge and discharge rates, in contrast to the sluggish intercalation of ions seen in other layered materials utilized in battery applications, such as graphite [155]. The rate performance of interdigitated thin MXenes electrodes on flexible substrates is significantly superior [439]. MXenes also have high cyclability, with $Ti_3C_2T_x$ electrodes reporting no change in capacitance after 10,000 cycles [155]. The mechanism behind MXenes's high volumetric capacitance was not immediately apparent. MXenes have no significant redox peaks in their cyclic voltammetry profiles, which are similar to those of carbon-based double-layer capacitors. The available specific surface area, on the other hand, is insufficient to explain the performance [155,437]. Electrochemical in situ X-ray absorption spectrometry (XAS) measurements for $Ti_3C_2T_x$ (HCl—LiF etched) in 1 M H_2SO_4 were conducted out to see if the charge storage process is pseudocapacitive (that is, it includes changes in the oxidation state of the transition metal) [440]. Changes in the titanium oxidation state were identified using XAS during cycling, similar to the situation for lithium-ion batteries, and were compatible with the experimental values of the material's capacitance [157]. As a result, it can be inferred that, at least, up to scan rates of 20 mV/s^1, the mechanism of electrochemical storage of $Ti_3C_2T_x$ MXenes in sulfuric acid is largely pseudocapacitive and not diffusion limited [155]. The volumetric capacitance of MXenes is influenced by a number of key parameters. For starters, the electrode density acts as a conversion factor for gravimetric to volumetric performance. Freestanding additive-free MXenes electrodes generally have densities of 3–4 g/cm^3, but MXenes-based composite electrodes containing polymer binders and conductive additives have densities ranging from 1 to 2.5 g/cm^3. The MXene surface chemistry is another major component that influences gravimetric and volumetric capacitance. When fluorine-containing functional groups are replaced with oxygen-containing ones, the capacitance tends to increase significantly. The gravimetric capacitance values improved by a factor of two to seven when HF-produced $Ti_3C_2T_x$ was chemically changed with KOH, N_2H_4, or DMSO solutions, depending on the electrolyte employed, with acidic electrolytes showing the most significant changes [437,441,442]. It was also shown that $Ti_3C_2T_x$ made with an HCl—LiF combination (rather than HF) had a high proportion of oxygen-containing functionalities [443]. Outstanding volumetric capacitances of up to 900 F/cm^3 have been demonstrated thanks to these features. The process scalability is noteworthy: electrodes with thicknesses of up to 75 m were easily created by rolling the as-synthesized $Ti_3C_2T_x$ (HCl—LiF etched) clay sample, and demonstrated capacitance of 350 F/cm^3 (Fig. 33d) [155]. It's also worth noting that MXenes other than $Ti_3C_2T_x$ show a lot of promise for supercapacitors. With rectangular cyclic voltammetry profiles, the Mo_2CT_x and $Mo_2TiC_2T_x$ demonstrated significant volumetric

capacitance [122,444]. Hybrid materials based on MXenes can improve the electrochemical and mechanical performance. It was also discovered, for example, that incorporating 5–10 wt% CNTs (Fig. 33e), graphene, or onion-like carbon improves the rate performance due to enhanced ion accessibility in aqueous and organic electrolytes (Fig. 33d) [445].

3.4. MXenes in batteries

MXenes are competitive with other 2D materials because of their chemical and structural diversity [446]. As a result, theoretical research can aid in the identification of the most promising candidates for energy storage applications. For example, MXenes with low formula weights, such as Ti_2C, Nb_2C, V_2C, and Sc_2C, have been shown to have the highest theoretical gravimetric capacity (that is, the amount of charge that can be stored per gram of material) [447]. As a result, M_2X electrodes should have larger gravimetric capacities than M_3X_2 and M_4X_3 electrodes. Because the connections between M and X are too strong to be easily broken, it's safe to believe that ions only pass through the MXene sheets. All available experimental evidence backs this up. Because Ti_3C_2 contains one inactive TiC layer, Ti_2C should have a 50% greater gravimetric capacitance than Ti_3C_2. This was demonstrated experimentally: Ti_2CT_x has a gravimetric capacity for Li^+ uptake that is 1.5 times more than $Ti_3C_2T_x$ synthesized in the same way [126]. It is vital to remember that the formula weight does not adequately specify the capacity. For example, all MXenes evaluated under identical settings (280 mAh^1g^1 at 1C and 125 mAh^1g^1 at 10C cycle rates), V_2CT_x had the greatest Li^+ capacity [150]. Furthermore, despite the fact that niobium atoms are heavier than titanium, Nb_2CT_x has a greater gravimetric capacity than Ti_2CT_x at the same cycle rate (180 mAh^1/g^1 for niobium carbide MXene multilayer nanoflakes (Nb_2CT_x) against 110 mAh^1/g^1 for Ti_2CT_x at 1C) [150]. This can be explained in part by the complicated nature of ion storage. As established by theoretical investigation, surface terminations are one element that might alter performance [157,447]. For example, oxygen terminations are preferred, whereas hydroxyls and fluorine result in decreased capacity and inhibited lithium-ion movement. Theoretically, and empirically, the main properties of ion intercalation into MXenes from organic electrolytes have been disclosed (Fig. 34a) [157]. When in situ X-ray absorption spectroscopy (XAS) was used to investigate the mechanism of lithium-ion charge storage in $Ti_3C_2T_x$, it was discovered that the transition metal (that is, titanium) oxidation state changes continuously during charge and discharge (Fig. 34b) up to 0.5 V against Li/Li^+ [157]. A further fall in potential, however, does not result in a change at oxidation state. Instead, lithium atoms can reversibly create an extra layer because of MXenes' 2D structure and conductivity (Fig. 34a). This results in a twofold increase in capacity, and this process should be applicable to various MXenes [448]. Optimization of the electrode design, which involved hybridizing porous MXene flakes with carbon nanotubes, resulted in a lithium-ion capacity of over 750 mAh/g^1. Between the 2D layers of $M_{n+1}X_nT_x$, MXenes may accept ions of different sizes. This qualifies them for non-lithium-ion batteries (NLiBs), for which the present electrode material option is restricted. The Fig. 34c shows the theoretical capacities of several oxygen-terminated MXenes in Na, K, Mg, Ca, and Al-ion batteries [448]. It's worth noting that the creation of an extra metal layer for Na^+ and other ions was expected, resulting in a capacity increase of twofold. Furthermore, various MXenes can give a range of working potentials due to chemical and structural heterogeneity as well as surface chemistry tunability, making some of them useful as either anodes or cathodes (Fig. 34d). The Li^+ [157] and other ions [448] have low diffusion barriers in MXenes, according to theoretical investigations. This is consistent with the experimentally reported very high-rate performance of various MXenes [449]. The MXenes-based electrodes have typical capacities of 50–200 mAh^1/g^1 at speeds more than 10C (i.e. a 6-minute charging period). As a result, MXenes in metal-ion batteries don't have a plateau area in their galvanostatic charge–discharge profiles (Fig. 34b), which is similar to supercapacitor behavior. Composite electrodes made up of MXenes have a lot of potential for high-performance, high-rate batteries. Because of the strong interaction of polysulfide species with MXenes functional groups, Ti_2CT_x or $Ti_3C_2T_x$ have been employed as conductive sulfur hosts in Li–S batteries, resulting in considerably increased cyclability and stability (Fig. 34e) [450]. Encapsulating tin nanoparticles between layers of $Ti_3C_2T_x$ produces consistent performance with a volumetric capacity reaching 2000 mAh^1/g^1 [451]. Other high-capacity electrode materials that suffer a major volume shift upon intercalation might benefit from a similar strategy of co-integration (hybridization) with MXenes to significantly boost cycle life and rate capability. MXenes are used in this method to create a conductive matrix that allows particles in order to expand and contract while retaining structural and electrical connectedness.

3.4.1. MXenes in lithium-ion batteries

The achievement of LIBs for portable devices was honored in 2019 when John B. Goodenough was awarded the Nobel Prize in Chemistry. M. Stanley Whittingham and Akira Yoshino, for their work in improving updated portable electronics [453]. The LIBs are widely employed nowadays in tiny electronics and electric cars due to their greater energy storage density, extended cycle life, and environmental friendliness when compared to other alternatives [454]. To yet, LIBs that use graphite as an anode material have been unable to fulfill the stringent requirements for its lower theoretical specific capacity (372 mAh/g^1) [455]. MXenes compete with previous 2D materials due to their diverse structural and chemical characteristics [446]. As a result, theoretical research into several types of materials can be beneficial in determining the most promising material for energy storage applications. The gravimetric capacity of low formula weight MXenes such as niobium carbide (Nb_2C), titanium carbide (Ti_2C), scandium carbide (Sc_2C), and vanadium carbide (V_2C) has been shown to be the most attractive materials by theoretical investigations [447]. The M_2X-based electrodes have greater anticipated gravimetric capacities than M_3X_2 and M_4X_3 electrodes. Because the M–X bonding is fairly strong, foreign ions can only reasonably penetrate between the MXene sheets. The results of the experiments support this notion. Because Ti_3C_2 contains one non-active TiC layer, Ti_2C MXenes should have a larger gravimetric capacitance (50%) than Ti_3C_2 MXenes, although having equal surface chemistry. This was demonstrated experimentally that Ti_2CT_x MXenes gravimetric capacity for Li^+ absorption is 1.5 times larger than $Ti_3C_2T_x$, despite the fact that both were synthesized via similar pattern [177]. It is important to note that the capacity of a material is not determined merely by its formula weight. When compared to other MXenes tested under the same conditions (280 mAh^1/g^1 at 1 C and 125 mAh^1/g^1 at 10 C cycle rates), the V_2CT_x has the greatest capacity for Li^+. Furthermore, at a comparable cycle rate of 1 C, the Nb_2CT_x (180 mAh/g) has a larger gravimetric capacity than the Ti_2CT_x (110 mAh/g), despite the fact that niobium (Nb) is heavier. This is explained in part by the complexity of ion storage. The researchers have determined that the surface terminations are the primary factor that influences the performance [447]. In terms of capacity and lithium-ion transport, for example, MXenes materials with oxygen terminations outperform hydroxyl and fluorine-based MXenes [456]. Because of their exceptional electrical conductivity, the possibility of numerous surface terminations, high mechanical strength, hydrophilic nature, advantageous layered structure for ion/electron transportation, and

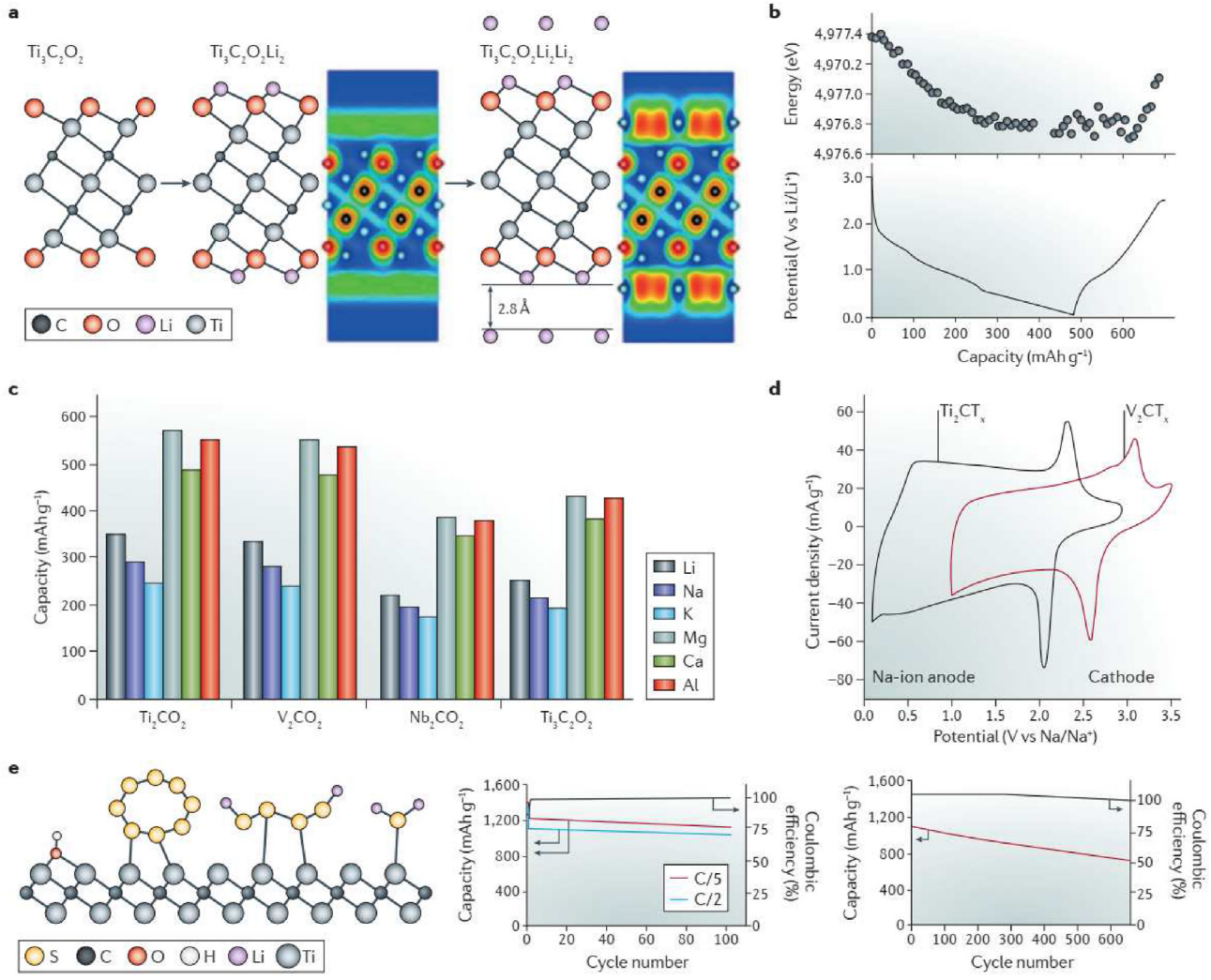

Fig. 34. MXene electrodes in batteries. (a) Mechanism of lithiation of $Ti_3C_2T_x$ [157]. (b) Changing titanium edges efficiency Adopted from Ref. [157], with the permission of American chemical society (c) Lithium/non-lithium ions affinities on O_2 terminating MXene nanomaterials. Adopted from Ref. [448], with the permission of American chemical society (d) Cyclic voltammetry (CV) of Ti_2C and V_2C. Adopted from ref [449,452], with the permission of American chemical Society (e) Efficiency of Ti_2C−S material in Li−S batteries [450], with the permission of Wiley-VCH.

the ability to accommodate intercalants [457]. The MXenes have recently been extensively investigated as LIB anodes both alone and in combination with other 2D materials such as molybdenum disulfide (MoS_2) [458], tungsten disulfide (WS_2) [459], and graphitic carbon nitride (g-C_3N_4) [460]. The multilayered flakes of $Ti_3C_2T_x$ MXenes were initially proposed as a suitable anode for lithium storage by Naguib et al., in 2011 [126], Later computational and experimental research into MXenes electrodes for lithium ion batteries (LIBs) has been conducted. The first application of $Ti_3C_2T_x$ MXenes in LIBs was described in 2012 by Naguib et al. who reported a high reversible capacity of 225 mAh/g at a current density of C/25. This discovery opens up a new line of inquiry for those looking at MXenes as a Li^+ intercalation host material for LIBs [447]. Later, as-obtained $Ti_3C_2T_x$ "paper" offered an improved reversible capacity of 410 mAh/g at 1 C, much better than etched- $Ti_3C_2T_x$ MXenes [177]. When MXenes are mixed with other 2D materials, they act as conductive spacers, preventing agglomeration and preserving some of the physicochemical features of monolayers [461]. Moreover, during the charge/discharge process, the active 2D space generated by MXenes can function as a nanoreactor to restrict the diffusion of intermediates [462], resulting in a reversible transition process between each layer and a well-preserved interfacial contact. The Chen et al. [463] studied the formation of MoS_2/MXenes 2D layered heterostructures by in situ sulfidation of $Mo_2TiC_2T_x$ precursors using this idea. To generate the ultimate MoS_2-on-MXenes hybrid materials, the sulfur nanoparticles were inserted between the MXene layers using the solution process approach. These sulfur nanoparticles can in situ react to $Mo_2TiC_2T_x$ surface with the Mo atom to form the ultimate MoS_2-on-MXenes hybrid materials. The pure $Mo_2TiC_2T_x$ X-ray diffraction (XRD) pattern (Fig. 35b) reveals the only peaks of (00l) with a displacing of 21.53 Å. In the filtered MXenes film, the presence of all the (00l) peaks shows the robust restacking of the flakes. For MoS_2/$Mo_2TiC_2T_x$-500 and MoS_2/$Mo_2TiC_2T_x$-700, the d-spacing of $Mo_2TiC_2T_x$ reduced from 21.53 Å to 14.06 and 13.71 Å, respectively. The lattice spacing of around 14.0 Å was measured in the transmission electron microscopy (TEM) picture (Fig. 35c), which agrees with the (002) peak in the XRD pattern of the $Mo_2TiC_2T_x$. Furthermore, an advanced-designed layered material with 37 displays that two layers of molybdenum disulfide (MoS_2) are in near contact with layers of $Mo_2TiC_2T_x$, allowing heterostructures of MoS_2-on-MXenes. Owing to synergistic effects, the MoS_2/

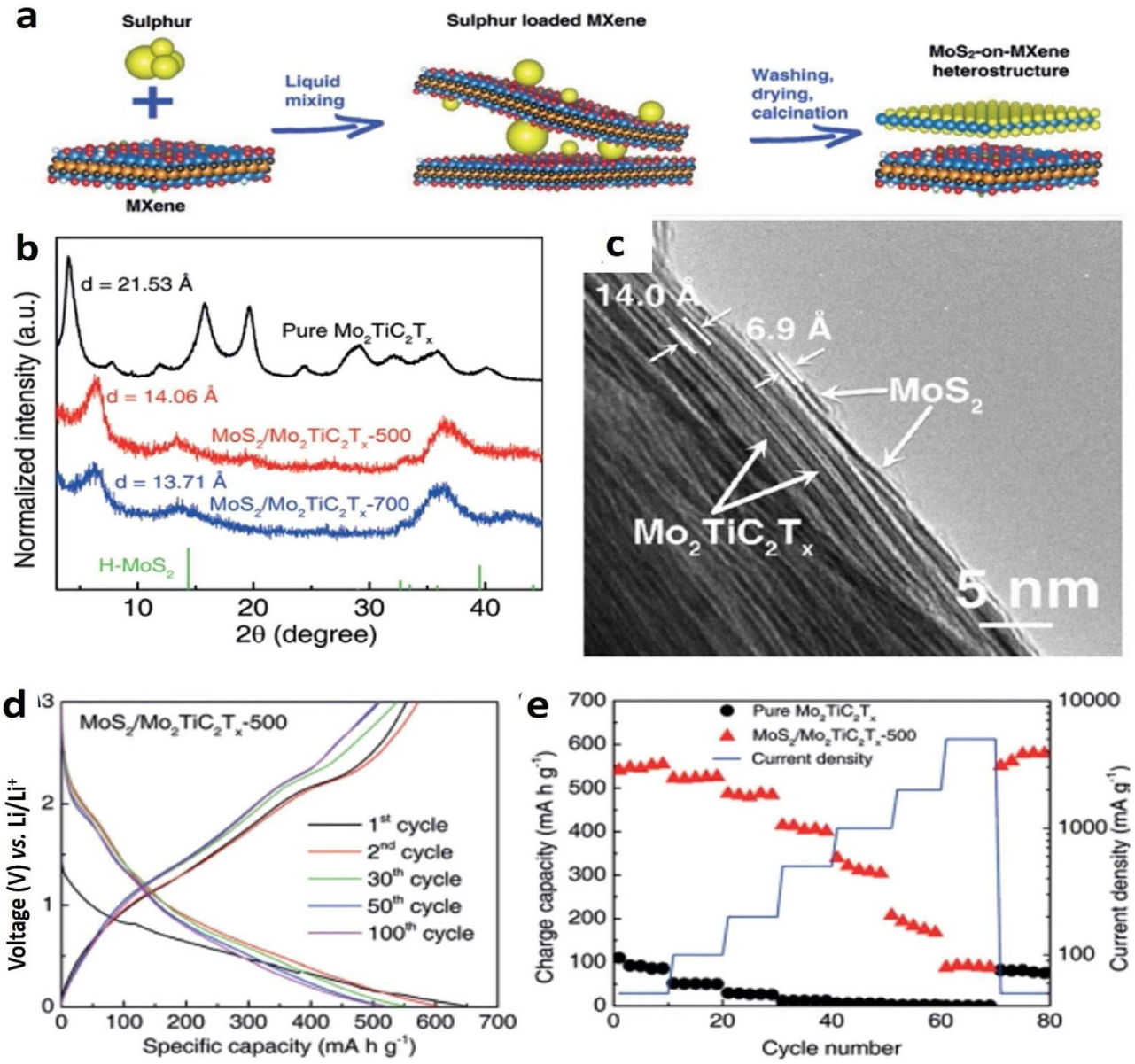

Fig. 35. Synergistic effect of MoS_2/MXene materials. (a) Fabrication of MoS_2/MXene; (b) XRD; (c) TEM. (d) Galvanostatic charge-discharge (GCD) depiction; (e) Rate activity. Adopted from Refs. [463,464], with the permission of. MoS_2-on-MXene heterostructures as highly reversible anode materials for lithium-ion batteries.

$Mo_2TiC_2T_x$-500 (500 shows that the heating temperature was 500°C) electrode illustrates an enhanced reversible capacity of 554 mAh/g at 100 mA/g^1 current density and maintains a capacity of 509 mAh^{1}g^1 after 100 cycles (Fig. 35d). The MoS_2/$Mo_2TiC_2T_x$-500 electrode demonstrated capacities of 484, 407, 315, and 182 mAh^1/g^1, when the current density was amplified to 200, 500, 1000, and 2000 mA/g, respectively. The MoS_2-on-MXenes hybrid material (MoS_2/$Mo_2TiC_2T_x$-500) electrode produced a capacity of 90 mAh/g even at a high current density of 5000 mA/g (Fig. 35e). In addition, the computational findings show that the 2D heterostructures exhibit metallic properties that additionally improve the electrochemical performance of LIBs. Due to the inclusion of various components, the MXenes-based composites exhibit increased electrochemical storage abilities. The 500 electrodes achieved a capacity of 90 mAh/g even at a high current density of 5000 mA/g (Fig. 35e). Furthermore, the theoretical results demonstrate that the 2D heterostructures have metallic features that help LIBs function better electrochemically. Due to the integration of various components, the MXenes-based composite displays improved electrochemical storage properties.

3.4.2. MXenes in sodium-ion batteries

Because sodium is abundant in nature, unlike lithium, the rechargeable sodium-ion batteries (SIBs) have piqued researchers' attention in recent decades as a cost-effective energy storage solution for sustainable energy, electric cars, and smart grid applications [465]. Despite this, as sodium ions are larger, an interlayer spacing of more than 0.37 nm is required to increase the sodium-ion diffusion in electrode materials for successful sodium-ion intercalation [466]. The development of ultrathin 2D layered electrode materials with extended interlayer gap might overcome this challenge. By reducing the sodium-ion insertion/removal channels, the diffusion route will be shortened [464]. Enlarging the interlayer distance, on the other hand, has a significant impact on ionic

conductivity, which is important for successful sodium-ion intercalation [467]. Apart from TMDs, graphene, and g-C_3N_4 [468], 2D metal carbides (MXenes) with atomically thin NSs, a rich chemical composition, additional functional groups, and good metallic conductivity have a bright future in energy storage and utilization [178,469]. Because of its low diffusion barrier for Na^+, excellent metallic conductivity, and intercalation capabilities, the MXenes has been discovered as a viable anode for NIBs with short electronic and ionic transportation pathways [470], While the diameter of 2D titanium carbide is on the atomic scale (monolayer TiC_3), it has a theoretical capacity of 1278 mAh^1/g^1 [471]. Open-circuit voltage and low barrier energy are reported in monolayer TiC_3 [472], according to first-principles calculations. When TiC_3 is alloyed with two-layer Na atoms, it retains a metallic state, proving its high electric conductivity and ultra-long cycle life [174]. In contrast to multilayered MXenes, such unique properties make the TiC_3 monolayer, notably a metal-rich MXenes, a desirable anode material for SIBs [469]. Various techniques were used to improve the sodium-storage properties, including enlarging interlayer distance [473], co-functioning with elevated capacity [474], and deterring the stuffing of MXene layers by developing permeable structures [475], by taking the benefits of MXenes matrix with its distinctive 2D structure, exceptional metallic conductivity, and intercalation ability. The Sun et al. [476] used a solution process approach based on electrostatic attraction to make sulfur-decorated Ti_3C_2 MXenes (S-Ti_3C_2). To get sodium-intercalated and sulfur-decorated S-Ti_3C_2 MXenes, the delaminated Ti_3C_2 MXenes were saturated in Na_2S solution (Fig. 36a). The uneven surface of Ti_3C_2 caused by sulfur impurities created by Na_2S solution treatment at the surface of Ti_3C_2 MXenes after soaking is seen in FESEM Fig. 36b. Because of the linked sulfur groups, more sodium storage was assigned, and extra rapid sodium diffusion pathways were discovered in sodium-pillared structures and 2D S-Ti_3C_2 MXenes interlayers [477]. While as an anode material for SIB (Fig. 36c) [476,478], S-Ti_3C_2 MXenes displayed a good reversible capacity of 135 mAh/g^1 at a current density of 2 A/g^1 after 1000 cycles due to self-enhanced kinetic, intercalation pseudo-capacitance, and surface-controlled pseudo-capacitance.

The Zhao et al. [479] mixed MXenes with NiCo bimetallic phosphide to improve the structural stability and electrochemical activity of MXenes as an anode material for SIBs (Fig. 37a). To construct a 3D wrinkled porous $Ti_3C_2T_x$ network, a colloidal solution of a few-layered well-etched $Ti_3C_2T_x$ MXenes was combined with NaOH solution (Fig. 37b) to displays the respective field emission scanning electron microscopy (FESEM) and TEM micrographs. The high concentration of Na^+ intercalates amid MXene layers to modify the Li^+, resulting in a wider layer space. Furthermore, because the saturated ^-OH in solution replaces the −F terminal groups, the chemical reactivity is substantially stronger. To generate the 3D crinkled porous Ti_3C_2/NiCo hybrid, wrinkled alkali-saturated MXenes Ti_3C_2/NiCo-LDH precursors were used, followed by in situ phosphorizations to obtain Ti_3C_2/NiCoP product (Fig. 37c). The operating concept of a Ti_3C_2/NiCoP-based half-cell anode is shown in Fig. 37d. The conductive bi-metallic particles could help to prevent the aggregation and pulverization, resulting in rich redox reaction sites, low charge transfer impedance, and excellent

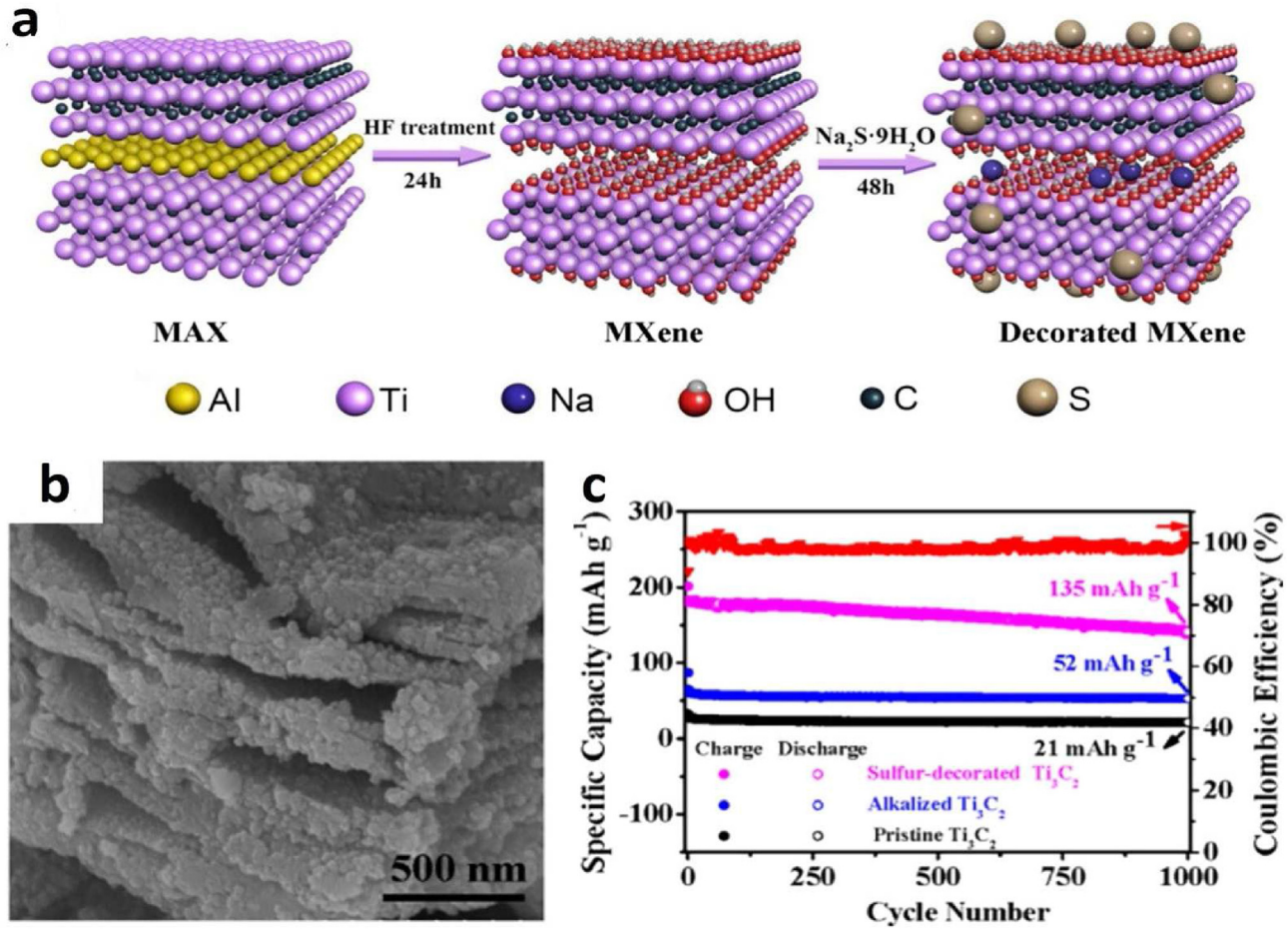

Fig. 36. S/Ti_3C_2 activity. (a) Fabrication of S/Ti_3C_2 MXene. (b) SEM. (c) Stability performance of S/Ti_3C_2 [476,478], with the permission of Elsevier.

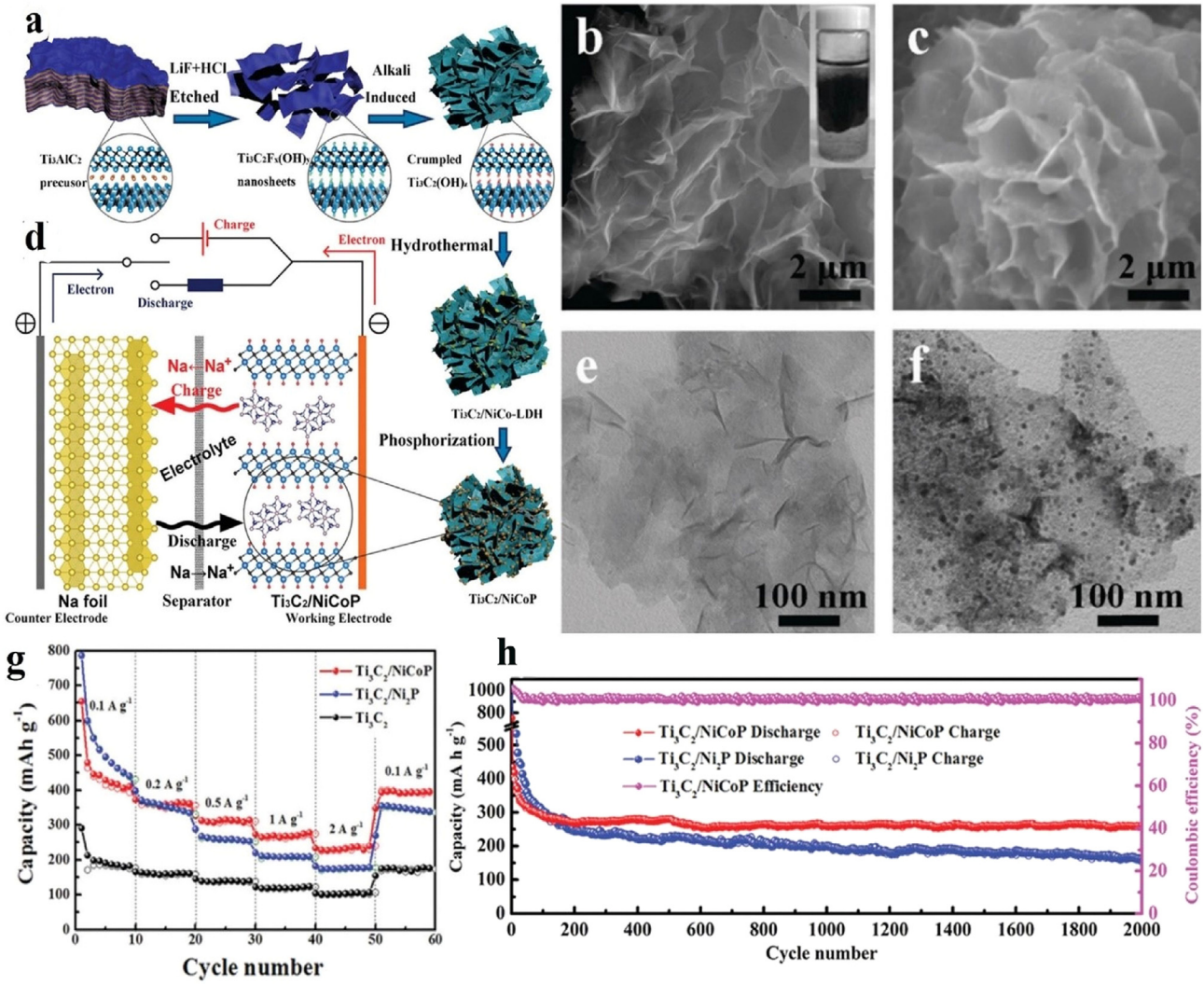

Fig. 37. Activity of Ti_3C_2/NiCoP heterojunction. (a) Fabrication of Ti_3C_2/NiCoP heterojunction. (b, c) SEM. (d) Charge-discharge process. (e, f) TEM. (g) Activity rate of Ti_3C_2, Ti_3C_2/Ni_2P, and Ti_3C_2/NiCoP electrodes. (h) Stability analysis of Ti_3C_2/Ni_2P, and Ti_3C_2/NiCoP electrodes. Adopted form Ref. [479], with the permission of Royal society of chemistry.

electrical conductivity [480]. The Fig. 37f shows that the NiCoP particles were homogeneously dispersed at the surface of Ti_3C_2, the conductive bi-metallic particles could help to prevent aggregation and pulverization, and overall resulted in rich redox reaction sites, low charge transfer. The outstanding electrochemical efficiency, the high specific capacity of 416.9 mAh^1/g^1 at the current density of 0.1 A^1g^1 (Fig. 37g), and the holding of a specific capacity of 261.7 mAh^1/g^1 at a current density of 1 A^1g^1 after 2000 cycles was determined by the synergistic effect between the high structural stability and electrochemical performance components of NiCoP and MXenes Ti_3C_2 (Fig. 37g and h). The intercalation of sodium and lithium is well recognized, but there is a need to further research the intercalation of multivalent ions, according to these latest discoveries. The MXenes is regarded as an interesting material for secondary storage batteries owing to its intrinsic redox characteristics. MXenes can also be used in Lithium–sulfur (Li–S), lithium, and solid-state batteries in various forms.

3.4.3. MXenes in zinc-metal batteries

The aqueous Zn-air batteries are considered highly effective energy sources owing to their higher energy density, cost effective, safer, environmentally friendly [481–483]. Moreover, it is very easy to process by showing high capacity (820 mAh/g), with low redox potential (−0.76 vs. SHE), [484,485]. But, further progress in Zn-metal batteries is mainly restricted due to side reactions and the formation of dendrite [486,487]. As, the coulombic efficiencies could be automatically decreased due to dendrite formation which pierce the separators, thereby leading into the short circuit of the cell [488,489]. In addition to this, the poor adhesion to metal substrate could exfoliate from anode by producing dead Zn, which in turn reduced the anode capacity [490,491]. On the other hand, the side reactions brought about the depletion of electrolytes along with corroded the anode surface [492,493]. The as-produced gas results in the inflation of the battery and the leakage of electrolyte [494,495]. Due to such contests, the Zn metal anode enticingly worsens the activity of Zn-metal batteries [484,488]. With the aim of stabilizing the Zn metal anode, considerable research has been paid towards the regulation of the interfacial electric field (highly conductive layer and 3D scaffold Zn anode), along with amending the coordination environment (F-rich interfacial layer, interface desolvation, and highly concentrated electrolyte), by persuading homogeneous deposition of Zn (epitaxial electrodeposition, electrostatic shield, zincophilic host, optimizing ion flux, and surface polar group) [481,496,497]. Our team developed MXenes as a

zincophilic host to indorse the uniform deposition of Zn [496]. As a result, dendrite-free Zn@MXenes anode were capable of providing steady cycling activity. As, Sb could act as active nucleation seeds to tempt the homogeneous deposition of Zn, same as the synthesis of uniform Sb engineered MXenes film was accomplished to manufacture 3D Zn@MXenes@Sb anode, to realize the stable cycling activity [498]. Also, we invented the MOFderived N/O-doped porous carbon altered Cu foam to homogenize the nucleation and the development of Zn [499]. Due to the zincophilic characteristics and porous structure, we produced a TiO2 modified 3D Ti substrate to attain 3D Zn anode, by obtaining dendrite-free morphology and steady cycling activity [500]. Another research team fabricated a protected layer with ZnS and 3D MXenes on the Zn anode surface [497]. The 3D MXenes can dismiss volume change, decrease the local current density, and the distribution of homogenized electric field, thus, ZnS may indorse the uniform distribution of Zn ions, by suppressing the side reactions. A F-rich layer in aqueous Zn metal batteries was realized after the addition of multifunctional ZnF2 additives into electrolyte [501]. The stable layer could act as a protected coating in counter of any side reactions by regulating the deposition of Zn. Hence, the anode-free and dendrite-free Zn metal batteries were achieved by this electrolyte. So, a series of recent methods were realized via creating extra safety layers or addition of foreign species, which results in enhancing cost and/or minimizing energy density due to certain volume and weight. Furthermore, the recent methods emphasis the construction of Zn anode and electrolyte. The swift progress in Zn batteries permits subtle analysis of other components, particularly the separator. Separator is more significant in the safety of cells as it might avert a short circuit from evading physical interaction amid anode and cathode. The GF separator is important for Zn batteries, owing to low electrical conductivity, good wetting activity, suitable porosity and high ionic conductivity toward electrolytes. Another group fabricated a lightweight, self-supporting engineered zincophilic MXenes/NiO separator for Zn metal batteries (Fig. 38a) [502]. The zincophilic MXenes@NiO layer on separator might indorse the uniform Zn ion flux, by facilitating ion diffusion kinetics and reduction of local current density along with homogenizing the dispersal of electric field. The MXenes@NiO solution which was achieved via self-assembly approach was further treated with GF separator. The XRD spectrum presented NiO and MXenes peaks, thereby, representing effective preparation of MXenes@NiO modified separator (Fig. 38b). The dense layer was observed to be deposited very well on the separator surface after modification (Fig. 38c and d). The coating layer thickness was about 6–8 μm. The constricted interaction amid MXenes and NiO was promising for gaining uniform coating structure (Fig. 38e). Due to such kind of preparation advantage, the Zn||Zn cells with engineering separators displayed a steady cycling performance with dendrite-free morphology (Fig. 38f). After conjugation with a self-standing 3D NS/MXenes@MnO_2 cathode (Fig. 38g), the full cell with modified separator revealed a better cycling performance and enhanced rate (Fig. 38h and i). The upgraded activity was credited to e zincophilic MXenes@NiO layer, which could ease in the transport of ion, homogenize distribution of electric field, indorse uniform ion flux, and the reduction in local current density, which might normalize the homogeneous deposition of Zn ion and constrain side reactions.

3.5. Biomedical applications

Currently, a wide range of MXenes-based materials have gained a lot of interest in biomedical applications. They include magnetic resonance (MR) contrast agents, X-ray computed tomography (CT), photo-controlled suppository proclamation, photodynamic treatment (PDT), photoacoustic imaging, and photothermal therapy (PTT). Moreover, owing to their fine bandgap, metallic nature, as well as their non-radiative properties, the bio-compatible MXenes could act as an effective photothermal alteration mediator, which is more advantageous towards the local tumor ablations (Fig. 39a and b). The Lin et al., stated that the Nb_2C MXenes photothermal conversion properties are strongly wavelength dependent [503]. At 808 nm and 1064 nm, the photothermal conversion efficiencies for Nb_2C MXenes are 36.4% and 45.65%. In addition, it is found that the longer wavelengths may also have a better diffusion deepness than smaller wavelengths owing to less absorption and scattering in tissue. As a result, a longer wavelength for photothermal treatment may be the best option. As an effective etchant, Yu et al. used tetrabutylammonium hydroxide (TBAOH) to make fluorine-free Ti_3C_2 quantum dots to increase the biocompatibility of MXenes agent for PTT. An even higher photothermal conversion efficiency of (52.2%) with photon annihilation coefficient (52.8 Lg^{-1} cm^{-1}) were achieved thanks to oxoanion surface modification, which in turn offer MXenes with robust and extensive light absorption. Over time, to avoid the problem of deposition and aggregation of MXenes nanosheets during dispersion, the MXenes nanosheets could be better covered with polyvinylpyrrolidone (PVP) and non-toxic soybean phospholipid (SP) [503,504]. According to Dai et al., the MnOx/Ti_3C_2 [504] and MnOx/Ta_4C_3 [505] composites were discovered as good agents towards the photoacoustic (PA) imaging and the magnetic resonance (MR) (Fig. 39g). Due to the dissolution of MnOx, they discovered that MR imaging is found to be highly subtle at ambient pH conditions. Addition of MoOx, therefore, may reduce the overall photothermal alteration efficiency from (30.6%) in pure Ti_3C_2 to (22.9%) with MnOx of 50 ppm. Despite this, the effectiveness of well-known Au nanorods [506] and Cu_2-xSe nanocrystals [507] is comparable. This group also discovered that soybean-phospholipid-coated Ta_4C_3 nanosheets may be used as dual-way/X-ray computed tomography (PA/CT)/photoacoustic tomography mediators towards the in vivo PTT therapy (Fig. 39d and e) [508]. In same MXene phase, the heftier element i.e. Ta ($Z = 73$), is thought to have a larger CT difference than that of Ti ($Z = 22$). The CT image's Hounsfield unit (HU) values were enhanced thrice after the Ta_4C_3 nanosheets were injected. The use of MR/PA/CT imaging in conjunction with laser irradiation and accurate photothermal tumor cell ablation can provide guidance for laser irradiation. The MXenes could be combined with the gadolinium polytungstate GdW10 polyoxometalates for the improved synergistic PTT and CT and MR tomography [509]. Recently, the fabrication of Core-shell nanocomposites (Ti_3C_2/Au) has been carried out to use them as dual-modal computers and photoacoustic imaging [510]. At both irradiation wavelengths, the addition of Au nano-particles greatly improved the photothermal conversion efficiency (808 nm and 1064 nm). Owing to the improved inter-band transition, shrinking MXenes QDs boosts, in vivo tissue penetration depth makes them an effective mediator towards the photoluminescence tomography. With the aid of a hydrothermal approach, Xue et al. [511] generated different kinds of Ti_3C_2 MXenes QDs. The obtained results indicate that with a maximum quantum yield of 10%, the inclusive photoluminescence with a region of (340 nm–440 nm) is found to be highly dependent onto the excitation wavelength. However, they revealed the remarkable potential towards the variegated cellular tomography of the RAW264.7 cells using their MXenes QDs (Fig. 39f). The graphene quantum dots (GQDs) produced from amphiphilic carbides may be made in dimethylformamide (DMF)

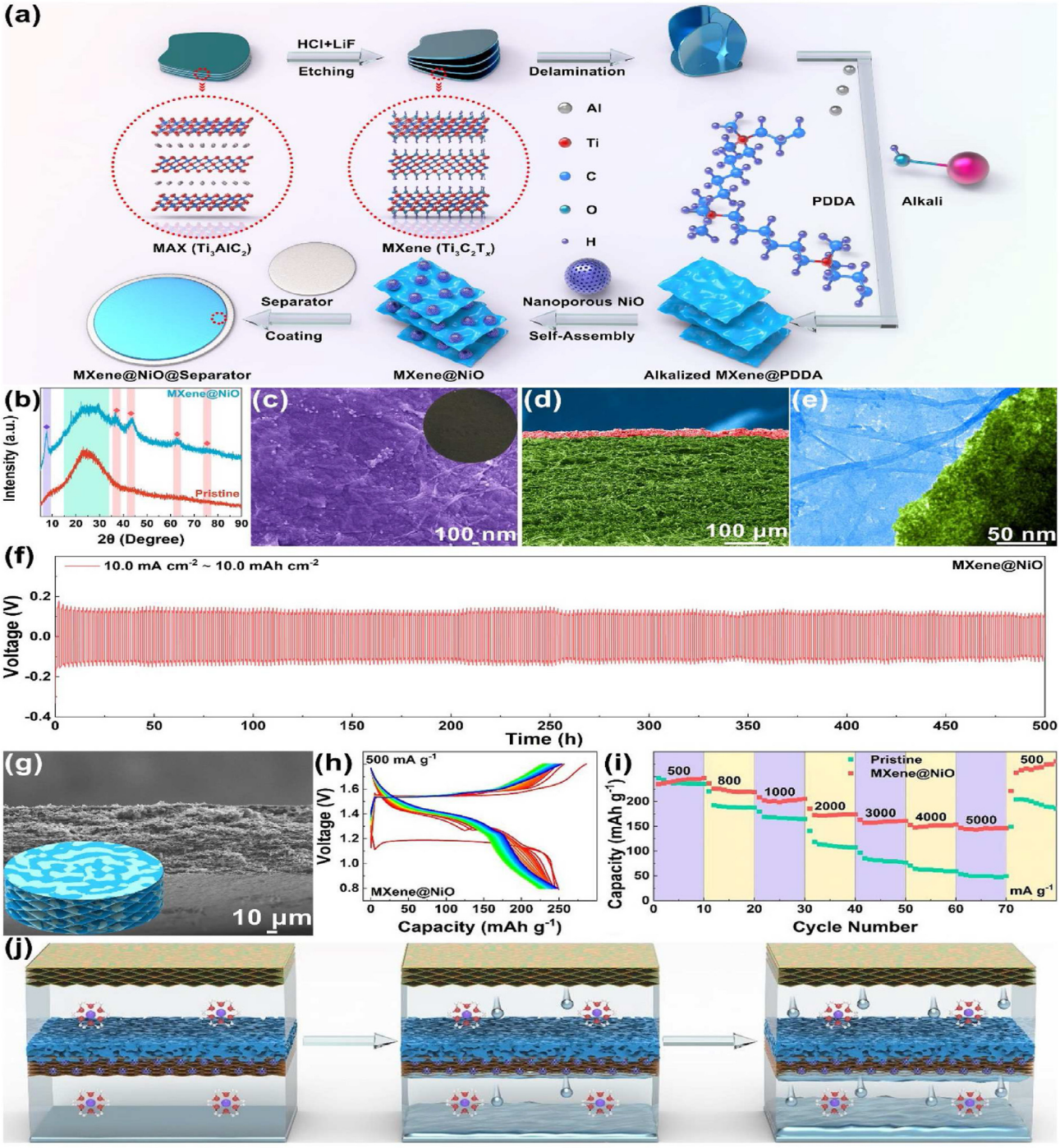

Fig. 38. Synthesis and characterization of MXene@NiO modified separator and their application in Zn-metal batteries. (a) Schematic of synthesis of MXene@NiO modified separator. (b) XRD patterns of pristine and MXene@NiO modified separators. (c and d) SEM of MXene@NiO modified separator. (e) TEM of MXene@NiO product. (f) Cycling property of Zn||Zn cells with engineered separator. (g) SEM image of 3D NS/MXene@MnO_2 cathode. (h) Charge/discharge profiles of full cell with engineered separator at 500 mA g-1. (i) Rate performance of full cell with pristine and modified separators. (j) Schematic of Zn deposition with and modified separators. Adopted from Ref. [502]· with the permission of American chemical society.

via Ti_3C_2 precursor solvothermal treatment [512]. As compared to that of fluorescein and Alexa fluor 488, the development of the nitrogen-doped GQDs might be a powerful luminous mediator with better optical solidity. However, it is well known that the GQDs could be the better photoluminescence mediators towards the cellular tomography due to their high organic solubility and minimal cytotoxicity. As previously stated, that the photoluminescence efficiency is strongly dependent on the in vivo milieu, such as ionic concentrations and pH, that in turn needs additional research. The MXenes nanosheets have a large specific area, making them ideal for drug loading and distribution. For synergistic photothermal/photodynamic/chemotherapy, the Ti_3C_2 nanosheets with extra Al_3^+ were produced [513]. The drug loading capacity and photothermal conversion efficiency were predicted to be 58.3% and 84.2%. Underneath the 808 nm laser irradiation, the production of singlet oxygen in MXenes nanosheets dispersions has been verified. The process of reactive oxygen species production, however, is yet unknown. The Han et al. [514] discovered that drug (doxorubicin

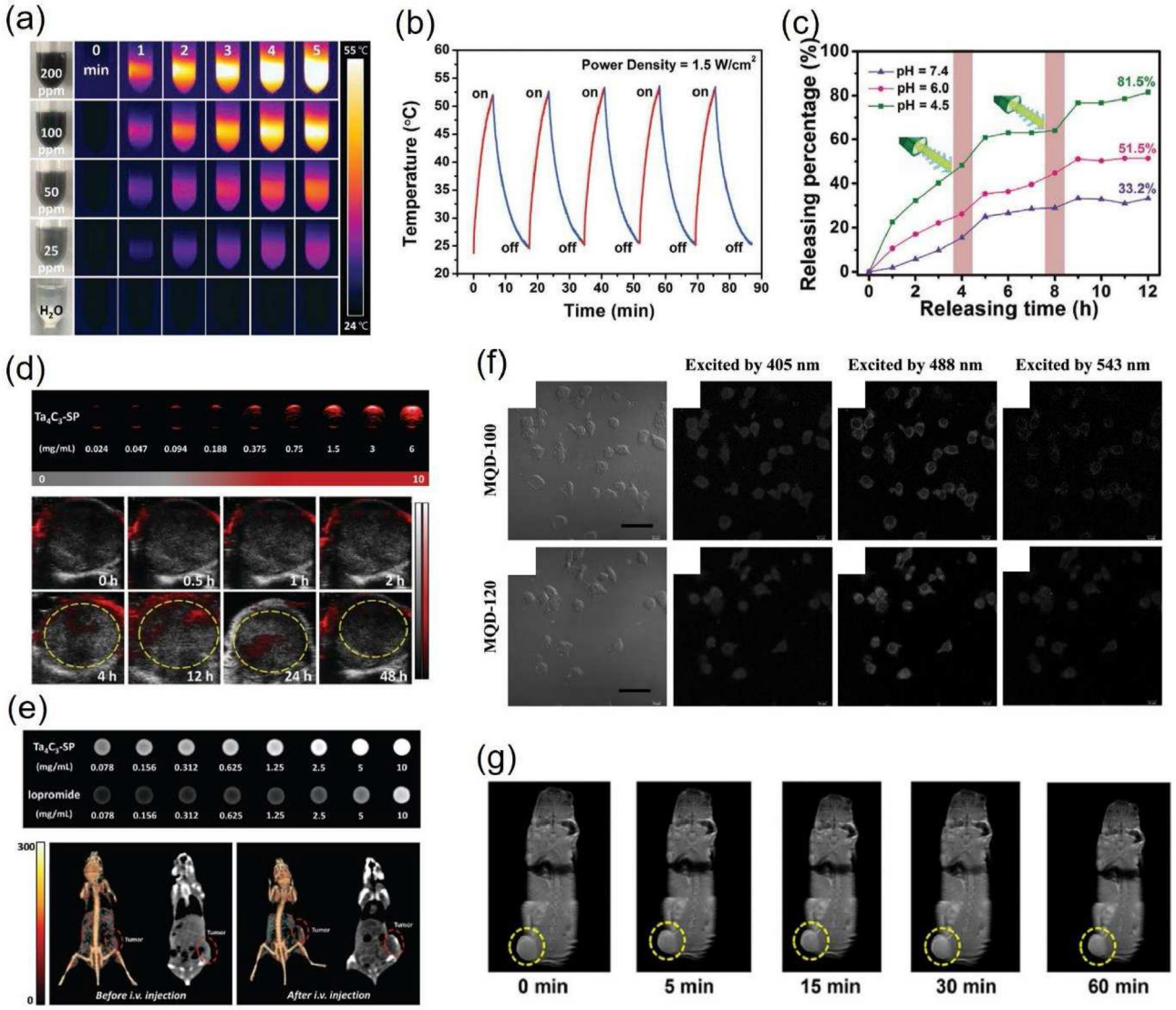

Fig. 39. (a) Changing the radiation duration and intensity of Ta_4C_3 nanostructure (b) On/off phases of Ta_4C_3 nanostructure [508], with the permission of John Wiley and Sons (c) Laser drug proclamation at various pH levels. Adopted from Ref. [514], with the permission of John Wiley and Sons (d) Ta_4C_3 nanostructures as a modulator in photothermal images in vitro/vivo. (e) Top: CT images of Ta_4C_3 nanostructure in iopromide. Bottom. In vivo CT images and 3D reconstruction of rats during Ta_4C_3 nanostructures infusion. Adopted form ref. [508], with the permission of John Wiley and Sons (f) Cellular photoluminescence [511]. (g) MR 4T1 tumour in mice against MnOx/Ta_4C_3 hybrid nanostructures insertion period. Adopted from Ref. [505], with the permission of American Chemical Society.

hydrochloride, DOX) loading of Ti_3C_2 may reach 211.8%, with electrostatic interaction being the predominant mechanism. The pH levels or light irradiation can both be used to regulate the drug release. They discovered that the drug delivery NIR light-controlled is found to be less responsive than that of the pH modulation (Fig. 39c). Recently, the cellulose/MXenes hydrogels based three-dimensional mesh structures with average water concentration (98 wt%) have been developed for the photothermal ablation and synergistic light-controlled drug management [515]. It is expected that cellulose/MXenes hydrogels have a loading capacity of 0.69 mg/ml. Moreover, the fabrication of highly porous silica-MXenes (Ti_3C_2 or Nb_2C) composite were developed by Chen et al. [516,517] with the aim of targeting and further increasing the synergistic photothermal and chemotherapy treatment of hepatocellular cancer by combining the standard mesoporous silica with surface modified MXenes. Currently, the use of MXenes has received immense attraction owing to their outstanding antibacterial properties [518]. The discovery of aged $Ti_3C_2T_x$ nanosheets by Rasool et al. further verified that it has the better antibacterial activity than that of fresh ones, which is attributed to the production of TiO_2/C over surfaces and the effect of nanosheet size.

3.6. Sensors

The MXenes-based sensing medium could be further employed towards the quantitative detection of different kinds of impetuses. They include temperatures [519], pH values [520], humidity [521], ionic/gas adsorptions [522], electrochemical reactions [523], photon irradiations [524], strains [525,526], and pressures [527,528], and which in turn have the significant impact on the electrical properties to change them more obviously such as reactance, impedance, conductivity and resistance. The internal resistance of multilayered MXenes could be effectively reduced by the external pressure thereby, lowering the overall interlayer separation. Fig. 40d shows that as the external pressure increases over the MXenes-sponge sensor, the LED grows brighter, indicating that

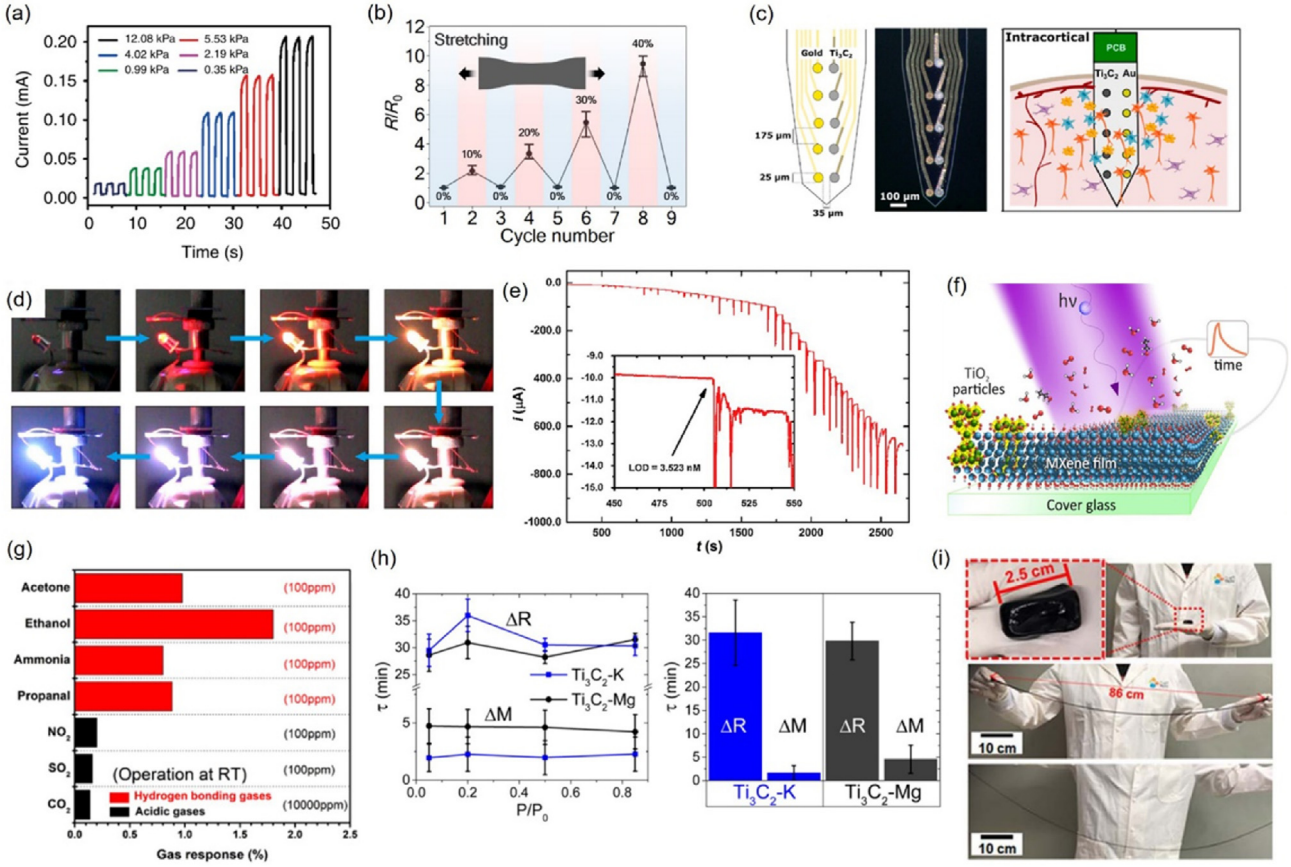

Fig. 40. (a) Pressure sensitivity of MXene sensors [528]. (b) Stabilized strain resistivity (R/R0) for 20-unit paired MXene multilayered on PDMS. Adopted from Ref. [525], with the permission of AAAS (c) Wide field microscopy shot [529], with the permission of American chemical society. (d) RGB-LED intensity fluctuation through MXene-sponge sensing distortion [527] (e) Chronoamperogram [530]. (f) UV photons sensor with oxidized MXene thin layer [524] (g) Largest confrontation variance [533] (h) Left: Exponential time constant. Right: Assessment of the average value [536] (i) $Ti_3C_2T_x$ MXene hydrogel sensor [526].

resistance is decreasing [527]. Such kind of characteristic could be employed to make a rapid reacting (30 ms), reversible MXenes-based piezoresistive sensor and highly sensitive (Gauge Factor 180.1), in order to further sensing the minor bending-release behaviors in humans (Fig. 40a) [528]. The peripheral strains such as stretching and bending could significantly change the assembling properties of MXene flakes, thereby, disturbing the overall inter-flake confrontation of devices. To detect the topographical scanning and human movements, the fabrication of recoverable MXenes-based strain sensors by having large stretching limit (40%) and a short bending radius (2.5 mm) after combining with poly(-diallyldimethylammonium chloride) (PDAC), has gained much interest recently (Fig. 40b) [525]. The Biocompatible $Ti_3C_2T_x$ brain electrodes provide superior sensitivity and resolution than gold electrodes due to MXenes' low impedance (Fig. 40c) [529]. This might be provide an alternative to the pricey noble metals now used in implanted sensors. The detection of a wide variety of gases and physiologically significant chemicals, such as urea, acetaminophen, dopamine, phenol, NH_3, CO_2, H_2O_2, and others [530–533] has also been possible by modifying the structural properties of MXenes with active surface terminations. The ability of charge carrier transfer in MXenes is often hampered after the adsorption of gas molecules. The MXenes-based sensor has dramatically pushed the detection limit of H_2O_2 to 0.7 nM with the reaction time in a cathodic potential window is 10 s (Fig. 40e) [530,534]. Use of $Ti_3C_2T_x$-MXene-based gas sensor (Fig. 40g), with low sensing confines of (50–100 ppb) towards the volatile organic molecules i.e. propanol, ammonia, ethanol, and acetone have been reported [533]. Furthermore, such a sensor has the ability for the high selectivity of the gases along with producing the hydrogen bonding phenomenon with most of the acids. A signal-to-noise ratio two orders of magnitude better than that of standard 2D materials has been achieved owing to the improved conductivity (3250 S/m) for low intensity signals. Due to charge depletion of trapped H_2O, the gravimetric reaction for water is reported to be (10 times) quicker as compared to electrical retort in the monitoring of humidity by employing the MXenes-based sensor (Fig. 40h) [533,535,536]. The Neutron scattering jointed with ab initio calculations and molecular dynamics demonstrated that a numeral of hydration measures results into the significant rise in the detachment among various MXene layers during the existence of Mg and K intercalants among different layers. These sensors have a detection threshold of (0.8%) relative humidity (RH) along with monotonic (RH) response of (085%) RH range. The partly oxidized $Ti_3C_2T_x$ MXene sensor has received the highly selective UV visible photon-current owing to the more photon energy to bridge, which is closely associated with the wide energy bandgap of TiO_2 [524]. The photo-induced charge carriers reduction needs more time (nearly 24 h), but it could be accelerated during the existence of water vapor and oxygen. The $Ti_3C_2T_x$ MXene and "crystal clay based ultra-stretchable (>3400%) hydrogel sensors´ have been reported to have a gauge factor (GF) with average compression and tensile strains value of 80 and 25, respectively, which in turn considerably enhance the probable use of MXenes-based sensors in wide variety of fields along with

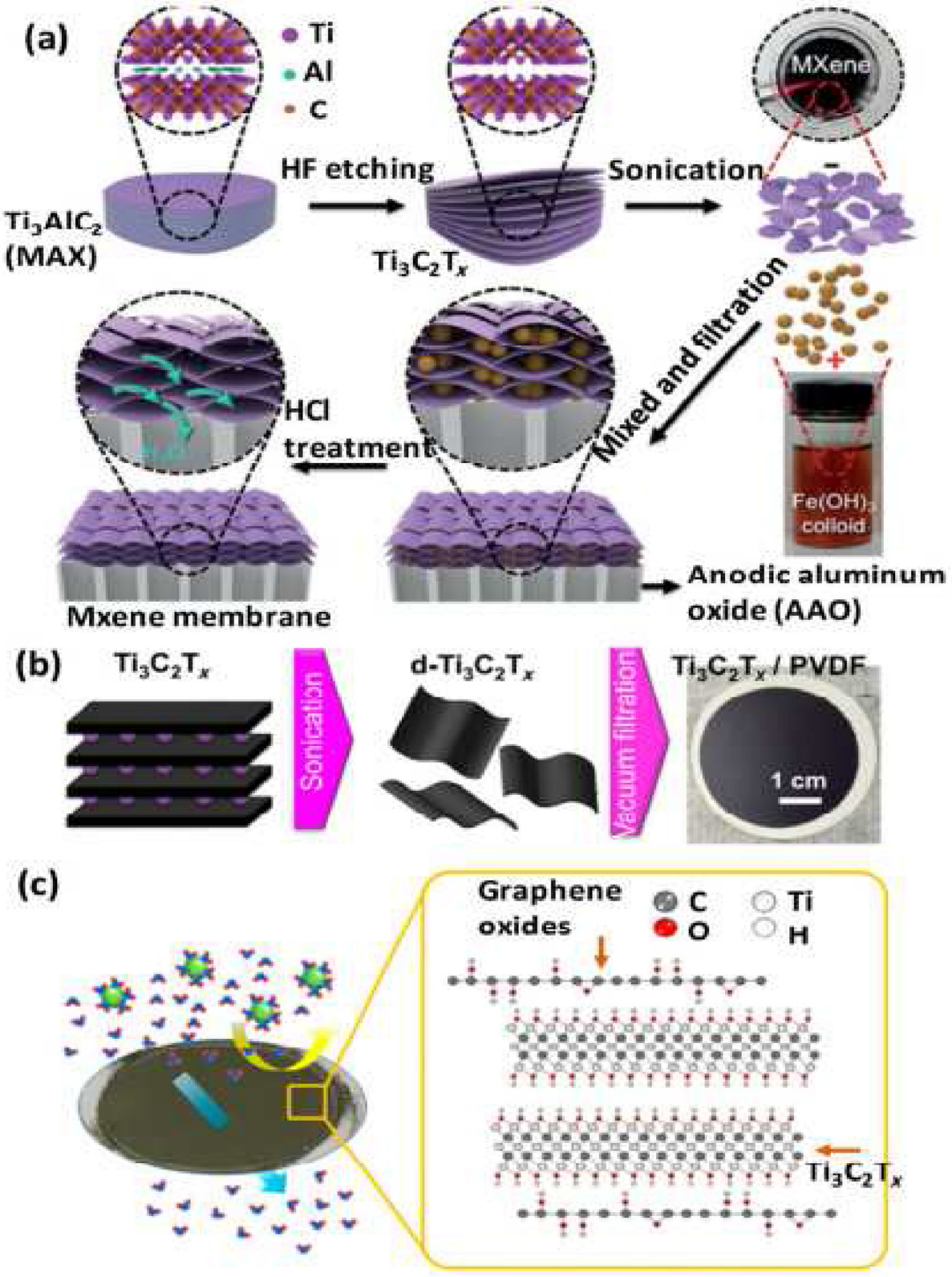

Fig. 41. Proposed Synthesis (a) Anodic aluminium oxide MXene membrane. Adopted from Ref. [545]' with the permission of Wiley and Sons (b) MXene membrane based on polyvinylidene fluoride (PVDF). Adopted from Ref. [546], with permission from Creative common attributions 4.0 international 2017. and (c) MXene-GO membrane based on polycarbonate. Adopted from Ref. [547], with the permission of American chemical society.

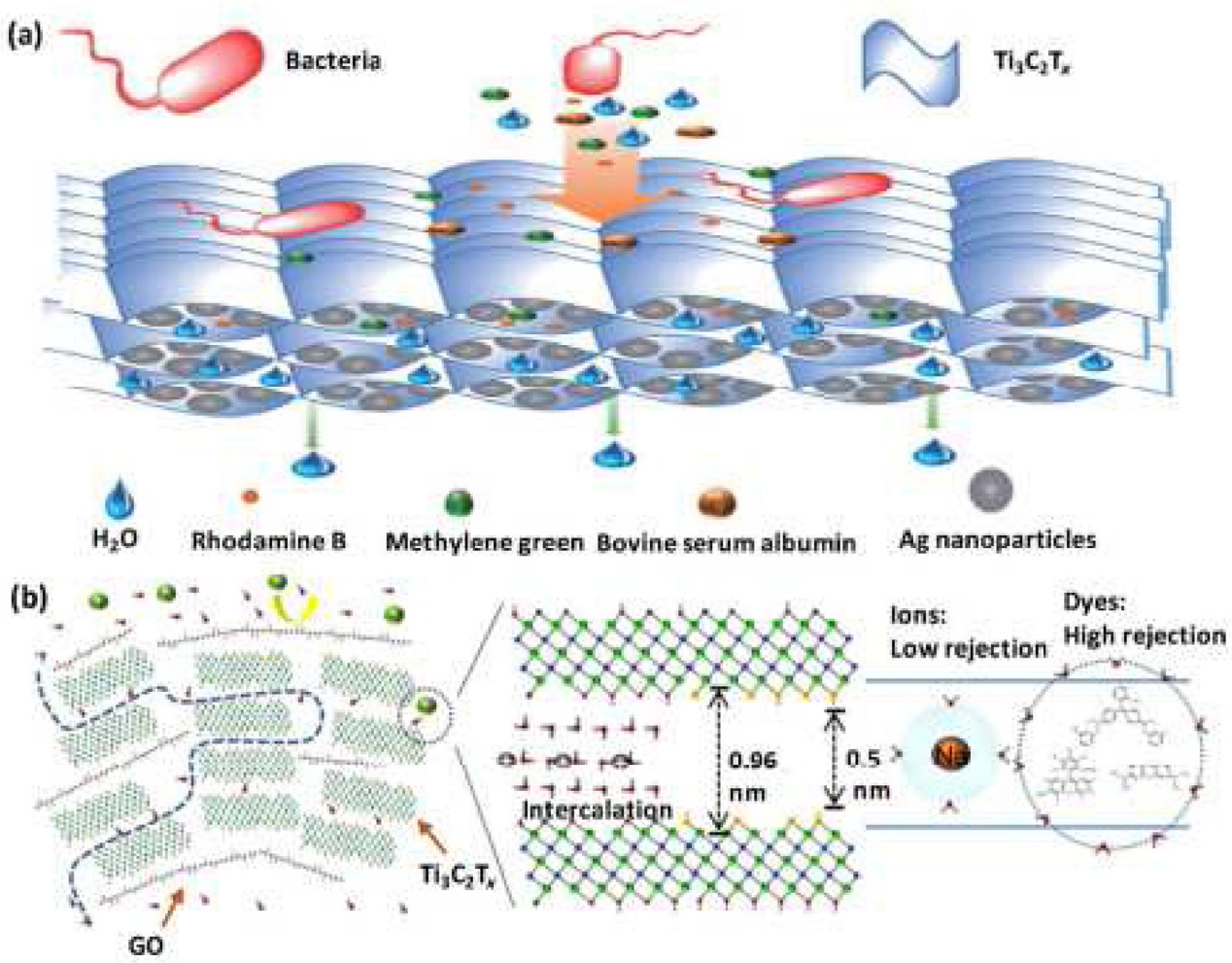

Fig. 42. (a) Elimination of the MXene-Ag hybrid membrane [543], and (b) steric confinement of hydrated particles and pigment moieties on the $Ti_3C_2T_x$-GO membrane [547].

operating the exceptional viscoelastic characteristics of hydrogels. This sensor has been shown to track object motion directions, signature fingerprints, and voices [526].

3.7. Membrane

Forward osmosis, reverse osmosis, nanofiltration, ultrafiltration, and microfiltration are all membrane techniques that have been utilized to treat water and wastewater [537,538]. Membrane filtration has various benefits (low-level/no chemical demand, high removal efficiency, and low carbon footprint), however membrane selectivity and permeability have trade-offs [539]. Many attempts have been made in recent years to overcome this limitation by developing ultrathin 2D membranes made of graphene-based nanomaterials (e.g. graphene, graphene oxides (GOs), and rGOs) [540], metal-organic frameworks [541], covalent organic nanosheets [542], and MXenes [543]. In comparison to traditional materials, 2D materials allow for the creation of ultrathin coating/separating layers that allow for the quick transit of chosen solutes, resulting in high permeation and selectivity [544]. Waterborne organic and inorganic components have been separated using MXenes-based membranes on various support materials (Fig. 41). Ding et al. used an anodic aluminum oxide support to build a 2D lamellar MXenes membrane with extraordinarily high water permeability (>1000 L/(m^2hbar)) and fast removal (>90%) of Evans blue, cytochrome, and gold nanoparticles [545]. The elimination of bovine serum albumin (>99%) and rhodamine B (85%) allowed for the measurement of membrane pore size (2–5 nm). The removal of big solutes/particles (Evans blue (1.2 nm 3.1 nm), cytochrome (2.5 nm 3.7 nm), and gold nanoparticles (5 nm)) from water was explained by size exclusion; however, a tiny molecule such as $K_3[Fe(CN)_6]$ (0.9 nm 0.9 nm) was not readily removed (32% only). The membrane's water permeability (1120 L/(m^2hbar)) was approximately 10-fold higher than that of commercial polyethersulfone membranes with nominal molecular weight cut-offs of 30 kDa (111 L/(m^2hbar)) and 50 kDa (130 L/(m^2hbar)), and the MXenes membrane removed all solutes/particles tested much better (32% vs 99%) than commercial membranes. The nanochannels and vast interspaces associated with the loosely lamellar structure of the MXene membrane are responsible for the increased water permeability. Also, with high-level removal of Congo red (93%) and gentian violet (80%), a new 2D MXenes-polyethersulfone composite membrane exhibited relatively small water fluxes (57.5 and 58.8 L/(m^2hbar)) due to fouling; larger water fluxes (230, 316, and 218 L/(m^2hbar)) were evident during low-level inorganic salt removal (23% of $MgCl_2$, These inorganic salts (5% of totals) were not efficiently removed by the virgin polyethersulfone ultrafiltration membrane (nominal molecular weight cut-off 10 kDa) [546,547].

In addition, the rhodamine B (79.9%), methyl green (92.3%), and bovine serum albumin (>99%) were effectively removed; however, both the extents of removal and flux were significantly affected by

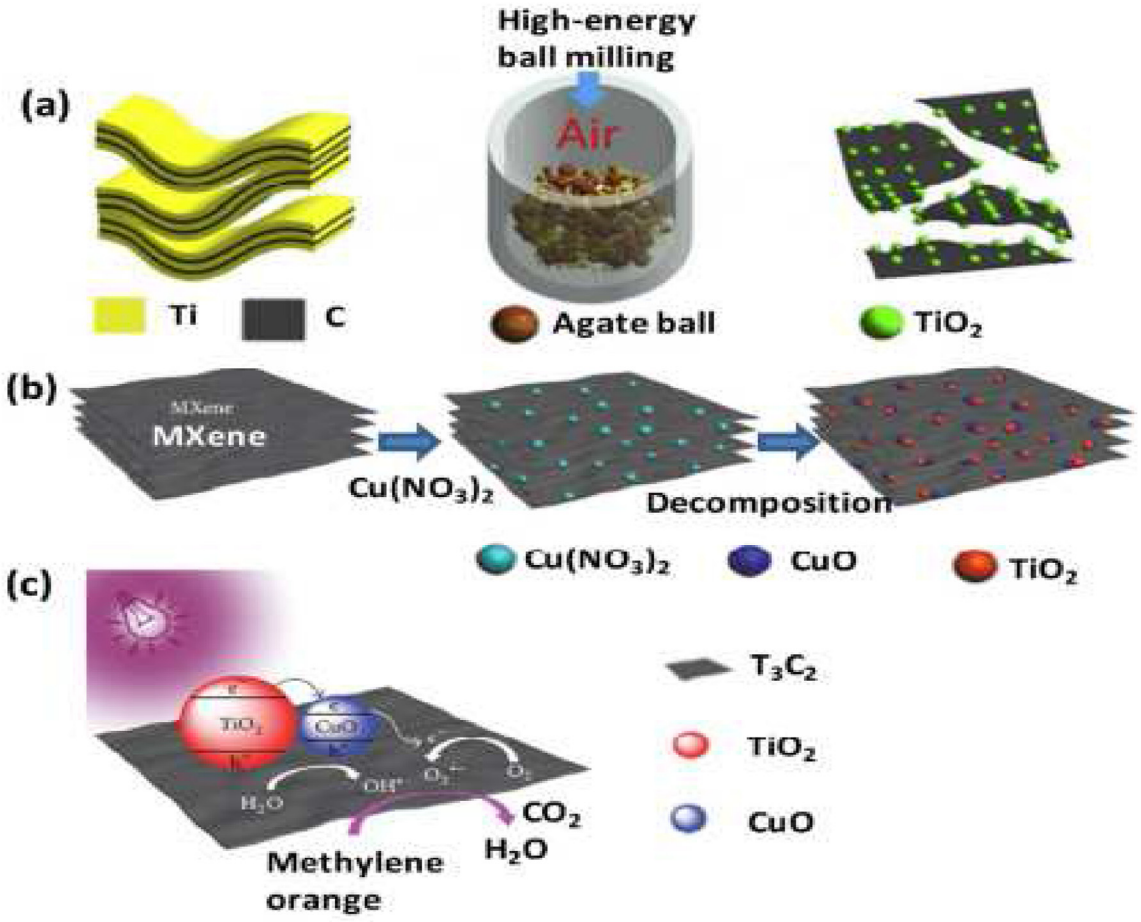

Fig. 43. (a) High intensity ball milling of Ti_2CTx to produce titania carbon. Adopted from Ref. [552], with the permission of Elsevier (b) The technique for synthesizing the Ti_3C_2-TiO_2-CuO nanomaterials, and (c) graphical representation of a probable photocatalytic pathway of Ti_3C_2-TiO_2-CuO nanomaterials [554].

membrane thickness. The optimum membrane thickness for rhodamine B removal (79.9%) was 470 nm at a water flux of 387 L/(m^2 h bar); the flux fell significantly to 234 and 125 L/(m^2 h bar) at membrane thicknesses of 969 and 1420 nm with similar extents of rhodamine B removal (81.6% and 82.8%). An MXenes-Ag membrane fouled with methyl green and bovine serum presented at 50 mg/L exhibited remarkable flux recoveries (91–97%) compared to those of the pristine MXenes membrane (81%–86%) [543], attributable to the enhanced hydrophilicity of the MXenes-Ag membrane with additional nanopores. The water contact angle decreased from 40° to 35° as the Ag nanoparticle level rose from 0 to 21%, confirming that Ag improved membrane surface hydrophilicity [548]. The Fig. 42a shows a schematic and the mechanism of dye removal by the MXenes-Ag composite membrane. The graphene is impermeable [549], and many studies have used graphene-based membranes for water treatment [550]. The Kang et al. fabricated a 90-nm-thick $Ti_3C_2T_x$-GO membrane on a porous support (polycarbonate/nylon) that inhibited target solute movement through inter-edge defects or poorly packed spaces [547]. A membrane with an effective interlayer spacing of approximately 0.5 nm exhibited high-level removal rates (68% for methyl red (neutral, 0.49 nm), 99% for methylene blue (positive, 0.51 nm), 94% for Rose Bengal (negative, 0.59 nm), and 100% for Coomassie brilliant blue (negative, 0.8 nm)). However, the pristine $Ti_3C_2T_x$ membrane exhibited lower removal rates (40% (methyl red), 95% (methylene blue), 66% (Rose Bengal), and 95.4% (Coomassie brilliant blue)). The poor removal of methyl red is attributable to its relatively small size and hydrodynamic diameter, and its neutral charge. However, Rose Bengal removal was less effective than that of methylene blue although the former is larger, presumably because the negative charge of the former triggered low-level electrostatic attraction to the MXene surface [547]. The ionic salts (NaCl, Na_2SO_4, $MgSO_4$, and $MgCl_2$) were very poorly removed (<10%). Thus, the interlayer spaces of the swollen $Ti_3C_2T_x$-GO membrane were too large to allow the complete removal of salt ion , but the negatively charged membrane surface removed some ions via electrostatic repulsion. The Fig. 42b shows schematics of the steric exclusion of hydrated ions and dyes by the $Ti_3C_2T_x$-GO membrane.

3.8. Photocatalytic application

The photocatalytic technology is regarded as an effective approach in term of environmental remediation [551]. When two cationic dyes (methylene blue and acid blue 80) were exposed to UV for 5 h in the presence of $Ti_3C_2T_x$, degradation was very rapid (8–62%) [82], but acid blue 80 was not degraded at all and methylene blue only 18% after 20 h in the dark, presumably because UV triggered the formation of TiH_4O_4 and/or TiO_2 on the $Ti_3C_2T_x$ surface, enhancing photocatalysis. Although the photocatalytic processes at work need to be investigated further, the MXenes-supported TiO_2 composites, like graphene-titania hybrids, might find uses in catalysis, environmental remediation, energy conversion, and energy storage [82]. The Li et al. investigated that in the presence of titania-carbon nanocomposites generated from 2D Ti_2CT_x, the photocatalytic degradation of methylene blue was increased under UV [552]. A schematic of high-energy ball-milling

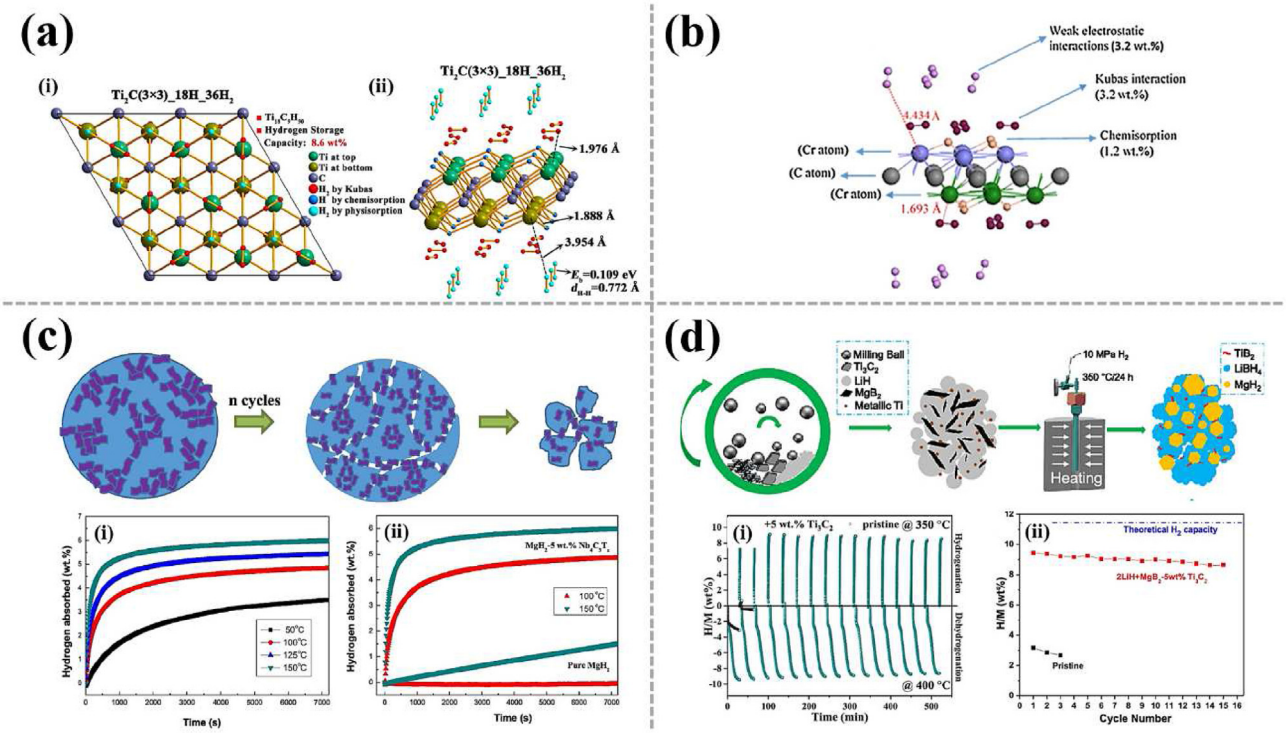

Fig. 44. (a) (i) Top and (ii) side opinions of the $Ti_2C(3X_3)18H_36H_2$ design that has the most hydrogen storage facility. Adopted from Ref. [563], with the permission of American chemical society (b) The illustration shows how hydrogen is stored in Cr_2C MXene. Adopted from Ref. [564], with the permission of Elsevier (c) The principle of hydrogen storage in the MgH_2−5wt. % $Nb_4C_3T_x$ hybrid. Adopted from Ref. [63], with the permission of Elsevier (d) hydrogen storage of $2LiH+MgB_2/2LiBH_4+MgH_2$ [569], with the permission of American chemical society.

of Ti_2CT_x to generate titania carbon is shown in Fig. 43a. The carbon effectively increased TiO_2photocatalytic capacity by limiting recombination of photoexcited e^- and h^+ couples, which has important photocatalytic applications [553]. Furthermore, the creation of O—Ti—C bonds in the nanosheets reduced recombination by transporting photo-excited electrons from TiO_2 conduction band to the nanosheets. The highly conductive electron acceptors include disordered, homogeneous graphitic carbon nanosheets with immobilized TiO_2 nanoparticles [552]. Another work [554] created Ti_3C_2-TiO_2-CuO nanocomposites by decomposing mixtures of 2D MXenes (Ti_3C_2) (Fig. 43b). The photocatalytic degradation of methyl orange by the nanocomposites was outstanding (>99% in 80 min), and UV significantly improved the photoelectron separation vacancies of CuO and Ti_3C_2, explaining photocatalysis by these nanocomposites (Fig. 43c).

3.9. MXenes as hydrogen storage source

The development of highly efficient materials by encompassing exceptional hydrogen adsorption/desorption performance along with high storage capacity at ambient conditions has become a major bottleneck for the researcher in this recent time. However, due to the weak physical attraction for H_2 molecules owing to van der Waals forces, the already prevailing hydrogen storage materials, such as graphene [555], fullerenes [556], carbon-based nanotubes [557], covalent organic frameworks and MOFs [558], are only capable of storing the hydrogen gas at low (cryogenic) temperatures. Comparatively, the H_2 is perceived to be chemically adsorbed in metal hydrides [559], and the stored hydrogen desorption further requires high temperatures. Currently, the MXenes-based compounds have shown considerable potential for the storage of hydrogen [560]. The H atoms are bound within MXenes via three routes: (i) chemisorption, (ii) physisorption, and (iii) Kubas-type interaction [561]. Due to Kubas-type interaction, the MXene use in term of storing hydrogen gas mainly lies in between reversible hydrogen storage materials at room conditions [562], for that the binding energy also lies between the binding energies for chemisorption and physisorption. Till now, some characteristics of MXenes are not well known through a series of concrete experiments, and the DFT-based first principles calculations are supposed to be a reliable technique to envisage the physical-chemical properties of MXenes. According to systematic density functional calculations, the adsorption of hydrogen onto 2D Ti_2C with optimum storage capacity of 8.6 wt, is mainly accomplished via various rotes on both sides, and the average 3.4 wt % of hydrogen molecules is adsorbed through the Kubastype interaction, which could be reversibly stored and then released at ambient temperature (Fig. 44a) [563]. According to Hu et al. [73] first-principles total energy pseudopotential calculations, the maximum gravimetric storage activity of 2D Sc_2C phase was found to be 9.0 wt% and the hydrogen was mainly seems to be bound via three routes: Kubas-type interactions, physisorption and chemisorption, with binding energies of 0.164 eV, 0.087 and 4.703, respectively. The adsorption of H_2 molecules over the surface of Cr_2C from different sites was also studied by Yadav et al. [564] through DFT calculation. According to their results, the maximum hydrogen storage capacity was found to be 7.6 wt%, from which the 3.2 wt% hydrogen seems to be adsorbed via Kubas-interaction, along with 1.2 wt% hydrogen was observed to be bounded via chemisorption and another 3.2 wt% via weak electrostatic interactions (Fig. 44b). MXenes which was synthesized via 48% HF by Osti and Gogotsi et al. (2017) was used for the investigation of the potential for hydrogen storage at room temperature According to their results the different voids were found to be the major factor to enable trapping the hydrogen molecules,

which were developed after the strong HF (used to etch MAX) during synthesis process. In addition to that, they described the potentials towards the storage mechanism of hydrogen [562] (i) due to its 2D crystal structure with a thin layer, H atoms could firmly retain over surface site and could be easily diffuse in the interior to be trapped between MXene layers; (ii) due to defect-induced morphological variations (e.g. by using strong etchant during MAX phase etching process), the hydrogen is trapped into the voids (defects i.e. vacancies, hollow sites and cavities); (iii) the H_2 could exist in huge pores or cavities or rather some isolated molecules of H_2 could exist in small structure openings, (iv) the enhancement in hydrogen storage is possible via creating carbon vacancies, ultimately decreasing the energy barricade for H dispersion from surface to solute. For the first time, the introduction of 2D Ti_3C_2 MXenes into $NaAlH_4$ was accomplished by Wu et al. [565]. The obtained finding indicated that the highest reversible hydrogen storage capacity of 4.9 wt% below 140 °C is achieved by the $NaAlH_4$-7 wt.% Ti_3C_2 composite. But, Liu et al. [566] showed that 5 wt%Ti_3C_2-containing MgH_2 achieved 6.1 wt% H_2. According to Shen et al. [567] investigation, compared to that of simple Ti_3C_2, the catalytic impact of $(Ti_{0.5}\ V_{0.5})_3C_2$ for hydrogen storage reaction of Mg was found to be outstanding. Liu et al. [63] reported that the 2D $Nb_4C_3T_x$ MXenes incorporation into MgH_2 via ball milling strategy, provide a robust MgH2-5 wt.% $Nb_4C_3T_x$ compound, which further revealed higher hydrogen storage as compared to Mg, whose storage capacity was (3.5 wt%) at 50 °C within 2 h (Fig. 44c). The superior activity regarding the hydrogen storage capacity might be due to the enhanced catalytic performance of in situ NbH_x formation and the exceptional layer-structured Nb_4C_3Tx for hydrogen storage reaction of MgH_2. The enhancement of the kinetics of de/re-hydrogenation reaction has also been reported by Chen et al. [568] who observed that it is only due to the considerable impact of Ti_3C_2 introduction into $4MgH_2$- $LiAlH_4$. Currently, Xian et al. [569] investigated that incorporating the 2D MXene phase of Ti_3C_2 into $2LiH^{+}MgB^{2}$ mixture through a ball milling strategy and initial hydrogenation, the as -prepared material showed an extraordinary release of H_2 about (9.0 wt% H_2) at 400 °C within 20 min (Fig. 44d). Therefore, the use of MXenes has been investigated as the most promising material in hydrogen energy storage strategy. Some further modifications are needed to develop highly robust and multidimensional material for higher hydrogen storage capacity.

3.10. Antimicrobial applications

Controlling microbial activity is typically difficult since surfaces are exposed to complex environments rich in bacteria and nutrients for lengthy periods of time [570]. Biofouling of membranes used in wastewater treatment facilities, in particular, is a big problem since membrane efficiency is severely harmed [571]. Nano-bio interaction inhibits bacterial growth on the surface of nanomaterials [572]. The MXenes-Ag (21%) membranes suppressed *E. coli* substantially more than pure MXenes and controlled polyvinylidene difluoride membranes, according to Pandey et al. [543]. Furthermore, the amounts of Ag nanoparticles in MXene were strongly connected with growth inhibition, probably because both Ag and TiO_2 particles formed on the membrane surfaces. The TiO_2 on the MXene surface improved antibacterial activity, especially when exposed to UV [573]. Antimicrobial drugs containing Ag nanoparticles are widely utilized [574]. The Rasool et al. found that a $Ti_3C_2T_x$ membrane on a polyvinylidene difluoride support suppressed Bacillus subtilis and *E. coli* grows more efficiently (>99%) than a control polyvinylidene difluoride membrane (73% for Bacillus subtilis and 67% for *E. coli*) [546]. The antibacterial efficiency of a $Ti_3C_2T_x$ MXenes against Gram-negative *E. coli* and Gram-positive Bacillus subtilis was investigated in another work [575]. The antibacterial activity of a MAX dispersion was quite poor (14% for *E. coli* and 18% for Bacillus subtilis). The growth inhibition rates were 98 and 97%, when bacteria were exposed to a colloidal solution of delaminated $Ti_3C_2T_x$ MXenes.

4. Conclusion and future perspectives

The purpose of this article is to familiarize the readers with the fundamentals of MXenes and their diverse applications in fuel storage and conversions. To begin with , the basics of MXenes are critically discussed, including their composition, fabrication, opto-electronic properties, complexation, diverse geometrical patterns and morphologies, and production techniques. The application aspects have been upgraded to include the latest breakthroughs in MXenes, including energy storage, electromagnetic interference protection, composites reinforcing, gas and biosensors, lubricating, and photo-, electro-, and chemical catalysis. MXenes have beneficial efficiency as electrode material in batteries, due to their multidimensional properties. Additionally, it has been shown that the porous shape of the MXene electrodes enhances the performance of supercapacitors. Other kinds of viable supercapacitors have been produced in addition to double symmetric electrodes for ion adsorption. These include the use of transition metal oxide hybrids as pseudocapacitors and electrochemical capacitors. Additionally, experimental developments on degradation of organic pollutants and electrocatalysts for the HER and OER were reported. MXenes' based photocatalytic and electrocatalytic properties for fuel generation are mostly unknown. Statistical estimates reveal that catalytic fuel generation processes such as H_2 evolution, CO_2 hydrogenation, and ammonia fuel synthesis are all economically beneficial. Numerous characteristics of MXenes remain unknown, including their total number of familial connections and their final potential capability for lithium storage and other fuel uses. Theoretical projections will contribute to both fundamental and applied extensions of the MXenes family through various element interactions in the future. MXenes' capabilities as rechargeable lithium-ion battery anodes will be increased with the addition of additional elements such as Si, Sn, Ge, and transition metal oxides. Additionally, photocatalytic processes may be controlled by including broad bandgap semiconductors such as TiO_2 and adjustable bandgap semiconductors such as phosphorene into MXenes composites. The synthesis and integration of the OER and ORR using MXenes electrocatalysts have shown solid evidence of performance in rechargeable zinc—air batteries. MXenes have absolutely great potential in energy applications. Despite its widespread usage in a variety of laboratory-based experiments and field-scale investigations, the utilization of MXenes as a resilient and versatile material needs more exploration for its prospective commercial applications:

- ❖ The development of material itself should be taken into account for the further application of MXenes' as effective and robust materials;
- ❖ Starting from synthetic procedures, the key observation regarding the methods of improving the stability of MXene structure should be at high priority with the aim of getting deeper understanding about its structural characteristics;
- ❖ Particular focus onto the photocatalytic liquid phase reactions, existence of surface defects over MXenes' surface sites and the exploration of its hydrophilicity should be a keen interest in terms of their value characteristics;
- ❖ In case of membrane separation and adsorption, the stability issue of MXene sheets is an important factor, and it has the significant impact on the whole life-span of MXenes during proposed applications. And we know that adsorption and

membrane separation processess rely on new surface sites. Hence, novel fabrication strategies are highly needed to uplift the selective adsorption capacity and the stability of MXenes-based adsorbents and membranes;

- ❖ During the photocatalytic pollutant degradation, the novel engineering methods for proper heterostructure formation with well-connected interfaces are highly sought after for MXenes-based materials for enhancing absorption of photons and charge-carrier separation and further transportation. Therefore, the novel heterojunctions with higher redox ability and better interfacial alignments, which can yield effective and multidimensional photocatalysts with robust degradation activity, are needed;
- ❖ The in-depth investigation is also highly needed to understand the consequent lattice change in MXene phase due to already existing various oxidation reaction routes in diverse solvents. In addition, the impact of various dopants, i.e. metal and non-metals onto the surface of MXenes, which in turn brought about the change in electronic structure of MXenes, must be taken into consideration for further investigation at atomic level to develop a highly proficient MXenes material;
- ❖ it is well known that the MXene flake size directly controls the water flux during membrane separation process. The MXenes-based membranes as well as the adsorbents are highly susceptible to the toxic species and highly selective sorption/isolation has become a convoluted task for scientist. However, the optimal flux rate concurrent with considerable salt and other impurities rejection rate must be deeply investigated via both experimental and theoretical point of view by constructing and using engineered MXene sheets with uniform terminations in the membrane separation field;
- ❖ MXenes has received immense attraction in field of electrocatalytic sensing of pollutants. Since, the MXenes has been regarded as an ideal candidate in electrocatalytic pollutant sensing system as a result of their high dispersibility and superior conductivity, which is totally different from graphene, it proposes better conductivity only at the cost of low hydrophilicity. Moreover, to overcome the anodic stability issue, the strategy of coupling the MXenes with electro-active polymers to develop composites-based material has been regarded as an efficient strategy for more efficient pollutant detection;
- ❖ Designing and properly tuning MXenes by means of surface termination groups has been proven to be the effective strategy to greatly enhance their overall performance;
- ❖ Until now, limited work has been done towards the synthesis of MXenes with tunable properties. Only the theoretical calculation helps to predict the semiconductor nature of MXenes, which further dictates its application in photocatalysis in a diverse range of research fields. Therefore, further research is highly needed to increase its wide-spread applications as a multidimensional and robust material such as energy conversion (HER, OER) and storage (researchable batteries and supercapacitors).
- ❖ MXenes without surface termination can only be synthesized by vacuum or other methods of vapor deposition. Due to its outstanding characteristics and performance, MXenes have been widely used in the field of catalysis. However, MXenes has poor stability in the catalytic process. To improve the catalytic performance of MXene catalysts, many strategies have been proposed, including boundary state control, functional group control, defect state control, single-atom loading, 2D material confinement effects, and heterostructure fabrication;
- ❖ Despite the predictions of the DFT, the inherent MXenes-based semiconductor has not yet been implemented experimentally. The DFT has already predicted some exciting properties, such as topological insulators, superconductivity, and semi-metallicity, which have yet to be tested experimentally. It has been predicted that even at room temperature some MXenes could strong magnetization, which is attractive to 2D spintronic. The optical properties of MXenes are of great interest. However, the mechanism of their interaction with electromagnetic waves, which are critical in EMI shielding, photonics, and plasma applications, is not yet clear. To date, although several other synthetic methods, including chemical vapor deposition, have been reported, there are some harmful etching agents, such as fluorine-containing acidic solutions, which are used in the production of MXenes;
- ❖ More engineering research on MXenes-based devices is required, especially to understand and develop the process of proper packaging of these air-sensitive nanomaterials. If the MXene film is exposed to the surrounding environment, the layered MXenes film is easily oxidized. Therefore, to extend the service life of MXenes-based devices, it is very useful and practical to develop a suitable packaging method;
- ❖ Furthermore, the improvement in the ability to synthesize high-quality new MAX and other layered carbide and nitride precursors and larger crystal sizes will be important to expand both functions and structures of MXenes. Finally, the theoretical modeling and experimental research should be conducted in parallel and in more depth. This includes screening new possible MXenes by predicting ion intercalation behavior and theoretical capacity, adsorption energy, and charge storage mechanisms.

Author's statment

Zeeshan Ajmal, Abdul Qadeer, Ubaid Khan, Muhammad Bilal Hussain: Conceptualization, Methodology, Software.

Muhammad Irfan, Rashid Mehmood, Muhammad Abid: Data curation, Writing-Original draft preparation.

Anuj Kumar, Hamid Ali, Abul Kalam, Abdullah G. Al-Sehemi, Hamed Algarni, Yas Al-Hadeethi, and Ridha Djellabi Visualization, Investigation.

Jin Qian, Asif Hayat, Huaqiang Zeng: Writing- Reviewing and Editing, Supervision

Declaration of competing interest

The authors declare that they have no known competing financial interests or personal relationships that could appeared to influence the work reported in this paper.

Data availability

The data that has been used is confidential.

Acknowledgment

Authors acknowledge support and funding of King Khalid University through Research Center for Advanced Materials Science (RCAMS) under grant no: RCAMS/KKU/0010/21.

References

[1] L. Wang, W. Tao, L. Yuan, Z.R. Liu, Q. Huang, Z. Chai, J. Gibson, W. Shi, Rational control of the interlayer space inside two-dimensional titanium carbides for highly efficient uranium removal and imprisonment, Chem. Commun. (2017) 12084–12087.

[2] A. Hayat, M. Sohail, T.A. Taha, S. Kumar Baburao Mane, A.G. Al-Sehemi, A.A. Al-Ghamdi, W.I. Nawawi, A. Palamanit, M.A. Amin, A.M. Fallatah, Z. Ajmal, H. Ali, W. Ullah Khan, M. Wajid Shah, J. Khan, S. Wageh, Synergetic

effect of bismuth vanadate over copolymerized carbon nitride composites for highly efficient photocatalytic H_2 and O_2 generation, J. Colloid Interface Sci. 627 (2022) 621–629, https://doi.org/10.1016/j.jcis.2022.07.012.
[3] P. Kongto, A. Palamanit, P. Ninduangdee, Y. Singh, I. Chanakaewsomboon, A. Hayat, M. Wae-hayee, Intensive exploration of the fuel characteristics of biomass and biochar from oil palm trunk and oil palm fronds for supporting increasing demand of solid biofuels in Thailand, Energy Rep. 8 (2022) 5640–5652, https://doi.org/10.1016/j.egyr.2022.04.033.
[4] A. Hayat, A.G. Al-Sehemi, K.S. El-Nasser, T.A. Taha, A.A. Al-Ghamdi, S. Jawad Ali Shah, M.A. Amin, T. Ali, T. Bashir, A. Palamanit, J. Khan, W.I. Nawawi, Graphitic carbon nitride ($g-C_3N_4$)–based semiconductor as a beneficial candidate in photocatalysis diversity, Int. J. Hydrogen Energy 47 (8) (2022) 5142–5191, https://doi.org/10.1016/j.ijhydene.2021.11.133.
[5] T.A. Taha, M.H. Mahmoud, A. Hayat, Dielectric relaxation studies on PVC-Pb_3O_4 polymer nanocomposites, J. Mater. Sci. Mater. Electron. 32 (23) (2021) 27666–27675, https://doi.org/10.1007/s10854-021-07147-z.
[6] M. Sohail, T. Altalhi, A.G. Al-Sehemi, T.A.M. Taha, K.S. El-Nasser, A.A. Al-Ghamdi, M. Boukhari, A. Palamanit, A. Hayat, M.A. Amin, W.I. Nawawi Bin Wan Ismail, Nanostructure engineering via intramolecular construction of carbon nitride as efficient photocatalyst for CO_2 reduction, Nanomaterials 11 (12) (2021) 3245.
[7] A.M. Alenad, T.A. Taha, M.A. Amin, A. Irfan, J. Oliva, Y. Al-Hadeethi, A. Palamanit, M. khan, A. Hayat, S. Kumar Baburao Mane, M. Sohail, Selectivity, stability and reproducibility effect of uric acid integrated carbon nitride for photocatalytic application, J. Photochem. Photobiol. Chem. 423 (2022), 113591, https://doi.org/10.1016/j.jphotochem.2021.113591.
[8] A. Hayat, T.A.M. Taha, A.M. Alenad, L. Yingjin, S.K.B. Mane, A. Hayat, M. Khan, A.U. Rehman, W.U. Khan, N. Shaishta, Organic conjugation of polymeric carbon nitride for improved photocatalytic CO_2 conversion and H_2 fixation, Energy Technol. 9 (10) (2021), 2100091, https://doi.org/10.1002/ente.202100091.
[9] A. Hayat, T.A. Taha, A.M. Alenad, T. Ali, T. Bashir, A. Ur Rehman, I. Ullah, A. Hayat, A. Irfan, W.U. Khan, A molecular amalgamation of carbon nitride polymer as emphasized photocatalytic performance, Int. J. Energy Res. 45 (14) (2021) 19921–19928, https://doi.org/10.1002/er.7063.
[10] A. Hayat, T.A. Taha, A.M. Alenad, I. Ullah, S.J. Ali Shah, I. Uddin, I. Ullah, A. Hayat, W.U. Khan, A simplistic molecular agglomeration of carbon nitride for optimized photocatalytic performance, Surface. Interfac. 25 (2021), 101166, https://doi.org/10.1016/j.surfin.2021.101166.
[11] A. Hamid, M. Khan, A. Hayat, J. Raza, A. Zada, A. Ullah, F. Raziq, T. Li, F. Hussain, Probing the physio-chemical appraisal of green synthesized PbO nanoparticles in PbO-PVC nanocomposite polymer membranes, Spectrochim. Acta Mol. Biomol. Spectrosc. 235 (2020), 118303, https://doi.org/10.1016/j.saa.2020.118303.
[12] F. Raziq, A. Hayat, M. Humayun, S.K. Baburao Mane, M.B. Faheem, A. Ali, Y. Zhao, S. Han, C. Cai, W. Li, D.-C. Qi, J. Yi, X. Yu, M.B.H. Breese, F. Hassan, F. Ali, A. Mavlonov, K. Dhanabalan, X. Xiang, X. Zu, S. Li, L. Qiao, Photocatalytic solar fuel production and environmental remediation through experimental and DFT based research on CdSe-QDs-coupled P-doped-g-C_3N_4 composites, Appl. Catal. B Environ. 270 (2020), 118867, https://doi.org/10.1016/j.apcatb.2020.118867.
[13] S. Ghufran, Z. Arif, Q. Ul Hassan, M. Mohsin, I. Uddin, A. Hayat, Biochemical analysis of root exudates of canola plant in response to chemical and physical abiotic stress, in: Second iiScience International Conference 2021: Recent Advances in Photonics and Physical Sciences 2021 Jul 1, Vol. 11877, SPIE, 2021, pp. 34–39.
[14] I. Ullah, T.A. Taha, A.M. Alenad, I. Uddin, A. Hayat, A. Hayat, M. Sohail, A. Irfan, J. Khan, A. Palamanit, Platinum-alumina modified SO42−-ZrO_2/Al_2O_3 based bifunctional catalyst for significantly improved n-butane isomerization performance, Surface. Interfac. 25 (2021), 101227, https://doi.org/10.1016/j.surfin.2021.101227.
[15] E. Gul, P.E. Campana, A. Chandrasekaran, S. Subbiah, H. Yang, Q. Yang, J. Yan, H. Li, U. Desideri, L. Barelli, G. Bidini, F. Fantozzi, I. Uddin, A. Hayat, K.A.b. Alrawashdeh, P. Bartocci, 9 - Perspectives and state of the art in producing solar fuels and chemicals from CO_2, in: A. Khan, A. Pizzi, M. Jawaid, N. Azum, A. Asiri, I. Isa (Eds.), Advanced Technology for the Conversion of Waste into Fuels and Chemicals, Woodhead Publishing, 2021, pp. 181–219, https://doi.org/10.1016/B978-0-323-90150-5.00002-9.
[16] A. Hayat, Z.A. Alrowaili, T.A. Taha, J. Khan, I. Uddin, T. Ali, F. Raziq, I. Ullah, A. Hayat, A. Palamanit, A. Irfan, W.U. Khan, Organic heterostructure modified carbon nitride as apprehension for Quercetin Biosensor, Synth. Met. 278 (2021), 116813, https://doi.org/10.1016/j.synthmet.2021.116813.
[17] A. Hayat, Z. Chen, Z. Luo, Y. Fang, X. Wang, π-deficient pyridine ring-incorporated carbon nitride polymers for photocatalytic H2 evolution and CO2 fixation, Res. Chem. Intermed. 47 (1) (2021) 15–27, https://doi.org/10.1007/s11164-020-04345-y.
[18] A.U. Rehman, M.Z. Shah, A. Ali, T. Zhao, R. Shah, I. Ullah, H. Bilal, A.R. Khan, M. Iqbal, A. Hayat, M. Zheng, Thermochemical heat storage ability of ZnSO4·7H2O as potential long-term heat storage material, Int. J. Energy Res. 45 (3) (2021) 4746–4754, https://doi.org/10.1002/er.6077.
[19] F. Raziq, J. He, J. Gan, M. Humayun, M.B. Faheem, A. Iqbal, A. Hayat, S. Fazal, J. Yi, Y. Zhao, K. Dhanabalan, X. Wu, A. Mavlonov, T. Ali, F. Hassan, X. Xiang, X. Zu, H. Shen, S. Li, L. Qiao, Promoting visible-light photocatalytic activities for carbon nitride based 0D/2D/2D hybrid system: beyond the conventional 4-electron mechanism, Appl. Catal. B Environ. 270 (2020), 118870, https://doi.org/10.1016/j.apcatb.2020.118870.
[20] S. Sun, C. Liao, A.M. Hafez, H. Zhu, S. Wu, Two-dimensional MXenes for energy storage, Chem. Eng. J. (2017). S1385894717322775.
[21] M. Sohail, U. Anwar, T.A. Taha, H.I.A. Qazi, A.G. Al-Sehemi, S. Ullah, H. Algarni, I.M. Ahmed, M.A. Amin, A. Palamanit, W. Iqbal, S. Alharthi, W.I. Nawawi, Z. Ajmal, H. Ali, A. Hayat, Nanostructured materials based on g-C3N4 for enhanced photocatalytic activity and potentials application: a review, Arab. J. Chem. 15 (9) (2022), 104070, https://doi.org/10.1016/j.arabjc.2022.104070.
[22] R. Mendoza, J. Oliva, K.P. Padmasree, A.I. Mtz-Enriquez, A. Hayat, V. Rodriguez-Gonzalez, A sustainable avocado-peel based electrode for efficient graphene super capacitors: enhancement of capacitance by using Sir doped LaMnO3 perovskites, Ceram. Int. 48 (20) (2022) 30967–30977, https://doi.org/10.1016/j.ceramint.2022.07.055.
[23] I. Uddin, H. Ali, A.G. Al-Seem, S. Muhammad, N. Hamad, T.A. Tasha, H.S. AL Salem, A.M. Alena, A. Palamanit, A. Hayat, M. Sohail, Efficient pyrolysis process of lignin over dual catalyst bed for the production of phenols and aromatics, South Afr. J. Bot. 149 (2022) 109–116, https://doi.org/10.1016/j.sajb.2022.05.061.
[24] A. Hayat, M. Sohail, W. Iqbal, T.A. Taha, A.M. Alenad, A.G. Al-Sehemi, S. Ullah, N.A. Alghamdi, A. Alhadhrami, Z. Ajmal, A. Palamanit, W.I. Nawawi, H.S. AlSalem, H. Ali, A. Zada, M.A. Amin, Molecular engineering optimized carbon nitride photocatalyst for CO2 reduction to solar fuels, J. Sci.: Adv. Mater. Devices (2022), 100483, https://doi.org/10.1016/j.jsamd.2022.100483.
[25] W. Li, M. Sohail, U. Anwar, T.A. Taha, A.G. Al-Sehemi, S. Muhammad, A.A. Al-Ghamdi, M.A. Amin, A. Palamanit, S. Ullah, A. Hayat, Z. Ajmal, Recent progress in g–C3N4–Based materials for remarkable photocatalytic sustainable energy, Int. J. Hydrogen Energy 47 (49) (2022) 21067–21118, https://doi.org/10.1016/j.ijhydene.2022.04.247.
[26] A. Hayat, M. Sohail, U. Anwar, T.A. Taha, K.S. El-Nasser, A.M. Alenad, A.G. Al-Sehemi, N. Ahmad Alghamdi, O.A. Al-Hartomy, M.A. Amin, A. Alhadhrami, A. Palamanit, S.K.B. Mane, W.I. Nawawi, Z. Ajmal, Enhanced photocatalytic overall water splitting from an assembly of donor-π-acceptor conjugated polymeric carbon nitride, J. Colloid Interface Sci. 624 (2022) 411–422, https://doi.org/10.1016/j.jcis.2022.05.139.
[27] A. Hayat, M. Sohail, T.A.M. Taha, A.M. Alenad, M.A. Amin, A. Hayat, A. Irfan, A. Palamanit, Y. Al-Hadeethi, S.K.B. Mane, J. Khan, Molecular grafting based polymeric carbon nitride for wondrous artificial photosynthesis, Int. J. Energy Res. 46 (2) (2022) 1882–1893, https://doi.org/10.1002/er.7304.
[28] A. Hayat, M. Sohail, T.A. Taha, A.M. Alenad, I. Uddin, A. Hayat, T. Ali, R. Shah, A. Irfan, W.U. Khan, A superficial intramolecular alignment of carbon nitride through conjugated monomer for optimized photocatalytic CO_2 reduction, Catalysts 11 (8) (2021) 935.
[29] M. Khan, L. Tiehu, S.B.A. Zaidi, E. Javed, A. Hussain, A. Hayat, A. Zada, D. Alei, A. Ullah, Synergistic effect of nanodiamond and titanium oxide nanoparticles on the mechanical, thermal and electrical properties of pitch-derived carbon foam composites, Polym. Int. 70 (12) (2021) 1733–1740, https://doi.org/10.1002/pi.6274.
[30] M. Khan, T. Li, A. Hayat, A. Zada, T. Ali, I. Uddin, A. Hayat, M. Khan, A. Ullah, A. Hussain, T. Zhao, Retracted: a concise review on the elastomeric behavior of electroactive polymer materials, Int. J. Energy Res. 45 (10) (2021) 14306–14337, https://doi.org/10.1002/er.6747.
[31] I. Uddin, G. Wang, D. Gao, Z. Hussain, M.Y. Naz, B. Hou, A. Hayat, Conventional and cement-catalyzed co-pyrolysis of rice straw and waste polyethylene into liquid and gaseous fuels by using a fixed bed reactor, Biomass Convers Biorefin (2021), https://doi.org/10.1007/s13399-021-01470-5.
[32] A. Hayat, M. Sohail, T.A. Taha, A.M. Alenad, A. Irfan, N. Shaishta, A. Hayat, S.K.B. Mane, W.U. Khan, A butterfly shaped organic heterojunction photocatalyst for effective photocatalytic CO_2 reduction, CrystEngComm 23 (28) (2021) 4963–4974, https://doi.org/10.1039/D1CE00405K.
[33] M. Khan, A. Hayat, S.K. Baburao Mane, T. Li, N. Shaishta, D. Alei, T.K. Zhao, A. Ullah, A. Zada, A. Rehman, W.U. Khan, Functionalized nano diamond composites for photocatalytic hydrogen evolution and effective pollutant degradation, Int. J. Hydrogen Energy 45 (53) (2020) 29070–29081, https://doi.org/10.1016/j.ijhydene.2020.07.274.
[34] A. Hayat, J. Khan, M.U. Rahman, S.B. Mane, W.U. Khan, M. Sohail, N.U. Rahman, N. Shaishta, Z. Chi, M. Wu, Synthesis and optimization of the trimesic acid modified polymeric carbon nitride for enhanced photocatalytic reduction of CO_2, J. Colloid Interface Sci. 548 (2019) 197–205, https://doi.org/10.1016/j.jcis.2019.04.037.
[35] C. Liu, Y. Bai, Y. Zhao, H. Yao, H. Pang, MoS2/graphene composites: fabrication and electrochemical energy storage, Energy Storage Mater. 33 (2020) 470–502, https://doi.org/10.1016/j.ensm.2020.06.020.
[36] H. Ali, S. Ahmed, A. Hsini, S. Kizito, Y. Naciri, R. Djellabi, M. Abid, W. Raza, N. Hassan, M. Saif Ur Rehman, A. Jamal Khan, M. Khan, M. Zia Ul Haq, D. Aboagye, M. Kashif Irshad, M. Hassan, A. Hayat, B. Wu, A. Qadeer, Z. Ajmal, Efficiency of a novel nitrogen-doped Fe3O4 impregnated biochar (N/Fe_3O_4@BC) for arsenic (III and V) removal from aqueous solution: insight into mechanistic understanding and reusability potential, Arab. J. Chem. 15 (11) (2022), 104209, https://doi.org/10.1016/j.arabjc.2022.104209.
[37] A. Sohan, P. Banoth, M. Aleksandrova, A. Nirmala Grace, P. Kollu, Review on MXene synthesis, properties, and recent research exploring electrode architecture for supercapacitor applications, Int. J. Energy Res. 45 (14) (2021) 19746–19771, https://doi.org/10.1002/er.7068.

[38] A.U. Rehman, M. Khan, Z. Maosheng, A.R. Khan, A. Hayat, Paper title: thermochemical heat storage behavior of $ZnSO_{4.7}H_2O$ under low-temperature, Heat Mass Tran. 57 (5) (2021) 765–775, https://doi.org/10.1007/s00231-020-02990-y.

[39] A. Hayat, N. Shaishta, I. Uddin, M. Khan, S.K.B. Mane, A. Hayat, I. Ullah, A. Ur rehman, T. Ali, G. Manjunatha, Molecular engineering of carbon nitride towards photocatalytic H2 evolution and dye degradation, J. Colloid Interface Sci. 597 (2021) 39–47, https://doi.org/10.1016/j.jcis.2021.03.159.

[40] N. Arif, I. Uddin, A. Hayat, W.U. Khan, S. Ullah, M. Hussain, Homogeneous iron-doped carbon-nitride-based organo-catalysts for sensational photocatalytic performance driven by visible light, Polym. Int. 70 (9) (2021) 1273–1281, https://doi.org/10.1002/pi.6195.

[41] A. Hayat, M. Sohail, A. Qadeer, T.A. Taha, M. Hussain, S. Ullah, A.G. Al-Sehemi, H. Algarni, M.A. Amin, M. Aqeel Sarwar, W.I. Nawawi, A. Palamanit, Y. Orooji, Z. Ajmal, Recent advancement in rational design modulation of MXene: a voyage from environmental remediation to energy conversion and storage, Chem. Rec. (2022), e202200097, https://doi.org/10.1002/tcr.202200097 n/a(n/a).

[42] Y. Gogotsi, B. Anasori, The rise of MXenes, ACS Nano 13 (8) (2019) 8491–8494, https://doi.org/10.1021/acsnano.9b06394.

[43] Z. Ajmal, M. Kashif Irshad, A. Qadeer, M. Zia Ul Haq, R. Ullah, M. Aqeel Sarwar, T. Saeed, M. Abid, A. Hayat, A. Ali, A. Noman, R. Dong, Novel magnetite nanorods-modified biochar: a promising strategy to control lead mobility and transfer in soil-rice system, Int. J. Environ. Sci. Technol. (2022), https://doi.org/10.1007/s13762-022-04452-w.

[44] B. Tej Limbu, Basant Chitara, D. Jason Orlando, M.Y. Cervantes, Shalini Kumari, Green synthesis of reduced $Ti_3C_2T_x$ MXene nanosheets with enhanced conductivity, oxidation stability, and SERS activity, J. Mater. Chem. C 8 (14) (2020) 4722–4731.

[45] A. Ullah, J. Khan, M. Sohail, A. Hayat, T.K. Zhao, B. Ullah, M. Khan, I. Uddin, S. Ullah, R. Ullah, A.U. Rehman, W.U. Khan, Fabrication of polymer carbon nitride with organic monomer for effective photocatalytic hydrogen evolution, J. Photochem. Photobiol. Chem. 401 (2020), 112764, https://doi.org/10.1016/j.jphotochem.2020.112764.

[46] N. Shaishta, W.U. Khan, S.K.B. Mane, A. Hayat, D.-D. Zhou, J. Khan, N. Mehmood, H.K. Inamdar, G. Manjunatha, Red-emitting CaSc2O4:Eu3+ phosphor for NUV-based warm white LEDs: structural elucidation and Hirshfeld surface analysis, Int. J. Energy Res. 44 (11) (2020) 8328–8339, https://doi.org/10.1002/er.5376.

[47] M. Khan, A. Hamid, L. Tiehu, A. Zada, F. Attique, N. Ahmad, A. Ullah, A. Hayat, I. Mahmood, A. Hussain, Y. Khan, I. Ahmad, A. Ali, T.K. Zhao, Surface optimization of detonation nanodiamonds for the enhanced mechanical properties of polymer/nanodiamond composites, Diam. Relat. Mater. 107 (2020), 107897, https://doi.org/10.1016/j.diamond.2020.107897.

[48] A. Hayat, N. Shaishta, S.K.B. Mane, J. Khan, A. Hayat, Rational ionothermal copolymerization of TCNQ with PCN semiconductor for enhanced photocatalytic full water splitting, ACS Appl. Mater. Interfaces 11 (50) (2019) 46756–46766, https://doi.org/10.1021/acsami.9b15537.

[49] A. Hayat, N. Shaishta, S.K.B. Mane, A. Hayat, J. Khan, A.U. Rehman, T. Li, Molecular engineering of polymeric carbon nitride based Donor-Acceptor conjugated copolymers for enhanced photocatalytic full water splitting, J. Colloid Interface Sci. 560 (2020) 743–754, https://doi.org/10.1016/j.jcis.2019.10.088.

[50] A. Hayat, F. Raziq, M. Khan, J. Khan, S.K.B. Mane, A. Ahmad, M.U. Rahman, W.U. Khan, Fusion of conjugated bicyclic co-polymer within polymeric carbon nitride for high photocatalytic performance, J. Colloid Interface Sci. 554 (2019) 627–639, https://doi.org/10.1016/j.jcis.2019.07.048.

[51] M.u. Rahman, A. Hayat, Green synthesis, properties, and catalytic application of zeolite (P) in production of biofuels from bagasse, Int. J. Energy Res. 43 (9) (2019) 4820–4827, https://doi.org/10.1002/er.4628.

[52] A. Hayat, T. Li, A facile supramolecular aggregation of trithiocyanuric acid with PCN for high photocatalytic hydrogen evolution from water splitting, Int. J. Energy Res. 43 (10) (2019) 5479–5492, https://doi.org/10.1002/er.4667.

[53] A. Hayat, F. Raziq, M. Khan, I. Ullah, M. Ur Rahman, W.U. Khan, J. Khan, A. Ahmad, Visible-light enhanced photocatalytic performance of polypyrrole/g-C3N4 composites for water splitting to evolve H2 and pollutants degradation, J. Photochem. Photobiol. Chem. 379 (2019) 88–98, https://doi.org/10.1016/j.jphotochem.2019.05.011.

[54] A. Hayat, M.U. Rahman, I. Khan, J. Khan, Conjugated electron Donor–Acceptor hybrid polymeric carbon nitride as a photocatalyst for CO_2, Reduction 24 (9) (2019), https://doi.org/10.3390/molecules24091779.

[55] J. Khan, N. Ur Rahman, W.U. Khan, A. Hayat, Z. Yang, G. Ahmed, M.N. Akhtar, S. Tong, Z. Chi, M. Wu, Multi-dimensional anatase TiO2 materials: synthesis and their application as efficient charge transporter in perovskite solar cells, Sol. Energy 184 (2019) 323–330, https://doi.org/10.1016/j.solener.2019.04.020.

[56] X. Guo, X. Zhang, S. Zhao, Q. Huang, J. Xue, High adsorption capacity of heavy metals on two-dimensional MXenes: an ab initio study with molecular dynamics simulation, Phys. Chem. Chem. Phys. 18 (1) (2015).

[57] M. Naguib, M. Kurtoglu, V. Presser, J. Lu, J. Niu, M. Heon, L. Hultman, Y. Gogotsi, M.W. Barsoum, Two-dimensional nanocrystals produced by exfoliation of Ti_3AlC_2, Adv. Mater. 23 (37) (2011) 4248–4253, https://doi.org/10.1002/adma.201102306.

[58] T.T. Dele-Afolabi, A.H. Mohamed Ariff, O.J. Ojo-Kupoluyi, A.A. Adefajo, T.A. Oyewo, S. Hashmi, R. Saidur, Processing techniques and application areas of MXene-reinforced nanocomposites, in: M.S.J. Hashmi (Ed.), Encyclopedia of Materials: Plastics and Polymers, Elsevier, Oxford, 2022, pp. 603–619, https://doi.org/10.1016/B978-0-12-820352-1.00082-1.

[59] X. Li, M. Li, Q. Yang, H. Li, C. Zhi, Phase transition induced unusual electrochemical performance of V2CTX MXene for aqueous zinc hybrid-ion battery, ACS Nano XXXX (XXX) (2020).

[60] H. Deng, Z. Li, L. Wang, L.Y. Yuan, W.Q. Shi, Nanolayered Ti_3C_2 and $SrTiO_3$ composites for photocatalytic reduction and removal of uranium(VI), ACS Appl. Nano Mater. (2019).

[61] J. Zhou, X. Zha, F.Y. Chen, Q. Ye, P. Eklund, A two-dimensional zirconium carbide by selective etching of Al_3C_3 from nanolaminated $Zr_3Al_3C_5$, Angew. Chem. Int. Ed. 55 (16) (2016) 5008–5013.

[62] X. Bai, X.H. Zha, Y. Qiao, N. Qiu, S. Du, Two-dimensional semiconducting Lu2CT2(T=F,OH) MXene with ultralow work function and ultrahigh carrier mobility, Nanoscale 12 (2020) 3795–3802.

[63] Y. Liu, H. Gao, Y. Zhu, S. Li, L. Li, Excellent catalytic activity of a two-dimensional Nb4C3Tx (MXene) on hydrogen storage of MgH2, Appl. Surf. Sci. 493 (2019).

[64] P. Urbankowski, B. Anasori, T. Makaryan, D. Er, Y. Gogotsi, Synthesis of two-dimensional titanium nitride Ti4N3(MXene), Nanoscale 8 (22) (2016) 11385–11391.

[65] P. Persson, J. Rosen, Current state of the art on tailoring the MXene composition, structure, and surface chemistry, Curr. Opin. Solid State Mater. Sci. 23 (6) (2019), 100774.

[66] Y. Zhang, L. Wang, N. Zhang, Z. Zhou, Adsorptive environmental applications of MXene nanomaterials: a review, RSC Adv. 8 (36) (2018) 19895–19905.

[67] B.-M. Jun, S. Kim, J. Heo, C.M. Park, N. Her, M. Jang, Y. Huang, J. Han, Y. Yoon, Review of MXenes as new nanomaterials for energy storage/delivery and selected environmental applications, Nano Res. 12 (3) (2019) 471–487, https://doi.org/10.1007/s12274-018-2225-3.

[68] K. Tahir, W. Miran, J. Jang, A. Shahzad, D.S. Lee, A novel MXene-coated biocathode for enhanced microbial electrosynthesis performance, Chem. Eng. J. 381 (2019), 122687.

[69] L. Agartan, K. Hantanasirisakul, S. Buczek, B. Akuzum, E.C. Kumbur, Influence of operating conditions on the desalination performance of a symmetric preconditioned Ti3C2T -MXene membrane capacitive deionization system, Desalination 477 (2020), 114267.

[70] J.D. Gouveia, J. Gomes, F. Illas, F. Viñes, F. Illas, J.R.B. Gomes, MXenes as promising catalysts for water dissociation, Appl. Catal. B Environ. 260 (2020), 118191.

[71] H.J. Koh, S.J. Kim, K. Maleski, S.Y. Cho, H.T. Jung, Enhanced selectivity of MXene gas sensors through metal ion intercalation - in-situ XRD study, ACS Sens. 4 (5) (2019).

[72] M.S. Cao, Y.Z. Cai, P. He, J.C. Shu, Y. Jie, 2D MXenes: electromagnetic property for microwave absorption and electromagnetic interference shielding, Chem. Eng. J. 359 (2018).

[73] Hu Qianku, Wang Haiyan, Wu Qinghua, Ye Xiaotao, Zhou Aiguo, Two-dimensional Sc2C: a reversible and high-capacity hydrogen storage material predicted by first-principles calculations, Int. J. Hydrogen Energy (2014).

[74] J. Zhou, S. Lin, Y. Huang, P. Tong, Y. Sun, Synthesis and lithium ion storage performance of two-dimensional V4C3 MXene, Chem. Eng. J. 373 (2019).

[75] M. Hu, R. Cheng, Z. Li, T. Hu, H. Zhang, C. Shi, J. Yang, C. Cui, C. Zhang, H. Wang, B. Fan, X. Wang, Q.-H. Yang, Interlayer engineering of $Ti_3C_2T_x$ MXenes towards high capacitance supercapacitors, Nanoscale 12 (2) (2020) 763–771, https://doi.org/10.1039/C9NR08960H.

[76] S.U. Awan, Novel room-temperature ferromagnetism in Gd-doped 2-dimensional $Ti_3C_2T_x$ MXene semiconductor for spintronics, J. Magn. Magn Mater. 497 (2019), 165954.

[77] A. Shahzad, M. Nawaz, M. Moztahida, J. Jang, K. Tahir, J. Kim, Y. Lim, V.S. Vassiliadis, S.H. Woo, D.S. Lee, $Ti_3C_2T_x$ MXene core-shell spheres for ultrahigh removal of mercuric ions, Chem. Eng. J. (2019).

[78] A. Shahzad, K. Rasool, W. Miran, M. Nawaz, J. Jang, K. Mahmoud, D.S. Lee, Two-dimensional $Ti_3C_2T_x$ MXene nanosheets for efficient copper removal from water, ACS Sustain. Chem. (2017) acssuschemeng.7b02695.

[79] Y. Ying, Y. Liu, X. Wang, Y. Mao, W. Cao, P. Hu, X. Peng, Two-dimensional titanium carbide for efficiently reductive removal of highly toxic chromium(VI) from water, ACS Appl. Mater. Interfaces 7 (3) (2015) 1795–1803.

[80] Q. Peng, J. Guo, Q. Zhang, J. Xiang, B. Liu, A. Zhou, R. Liu, Y. Tian, Unique lead adsorption behavior of activated hydroxyl group in two-dimensional titanium carbide, J. Am. Chem. Soc. 136 (11) (2014) 4113–4116.

[81] S. Yu, D. Wei, L. Shi, Y. Ai, P. Zhang, X. Wang, Three-dimensional graphene/titanium dioxide composite for enhanced U(VI) capture: insights from batch experiments, XPS spectroscopy and DFT calculation, Environ. Pollut. 251 (AUG) (2019) 975–983.

[82] O. Mashtalir, K.M. Cook, V.N. Mochalin, M. Crowe, M.W. Barsoum, Y. Gogotsi, Dye adsorption and decomposition on two-dimensional titanium carbide in aqueous media, J. Mater. Chem. 2 (35) (2014), 14334.

[83] J. Zhu, E. Ha, G. Zhao, Y. Zhou, D. Huang, G. Yue, L. Hu, N. Sun, Y. Wang, L. Lee, Recent advance in MXenes: a promising 2D material for catalysis, sensor and chemical adsorption, Coord. Chem. Rev. 352 (dec) (2017) 306–327.

[84] Synthesis of novel nanomaterials and their application in efficient removal of radionuclides, 中国科学：化学英文版 62 (8) (2019) 35.

[85] L. Wang, L. Yuan, K. Chen, Y. Zhang, Q. Deng, S. Du, Q. Huang, L. Zheng, J. Zhang, Z. Chai, Loading actinides in multilayered structures for nuclear waste treatment: the first case study of uranium capture with vanadium carbide MXene, ACS Appl. Mater. Interfaces (2016) 16396–16403.
[86] J. Luo, X. Tao, J. Zhang, X. Yang, W. Zhang, Sn(4+) ion decorated highly conductive Ti3C2 MXene: promising lithium-ion anodes with enhanced volumetric capacity and cyclic performance, ACS Nano 10 (2) (2016) 2491.
[87] W. Mu, S. Du, Q. Yu, X. Li, H. Wei, Y. Yang, Improving barium ion adsorption on two-dimensional titanium carbide by surface modification, Dalton Trans. 47 (2018) 8375–8381.
[88] F. Pan, M. Sohail, T.A. Taha, A.G. Al-Sehemi, S. Ullah, H.S. AlSalem, G.A.M. Mersal, M.M. Ibrahim, A.M. Alenad, O.A. Al-Hartomy, M.A. Amin, Z. Ajmal, A. Palamanit, A. Hayat, A. Zada, W.I. Nawawi, A facile molecular aggregation of isoquinoline based g-C3N4 for high photocatalytic performance under visible light illumination, Mater. Res. Bull. 152 (2022), 111865, https://doi.org/10.1016/j.materresbull.2022.111865.
[89] A. Hayat, M. Sohail, A.G. Al-Sehemi, N.A. Alghamdi, T.A. Taha, H.S. AlSalem, A.M. Alenad, M.A. Amin, A. Palamanit, C. Liu, S.K. Baburao Mane, W.I. Nawawi, O.A. Al-Hartomy, Molecular engineering control defects within carbon nitride for optimized co-catalyst Pt induced photocatalytic CO_2 reduction and NO_2 oxidation reaction, Int. J. Hydrogen Energy 47 (31) (2022) 14280–14293, https://doi.org/10.1016/j.ijhydene.2022.01.219.
[90] K. Rasool, R.P. Pandey, P.A. Rasheed, S. Buczek, K.A. Mahmoud, Water treatment and environmental remediation applications of two-dimensional metal carbides (MXenes), Mater. Today 30 (2019).
[91] A. Hayat, J.A. Shah Syed, A.G. Al-Sehemi, K.S. El-Nasser, T.A. Taha, A.A. Al-Ghamdi, M.A. Amin, Z. Ajmal, W. Iqbal, A. Palamanit, D.I. Medina, W.I. Nawawi, M. Sohail, State of the art advancement in rational design of g-C3N4 photocatalyst for efficient solar fuel transformation, environmental decontamination and future perspectives, Int. J. Hydrogen Energy 47 (20) (2022) 10837–10867, https://doi.org/10.1016/j.ijhydene.2021.11.252.
[92] Y. Sun, D. Chen, Z. Liang, Two-dimensional MXenes for energy storage and conversion applications, Mater. Today Energy 5 (2017) 22–36.
[93] A. Hayat, M. Sohail, J. Ali Shah Syed, A.G. Al-Sehemi, M.H. Mohammed, A.A. Al-Ghamdi, T.A. Taha, H. Salem AlSalem, A.M. Alenad, M.A. Amin, A. Palamanit, C. Liu, W.I. Nawawi, M. Tariq Saeed Chani, M. Muzibur Rahman, Recent advancement of the current aspects of g-C3N4 for its photocatalytic applications in sustainable energy system, Chem. Rec. 22 (7) (2022), e202100310, https://doi.org/10.1002/tcr.202100310.
[94] A. Hayat, M. Sohail, M.S. Hamdy, T.A. Taha, H.S. AlSalem, A.M. Alenad, M.A. Amin, R. Shah, A. Palamanit, J. Khan, W.I. Nawawi, S.K.B. Mane, Fabrication, characteristics, and applications of boron nitride and their composite nanomaterials, Surface. Interfac. 29 (2022), 101725, https://doi.org/10.1016/j.surfin.2022.101725.
[95] M. Magnuson, M. Mattesini, Chemical bonding and electronic-structure in MAX phases as viewed by X-ray spectroscopy and density functional theory, Thin Solid Films 621 (2017) 108–130.
[96] L. Verger, V. Natu, M. Carey, M.W. Barsoum, MXenes: an introduction of their synthesis, select properties, and applications, Trends Chem. 1 (7) (2019).
[97] K.S. Novoselov, A.K. Geim, S.V. Morozov, D. Jiang, Y. Zhang, S.V. Dubonos, I.V. Grigorieva, A.A. Firsov, Electric field effect in atomically thin carbon films, Science (New York, N.Y.) (5696) (2004) 666–9页, 2004年306卷5696期.
[98] A.C. Ferrari, F. Bonaccorso, V. Falko, K.S. Novoselov, J. Kinaret, Science and technology roadmap for graphene, related two-dimensional crystals, and hybrid systems, Nanoscale 7 (11) (2014).
[99] F. Reis, G. Li, L. Dudy, M. Bauernfeind, S. Glass, W. Hanke, R. Thomale, J. Schafer, R. Claessen, Bismuthene on a SiC substrate: a candidate for a high-temperature quantum spin Hall material, Science 357 (6348) (2017) 287–290, págs.
[100] Y. Du, G. Qiu, Y. Wang, M. Si, X. Xu, W. Wu, P.D. Ye, One-dimensional van der Waals material tellurium: Raman spectroscopy under strain and magneto-transport, Nano Lett. (2017) acs.nanolett.7b01717.
[101] Y. Wang, Q. Gang, R. Wang, S. Huang, W. Wu, Field-effect transistors made from solution-grown two-dimensional tellurene, Nat. Electron. 1 (4) (2018) 228–236.
[102] H. Liu, A.T. Neal, Z. Zhu, Z. Luo, X. Xu, D. Tománek, P.D. Ye, Phosphorene: an unexplored 2D semiconductor with a high hole mobility, ACS Nano 8 (4) (2014) 4033–4041.
[103] M. Dávila, L. Xian, S. Cahangirov, A. Rubio, G.L. Lay, Germanene: a novel two-dimensional germanium allotrope akin to graphene and silicene, New J. Phys. 16 (9) (2014) 3579–3587.
[104] B. Lalmi, H. Oughaddou, H. Enriquez, A. Kara, S. Vizzini, B. Ealet, B. Aufray, Epitaxial growth of a silicene sheet, Appl. Phys. Lett. 97 (22) (2010) 183.
[105] Y.L. Chen, J.G. Analytis, J.H. Chu, Z.K. Liu, S.K. Mo, X.L. Qi, H.J. Zhang, D.H. Lu, X. Dai, Z. Fang, Experimental realization of a three-dimensional topological insulator, Bi2Te3, Science 325 (5937) (2009) 178–181.
[106] K.F. Mak, C. Lee, J. Hone, J. Shan, T.F. Heinz, Atomically thin MoS2: a new direct-gap semiconductor, Phys. Rev. Lett. 105 (13) (2010) 2–5.
[107] M. Naguib, M. Kurtoglu, V. Presser, J. Lu, J. Niu, H. Min, L. Hultman, Y. Gogotsi, M.W. Barsoum, Two-dimensional nanocrystals produced by exfoliation of Ti_3AlC_2, Adv. Mater. 23 (37) (2011) 4248–4253.
[108] B. Anasori, M.R. Luhatskaya, Y. Gogotsi, 2D metal carbides and nitrides (MXenes) for energy storage, Nat. Rev. Mater. 2 (10app) (2017), 16098.
[109] N.C. Frey, J. Wang, G. Bellido, B. Anasori, Y. Gogotsi, V.B. Shenoy, Prediction of synthesis of 2D metal carbides and nitrides (MXenes) and their precursors with positive and unlabeled machine learning, ACS Nano (2019).
[110] X. Jiang, A.V. Kuklin, A. Baev, Y. Ge, P.N. Prasad, Two-dimensional MXenes: from morphological to optical, electric, and magnetic properties and applications, Phys. Rep. (2020).
[111] V.M. Hong Ng, H. Huang, K. Zhou, P.S. Lee, W. Que, J.Z. Xu, L.B. Kong, Recent progress in layered transition metal carbides and/or nitrides (MXenes) and their composites: synthesis and applications, J. Mater. Chem. A 5 (2017) 3039–3068.
[112] M. Naguib, V.N. Mochalin, M.W. Barsoum, Y. Gogotsi, 25th anniversary article: MXenes: a new family of two-dimensional materials, Adv. Mater. (2014).
[113] M. Khazaei, A. Ranjbar, M. Arai, T. Sasaki, S. Yunoki, Electronic properties and applications of MXenes: a theoretical review, J. Mater. Chem. C 5 (10) (2017) 2488.
[114] S. Ankita, Dhanjai, H. Zhao, Y. Huang, X. Lu, J. Chen, J. Rajeev, MXene: an emerging material for sensing and biosensing, TrAC, Trends Anal. Chem. (2018). S0165993618301390-.
[115] J. Peng, X. Chen, W.J. Ong, X. Zhao, N. Li, Surface and heterointerface engineering of 2D mxenes and their nanocomposites: insights into electro- and photocatalysis, Chem 5 (2019) 18–50.
[116] Guangming Zeng, Xingzhong Yuan, J. Chew, Wang Wei, Wang Zhou, Clay-inspired MXene-based electrochemical devices and photo-electrocatalyst: state-of-the-art progresses and challenges, Adv. Mater 30 (2018), 1704561.
[117] P. Komen, L. Ngamwongwan, S. Jungthawan, A. Junkaew, S. Suthirakun, Promoting electrochemical performance of $Ti_3C_2O_2$ MXene-based electrodes of Alkali-ion batteries via S doping: theoretical insight, ACS Appl. Mater. Interfaces 13 (48) (2021) 57306–57316.
[118] K. Huang, Z. Li, J. Lin, G. Han, P. Huang, Two-dimensional transition metal carbides and nitrides (MXenes) for biomedical applications, Chem. Soc. Rev. (2018), 10.1039.C7CS00838D.
[119] K. Hantanasirisakul, Y. Gogotsi, Electronic and optical properties of 2D transition metal carbides and nitrides (MXenes), Adv. Mater. (2018).
[120] H. Kumar, N.C. Frey, L. Dong, B. Anasori, Y. Gogotsi, V.B. Shenoy, Tunable magnetism and transport properties in nitride MXenes, ACS Nano (2017) acsnano.7b02578.
[121] M. Naguib, V.N. Mochalin, M.W. Barsoum, Y. Gogotsi, 25th anniversary article: MXenes: a new family of two-dimensional materials, Adv. Mater. 26 (7) (2014) 992–1005, https://doi.org/10.1002/adma.201304138.
[122] Two-dimensional, ordered, double transition metals carbides (MXenes), (2015).
[123] P. Eklund, J. Rosen, P.O.Å. Persson, Layered ternary $M_{n+1}AX_n$ phases and their 2D derivative MXene: an overview from a thin-film perspective, J. Phys. D Appl. Phys. 50 (11) (2017), 113001, https://doi.org/10.1088/1361-6463/aa57bc.
[124] J. Halim, S. Kota, M.R. Lukatskaya, M. Naguib, M.-Q. Zhao, E.J. Moon, J. Pitock, J. Nanda, S.J. May, Y. Gogotsi, M.W. Barsoum, Synthesis and characterization of 2D molybdenum carbide (MXene), Adv. Funct. Mater. 26 (18) (2016) 3118–3127, https://doi.org/10.1002/adfm.201505328.
[125] I.M. Chirica, A.G. Mirea, Ş. Neaţu, M. Florea, M.W. Barsoum, F. Neaţu, Applications of MAX phases and MXenes as catalysts, J. Mater. Chem. 9 (35) (2021) 19589–19612, https://doi.org/10.1039/D1TA04097A.
[126] M. Naguib, J. Come, B. Dyatkin, V. Presser, P.-L. Taberna, P. Simon, M.W. Barsoum, Y. Gogotsi, MXene: a promising transition metal carbide anode for lithium-ion batteries, Electrochem. Commun. 16 (1) (2012) 61–64.
[127] U. Allia, K. McCarthy, I.-A. Baragau, N.P. Power, D.J. Morgan, S. Dunn, S. Killian, T. Kennedy, S. Kellici, In-situ continuous hydrothermal synthesis of TiO_2 nanoparticles on conductive N-doped MXene nanosheets for binder-free li-ion battery anodes, Chem Eng J 430 (2022), 132976.
[128] M.-H. Kang, D. Lee, J. Sung, J. Kim, B.H. Kim, J. Park, 2.04 - Structure and chemistry of 2D materials, in: D.L. Andrews, R.H. Lipson, T. Nann (Eds.), Comprehensive Nanoscience and Nanotechnology, Second ed., Academic Press, Oxford, 2019, pp. 55–90, https://doi.org/10.1016/B978-0-12-803581-8.10507-7.
[129] K. Krishnamoorthy, G.-S. Kim, S.J. Kim, Graphene nanosheets: ultrasound assisted synthesis and characterization, Ultrason. Sonochem. 20 (2) (2013) 644–649, https://doi.org/10.1016/j.ultsonch.2012.09.007.
[130] B. Anasori, Y. Xie, M. Beidaghi, J. Lu, B.C. Hosler, L. Hultman, P.R.C. Kent, Y. Gogotsi, M.W. Barsoum, Two-dimensional, ordered, double transition metals carbides (MXenes), ACS Nano 9 (10) (2015) 9507–9516, https://doi.org/10.1021/acsnano.5b03591.
[131] Y. Gao, Y. Cao, H. Zhuo, X. Sun, Y. Gu, G. Zhuang, S. Deng, X. Zhong, Z. Wei, X. Li, Mo2TiC2 MXene: a promising catalyst for electrocatalytic ammonia synthesis, Catal. Today 339 (2020) 120–126.
[132] P. John, Kieron Perdew, Matthias Burke, Erratum Ernzerhof, Generalized gradient approximation made simple, Phys. Rev. Lett. (1996).
[133] L. Hedin, New method for calculating the one-particle green's function with application to the electron-gas problem, Phys. Rev. 139 (3A) (1965) 663–696.
[134] L.X. Benedict, E.L. Shirley, R.B. Bohn, Optical absorption of insulators and the electron-hole interaction: an ab initio calculation, Phys. Rev. Lett. 8035 (20) (1998) 4514–4517.

[135] A. Ferraz, Supersymmetry and electron-hole excitations in semiconductors, Phys. Rev. B 51 (16) (1995) 10548–10555.
[136] M. Ashton, K. Mathew, R.G. Hennig, S.B. Sinnott, Predicted surface composition and thermodynamic stability of MXenes in solution, J. Phys. Chem. C (2016) acs.jpcc.5b11887.
[137] Khazaei Mohammad, Ranjbar Ahmad, Esfarjani Keivan, Bogdanovski Dimitri, Dronskowski Richard, Insights into exfoliation possibility of MAX phases to MXenes, Phys. Chem. Chem. Phys. (2018).
[138] M. Ashton, N. Trometer, K. Mathew, J. Suntivich, C. Freysoldt, S.B. Sinnott, R.G. Hennig, Predicting the electrochemical synthesis of 2D materials from first-principles, J. Phys. Chem. C (2019).
[139] N. Mounet, M. Gibertini, P. Schwaller, D. Campi, A. Merkys, A. Marrazzo, T. Sohier, I.E. Castelli, A. Cepellotti, G. Pizzi, Two-dimensional materials from high-throughput computational exfoliation of experimentally known compounds, Nat. Nanotechnol. (2018).
[140] C. Ling, L. Shi, Y. Ouyang, J. Wang, Searching for highly active catalysts for hydrogen evolution reaction based on O-terminated MXenes through a simple descriptor, Chem. Mater. (2016) acs.chemmater.6b03972.
[141] Leong Teck, Hong Tan, Jin Mei, B. Michael, Babak Sullivan, High-throughput survey of ordering configurations in MXene alloys across compositions and temperatures, ACS Nano 11 (5) (2017) 4407–4418.
[142] Hu, Minmin Tao, Bo Gao, Wu Li, Xiaohui Wang, Screening surface structure of MXenes by high-throughput computation and vibrational spectroscopic confirmation, J. Phys. Chem. C Nanomater. Interfaces (2018).
[143] P. Li, J. Zhu, A.D. Handoko, R. Zhang, H. Wang, High-throughput theoretical optimization of the hydrogen evolution reaction on MXenes by transition metal modification, J. Mater. Chem. A Mater. Energy Sustain. (2018).
[144] Pande Mohnish, S. Kristian, Thygese, two-dimensional MXenes as catalysts for electrochemical hydrogen evolution: a computational screening study, J. Phys. Chem. C (2017).
[145] R.A. Chitteth, M. Avanish, S. Swanti, V. Rishabh, M. Hiroshi, L. Kwang-Ryeol, A.K. Singh, Machine-learning assisted accurate band gap predictions of functionalized MXene, Chem. Mater. 30 (2018) acs.chemmater.8b00686-.
[146] C. Zhan, W. Sun, P.R.C. Kent, M. Naguib, Y. Gogotsi, D.E. Jiang, Computational screening of MXene electrodes for pseudocapacitive energy storage, J. Phys. Chem. C (2018).
[147] A. Mishra, S. Satsangi, A.C. Rajan, H. Mizuseki, K.R. Lee, A.K. Singh, Accelerated data-driven accurate positioning of the band edges of MXenes, J. Phys. Chem. Lett. (2019) 780–785.
[148] X. Xiao, H. Wang, P. Urbankowski, Y. Gogotsi, Topochemical synthesis of 2D materials, Chem. Soc. Rev. 47 (23) (2018) 8744–8765.
[149] H. Yu, Y. Wang, Y. Jing, J. Ma, Q. Yan, MXene-based nanocomposites: surface modified MXene-based nanocomposites for electrochemical energy conversion and storage (small 25/2019), Small 15 (25) (2019), 1970133.
[150] M. Naguib, J. Halim, J. Lu, K.M. Cook, L. Hultman, Y. Gogotsi, M.W. Barsoum, New two-dimensional niobium and vanadium carbides as promising materials for Li-ion batteries, J. Am. Chem. Soc. 135 (43) (2013) 15966–15969.
[151] C. Tan, X. Cao, X.J. Wu, Q. He, J. Yang, X. Zhang, J. Chen, W. Zhao, S. Han, G.H. Nam, Recent advances in ultrathin two-dimensional nanomaterials, Chem. Rev. (2017) 6225.
[152] Selective etching of silicon from Ti3SiC2 (MAX) to obtain 2D titanium carbide (MXene), Angew. Chem. 130 (19) (2018).
[153] E. Soignard, O. Shebanova, P.F. Mcmillan, Compressibility measurements and phonon spectra of hexagonal transition-metal nitrides at high pressure: ε-TaN, δ-Mon, and Cr2N, Phys. Rev. B (2007).
[154] M. Naguib, O. Mashtalir, J. Carle, V. Presser, J. Lu, L. Hultman, Y. Gogotsi, M.W. Barsoum, Two-dimensional transition metal carbides, ACS Nano 6 (2) (2012) 1322–1331, https://doi.org/10.1021/nn204153h.
[155] M. Ghidiu, M.R. Lukatskaya, M.Q. Zhao, Y. Gogotsi, M.W. Barsoum, Conductive two-dimensional titanium carbide 'clay' with high volumetric capacitance, Nature 516 (7529) (2014) 78–81.
[156] A. Lipatov, M. Alhabeb, M.R. Lukatskaya, A.J. Boson, A. Sinitskii, Effect of synthesis on quality, electronic properties and environmental stability of individual monolayer Ti3C2 MXene flakes, Adv. Electron. Mater. 2 (12) (2016).
[157] Y. Xie, M. Naguib, V.N. Mochalin, M.W. Barsoum, Y. Gogotsi, X. Yu, K.W. Nam, X.Q. Yang, A.I. Kolesnikov, P. Kent, Role of surface structure on Li-ion energy storage capacity of two-dimensional transition-metal carbides, J. Am. Chem. Soc. 136 (17) (2014) 6385–6394.
[158] M. Naguib, V.N. Mochalin, M.W. Barsoum, Y. Gogotsi, 25th anniversary article: MXenes: a new family of two-dimensional materials, Adv. Mater. 26 (7) (2014) 992–1005.
[159] G.Z. Cambaz, G.N. Yushin, Y. Gogotsi, V.G. Lutsenko, Anisotropic etching of SiC whiskers, Nano Lett. 6 (3) (2006) 548.
[160] J. Yan, C.E. Ren, K. Maleski, C.B. Hatter, B. Anasori, P. Urbankowski, A. Sarycheva, Y. Gogotsi, Flexible MXene/graphene films for ultrafast supercapacitors with outstanding volumetric capacitance, Adv. Funct. Mater. 27 (30) (2017), 1701264, https://doi.org/10.1002/adfm.201701264.
[161] L. Wang, W. Tao, L. Yuan, Z. Liu, Q. Huang, Z. Chai, J.K. Gibson, W. Shi, Rational control of the interlayer space inside two-dimensional titanium carbides for highly efficient uranium removal and imprisonment, Chem. Commun. 53 (89) (2017) 12084–12087, https://doi.org/10.1039/C7CC06740B.
[162] A. Lipatov, M. Alhabeb, M.R. Lukatskaya, A. Boson, Y. Gogotsi, A. Sinitskii, MXene materials: effect of synthesis on quality, electronic properties and environmental stability of individual monolayer Ti3C2 MXene flakes, Adv. Electron. Mater. 12/2016), Advanced Electronic Materials 2 (12) (2016), https://doi.org/10.1002/aelm.201670068.
[163] A. Lipatov, M. Alhabeb, M.R. Lukatskaya, A. Boson, Y. Gogotsi, A. Sinitskii, Effect of synthesis on quality, electronic properties and environmental stability of individual monolayer Ti_3C_2 MXene flakes, Adv. Electron. Mater. 2 (12) (2016), 1600255, https://doi.org/10.1002/aelm.201600255.
[164] Yang Sheng, Zhang Panpan, Wang Faxing, Gaetano Antonio, Martin Ricciardulli, Fluoride-free synthesis of two-dimensional titanium carbide (MXene) using A binary aqueous system, Angew. Chem. (2018).
[165] I.R. Shein, A.L. Ivanovskii, Graphene-like titanium carbides and nitrides Tin+1Cn, Tin+1Nn (n = 1, 2, and 3) from de-intercalated MAX phases: first-principles probing of their structural, electronic properties and relative stability, Comput. Mater. Sci. 65 (2012) 104–114.
[166] Y. Yang, S. Umrao, S. Lai, S. Lee, Large-area highly conductive transparent two-dimensional Ti2CTx film, J. Phys. Chem. Lett. (2017).
[167] Z. Lin, L. Cai, W. Lu, Y. Chai, Phase and Facet Control of Molybdenum Carbide Nanosheet Observed by in Situ TEM, Small 13 (2017).
[168] J. Jeon, Y. Park, S. Choi, J. Lee, S.S. Lim, B.H. Lee, Y.J. Song, J.H. Cho, Y.H. Jang, S. Lee, Epitaxial synthesis of molybdenum carbide and formation of a Mo2C/MoS2 hybrid structure via chemical conversion of molybdenum disulfide, ACS Nano (2018) acsnano.7b06417.
[169] P. Urbankowski, B. Anasori, K. Hantanasirisakul, L. Yang, L. Zhang, B. Haines, S. May, S. Billinge, Y. Gogotsi, 2D molybdenum and vanadium nitrides synthesized by ammoniation of 2D transition metal carbides (MXenes), Nanoscale (2017), 10.1039.C7NR06721F.
[170] S. Chen, R. Tao, C. Guo, W. Zhang, X. Liu, G. Yang, P. Guo, G. Sun, J. Liang, S.-Y. Lu, A new trick for an old technology: ion exchange syntheses of advanced energy storage and conversion nanomaterials, Energy Storage Mater. 41 (2021) 758–790, https://doi.org/10.1016/j.ensm.2021.06.043.
[171] Y. Gogotsi, Transition metal carbides go 2D, Nat. Mater. 14 (11) (2015) 1079–1080.
[172] M. Driess, C. Walter, P.W. Menezes, M. Lerch, P. Connor, A molecular approach to manganese nitride acting as a high performance electrocatalyst in the oxygen evolution reaction, Angew. Chem. Int. Ed. 57 (3) (2017).
[173] L. Verger, C. Xu, V. Natu, H.M. Cheng, W. Ren, M.W. Barsoum, Overview of the synthesis of MXenes and other ultrathin 2D transition metal carbides and nitrides, Curr. Opin. Solid State Mater. Sci. (2019).
[174] S. Kajiyama, L. Szabova, K. Sodeyama, H. Iinuma, A. Yama da sodium-ion intercalation mechanism in MXene nanosheets, ACS Nano 10 (3) (2016) 3334.
[175] M. Naguib, R.R. Unocic, B.L. Armstrong, J. Nanda, Large-scale delamination of multi-layers transition metal carbides and carbonitrides "MXenes", Dalton Trans. (2015).
[176] J. Luo, W. Zhang, H. Yuan, C. Jin, X. Tao, Pillared structure design of MXene with ultra-large interlayer spacing for high performance lithium-ion capacitors, ACS Nano 11 (3) (2016) 2459.
[177] O. Mashtalir, M. Naguib, V.N. Mochalin, Y. Dall'Agnese, H. Min, M.W. Barsoum, Y. Gogotsi, Intercalation and delamination of layered carbides and carbonitrides, Nat. Commun. 4 (2013), 1716.
[178] J. Pang, R.G. Mendes, A. Bachmatiuk, L. Zhao, H.Q. Ta, T. Gemming, H. Liu, Z. Liu, M.H. Rummeli, Applications of 2D MXenes in energy conversion and storage systems, Chem. Soc. Rev. (2018).
[179] K. Malesk, V.N. Mochalin, Y. Gogots, Dispersions of two-dimensional titanium carbide MXene in organic solvents, Chem. Mater. (2017).
[180] Y. Vasseghian, E.-N. Dragoi, F. Almomani, V.T. Le, A comprehensive review on MXenes as new nanomaterials for degradation of hazardous pollutants: deployment as heterogeneous sonocatalysis, Chemosphere 287 (2022), 132387, https://doi.org/10.1016/j.chemosphere.2021.132387.
[181] Z. Ling, C.E. Ren, M.Q. Zhao, J. Yang, J.M. Giammarco, J. Qiu, M.W. Barsoum, Y. Gogotsi, Flexible and conductive MXene films and nanocomposites with high capacitance, Proc. Natl. Acad. Sci. USA 111 (47) (2014) 16676–16681.
[182] Y. Cai, J. Shen, G. Ge, Y. Zhang, W. Jin, W. Huang, J. Shao, J. Yang, X. Dong, Stretchable $Ti_3C_2T_x$ MXene/carbon nanotube composite based strain sensor with ultrahigh sensitivity and tunable sensing range, ACS Nano (2017) acsnano.7b06251.
[183] A.N. Enyashin, A.L. Ivanovskii, Two-dimensional titanium carbonitrides and their hydroxylated derivatives: structural, electronic properties and stability of MXenes Ti3C2xNx(OH)2 from DFTB calculations, J. Solid State Chem. 207 (2013) 42–48.
[184] C.J. Zhang, S. Pinilla, N. Mcevoy, C.P. Cullen, B. Anasori, E. Long, S.H. Park, A. Seralascaso, A. Shmeliov, D. Krishnan, Oxidation stability of colloidal two-dimensional titanium carbides (MXenes), Chem. Mater. 29 (11) (2017) 4848–4856.
[185] J. Li, Y. Du, C. Huo, S. Wang, C. Chong, Thermal stability of two-dimensional Ti2C nanosheets, Ceram. Int. 41 (2) (2015) 2631–2635.
[186] K. Wang, Y. Zhou, W. Xu, D. Huang, Z. Wang, M. Hong, Fabrication and thermal stability of two-dimensional carbide Ti3C2 nanosheets, Ceram. Int. (2016) 8419–8424.

[187] Y. Wu, P. Nie, J. Wang, H. Dou, X. Zhan, Few-layer MXenes delaminated via high-energy mechanical milling for enhanced sodium-ion batteries performance, ACS Appl. Mater. Interfaces (2017).
[188] X. Wu, Z. Wang, M. Yu, L. Xiu, J. Qiu, Stabilizing the MXenes by carbon nanoplating for developing hierarchical nanohybrids with efficient lithium storage and hydrogen evolution capability, Adv. Mater. 29 (24) (2017), 1607017.
[189] I.R. Shein, A.L. Ivanovskii, Graphene-like nanocarbides and nanonitrides of d metals (MXenes): synthesis, properties and simulation, Iet Micro Nano Lett. 8 (2) (2013) 59–62.
[190] Y. Lee, Y. Hwang, S.B. Cho, Y.C. Chung, Achieving a direct band gap in oxygen functionalized-monolayer scandium carbide by applying an electric field, Phys. Chem. Chem. Phys. 16 (47) (2014) 26273–26278.
[191] Y. Lee, S.B. Cho, Y.C. Chung, Tunable indirect to direct band gap transition of monolayer Sc2CO2 by the strain effect, ACS Appl. Mater. Interfaces 6 (16) (2014).
[192] S. Sarikurt, D. Akr, M. Keeli, C. Sevik, The influence of surface functionalization on thermal transport and thermoelectric properties of MXene monolayers, Nanoscale 10 (2018).
[193] G.R. Berdiyorov, Effect of Surface Functionalization on the Electronic Transport Properties of Ti3C2 MXene, EPL (Europhysics Letters) (2015).
[194] M. Khazaei, A. Ranjbar, M. Ghorbani-Asl, M. Arai, T. Sasaki, Y. Liang, S. Yunoki, Nearly free electron states in MXenes, Phys. Rev. B 93 (20) (2016), 205125.
[195] H. Fashandi, V. Ivády, P. Eklund, A.L. Spetz, M.I. Katsnelson, I.A. Abrikosov, Dirac points with giant spin-orbit splitting in the electronic structure of two-dimensional transition-metal carbides, Physics 92 (2015) 455–457.
[196] X.H. Zha, Z. Jie, L. Kan, J. Lang, S. Du, Controllable magnitude and anisotropy of the electrical conductivity of Hf3C2O2 MXene, J. Phys. Condens. Matter 29 (16) (2017), 165701.
[197] Y. Zhang, F. Li, Robust Half-Metallic Ferromagnetism in Cr3C2 MXene, J. Magnet. Magnet. Mater. 433 (2017) 222–226.
[198] C.J. Zhang, B. Anasori, A. Seral-Ascaso, Park S.-H., N. McEvoy, Transparent, flexible, and conductive 2D titanium carbide (MXene) films with high volumetric capacitance, Adv. Mater. (Deerfield Beach, Fla.) (2017).
[199] L. Hong, R.F. Klie, S. Oeguet, First-principles study of size- and edge-dependent properties of MXene nanoribbons, Phys. Rev. B 93 (11) (2016) 115412.1–115412.12.
[200] E. Balci, Ü.Ö. Akkuş, S. Berber, Doped Sc2C(OH)(2) MXene: new type s-pd band inversion topological insulator, J. Phys. Condens. Matter 30 (15) (2018).
[201] Z.M. Wong, T.L. Tan, S.-W. Yang, G. Xu, Enhancing the photocatalytic performance of MXenes via stoichiometry engineering of their electronic and optical properties, ACS Appl. Mater. Interfaces (2018).
[202] B. Erdem, A.ü. zden, B. Savas, Controlling topological electronic structure of multifunctional MXene layer, Appl. Phys. Lett. 113 (8) (2018), 083107.
[203] E. Balci, Ü.Ö. Akkuş, S. Berber, Band gap modification doped MXene: Sc2CF2, J. Mater. Chem. C 5 (2017) 5956–5961, 10.1039.C7TC01765K.
[204] H. Lashgari, M.R. Abolhassani, A. Boochani, S.M. Elahi, J. Khodadadi, Electronic and optical properties of 2D graphene-like compounds titanium carbides and nitrides: DFT calculations, Solid State Commun. 195 (2014) 61–69.
[205] K. Chaudhuri, Z. Wang, M. Alhabeb, K. Maleski, Y. Gogotsi, V. Shalaev, A. Boltasseva, Optical properties of MXenes, in: B. Anasori, Y. Gogotsi (Eds.), 2D Metal Carbides and Nitrides (MXenes): Structure, Properties and Applications, Springer International Publishing, Cham, 2019, pp. 327–346, https://doi.org/10.1007/978-3-030-19026-2_17.
[206] G.R. Berdiyorov, Optical properties of functionalized Ti3C2T2 (T = F, O, OH) MXene: first-principles calculations, AIP Adv. 6 (5) (2016) 1079.
[207] J.L. Hart, K. Hantanasirisakul, A.C. Lang, B. Anasori, D. Pinto, Y. Pivak, J.T. Van Omme, S.J. May, Y. Gogotsi, M.L. Taheri, Control of MXenes' electronic properties through termination and intercalation, Nat. Commun. 10 (1) (2019).
[208] H. Zhang, G. Yang, X. Zuo, H. Tang, Q. Yang, G. Li, Computational studies on the structural, electronic and optical properties of graphene-like MXenes (M2CT2, M = Ti, Zr, Hf; T = O, F, OH) and their potential applications as visible-light driven photocatalysts, J. Mater. Chem. A 4 (2016) 12913–12920.
[209] J. Guo, Y. Sun, B. Liu, Q. Zhang, Q. Peng, Two-dimensional scandium-based carbides (MXene): band gap modulation and optical properties, J. Alloys Compd. (2017).
[210] A. Mostafaei, E. Faizabadi, E.H. Semiromi, Theoretical studies and tuning the electronic and optical properties of Zr2CO2 monolayer using biaxial strain effect: modified Becke–Johnson calculation, Phys. E Low-Dimens. Syst. Nanostruct. 114 (5) (2019), 113559.
[211] D.Y. Qiu, F.H. Da Jornada, S.G. Louie, Optical spectrum of MoS2: many-body effects and diversity of exciton states, Phys. Rev. Lett. 111 (21) (2013) 1352–1355.
[212] S. Albrecht, L. Reining, R.D. Sole, G. Onida, Ab initio calculation of excitonic effects in the optical spectra of semiconductors, Phys. Rev. Lett. (1998).
[213] L. Zhou, Y. Zhang, Z. Zhuo, A.J. Neukirch, S. Tretiak, Interlayer-decoupled Sc-based mxene with high carrier mobility and strong light-harvesting ability, J. Phys. Chem. Lett. 9 (23) (2018).
[214] S.A. Khan, G. Rehman, I. Ahmad, M. Maqbool, B. Amin, Intriguing electronic and optical properties of M2CX2 (M=Mo, W; X=O, F) MXenes and their van der Waals heterostructures, Chem. Phys. Lett. 731 (2019), 136614.
[215] M. Khazaei, A. Mishra, V.N. Sathiyamoorthy, A.K. Singh, S. Yunoki, Recent advances in MXenes: from fundamentals to applications, Curr. Opin. Solid State Mater. Sci. 23 (3) (2019) 164–178.
[216] Z. Zhang, X. Liu, Y. Jin, H. Yang, W. Guo, Tunable electronic and magnetic properties of two-dimensional materials and their one-dimensional derivatives, Wiley Interdiscip. Rev. Comput. Mol. Sci. 6 (4) (2016) n/a-n/a.
[217] A.S. Ingason, M. Dahlqvist, J. Rosen, Magnetic MAX phases from theory and experiments; a review, J. Phys. Condens. Matter Inst. Phys. J. 28 (43) (2016), 433003.
[218] G. Gao, G. Ding, L. Jie, K.L. Yao, M. Qian, Monolayer MXenes: promising half-metals and spin gapless semiconductors, Nanoscale 8 (16) (2016).
[219] L. Hu, X. Wu, J. Yang, Mn2C monolayer: a 2D antiferromagnetic metal with high Néel temperature and large spin–orbit coupling, Nanoscale (2016) 12939–12945.
[220] J. He, P. Lyu, P. Nachtigall, New two-dimensional Mn-based MXenes with room-temperature ferromagnetism and half-metallicity, J. Mater. Chem. C (2016) 11143–11149.
[221] M. Alhabeb, K. Maleski, B. Anasori, P. Lelyukh, L. Clark, S. Sin, Y. Gogotsi, Guidelines for Synthesis and Processing of 2D Titanium Carbide ($Ti_3C_2T_x$ MXene), Chem. Mater. (2017) acs.chemmater.7b02847.
[222] M. Gharavi-Alkhansari, A. Tabatabai, Intra Prediction with Adaptive Interpolation Filtering for Image Compression, US, 2010.
[223] J. He, P. Lyu, L.Z. Sun, A.M. Garcia, P. Nachtigall, High temperature spin-polarized semiconductivity with zero magnetization in two-dimensional Janus MXenes, J. Mater. Chem. C 4 (2016) 6500–6509.
[224] C. Si, J. Zhou, Z. Sun, Half-metallic ferromagnetism and surface functionalization-induced metal-insulator transition in graphene-like two-dimensional Cr_2C crystals, ACS Appl. Mater. Interfaces 7 (31) (2015) 17510–17515, https://doi.org/10.1021/acsami.5b05401.
[225] Wang Guo, Theoretical prediction of the intrinsic half-metallicity in surface-oxygen-passivated Cr_2N MXene, J. Phys. Chem. C (2016).
[226] J. Yang, X. Luo, X. Zhou, S. Zhang, J. Liu, Y. Xie, L. Lv, L. Chen, Tuning Magnetic Properties of Cr2M2C3T2 (M=Ti and V) Using Extensile Strain, Comput. Mater. Sci. (2017).
[227] Bipolar magnetic semiconductors among intermediate states during the conversion from Sc2C(OH)2 to Sc2CO2 MXene, Nanoscale 10 (2018).
[228] N.C. Frey, K. Hemant, A. Babak, G. Yury, V.B. Shenoy, Tuning noncollinear spin structure and anisotropy in ferromagnetic nitride MXenes, ACS Nano (2018) acsnano.8b03472-.
[229] J. Yang, X. Zhou, X. Luo, S. Zhang, L. Chen, Tunable electronic and magnetic properties of Cr2M′C2T2(M′=Ti or V; T=O, OH or F), Appl. Phys. Lett. 109 (20) (2016) 1695.
[230] L. Dong, H. Kumar, B. Anasori, Y. Gogotsi, V.B. Shenoy, Rational design of two-dimensional metallic and semiconducting spintronic materials based on ordered double-transition-metal MXenes, J. Phys. Chem. Lett. 8 (2) (2016).
[231] Y. Yue, Fe2C monolayer: an intrinsic ferromagnetic MXene, J. Magn. Magn Mater. 434 (Jul) (2017) 164–168.
[232] N.C. Frey, A. Bandyopadhyay, H. Kumar, B. Anasori, Y. Gogotsi, V.B. Shenoy, Surface-engineered MXenes: electric field control of magnetism and enhanced magnetic anisotropy, ACS Nano 13 (3) (2019) 2831–2839, https://doi.org/10.1021/acsnano.8b09201.
[233] S. Chen, J. You, W. Shi, Z. Jian, Z. Sun, Quantum spin Hall phase in Mo2M2C3O2 (M = Ti, Zr, Hf) MXenes, J. Mater. Chem. C 4 (2016).
[234] W. Tian, W. Yu, S. Jing, Y. Wang, The property, preparation and application of topological insulators: a review, Materials 10 (7) (2017) 814.
[235] Y.V. Toporov, A.A. Kordyuk, Mechanisms of scattering of surface electrons in topological insulators, Low Temp. Phys. 45 (1) (2019) 118–122.
[236] H. Weng, A. Ranjbar, Y. Liang, Z. Song, M. Khazaei, S. Yunoki, M. Arai, Y. Kawazoe, F. Zhong, D. Xi, Large-gap two-dimensional topological insulator in oxygen functionalized MXene, Phys. Rev. B 92 (7) (2015), 75436-75436.
[237] C. Si, K.H. Jin, J. Zhou, Z. Sun, F. Liu, Large-gap quantum spin Hall state in MXenes: d-band topological order in a triangular lattice, Nano Lett. (2016).
[238] Y. Liang, M. Khazaei, A. Ranjbar, M. Arai, S. Yunoki, Y. Kawazoe, H. Weng, Z. Fang, Theoretical prediction of two-dimensional functionalized MXene nitrides as topological insulators, Phys. Rev. B 96 (19) (2017), 195414.
[239] S. Sen, B. Kawahara, G. Chaudhuri, Maintenance of higher H2O2 levels, and its mechanism of action to induce growth in breast cancer cells: important roles of bioactive catalase and PP2A, Free Radic. Biol. Med. 53 (8) (2012) 1541–1551.
[240] H.A. Tahini, X. Tan, S.C. Smith, The origin of low workfunctions in OH terminated MXenes, Nanoscale 9 (21) (2017) 7016–7020, https://doi.org/10.1039/C7NR01601H.
[241] M. Khazaei, M. Arai, T. Sasaki, A. Ranjbar, Y. Liang, S. Yunoki, OH-terminated two-dimensional transition metal carbides and nitrides as ultralow work function materials, Phys. Rev. B 92 (7) (2015), 075411, https://doi.org/10.1103/PhysRevB.92.075411.
[242] M. Khazaei, M. Arai, T. Sasaki, A. Ranjbar, Y. Liang, S. Yunoki, OH-terminated two-dimensional transition metal carbides and nitrides as ultralow work function materials, Phys. Rev. B. Condens. Matter Mater. Phys. (2015).

[243] T. Schultz, N.C. Frey, K. Hantanasirisakul, S. Park, N. Koch, Surface termination dependent work function and electronic properties of $Ti_3C_2T_x$ MXene, Chem. Mater. 31 (17) (2019).
[244] Z. Wang, H. Kim, H.N. Alshareef, Oxide thin-film electronics using all-MXene electrical contacts, Adv Mater 30 (2018), 1706656.
[245] Z. Kang, Y. Ma, X. Tan, M. Zhu, Y. Gao, MXene–silicon van der Waals heterostructures for high-speed self-driven photodetectors, Adv. Electron. Mater. 3 (9) (2017).
[246] Y. Liu, X. Hai, W.A. Goddard III, Schottky-Barrier-Free contacts with two-dimensional semiconductors by surface-engineered MXenes, J. Am. Chem. Soc. 138 (49) (2016).
[247] A.K. Geim, I.V. Grigorieva, Van der Waals heterostructures, Nature 499 (7459) (2013) 419–425, https://doi.org/10.1038/nature12385.
[248] X. Li, Y. Dai, Y. Ma, Q. Liu, B. Huang, Intriguing electronic properties of two-dimensional MoS2/TM2CO2 (TM = Ti, Zr, or Hf) hetero-bilayers: type-II semiconductors with tunable band gaps, Nanotechnology 26 (13) (2015), 135703-135703.
[249] P. Zhao, H. Jin, X. Lv, B. Huang, Y. Ma, Y. Dai, Modified MXene: promising electrode materials for constructing ohmic contacts with MoS2 for electronic device applications, Phys. Chem. Chem. Phys. (2018).
[250] P. Paul, P. Chakraborty, T. Das, D. Nafday, T. Saha-Dasgupta, Properties at the Interface of Graphene and Ti2C MXene, 2017.
[251] L. Gan, D. Huang, U. Schwingenschlögl, Y.J. Zhao, First-principles analysis of MoS2/Ti2C and MoS2/Ti2CY2 (Y=F and OH) all-2D semiconductor/metal contacts, Phys. Rev. B 87 (24) (2013) 112–115.
[252] Z. Ma, Z. Hu, X. Zhao, Q. Tang, D. Wu, Tunable band structures of heterostructured bilayers with transition-metal dichalcogenide and MXene monolayer, J. Phys. Chem. C (2014).
[253] Y. Lee, Y. Hwang, Y.C. Chung, Achieving type I, II, and III heterojunctions using functionalized MXene, ACS Appl. Mater. Interfaces 7 (13) (2015) 7163–7169, https://doi.org/10.1021/acsami.5b00063.
[254] A.N. Gandi, H.N. Alshareef, U. Schwingenschlögl, Thermal response in van der Waals heterostructures, J. Phys. Condens. Matter 29 (3) (2016), 035504.
[255] R. Li, W. Sun, C. Zhan, P.R.C. Kent, D.E. Jiang, Interfacial and electronic properties of heterostructures of MXene and graphene, Phys. Rev. B Condens. Matter 99 (8) (2019), 085429, 1-085429.8.
[256] Y. Aierken, C. Sevik, O. Gulseren, F.M. Peeters, D. Cakir, MXenes/graphene heterostructures for Li battery applications: a first principles study, J. Mater. Chem. A 6 (5) (2018) 2337–2345.
[257] Q. Tang, Z. Zhen, P. Shen, Are MXenes promising anode materials for Li ion batteries? Computational studies on electronic properties and Li storage capability of Ti3C2 and Ti3C2X2 (X = F, OH) monolayer, J. Am. Chem. Soc. 134 (40) (2012) 16909–16916.
[258] H. Zhao, C. Zhang, S. Li, W. Ji, P. Wang, First-principles design of silicene/Sc2CF2 heterojunction as a promising candidate for field effect transistor, J. Appl. Phys. 117 (8) (2015), 236804.
[259] Xu Chuan, Wang Libin, Liu Zhibo, Chen Long, Guo Jingkun, Large-area high-quality 2D ultrathin Mo2C superconducting crystals, Nat. Mater. (2015).
[260] Synthesis of two-dimensional $Nb_{1.33}C$ (MXene) with randomly distributed vacancies by etching of the quaternary solid solution $(Nb_{2/3}Sc_{1/3})_2AlC$ MAX phase, ACS Appl. Nano Mater. 1 (6) (2018) 2455–2460.
[261] A. Mishra, P. Srivastava, A. Carreras, I. Tanaka, H. Mizuseki, K.R. Lee, A.K. Singh, Atomistic origin of phase stability in oxygen functionalized MXene: a comparative study, J. Phys. Chem. C (2017) acs.jpcc.7b06162.
[262] L. Zhang, W. Su, Y. Huang, H. Li, L. Fu, K. Song, X. Huang, J. Yu, C.T. Lin, In situ high-pressure X-ray diffraction and Raman spectroscopy study of Ti3C2Tx MXene, Nanoscale Res. Lett. 13 (1) (2018).
[263] C. Xu, L. Wang, Z. Liu, L. Chen, J. Guo, N. Kang, X.-L. Ma, H.-M. Cheng, W. Ren, Large-area high-quality 2D ultrathin Mo_2C superconducting crystals, Nat. Mater. 14 (11) (2015) 1135–1141, https://doi.org/10.1038/nmat4374.
[264] V. Natu, M. Sokol, L. Verger, M.W. Barsoum, Effect of edge charges on stability and aggregation of Ti3C2Tz MXene colloidal suspensions, J. Phys. Chem. C (2018).
[265] L. Xiu, Z. Wang, M. Yu, X. Wu, J. Qiu, Aggregation-resistant 3D MXene-based architecture as efficient bifunctional electrocatalyst for overall water splitting, ACS Nano (2018) acsnano.8b02849-.
[266] J. Liu, H.B. Zhang, R. Sun, Y. Liu, Z. Liu, A. Zhou, Z.Z. Yu, Hydrophobic, flexible, and lightweight MXene foams for high-performance electromagnetic-interference shielding, Adv. Mater. 29 (38) (2017), 1702367.
[267] R. Bian, G. He, W. Zhi, S. Xiang, T. Wang, D. Cai, Ultralight MXene-based aerogels with high electromagnetic interference shielding performance, J. Mater. Chem. C 7 (3) (2019) 474–478, https://doi.org/10.1039/C8TC04795B.
[268] X. Yang, N. Gao, S. Zhou, J. Zhao, MXene nanoribbons as electrocatalysts for the hydrogen evolution reaction with fast kinetics, Phys. Chem. Chem. Phys. (2018).
[269] W. Yuan, L. Cheng, Y. An, H. Wu, N. Yao, X. Fan, X. Guo, MXene nanofibers as highly active catalysts for hydrogen evolution reaction, ACS Sustain. Chem. Eng. (2018) acssuschemeng.8b01348-.
[270] P. Lian, Y. Dong, Z.-S. Wu, S. Zheng, X. Wang, W. Sen, C. Sun, J. Qin, X. Shi, X. Bao, Alkalized Ti_3C_2 MXene nanoribbons with expanded interlayer spacing for high-capacity sodium and potassium ion batteries, Nano Energy 40 (2017) 1–8, https://doi.org/10.1016/j.nanoen.2017.08.002.
[271] D. Huang, Y. Xie, D. Lu, Z. Wang, H. Zhang, Demonstration of a white laser with V2C MXene-based quantum dots, Adv. Mater. 31 (24) (2019), 1901117.
[272] I. Wiesel, R. Popovitz-Biro, R. Tenne, Encapsulation of Mo_2C in MoS_2 inorganic fullerene-like nanoparticles and nanotubes, Nanoscale 5 (4) (2013) 1499–1502, https://doi.org/10.1039/C2NR33828A.
[273] Z. Zeng, Y. Yan, J. Chen, P. Zan, P. Chen, Boosting the photocatalytic ability of Cu2O nanowires for CO2 conversion by MXene quantum dots, Adv. Funct. Mater. 29 (2) (2018), 1806500.
[274] J. Ran, G. Gao, F.T. Li, T.Y. Ma, A. Du, S.Z. Qiao, MXene co-catalyst on metal sulfide photo-absorbers for enhanced visible-light photocatalytic hydrogen production, Nat. Commun. 8 (2017), 13907.
[275] Y. Qian, H. Wei, J. Dong, Y. Du, X. Fang, W. Zheng, Y. Sun, Z. Jiang, Fabrication of urchin-like ZnO-MXene nanocomposites for high-performance electromagnetic absorption, Ceram. Int. 43 (14) (2017) 10757–10762.
[276] T. Hu, J. Wang, H. Zhang, Z. Li, M. Hu, X. Wang, Vibrational properties of Ti3C2 and Ti3C2T2 (T = O, F, OH) monosheets by first-principles calculations: a comparative study, Phys. Chem. Chem. Phys. 17 (15) (2015) 9997–10003.
[277] K.J. Harris, M. Bugnet, M. Naguib, M.W. Ba Rsoum, G.R. Goward, Direct measurement of surface termination groups and their connectivity in the 2D MXene V2CTx using NMR spectroscopy, J. Phys. Chem. C 119 (24) (2015) 13700–13712.
[278] J. Yang, A. Wang, S. Zhang, H. Wu, C. Liang, Stability and electronic properties of sulfur terminated two-dimensional early transition metal carbides and nitrides (MXene), Comput. Mater. Sci. 153 (2018) 303–308.
[279] M. Magnuson, J. Halim, L.Å. Näslund, Chemical bonding in carbide MXene nanosheets, J. Electron. Spectrosc. Relat. Phenom. (2017). S0368204816301608.
[280] X. Wang, X. Shen, Y. Gao, Z. Wang, R. Yu, L. Chen, Atomic-scale recognition of surface structure and intercalation mechanism of Ti3C2X, J. Am. Chem. Soc. 137 (7) (2015), 150206072156001.
[281] M.A. Hope, A.C. Forse, K.J. Griffith, M.R. Lukatskaya, M. Ghidiu, Y. Gogotsi, C.P. Grey, NMR reveals the surface functionalisation of Ti_3C_2 MXene, Phys. Chem. Chem. Phys. 18 (7) (2016) 5099–5102, https://doi.org/10.1039/C6CP00330C.
[282] J. Halim, K.M. Cook, M. Naguib, P. Eklund, M.W. Barsoum, X-ray photoelectron spectroscopy of select multi-layered transition metal carbides (MXenes), Appl. Surf. Sci. 362 (2016).
[283] H.W. Wang, M. Naguib, K. Page, D.J. Wesolowski, Y. Gogotsi, Resolving the structure of $Ti_3C_2T_x$ MXenes through multilevel structural modeling of the atomic pair distribution function, Chem. Mater. 28 (1) (2015).
[284] D. Magne, V. Mauchamp, S. Célérier, P. Chartier, T. Cabioc'h, Site-projected electronic structure of two-dimensional Ti3C2MXene: the role of the surface functionalization groups, Phys. Chem. Chem. Phys. 18 (45) (2016).
[285] Roghayyeh Lotfi, Michael Naguib, E. Dundar Yilmaz, Jagjit Nanda, V. Duin, A.C.T. van Duin, A comparative study on the oxidation of two-dimensional Ti3C2 MXene structures in different environments, J. Mater. Chem. A 6 (2018) 12733–12743.
[286] S. Célérier, S. Hurand, C. Garnero, S. Morisset, M. Benchakar, A. Habrioux, P. Chartier, V. Mauchamp, N. Findling, B. Lanson, Hydration of $Ti_3C_2T_X$ MXene: an interstratification process with major implications on physical properties, Chem. Mater. (2018).
[287] L.H. Karlsson, J. Birch, J. Halim, M.W. Barsoum, P. Persson, Atomically resolved structural and chemical investigation of single MXene sheets, Nano Lett. 15 (8) (2015).
[288] I. Persson, L.N.? Slund, J. Halim, M.W. Barsoum, V. Darakchieva, J. Palisaitis, J. Rosen, P. Persson, On the organization and thermal behavior of functional groups on Ti_3C_2 MXene surfaces in vacuum, 2D Mater. 5 (2018), 015002.
[289] O. Kaipoldayev, Y. Mukhametkarimov, R. Nemkaeva, G. Baigarinova, M. Aitzhanov, A. Muradov, N. Guseinov, Studying of 2D titanium carbide structure by raman spectroscopy after heat treatment in argon and hydrogen atmospheres, Eurasian Chem.-Technol. J. 19 (2017) 197–200.
[290] In situ environmental transmission electron microscopy study of oxidation of two-dimensional Ti3C2 and formation of carbon-supported TiO2, J. Mater. Chem. 2 (2014).
[291] High photoluminescence quantum yield of 18.7% by using nitrogen-doped Ti3C2 MXene quantum dots, J. Mater. Chem. C 6 (2018).
[292] A. Sarycheva, T. Makaryan, K. Maleski, E. Satheeshkumar, A.H. Melikyan, H. Minassian, M. Yoshimura, Y. Gogotsi, Two-dimensional titanium carbide (MXene) as surface-enhanced Raman scattering substrate, J. Phys. Chem. C (2017) acs.jpcc.7b08180.
[293] Tetsuka Hiroyuki, Asahi Ryoji, Nagoya Akihiro, Okamoto Kazuo, Tajima Ichiro, Optically tunable amino-functionalized graphene quantum dots, Adv. Mater. (2012).
[294] Preparation of $Ti_3C_2T_x$ MXene ϧ erived quantum dots with white/blue ⊥ mitting photoluminescence and electrochemiluminescence, Adv. Opt. Mater. 6 (24) (2018).
[295] Z. Wang, X. Meng, K. Chaudhuri, M. Alhabeb, Y.L. Kim, V.M. Shalaev, Y. Gogotsi, A. Boltasseva, Active metamaterials based on monolayer titanium carbide MXene for random lasing, in: 2017 Conference on Lasers and Electro-Optics (CLEO), 2017.
[296] Q. Xu, L. Ding, Y. Wen, W. Yang, H. Zhou, X. Chen, J. Street, A. Zhou, W.-J. Ong, N. Li, High photoluminescence quantum yield of 18.7% by using nitrogen-doped Ti_3C_2 MXene quantum dots, J. Mater. Chem. C 6 (24) (2018) 6360–6369, https://doi.org/10.1039/C8TC02156B.

[297] X. Chen, X. Sun, W. Xu, G. Pan, D. Zhou, J. Zhu, H. Wang, X. Bai, B. Dong, H. Song, Ratiometric photoluminescence sensing based on Ti3C2 MXene quantum dots as an intracellular pH sensor, Nanoscale (2017), 10.1039.C7NR06958H.
[298] Z. Wang, J.N. Xuan, Z. Zhao, Q. Li, F. Geng, A versatile cutting method for producing fluorescent ultrasmall MXene sheets, ACS Nano (2017) acsnano.7b06476.
[299] X. Jiang, S. Gross, H. Zhang, Z. Guo, M.J. Withford, A. Fuerbach, Bismuth telluride topological insulator nanosheet saturable absorbers for Q-switched mode-locked Tm:ZBLAN waveguide lasers, Annalen Der Physik 528 (7-8) (2016) 543–550.
[300] X. Jiang, S. Liu, W. Liang, S. Luo, Z. He, Y. Ge, H. Wang, R. Cao, F. Zhang, Q. Wen, Broadband nonlinear photonics in few-layer MXene $Ti_3C_2T_x$ (T = F, O, or OH), Laser Photon. Rev. 12 (2) (2018) 1700229.1–1700229.10.
[301] X. Jiang, S. Gross, M.J. Withford, H. Zhang, D.I. Yeom, F. Rotermund, A. Fuerbach, Low-dimensional nanomaterial saturable absorbers for ultrashort-pulsed waveguide lasers, Opt. Mater. Express 8 (10) (2018).
[302] Y.I. Jhon, J. Koo, B. Anasori, M. Seo, J.H. Lee, Y. Gogotsi, Y.M. Jhon, Metallic MXene saturable absorber for femtosecond mode-locked lasers, Adv. Mater. 29 (40) (2017) 1702496.1–1702496.8.
[303] X. Jiang, W. Li, T. Hai, R. Yue, Z. Chen, C. Lao, Y. Ge, G. Xie, Q. Wen, H. Zhang, Inkjet-printed MXene micro-scale devices for integrated broadband ultrafast photonics, npj. 2D. Mater. Appl. 3 (1) (2019) 34, https://doi.org/10.1038/s41699-019-0117-3.
[304] Xiao-Yue Feng, Bao-Yong Ding, Wei-Yuan Liang, Ning Zhang, Liu Ting-Yin, MXene $Ti_3C_2T_x$ absorber for a 1.06 mu m passively Q-switched ceramic laser, Laser Phys. Lett. (2018).
[305] C.B. Yao, E. Kponou, Y.D. Zhang, J.F. Wang, P. Yuan, Determination of the triplet state lifetime of C60/toluene solution and C60 thin films by pump-probe method, Opt Photon. J. (2011).
[306] L. Wu, Y. Dong, J. Zhao, D. Ma, W. Huang, Y. Zhang, Y. Wang, X. Jiang, Y. Xiang, J. Li, Kerr nonlinearity in 2D graphdiyne for passive photonic diodes, Adv. Mater. 31 (14) (2019) 1807981.1–1807981.10.
[307] L. Wu, X. Jiang, J. Zhao, W. Liang, H. Zhang, MXene-based nonlinear optical information converter for all-optical modulator and switcher, Laser Photon. Rev. 12 (12) (2018).
[308] Yongchang Dong, Sergii Chertopalov, Kathleen Maleski, Babak Anasori, Longyu Hu, Saturable absorption in 2D Ti_3C_2 MXene thin films for passive photonic diodes, Adv. Mater. (2018).
[309] E. Satheeshkumar, T. Makaryan, A. Melikyan, H. Minassian, Y. Gogotsi, M. Yoshimura, One-step solution processing of Ag, Au and Pd@MXene hybrids for SERS, For. Rep. 6 (2016), 32049.
[310] V. Mauchamp, M. Bugnet, E.P. Bellido, G.A. Botton, M.W. Barsoum, Enhanced and tunable surface plasmons in two-dimensional Ti_3C_2 stacks: electronic structure versus boundary effects, Phys. Rev. B 89 (23) (2014), 235428.
[311] J.K. El-Demellawi, S. Lopatin, J. Yin, O.F. Mohammed, H.N. Alshareef, Tunable multipolar surface plasmons in 2D $Ti_3C_2T_x$ MXene flakes, ACS Nano 12 (8) (2018).
[312] E. Kretschmann, Decay of non radiative surface plasmons into light on rough silver films. Comparison of experimental and theoretical results, Opt Commun. 6 (2) (1972) 185–187.
[313] L. Wu, Q. You, Y. Shan, S. Gan, Y.J. Xiang, Few-layer $Ti_3C_2T_x$ MXene: a promising surface plasmon resonance biosensing material to enhance the sensitivity, Sensors Actuators B Chem. 277 (2019) 210–215.
[314] Y. Xu, Y. Ang, L. Wu, L. Ang, High sensitivity surface plasmon resonance sensor based on two-dimensional MXene and transition metal dichalcogenide: a theoretical study, Nanomaterials 9 (2) (2019).
[315] Photonic spin Hall effect in robust phase gradient metasurfaces utilizing transition metal nitrides, ACS Photonics 6 (1) (2019) 99–106.
[316] K. Chaudhuri, M. Alhabeb, Z. Wang, V.M. Shalaev, Y. Gogotsi, A. Boltasseva, Highly broadband absorber using plasmonic titanium carbide (MXene), ACS Photonics (2018) acsphotonics.7b01439.
[317] R.R. Gattass, E. Mazur, Femtosecond laser micromachining in transparent materials, Nat. Photonics 2 (4) (2008) 219–225.
[318] H. Joseph, M.E. Ju, E. Per, R. Johanna, M.W. Barsoum, O. Thierry, Variable range hopping and thermally activated transport in molybdenum-based MXenes, Phys. Rev. B Condens. Matter 98 (10) (2018) 104202.1–104202.11.
[319] R. Li, L. Zhang, S. Le, W. Peng, MXene Ti3C2: an effective 2D light-to-heat conversion material, ACS Nano 11 (4) (2017).
[320] G.W. Ni, G. Li, S.V. Boriskina, H. Li, C. Gang, Steam generation under one sun enabled by a floating structure with thermal concentration, Nat. Energy (2016).
[321] Y. Liu, S. Yu, R. Feng, A. Bernard, Y. Liu, A bioinspired, reusable, paper-based system for high-performance large-scale evaporation, Adv. Mater. (2015).
[322] Chenyan Xing, Shiyou Chen, Xin Liang, Quan Liu, Mengmeng Qu, Two-dimensional MXene (Ti3C2)-integrated cellulose hydrogels: toward smart three-dimensional network nanoplatforms exhibiting light-induced swelling and bimodal photothermal/chemotherapy anticancer activity, ACS Appl. Mater. Interfaces (2018).
[323] W.-T. Cao, W. Feng, Y.-Y. Jiang, C. Ma, Z.-F. Zhou, M.-G. Ma, Y. Chen, F. Chen, Two-dimensional MXene-reinforced robust surface superhydrophobicity with self-cleaning and photothermal-actuating binary effects, Mater. Horiz. 6 (2019) 1057–1065.
[324] C. Wang, Y. Wang, X. Jiang, J. Xu, W. Huang, F. Zhang, J. Liu, F. Yang, Y. Song, Y. Ge, MXene Ti_3C_2T_x, A promising photothermal conversion material and application in all-optical modulation and all-optical information loading, Adv. Opt. Mater. 7 (12) (2019) 1900060.1–1900060.7.
[325] J. Wang, F. Ma, W. Liang, M. Sun, Electrical properties and applications of graphene, hexagonal boron nitride (h-BN), and graphene/h-BN heterostructures, Mater.Today. Phy. 2 (2017) 6–34, https://doi.org/10.1016/j.mtphys.2017.07.001.
[326] U. Krishnan, M. Kaur, K. Singh, M. Kumar, A. Kumar, A synoptic review of MoS_2: synthesis to applications, Superlatt. Microstruct 128 (2019) 274–297, https://doi.org/10.1016/j.spmi.2019.02.005.
[327] R. Mendoza, J. Oliva, K.P. Padmasree, A.I. Mtz-Enriquez, A. Hayat, V. Rodriguez-Gonzalez, A sustainable avocado-peel based electrode for efficient graphene supercapacitors: enhancement of capacitance by using Sr doped LaMnO3 perovskites, Ceram. Int. (2022), https://doi.org/10.1016/j.ceramint.2022.07.055.
[328] A. Hayat, M. Sohail, M.S. Hamdy, S.K.B. Mane, M.A. Amin, A. Zada, T.A. Taha, M.M. Rahman, A. Palamanit, D.I. Medina, J. Khan, W.I. Nawawi, Biomass lignin integrated polymeric carbon nitride for boosted photocatalytic hydrogen and oxygen evolution reactions, Mol. Catal. 518 (2022), 112064, https://doi.org/10.1016/j.mcat.2021.112064.
[329] V. Shukla, Review of electromagnetic interference shielding materials fabricated by iron ingredients, Nanoscale Adv. 1 (5) (2019) 1640–1671, https://doi.org/10.1039/C9NA00108E.
[330] V. Shukla, Observation of critical magnetic behavior in 2D carbon based composites, Nanoscale Adv. 2 (3) (2020) 962–990, https://doi.org/10.1039/C9NA00663J.
[331] A. Saboor, S.M. Khalid, R. Jan, A.N. Khan, T. Zia, M.U. Farooq, S. Afridi, M. Sadiq, M. Arif, PS/PANI/MoS_2 hybrid polymer composites with high dielectric behavior and electrical conductivity for EMI shielding effectiveness, Materials 12 (17) (2019) 2690.
[332] J. Prasad, A.K. Singh, K.K. Haldar, V. Gupta, K. Singh, Electromagnetic interference shielding effectiveness in 3D flower-like MoS_2-rGO/gadolinium-doped nanocomposites, J. Alloys Compd. 788 (2019) 861–872, https://doi.org/10.1016/j.jallcom.2019.02.246.
[333] J. Prasad, A.K. Singh, J. Shah, R.K. Kotnala, K. Singh, Synthesis of MoS_2 reduced graphene oxide/Fe_3O_4 nanocomposite for enhanced electromagnetic interference shielding effectiveness, Mater. Res. Express 5 (5) (2018), 055028, https://doi.org/10.1088/2053-1591/aac0c2.
[334] Y. Zhou, Z. Peng, Y. Chen, K. Luo, J. Zhang, S. Du, First-principles study of the electronic, optical and transport of few-layer semiconducting MXene, Comput. Mater. Sci. 168 (2019) 137–143, https://doi.org/10.1016/j.commatsci.2019.05.051.
[335] J. Zheng, R. He, Y. Wan, P. Zhao, P. Guo, Z. Jiang, Half-metal state of a Ti_2C monolayer by asymmetric surface decoration, Phys. Chem. Chem. Phys. 21 (6) (2019) 3318–3326, https://doi.org/10.1039/C8CP07157H.
[336] M. Kunitski, N. Eicke, P. Huber, J. Köhler, S. Zeller, J. Voigtsberger, N. Schlott, K. Henrichs, H. Sann, F. Trinter, L.P.H. Schmidt, A. Kalinin, M.S. Schöffler, T. Jahnke, M. Lein, R. Dörner, Double-slit photoelectron interference in strong-field ionization of the neon dimer, Nat. Commun. 10 (1) (2019) 1, https://doi.org/10.1038/s41467-018-07882-8.
[337] R. Han, X. Ma, Y. Xie, D. Teng, S. Zhang, Preparation of a new 2D MXene/PES composite membrane with excellent hydrophilicity and high flux, RSC Adv. 7 (89) (2017) 56204–56210, https://doi.org/10.1039/C7RA10318B.
[338] K. Huang, G. Liu, Y. Lou, Z. Dong, J. Shen, W. Jin, A graphene oxide membrane with highly selective molecular separation of aqueous organic solution, Angew. Chem. Int. Ed. 53 (27) (2014) 6929–6932, https://doi.org/10.1002/anie.201401061.
[339] S. Wei, Y. Xie, Y. Xing, L. Wang, H. Ye, X. Xiong, S. Wang, K. Han, Two-dimensional graphene Oxide/MXene composite lamellar membranes for efficient solvent permeation and molecular separation, J. Membr. Sci. 582 (2019) 414–422, https://doi.org/10.1016/j.memsci.2019.03.085.
[340] K. Rasool, R.P. Pandey, P.A. Rasheed, S. Buczek, Y. Gogotsi, K.A. Mahmoud, Water treatment and environmental remediation applications of two-dimensional metal carbides (MXenes), Mater. Today Off. 30 (2019) 80–102, https://doi.org/10.1016/j.mattod.2019.05.017.
[341] X. Li, L. Zhi, Graphene hybridization for energy storage applications, Chem. Soc. Rev. 47 (9) (2018) 3189–3216, https://doi.org/10.1039/C7CS00871F.
[342] H. Huang, J. Cui, G. Liu, R. Bi, L. Zhang, Carbon-coated $MoSe_2$/MXene hybrid nanosheets for superior potassium storage, ACS Nano 13 (3) (2019) 3448–3456, https://doi.org/10.1021/acsnano.8b09548.
[343] M. Han, Y. Mu, J. Yu, Nanoscopically and uniformly distributed SnO_2@TiO_2/C composite with highly mesoporous structure and bichemical bonds for enhanced lithium ion storage performances, Mater. Adv. 1 (3) (2020) 421–429, https://doi.org/10.1039/D0MA00140F.
[344] Y. Cao, X. Zhu, J. Jiang, C. Liu, J. Zhou, J. Ni, J. Zhang, J. Pang, Rotational design of charge carrier transport layers for optimal antimony trisulfide solar cells and its integration in tandem devices, Sol. Energy Mater. Sol. Cells 206 (2020), 110279, https://doi.org/10.1016/j.solmat.2019.110279.
[345] S. Cao, B. Shen, T. Tong, J. Fu, J. Yu, 2D/2D heterojunction of ultrathin MXene/Bi2WO6 nanosheets for improved photocatalytic CO2 reduction, Adv. Funct. Mater. (2018), 1800136.
[346] K. Xiong, P. Wang, G. Yang, Z. Liu, H. Zhang, S. Jin, X. Xu, Functional group effects on the photoelectronic properties of MXene (Sc2CT2, T = O, F, OH) and their possible photocatalytic activities, For. Rep. 7 (1) (2017), 15095.

[347] A Ti-anchored Ti2CO2 monolayer (MXene) as a single-atom catalyst for CO oxidation, J. Mater. Chem. 4 (2016).
[348] C. Cheng, X. Zhang, Z. Yang, Z. Zhou, Cu3-Cluster-Doped monolayer Mo2CO2 (MXene) as an electron reservoir for catalyzing a CO oxidation reaction, ACS Appl. Mater. Interfaces 10 (2018) acsami.8b12318-.
[349] Y. Luo, G.F. Chen, L. Ding, X. Chen, L.X. Ding, H. Wang, Efficient electrocatalytic n2 fixation with MXene under ambient conditions, Joule (2018).
[350] L.M. Azofra, N. Li, D. Macfarlane, C. Sun, Promising prospects for 2D d2−d4 M3C2 transition metal carbides (MXenes) in N2 capture and conversion into ammonia, Energy Environ. Sci. (2016), 10.1039.C6EE01800A.
[351] Y.M. Tian, L.C. Jian, M. Jaronie, Z.Q. Shi, Interacting carbon nitride and titanium carbide nanosheets for high-performance oxygen evolution, Angew. Chem. (2015).
[352] L. Zhao, B. Dong, S. Li, L. Zhou, L. Lai, Z. Wang, S. Zhao, Interdiffusion reaction-assisted hybridization of two-dimensional metal-organic frameworks and Ti3C2Tx nanosheets for electrocatalytic oxygen evolution, ACS Nano 11 (6) (2017) 5800−5807.
[353] Y. Zhang, H. Jiang, Y. Lin, H. Liu, L. Song, In situ growth of cobalt nanoparticles encapsulated nitrogen-doped carbon nanotubes among Ti3C2Tx (MXene) matrix for oxygen reduction and evolution, Adv. Mater. Interfac. 5 (16) (2018), 1800392.
[354] C.Y. Liu, E.Y. Li, Termination effects of Pt/v -$Ti_{n+1}C_nT_2$ MXene surfaces for oxygen reduction reaction catalysis, ACS Appl. Mater. Interfaces 11 (1) (2018).
[355] X. Yu, T. Wang, W. Yin, Y. Zhang, Ti3C2 MXene nanoparticles modified metal oxide composites for enhanced photoelectrochemical water splitting, Int. J. Hydrogen Energy (2018).
[356] B. Cui, B. Hu, J. Liu, M. Wang, Y. Song, K. Tian, Z. Zhang, L. He, Solution-plasma-assisted bimetallic oxide alloy nanoparticles of Pt and Pd embedded within two-dimensional Ti3C2TX nanosheets as highly active electrocatalysts for overall water splitting, ACS Appl. Mater. Interfaces 10 (2018) 28.
[357] Z.W. Seh, K.D. Fredrickson, B.A. nasori, J. Kibsgaard, A.L. Strickler, M.R. Lukatskaya, Y. Gogotsi, T.F. Jaramillo, A. Vojvodic, Two-dimensional molybdenum carbide (MXene) as an efficient electrocatalyst for hydrogen evolution, ACS Energy Lett. (2016) 589−594.
[358] G. Gao, A.P.O" Mullane, A. Du, 2D MXenes: a new family of promising catalysts for the hydrogen evolution reaction, ACS Catal. (2017) acscatal.6b02754.
[359] M. Yu, H. Liang, R. Zhan, L. Xu, J. Niu, Sm-doped g-C3N4/Ti3C2 MXene heterojunction for visible-light photocatalytic degradation of ciprofloxacin, Chin. Chem. Lett. 32 (7) (2020).
[360] A. Bs, A. Ft, A. Zh, Y.A. Wei, A. Yz, A. Xd, W.B. Yue, A. Gz, Ti3C2 MXene-bridged Ag/Ag3PO4 hybrids toward enhanced visible-light-driven photocatalytic activity - ScienceDirect, Appl. Surf. Sci. 535 (2020).
[361] Y. Naciri, A. Hsini, A. Bouziani, R. Djellabi, Z. Ajmal, M. Laabd, J.A. Navío, A. Mills, C.L. Bianchi, H. Li, B. Bakiz, A. Albourine, Photocatalytic oxidation of pollutants in gas-phase via Ag3PO4-based semiconductor photocatalysts: recent progress, new trends, and future perspectives, Crit. Rev. Environ. Sci. Technol. (2021) 1−44, https://doi.org/10.1080/10643389.2021.1877977.
[362] Y. Naciri, A. Hsini, Z. Ajmal, J.A. Navío, B. Bakiz, A. Albourine, M. Ezahri, A. Benlhachemi, Recent progress on the enhancement of photocatalytic properties of $BiPO_4$ using π−conjugated materials, Adv. Colloid Interface Sci. 280 (2020), 102160, https://doi.org/10.1016/j.cis.2020.102160.
[363] Y. Naciri, A. Hsini, Z. Ajmal, A. Bouddouch, B. Bakiz, J.A. Navío, A. Albourine, J.C. Valmalette, M. Ezahri, A. Benlhachemi, Influence of Sr-doping on structural, optical and photocatalytic properties of synthesized $Ca_3(PO4)_2$, J. Colloid Interface Sci. 572 (2020) 269−280, https://doi.org/10.1016/j.jcis.2020.03.105.
[364] Y. Jiao, Y. Zheng, M. Jaroniec, S.Z. Qiao, Design of electrocatalysts for oxygen- and hydrogen-involving energy conversion reactions, Chem. Soc. Rev. 44 (2015) 2060−2086.
[365] J.K. Nørskov, T. Bligaard, A. Logadottir, J.R. Kitchin, J.G. Chen, S. Pandelov, U. Stimming, Trends in the exchange current for hydrogen evolution, J. Electrochem. Soc. 152 (3) (2005), 0-0.
[366] J. Ran, G. Gao, F.-T. Li, T.-Y. Ma, A. Du, S.-Z. Qiao, Ti_3C_2 MXene co-catalyst on metal sulfide photo-absorbers for enhanced visible-light photocatalytic hydrogen production, Nat. Commun. 8 (1) (2017), 13907, https://doi.org/10.1038/ncomms13907.
[367] Yanan Jiang, Tao Sun, Xi Xie, Wei Jiang, Jia Li, Oxygen-functionalized ultrathin Ti3C2Tx MXene for enhanced electrocatalytic hydrogen evolution, Chemsuschem 12 (2019) 1368−1373.
[368] X. Zang, W. Chen, X. Zou, J.N. Hohman, L. Yang, B. Li, M. Wei, C. Zhu, J. Liang, M. Sanghadasa, J. Gu, L. Lin, Self-assembly of large-area 2D polycrystalline transition metal carbides for hydrogen electrocatalysis, Adv. Mater. 30 (50) (2018), 1805188, https://doi.org/10.1002/adma.201805188.
[369] B.E. Conway, B.V. Tilak, Interfacial processes involving electrocatalytic evolution and oxidation of H2, and the role of chemisorbed H, Electrochim. Acta 47 (22−23) (2002) 3571−3594.
[370] J. Zhang, Y. Zhao, X. Guo, C. Chen, C.-L. Dong, R.-S. Liu, C.-P. Han, Y. Li, Y. Gogotsi, G. Wang, Single platinum atoms immobilized on an MXene as an efficient catalyst for the hydrogen evolution reaction, Nat Catal 1 (12) (2018) 985−992, https://doi.org/10.1038/s41929-018-0195-1.
[371] W. Yuan, L. Cheng, Y. An, S. Lv, H. Wu, X. Fan, Y. Zhang, X. Guo, J. Tang, Laminated hybrid junction of sulfur-doped TiO_2 and a carbon substrate derived from Ti_3C_2 MXenes: toward highly visible light-driven photocatalytic hydrogen evolution, Adv. Sci. 5 (6) (2018), 1700870, https://doi.org/10.1002/advs.201700870.
[372] Self-assembly of large-area 2D polycrystalline transition metal carbides for hydrogen electrocatalysis, Adv. Mater. (2018).
[373] T.Y. Ma, J.L. Cao, M. Jaroniec, S.Z. Qiao, Interacting carbon nitride and titanium carbide nanosheets for high-performance oxygen evolution, Angew. Chem. Int. Ed. 55 (3) (2016) 1138−1142, https://doi.org/10.1002/anie.201509758.
[374] H. Wang, H.W. Lee, Y. Deng, Z. Lu, P.C. Hsu, Y. Liu, D. Lin, Y. Cui, Bifunctional non-noble metal oxide nanoparticle electrocatalysts through lithium-induced conversion for overall water splitting, Nat. Commun. 6 (2015) 7261.
[375] Haiyuan Zou, Bowen He, Panyong Kuang, Jiaguo Yu, Ke Fan, Metal-organic framework-derived nickel-cobalt sulfide on ultrathin mxene nanosheets for electrocatalytic oxygen evolution, ACS Appl. Mater. Interfaces 10 (2018) 26.
[376] Yi Tang, C. Yang, Y. Yang, X. Yu, W. Que, J. Zhu, Three dimensional hierarchical network structure of S-$NiFe_2O_4$ modified few-layer titanium carbides (MXene) flakes on nickel foam as a high efficient electrocatalyst for oxygen evolution, Electrochim Acta 296 (2019) 762−770.
[377] H.W. Liang, W. Wei, Z.S. Wu, X. Feng, K. Müllen, Mesoporous metal-nitrogen-doped carbon electrocatalysts for highly efficient oxygen reduction reaction, J. Am. Chem. Soc. 135 (43) (2013) 16002−16005.
[378] L. Zilan, Z. Zechao, L. Fan, Z. Han, Z. Liang, L. Mingchuan, Z. Jiexin, L. Zhiquan, F. Shihao, C. Wei, The marriage of the FeN4 moiety and MXene boosts oxygen reduction catalysis: Fe 3d electron delocalization matters, Adv. Mater. 30 (2018), 1803220.
[379] X. Yu, W. Yin, T. Wang, Y. Zhang, Decorating g-C3N4 nanosheets with Ti3C2 MXene nanoparticles for efficient oxygen reduction reaction, Langmuir 35 (8) (2019).
[380] C. Cheng, Z. Xilin, F. Zhaoming, Y. Zongxian, Strong metal-support interactions impart activity in the oxygen reduction reaction: Au monolayer on Mo2C (MXene), J. Phys. Condens. Matter (2019) 475201页, 2018年30卷47期.
[381] R. Kang, A.D. Handoko, S.K. Nemani, B. Wyatt, W.S. Zhi, Rational design of two-dimensional transition metal carbide/nitride (MXene) hybrids and nanocomposites for catalytic energy storage and conversion, ACS Nano XXXX (XXX) (2020).
[382] N.P. Dileep, P.V. Sarma, R. Prasannachandran, V. Surendran, M.M. Shaijumon, Electrostatically coupled nanostructured Co(OH) 2 −MoS2 heterostructures for enhanced alkaline hydrogen evolution, ACS Appl. Nano Mater. 4 (7) (2021) 7206−7212.
[383] J. Ren, H. Zong, Y. Sun, S. Gong, Z. Zhu, 2D organ-like molybdenum carbide (MXene) coupled with MoS2 nanoflowers enhances catalytic activity in the hydrogen evolution reaction, CrystEngComm 22 (8) (2020).
[384] B. Sla, A. Js, B. Jg, Strategies to improve electrocatalytic and photocatalytic performance of two-dimensional materials for hydrogen evolution reaction, Chin. J. Catal. 42 (4) (2021) 511−556.
[385] D.A. Kuznetsov, Z. Chen, P.V. Kumar, A. Tsoukalou, C.R. Muller, Single site cobalt substitution in 2D molybdenum carbide (MXene) enhances catalytic activity in the hydrogen evolution reaction, J. Am. Chem. Soc. 2019 (2019). XXXX.
[386] A. Djire, H. Zhang, J. Liu, E.M. Miller, N.R. Neale, Electrocatalytic and optoelectronic characteristics of the two-dimensional titanium nitride Ti4N3Tx MXene, ACS Appl. Mater. Interfaces 11 (12) (2019).
[387] X. Xie, M.Q. Zhao, B. Anasori, K. Maleski, C.E. Ren, J. Li, B.W. Byles, E. Pomerantseva, G. Wang, Y. Gogotsi, Porous heterostructured MXene/carbon nanotube composite paper with high volumetric capacity for sodium-based energy storage devices, Nano Energy (2016) 513−523.
[388] C. Hao, Y. Wu, Y. An, B. Cui, J. Lin, X. Li, D. Wang, M. Jiang, Z. Cheng, S. Hu, Interface-coupling of CoFe-LDH on MXene as high-performance oxygen evolution catalyst, Materials Today Energy 12 (2019) 453−462.
[389] X.D. Zhu, Y. Xie, Y.T. Liu, Exploring the synergy of 2D MXene-supported black phosphorus quantum dots in hydrogen and oxygen evolution reactions, J. Mater. Chem. 6 (43) (2018).
[390] C.F. Du, K.N. Dinh, Q. Liang, Y. Zheng, Y. Luo, J. Zhang, Q. Yan, Self-assemble and in situ formation of Ni 1 x Fe x PS 3 nanomosaic-decorated MXene hybrids for overall water splitting, Adv. Energy Mater. 8 (26) (2018) 1801127.1−1801127.9.
[391] H. Wang, J.M. Lee, Recent advances in structural engineering of MXene electrocatalysts, J. Mater. Chem. 8 (2020).
[392] Y.N. Regmi, G.R. Waetzig, K.D. Duffee, S.M. Schmuecker, J.M. Thode, B.M. Leonard, Carbides of group IVA, VA and VIA transition metals as alternative HER and ORR catalysts and support materials, J. Mater. Chem. A. 3 (18) (2015) 10085−10091.
[393] W.T. Wang, N. Batool, T.H. Zhang, J. Liu, X.F. Han, J.H. Tian, R. Yang, When MOFs meet MXenes: superior ORR performance in both alkaline and acidic solutions, J. Mater. Chem. A 9 (2021) 3952−3960.

[394] Y. Liu, Y.H. Li, X. Li, Q. Zhang, F. Peng, Regulating electron-hole separation to promote photocatalytic H2 evolution activity of nanoconfined Ru/MXene/TiO2 catalysts, ACS Nano 14 (10) (2020) 14181–14189.
[395] A. Qurashi, Z. Zhang, M. Asif, T. Yamazaki, Template-less surfactant-free hydrothermal synthesis NiO nanoflowers and their photoelectrochemical hydrogen production, Int. J. Hydrogen Energy 40 (45) (2015) 15801–15805.
[396] Y. Liu, Y. Li, F. Peng, Y. Lin, S. Yang, S. Zhang, H. Wang, Y. Cao, H. Yu, 2H- and 1T- mixed phase few-layer MoS2 as a superior to Pt co-catalyst coated on TiO_2 nanorod arrays for photocatalytic hydrogen evolution, Appl. Catal. B Environ. 241 (2018) 236–245.
[397] R. Xiaoo, C. Zhao, Z. Zou, Z. Chen, L. Tian, H. Xu, H. Tang, Q. Liu, Z. Lin, X. Yang, In situ fabrication of 1D CdS nanorod/2D Ti_3C_2 MXene nanosheet Schottky heterojunction toward enhanced photocatalytic hydrogen evolution, Appl. Catal. B Environ. 268 (2020), 118382.
[398] T. Wang, Y. Chai, D. Ma, C. Wei, S. Huang, Multidimensional CdS nanowire/$CdIn_2S_4$ nanosheet heterostructure for photocatalytic and photoelectrochemical applications, Nano Res. 10 (2017) 2699–2711.
[399] K. Huang, C. Li, X. Meng, In-situ construction of ternary Ti3C2 MXene@TiO2/ZnIn2S4 composites for highly efficient photocatalytic hydrogen evolution, J. Colloid Interface Sci. 580 (2020).
[400] Q. Li, K. Lv, L. Mei, Heterojunction Construction between TiO2 Hollowsphere and ZnIn2S4 Flower for Photocatalysis Application, Appl. Surf. Sci. 398 (2017) 81–88.
[401] W.A. Hou, B. Ys, W.A. Yan, A. Wt, A. Sw, C. Xy, C. Gz, B. Zjx, B. Sl, W. Jia, Electrical promotion of spatially photoinduced charge separation via interfacial-built-in quasi-alloying effect in hierarchical Zn2In2S5/Ti3C2(O,OH)x hybrids toward efficient photocatalytic hydrogen evolution and environmental remediation, Appl. Catal. B Environ. 245 (2019) 290–301.
[402] S.M. Kang, M. Rethinasabapathy, S.K. Hwang, G.W. Lee, S.C. Jang, C.H. Kwak, S.R. Choe, Y.S. Huh, Microfluidic generation of prussian blue-laden magnetic micro-adsorbents for cesium removal, Chem. Eng. J. (2018). S1385894718302225.
[403] I. Lee, S.H. Kim, M. Rethinasabapathy, Y. Haldorai, G.W. Lee, S.R. Choe, S.C. Jang, S.M. Kang, Y.K. Han, C. Roh, Porous 3D Prussian blue/cellulose aerogel as a decorporation agent for removal of ingested cesium from the gastrointestinal tract, Sci. Rep. 8 (1) (2018) 4540.
[404] S.C. Jang, S.M. Kang, Y. Haldorai, K. Giribabu, G.W. Lee, Y.C. Lee, M.S. Hyun, Y.K. Han, C. Roh, S.H. Yun, Synergistically strengthened 3D micro-scavenger cage adsorbent for selective removal of radioactive cesium, Sci. Rep. 6 (2016) 38384.
[405] S. Ahmed, H.U. Rehman, Z. Ali, A. Qadeer, A. Haseeb, Z. Ajmal, Solvent assisted synthesis of hierarchical magnesium oxide flowers for adsorption of phosphate and methyl orange: kinetic, isotherm, thermodynamic and removal mechanism, Surface Interface. 23 (2021), 100953, https://doi.org/10.1016/j.surfin.2021.100953.
[406] Z. Ajmal, A. Muhmood, R. Dong, S. Wu, Probing the efficiency of magnetically modified biomass-derived biochar for effective phosphate removal, J. Environ. Manag. 253 (2020), 109730, https://doi.org/10.1016/j.jenvman.2019.109730.
[407] Z. Ajmal, A. Muhmood, M. Usman, S. Kizito, J. Lu, R. Dong, S. Wu, Phosphate removal from aqueous solution using iron oxides: adsorption, desorption and regeneration characteristics, J. Colloid Interface Sci. 528 (2018) 145–155, https://doi.org/10.1016/j.jcis.2018.05.084.
[408] Z. Ajmal, M. Usman, I. Anastopoulos, A. Qadeer, R. Zhu, A. Wakeel, R. Dong, Use of nano-/micro-magnetite for abatement of cadmium and lead contamination, J. Environ. Manag. 264 (2020), 110477, https://doi.org/10.1016/j.jenvman.2020.110477.
[409] Z. Ajmal, Y. Naciri, A. Hsini, B.M. Bresolin, A. Qadeer, M. Nauman, M. Arif, M.K. Irshad, K.A. Khan, R. Djellabi, C.L. Bianchi, M. Laabd, A. Albourine, R. Dong, Prospects of photocatalysis in the management of nitrate contamination in potable water, in: N.A. Oladoja, E.I. Unuabonah (Eds.), Progress and Prospects in the Management of Oxyanion Polluted Aqua Systems, Springer International Publishing, Cham, 2021, pp. 185–217, https://doi.org/10.1007/978-3-030-70757-6_7.
[410] S. Kizito, T. Lv, S. Wu, Z. Ajmal, H. Luo, R. Dong, Treatment of anaerobic digested effluent in biochar-packed vertical flow constructed wetland columns: role of media and tidal operation, Sci. Total Environ. 592 (2017) 197–205, https://doi.org/10.1016/j.scitotenv.2017.03.125.
[411] S. Kizito, H. Luo, S. Wu, Z. Ajmal, T. Lv, R. Dong, Phosphate recovery from liquid fraction of anaerobic digestate using four slow pyrolyzed biochars: dynamics of adsorption, desorption and regeneration, J. Environ. Manag. 201 (2017) 260–267, https://doi.org/10.1016/j.jenvman.2017.06.057.
[412] A. Essekri, A. Hsini, Y. Naciri, M. Laabd, Z. Ajmal, M. El Ouardi, A. Ait Addi, A. Albourine, Novel citric acid-functionalized brown algae with a high removal efficiency of crystal violet dye from colored wastewaters: insights into equilibrium, adsorption mechanism, and reusability, Int. J. Phytoremediation 23 (4) (2021) 336–346, https://doi.org/10.1080/15226514.2020.1813686.
[413] L. Brini, A. Hsini, Y. Naciri, A. Bouziani, Z. Ajmal, K. H'Maida, A. Boulahya, M. Arahou, B. Bakiz, A. Albourine, M. Fekhaoui, Synthesis and characterization of arginine-doped heliotrope leaves with high clean-up capacity for crystal violet dye from aqueous media, Water Sci. Technol. 84 (9) (2021) 2265–2277, https://doi.org/10.2166/wst.2021.446 %J Water Science and Technology.
[414] A. Qadeer, Z. Ajmal, M. Usman, X. Zhao, S. Chang, Agricultural plastic mulching as a potential key source of microplastic pollution in the terrestrial ecosystem and consequences, Resour. Conserv. Recycl. 175 (2021), 105855, https://doi.org/10.1016/j.resconrec.2021.105855.
[415] A. Hsini, Y. Naciri, M. Benafqir, Z. Ajmal, N. Aarab, M. Laabd, J.A. Navío, F. Puga, R. Boukherroub, B. Bakiz, A. Albourine, Facile synthesis and characterization of a novel 1,2,4,5-benzene tetracarboxylic acid doped polyaniline@zinc phosphate nanocomposite for highly efficient removal of hazardous hexavalent chromium ions from water, J. Colloid Interface Sci. 585 (2021) 560–573, https://doi.org/10.1016/j.jcis.2020.10.036.
[416] A. Hsini, Y. Naciri, M. Laabd, M. El Ouardi, Z. Ajmal, R. Lakhmiri, R. Boukherroub, A. Albourine, Synthesis and characterization of arginine-doped polyaniline/walnut shell hybrid composite with superior clean-up ability for chromium (VI) from aqueous media: equilibrium, reusability and process optimization, J. Mol. Liq. 316 (2020), 113832, https://doi.org/10.1016/j.molliq.2020.113832.
[417] A. Malik, M. Hussain, F. Uddin, W. Raza, S. Hussain, U.-e.- Habiba, T. Malik, Z. Ajmal, Investigation of textile dyeing effluent using activated sludge system to assess the removal efficiency, Water. Environ. Res. 93 (12) (2021) 2931–2940, https://doi.org/10.1002/wer.1639.
[418] A. Essekri, N. Aarab, A. Hsini, Z. Ajmal, M. Laabd, M. El Ouardi, A. Ait Addi, R. Lakhmiri, A. Albourine, Enhanced adsorptive removal of crystal violet dye from aqueous media using citric acid modified red-seaweed: experimental study combined with RSM process optimization, J. Dispersion Sci. Technol. (2020) 1–14, https://doi.org/10.1080/01932691.2020.1857263.
[419] A. Qadeer, Z.A. Saqib, Z. Ajmal, C. Xing, S. Khan Khalil, M. Usman, Y. Huang, S. Bashir, Z. Ahmad, S. Ahmed, K.H. Thebo, M. Liu, Concentrations, pollution indices and health risk assessment of heavy metals in road dust from two urbanized cities of Pakistan: comparing two sampling methods for heavy metals concentration, Sustain. Cities Soc. 53 (2020), 101959, https://doi.org/10.1016/j.scs.2019.101959.
[420] A. Qadeer, K.L. Kirsten, Z. Ajmal, X. Jiang, X. Zhao, Alternative plasticizers as emerging global environmental and health threat: another regrettable substitution? Environ. Sci. Technol. 56 (3) (2022) 1482–1488, https://doi.org/10.1021/acs.est.1c08365.
[421] P. Zhang, L. Wang, Z. Huang, J. Yu, W. Shi, Aryl diazonium-assisted amidoximation of MXene for boosting water stability and uranyl sequestration via electrochemical sorption, ACS Appl. Mater. Interfaces XXXX (XXX) (2020).
[422] I. Lee, S.M. Kang, S.C. Jang, G.W. Lee, H.E. Shim, M. Rethinasabapathy, C. Roh, Y.S. Huh, One-pot gamma ray-induced green synthesis of a Prussian blue-laden polyvinylpyrrolidone/reduced graphene oxide aerogel for the removal of hazardous pollutants, J. Mater. Chem. 7 (4) (2019) 1737–1748.
[423] S. Wu, T. Lv, Q. Lu, Z. Ajmal, R. Dong, Treatment of anaerobic digestate supernatant in microbial fuel cell coupled constructed wetlands: evaluation of nitrogen removal, electricity generation, and bacterial community response, Sci. Total Environ. 580 (2017) 339–346, https://doi.org/10.1016/j.scitotenv.2016.11.138.
[424] A. Qadeer, S. Liu, M. Liu, X. Liu, Z. Ajmal, Y. Huang, Y. Jing, S.K. Khalil, D. Zhao, D. Weining, X.-Y. Wei, Y. Liu, Historically linked residues profile of OCPs and PCBs in surface sediments of typical urban river networks, Shanghai: ecotoxicological state and sources, J. Clean. Prod. 231 (2019) 1070–1078, https://doi.org/10.1016/j.jclepro.2019.05.203.
[425] A.K. Fard, G. Mckay, R. Chamoun, T. Rhadfi, H. Preud'Homme, M.A. Atieh, Barium removal from synthetic natural and produced water using MXene as two dimensional (2-D) nanosheet adsorbent, Chem. Eng. J. 317 (Complete) (2017) 331–342.
[426] S. Li, L. Wang, J. Peng, M. Zhai, W. Shi, Efficient thorium(IV) removal by two-dimensional Ti 2 CT x MXene from aqueous solution, Chem. Eng. J. (2019).
[427] L. Brini, K. H'Maida, A. Imgharn, A. Hsini, Y. Naciri, Z. Ajmal, A. Bouziani, A. Boulahya, M. Arahou, B. Bakiz, A. Albourine, M. Fekhaoui, Synthesis and characterisation of PANI- coated Heliotrope Leaves (PANI@HL) with high clean-up capacity for Orange G dye from aqueous media, Int. J. Environ. Anal. Chem. (2021) 1–17, https://doi.org/10.1080/03067319.2021.1994557.
[428] B.M. Jun, M.P. Chang, J. Heo, Y. Yoon, Adsorption of Ba2+ and Sr2+ on Ti3C2Tx MXene in model fracking wastewater, J. Environ. Manag. 256 (2019), 109940.
[429] W. Mu, S. Du, Q. Yu, X. Li, H. Wei, Y. Yang, Improving barium ion adsorption on two-dimensional titanium carbide by surface modification, Dalton Trans. 47 (25) (2018) 8375–8381, https://doi.org/10.1039/C8DT00917A.
[430] K. Naito, T. Matsui, H. Nakahira, M. Kitagawa, H. Okada, Recovery and mutual separation of noble metals from the simulated insoluble residue of spent fuel, J. Nucl. Mater. 184 (1) (1991) 30–38.
[431] W. Mu, S. Du, X. Li, Q. Yu, S. Peng, Removal of radioactive palladium based on novel 2D titanium carbides, Chem. Eng. J. 358 (2018).
[432] A. Qadeer, K.L. Kirsten, Z. Ajmal, Z. Xingru, Rebuttal to comment on "alternative plasticizers as emerging global environmental and health threat: another regrettable substitution?" Focus on DINCH as an example, Environ. Sci. Technol. (2022), https://doi.org/10.1021/acs.est.2c01849.
[433] Z. Ajmal, M. Kashif Irshad, A. Qadeer, M. Zia Ul Haq, R. Ullah, M. Aqeel Sarwar, T. Saeed, M. Abid, A. Hayat, A. Ali, A. Noman, R. Dong, Novel magnetite nano-rods-modified biochar: a promising strategy to control lead mobility and transfer in soil-rice system, Int. J. Environ. Sci. Technol. (2022), https://doi.org/10.1007/s13762-022-04452-w.

[434] Z. Lu, Z. Hao, W. Jian, C. Lei, Efficient removal of europium from aqueous solutions using attapulgite-iron oxide magnetic composites, J. Ind. Eng. Chem. 34 (2016) 374–381.
[435] P. Zhang, L. Wang, L.-Y. Yuan, J.-H. Lan, Z.-F. Chai, W.-Q. Shi, Sorption of Eu(III) on MXene-derived titanate structures: the effect of nano-confined space, Chem. Eng. J. 370 (2019) 1200–1209, https://doi.org/10.1016/j.cej.2019.03.286.
[436] L. Wang, H. Song, L.Y. Yuan, Z. Li, W.Q. Shi, Effective removal of anionic Re(VII) by surface-modified Ti2CTx MXene nanocomposites: implications for Tc(VII) sequestration, Environ. Sci. Technol. 53 (7) (2019).
[437] M.R. Lukatskaya, O. Mashtalir, C.E. Ren, Y. Dall'Agnese, P. Rozier, P.L. Taberna, M. Naguib, P. Simon, M.W. Barsoum, Y. Gogotsi, Cation intercalation and high volumetric capacitance of two-dimensional titanium carbide, Science 341 (6153) (2013) 1502–1505.
[438] J. Come, J.M. Black, M.R. Lukatskaya, M. Naguib, N. Balke, Controlling the actuation Properties of MXene paper Electrodes upon cation intercalation, Nano Energy 17 (2015) 27–35.
[439] B.S. Shen, H. Wang, L.J. Wu, R.S. Guo, Q. Huang, X.B. Yanx, All-solid-state flexible microsupercapacitor based on two-dimensional titanium carbide, 中国化学快报：英文版 27 (10) (2016) 6.
[440] M.R. Lukatskaya, S.i. Bak, X. Yu, X.i. Yang, Y. Gogotsi, Probing the mechanism of high capacitance in 2D titanium carbide using in situ X-ray absorption spectroscopy, Adv. Energy Mater. 5 (15) (2015).
[441] Y. Dall'Agnese, M.R. Lukatskaya, K.M. Cook, P.-L. Taberna, Y. Gogotsi, P. Simon, High capacitance of surface-modified 2D titanium carbide in acidic electrolyte, Electrochem. Commun. 48 (2014) 118–122.
[442] O. Mashtalir, M.R. Lukatskaya, A. Kolesnikov, E. Raymundo-Pin?Ero, M. Naguib, M.W. Barsoum, Y. Gogotsi, The effect of hydrazine intercalation on the structure and capacitance of 2D titanium carbide (MXene), Nanoscale (2016) 9128–9133.
[443] M.A. Hope, A.C. Forse, K.J. Griffith, M.R. Lukatskaya, C.P. Grey, NMR reveals the surface functionalisation of Ti3C2 MXene, Phys. Chem. Chem. Phys. 18 (7) (2016).
[444] E. Soignard, O. Shebanova, P.F. Mcmillan, Compressibility measurements and phonon spectra of hexagonal transition-metal nitrides at high pressure: {epsilon}-TaN, {delta}-Mon, and Cr{sub 2}N, Phys. Rev. B 75 (75) (2007), 014104.
[445] O. Mashtalir, M.R. Lukatskaya, M.Q. Zhao, M.W. Barsoum, Y. Gogotsi, Amine-assisted delamination of Nb2C MXene for Li-ion energy storage devices, Adv. Mater. 27 (23) (2015) 3501–3506.
[446] F. Bonaccorso, L. Colombo, G. Yu, M. Stoller, V. Tozzini, A.C. Ferrari, R.S. Ruoff, V. Pellegrini, Graphene, related two-dimensional crystals, and hybrid systems for energy conversion and storage, Science 347 (6217) (2015), 41-41.
[447] C. Eames, I.M. Saiful, Ion intercalation into two-dimensional transition-metal carbides: global screening for new high-capacity battery materials, J. Am. Chem. Soc. 46 (14) (2015) 16270–16276.
[448] X. Yu, Y. Dall'Agnese, M. Naguib, Y. Gogotsi, P. Kent, Prediction and characterization of MXene nanosheet anodes for non-lithium-ion batteries, ACS Nano 8 (9) (2014) 9606–9615.
[449] X. Wang, S. Kajiyama, H. Iinuma, E. Hosono, S. Oro, I. Moriguchi, M. Okubo, A. Yamada, Pseudocapacitance of MXene nanosheets for high-power sodium-ion hybrid capacitors, Nat. Commun. 6 (2015) 6544.
[450] X. Liang, A. Garsuch, L.F. Nazar, Sulfur cathodes based on conductive MXene nanosheets for high-performance lithium–sulfur batteries, Angew. Chem. 54 (13) (2015) 3907–3911.
[451] Chu Liang, Xinyong Tao, Jun Zhang, Hui Huang, Jianmin Luo, Se4+ ion decorated highly conductive Ti3C2 MXene: promising lithium-ion anodes with enhanced volumetric capacity and cyclic performance, ACS Nano (2016).
[452] Y. Dall'Agnese, P.L. Taberna, Y. Gogotsi, P. Simon, Two-dimensional vanadium carbide (MXene) as positive electrode for sodium-ion capacitors, J. Phys. Chem. Lett. 6 (12) (2015) 2305–2309.
[453] J.W. Choi, D. Aurbach, Promise and reality of post-lithium-ion batteries with high energy densities, Nat. Rev. Mater. 1 (4) (2016), 16013.
[454] G.E. Blomgren, The development and future of lithium ion batteries, J. Electrochem. Soc. 164 (2016) A5019.
[455] G. Wang, X. Shen, J. Yao, J. Park, Graphene nanosheets for enhanced lithium storage in lithium ion batteries, Carbon 47 (8) (2009) 2049–2053.
[456] A. Kushwaha, M.K. Jangid, B.B. Bhatt, A. Mukhopadhyay, D. Gupta, Inkjet-printed environmentally friendly graphene film for application as a high-performance anode in Li-ion batteries, ACS Appl. Energy Mater. 4 (8) (2021).
[457] J. Nan, X. Guo, J. Xiao, X. Li, W. Chen, W. Wu, H. Liu, Y. Wang, M. Wu, G. Wang, Nanoengineering of 2D MXene-based materials for energy storage applications, Small (2019).
[458] H. Jiang, D. Ren, H. Wang, Y. Hu, S. Guo, H. Yuan, P. Hu, L. Zhang, C. Li, 2D monolayer MoS2–carbon interoverlapped superstructure: engineering ideal atomic interface for lithium ion storage, Adv. Mater. 27 (24) (2015) 3687–3695.
[459] X. Yu, C. Pei, W. Chen, L. Feng, 2 dimensional WS 2 tailored nitrogen-doped carbon nanofiber as a highly pseudocapacitive anode material for lithium-ion battery, Electrochim. Acta 272 (2018) 119–126.
[460] S. Wang, Y. Shi, C.-Y. Fan, J. Liu, Y. Li, X.-L. Wu, Layered G-C3N4@reduced graphene oxide composites as anodes with improved rate performance for lithium-ion batteries, ACS Appl. Mater. Interfaces 10 (2018) 36.
[461] Fan Zhimin, Wang Youshan, Duola Xie, Yuan Yin, Kang Hongjun, Modified MXene/holey graphene films for advanced supercapacitor electrodes with superior energy storage, Adv. Sci. (2018).
[462] Y. Zhu, W. Peng, Y. Li, G. Zhang, X. Fan, Multiple roles of heterointerface in two-dimensional van der Waals heterostructures: insights into energy-related applications, J. Mater. Chem. 7 (41) (2019).
[463] Chen Chi, Xie Xiuqiang, Anasori Babak, Sarycheva Asya, Makaryan Taron, MoS2-on-MXene heterostructures as highly reversible anode materials for lithium-ion batteries, Angew. Chem. (2017).
[464] S. Anwer, Y. Huang, B. Li, B. Govindan, L. Zheng, Nature-inspired, graphene-wrapped 3D MoS2 ultrathin microflower architecture as a high-performance anode material for sodium-ion batteries, ACS Appl. Mater. Interfaces 11 (25) (2019).
[465] T. Liu, Y. Zhang, Z. Jiang, X. Zeng, J. Ji, Z. Li, X. Gao, M. Sun, Z. Lin, M. Ling, Exploring competitive features of stationary sodium ion batteries for electrochemical energy storage, Energy Environ. Sci. 12 (5) (2019) 1512–1533.
[466] Y. Cao, L. Xiao, M.L. Sushko, W. Wang, B. Schwenzer, J. Xiao, Z. Nie, L.V. Saraf, Z. Yang, J. Liu, Sodium ion insertion in hollow carbon nanowires for battery applications, Nano Lett. 12 (7) (2012) 3783–3787.
[467] W. Kang, Y. Wang, J. Xu, Recent progress in layered metal dichalcogenide nanostructures as electrodes for high-performance sodium-ion batteries, J. Mater. Chem. (2017), 10.1039.C7TA00003K.
[468] S.M. Oh, J.Y. Hwang, C.S. Yoon, J. Lu, K. Amine, I. Belharouak, Y.K. Sun, High electrochemical performances of microsphere C-TiO2 anode for sodium-ion battery, ACS Appl. Mater. Interfaces 6 (14) (2014) 11295–11301.
[469] R. Pothu, A. Saran, P.K. Kalambate, R. Boddula, Book review: layered materials for energy storage and conversion, Curr. Anal. Chem. 16 (2) (2020).
[470] M.Q. Zhao, X. Xie, C.E. Ren, T. Makaryan, B. Anasori, G. Wang, Y. Gogotsi, Hollow MXene spheres and 3D macroporous MXene frameworks for Na-ion storage, Adv. Mater. 29 (37) (2017) 1702410.1–1702410.7.
[471] D. Xiong, X. Li, Z. Bai, S. Lu, Recent advances in layered Ti3C2Tx MXene for electrochemical energy storage, Small 14 (17) (2018).
[472] T. Yu, Z. Zhao, L. Liu, S. Zhang, G. Yang, TiC3 monolayer with high specific capacity for sodium-ion batteries, J. Am. Chem. Soc. 140 (18) (2018).
[473] P. Lian, Y. Dong, Z.-S. Wu, S. Zheng, X. Wang, S. Wang, C. Sun, J. Qin, X. Shi, X. Bao, Alkalized Ti3C2 MXene nanoribbons with expanded interlayer spacing for high-capacity sodium and potassium ion batteries, Nano Energy 40 (2017) 1–8.
[474] Sinho Choi, Song Chang, Guoxiu Wang, Hao Liu, Xin Guo, Sb2O3/MXene(-Ti3C2Tx) hybrid anode materials with enhanced performance for sodium-ion batteries, J. Mater. Chem. A Mater. Energy Sustain. (2017).
[475] X. Guo, X. Xie, S. Choi, Y. Zhao, H. Liu, C. Wang, S. Chang, G. Wang, Sb2O3/MXene(Ti3C2Tx) hybrid anode materials with enhanced performance for sodium-ion batteries, J. Mater. Chem. 5 (24) (2017) 12445–12452, https://doi.org/10.1039/C7TA02689G.
[476] S. Sun, Z. Xie, Y. Yan, S. Wu, Hybrid energy storage mechanisms for sulfur-decorated Ti3C2 MXene anode material for high-rate and long-life sodium-ion batteries, Chem. Eng. J. 366 (2019) 460–467.
[477] S. Kajiyama, L. Szabova, K. Sodeyama, H. Iinuma, R. Morita, K. Gotoh, Y. Tateyama, M. Okubo, A. Yamada, Sodium-ion intercalation mechanism in MXene nanosheets, ACS Nano 10 (3) (2016) 3334–3341.
[478] Z. Deng, Z. Zhang, Y. Lai, J. Liu, J. Li, Y. Liu, Electrochemical impedance spectroscopy study of a lithium/sulfur battery: modeling and analysis of capacity fading, J. Electrochem. Soc. 160 (4) (2013) A553.
[479] D. Zhao, R. Zhao, S. Dong, X. Miao, Z. Zhang, C. Wang, L. Yin, Alkali-induced 3D crinkled porous Ti_3C_2 MXene architectures coupled with NiCoP bimetallic phosphide nanoparticles as anodes for high-performance sodium-ion batteries, Energy Environ. Sci. 12 (8) (2019) 2422–2432.
[480] X. Li, H. Wu, A.M. Elshahawy, L. Wang, S.J. Pennycook, C. Guan, J. Wang, Cactus-like NiCoP/NiCo-OH 3D architecture with tunable composition for high-performance electrochemical capacitors, Adv. Funct. Mater. 28 (20) (2018), 1800036.
[481] Y. Tian, Y. An, Y. Yang, B. Xu, Robust nitrogen/selenium engineered MXene/ZnSe hierarchical multifunctional interfaces for dendrite-free zinc-metal batteries, Energy Storage Mater. 49 (2022) 122–134, https://doi.org/10.1016/j.ensm.2022.03.045.
[482] Y. Zhao, Y. Lu, H. Li, Y. Zhu, Y. Meng, N. Li, D. Wang, F. Jiang, F. Mo, C. Long, Y. Guo, X. Li, Z. Huang, Q. Li, J.C. Ho, J. Fan, M. Sui, F. Chen, W. Zhu, W. Liu, C. Zhi, Few-layer bismuth selenide cathode for low-temperature quasi-solid-state aqueous zinc metal batteries, Nat. Commun. 13 (1) (2022) 752, https://doi.org/10.1038/s41467-022-28380-y.
[483] J. Song, K. Xu, N. Liu, D. Reed, X. Li, Crossroads in the renaissance of rechargeable aqueous zinc batteries, Mater. Today 45 (2021) 191–212, https://doi.org/10.1016/j.mattod.2020.12.003.
[484] D. Han, Z. Wang, H. Lu, H. Li, C. Cui, Z. Zhang, R. Sun, C. Geng, Q. Liang, X. Guo, Y. Mo, X. Zhi, F. Kang, Z. Weng, Q.-H. Yang, A self-regulated interface toward highly reversible aqueous zinc batteries, Adv. Energy Mater. 12 (9) (2022), 2102982, https://doi.org/10.1002/aenm.202102982.
[485] Y. Yang, C. Liu, Z. Lv, H. Yang, Y. Zhang, M. Ye, L. Chen, J. Zhao, C.C. Li, Synergistic manipulation of Zn^{2+} ion flux and desolvation effect enabled by anodic growth of a 3D ZnF2 matrix for long-lifespan and dendrite-free Zn metal anodes, Adv. Mater. 33 (11) (2021), 2007388, https://doi.org/10.1002/adma.202007388.

[486] Y. Yang, C. Liu, Z. Lv, H. Yang, X. Cheng, S. Zhang, M. Ye, Y. Zhang, L. Chen, J. Zhao, C.C. Li, Redistributing Zn-ion flux by interlayer ion channels in Mg-Al layered double hydroxide-based artificial solid electrolyte interface for ultra-stable and dendrite-free Zn metal anodes, Energy Storage, Mater 41 (2021) 230–239, https://doi.org/10.1016/j.ensm.2021.06.002.
[487] Y. Tang, C. Liu, H. Zhu, X. Xie, J. Gao, C. Deng, M. Han, S. Liang, J. Zhou, Ion-confinement effect enabled by gel electrolyte for highly reversible dendrite-free zinc metal anode, Energy Storage, Mater 27 (2020) 109–116, https://doi.org/10.1016/j.ensm.2020.01.023.
[488] D. Han, S. Wu, S. Zhang, Y. Deng, C. Cui, L. Zhang, Y. Long, H. Li, Y. Tao, Z. Weng, Q.-H. Yang, F. Kang, A corrosion-resistant and dendrite-free zinc metal anode in aqueous systems, Small 16 (29) (2020), 2001736, https://doi.org/10.1002/smll.202001736.
[489] C. Li, X. Xie, S. Liang, J. Zhou, Issues and future perspective on zinc metal anode for rechargeable aqueous zinc-ion batteries, Energy Environ. Mater. 3 (2) (2020) 146–159, https://doi.org/10.1002/eem2.12067.
[490] S. Liu, H. Zhu, B. Zhang, G. Li, H. Zhu, Y. Ren, H. Geng, Y. Yang, Q. Liu, C.C. Li, Tuning the kinetics of zinc-ion insertion/extraction in V_2O_5 by in situ polyaniline intercalation enables improved aqueous zinc-ion storage performance, Adv. Mater. 32 (26) (2020), 2001113, https://doi.org/10.1002/adma.202001113.
[491] C. Deng, X. Xie, J. Han, Y. Tang, J. Gao, C. Liu, X. Shi, J. Zhou, S. Liang, A sieve-functional and uniform-porous kaolin layer toward stable zinc metal anode, Adv. Funct. Mater. 30 (21) (2020), 2000599, https://doi.org/10.1002/adfm.202000599.
[492] W. Du, E.H. Ang, Y. Yang, Y. Zhang, M. Ye, C.C. Li, Challenges in the material and structural design of zinc anode towards high-performance aqueous zinc-ion batteries, Energy Environ. Sci. 13 (10) (2020) 3330–3360, https://doi.org/10.1039/D0EE02079F.
[493] X. Li, M. Li, Q. Yang, D. Wang, L. Ma, G. Liang, Z. Huang, B. Dong, Q. Huang, C. Zhi, Vertically aligned Sn^{4+} preintercalated Ti_2CT_X MXene sphere with enhanced Zn ion transportation and superior cycle lifespan, Adv. Energy Mater. 10 (35) (2020), 2001394, https://doi.org/10.1002/aenm.202001394.
[494] Z. Chen, X. Li, D. Wang, Q. Yang, L. Ma, Z. Huang, G. Liang, A. Chen, Y. Guo, B. Dong, X. Huang, C. Yang, C. Zhi, Grafted MXene/polymer electrolyte for high performance solid zinc batteries with enhanced shelf life at low/high temperatures, Energy Environ. Sci. 14 (6) (2021) 3492–3501, https://doi.org/10.1039/D1EE00409C.
[495] X. Li, Q. Li, Y. Hou, Q. Yang, Z. Chen, Z. Huang, G. Liang, Y. Zhao, L. Ma, M. Li, Q. Huang, C. Zhi, Toward a practical Zn powder anode: Ti_3C_2Tx MXene as a lattice-match electrons/ions redistributor, ACS Nano 15 (9) (2021) 14631–14642, https://doi.org/10.1021/acsnano.1c04354.
[496] Y. Tian, Y. An, C. Wei, B. Xi, S. Xiong, J. Feng, Y. Qian, Flexible and free-standing Ti_3C_2Tx MXene@Zn paper for dendrite-free aqueous zinc metal batteries and nonaqueous lithium metal batteries, ACS Nano 13 (10) (2019) 11676–11685, https://doi.org/10.1021/acsnano.9b05599.
[497] Y. An, Y. Tian, C. Liu, S. Xiong, J. Feng, Y. Qian, Rational design of sulfur-doped three-dimensional Ti_3C_2Tx MXene/ZnS heterostructure as multifunctional protective layer for dendrite-free zinc-ion batteries, ACS Nano 15 (9) (2021) 15259–15273, https://doi.org/10.1021/acsnano.1c05934.
[498] Y. Tian, Y. An, C. Liu, S. Xiong, J. Feng, Y. Qian, Reversible zinc-based anodes enabled by zincophilic antimony engineered MXene for stable and dendrite-free aqueous zinc batteries, Energy Storage Mater. 41 (2021) 343–353, https://doi.org/10.1016/j.ensm.2021.06.019.
[499] Y. An, Y. Tian, Y. Li, C. Wei, Y. Tao, Y. Liu, B. Xi, S. Xiong, J. Feng, Y. Qian, Heteroatom-doped 3D porous carbon architectures for highly stable aqueous zinc metal batteries and non-aqueous lithium metal batteries, Chem. Eng. J. 400 (2020), 125843, https://doi.org/10.1016/j.cej.2020.125843.
[500] Y. An, Y. Tian, S. Xiong, J. Feng, Y. Qian, Scalable and controllable synthesis of interface-engineered nanoporous host for dendrite-free and high rate zinc metal batteries, ACS Nano 15 (7) (2021) 11828–11842, https://doi.org/10.1021/acsnano.1c02928.
[501] Y. An, Y. Tian, K. Zhang, Y. Liu, C. Liu, S. Xiong, J. Feng, Y. Qian, Stable Aqueous anode-free zinc batteries enabled by interfacial engineering, Adv. Funct. Mater. 31 (26) (2021), 2101886, https://doi.org/10.1002/adfm.202101886.
[502] Y. An, Y. Tian, Q. Man, H. Shen, C. Liu, Y. Qian, S. Xiong, J. Feng, Y. Qian, Highly reversible Zn metal anodes enabled by freestanding, lightweight, and zincophilic MXene/nanoporous oxide heterostructure engineered separator for flexible Zn-MnO_2 batteries, ACS Nano 16 (4) (2022) 6755–6770, https://doi.org/10.1021/acsnano.2c01571.
[503] H. Lin, S. Gao, C. Dai, Y. Chen, J. Shi, A two-dimensional biodegradable niobium carbide (MXene) for photothermal tumor eradication in NIR-I and NIR-II biowindows, J. Am. Chem. Soc. 139 (45) (2017) 16235–16247.
[504] C. Dai, H. Lin, G. Xu, Z. Liu, R. Wu, Y. Chen, Biocompatible 2D titanium carbide (MXenes) composite nanosheets for pH-responsive MRI-guided tumor hyperthermia, Chem. Mater. 29 (20) (2017) 8637–8652.
[505] C. Dai, Y. Chen, X. Jing, L. Xiang, D. Yang, H. Lin, Z. Liu, X. Han, R. Wu, Two-dimensional tantalum carbide (MXenes) composite nanosheets for multiple imaging-guided photothermal tumor ablation, ACS Nano 11 (12) (2017) 12696–12712.
[506] J. Zeng, D. Goldfeld, Y. Xia, A plasmon-assisted optofluidic (PAOF) system for measuring the photothermal conversion efficiencies of gold nanostructures and controlling an electrical switch, Angew. Chem. 125 (15) (2013) 4263–4267.
[507] C.M. Hessel, V.P. Pattani, M. Rasch, M.G. Panthani, B. Koo, J.W. Tunnell, B.A. Korgel, Copper selenide nanocrystals for photothermal therapy, Nano Lett. 11 (6) (2011) 2560–2566.
[508] H. Lin, Y. Wang, S. Gao, Y. Chen, J. Shi, Theranostic 2D tantalum carbide (MXene), Adv. Mater. 30 (4) (2018), 1703284.
[509] L. Zong, H. Wu, H. Lin, Y. Chen, A polyoxometalate-functionalized two-dimensional titanium carbide composite MXene for effective cancer theranostics, Nano Res. 11 (8) (2018) 4149–4168.
[510] W. Tang, Z. Dong, R. Zhang, X. Yi, K. Yang, M. Jin, C. Yuan, Z. Xiao, Z. Liu, L. Cheng, Multifunctional two-dimensional core–shell mxene@ gold nanocomposites for enhanced photo–radio combined therapy in the second biological window, ACS Nano 13 (1) (2018) 284–294.
[511] Q. Xue, H. Zhang, M. Zhu, Z. Pei, H. Li, Z. Wang, Y. Huang, Y. Huang, Q. Deng, J. Zhou, Photoluminescent Ti3C2 MXene quantum dots for multicolor cellular imaging, Adv. Mater. 29 (15) (2017), 1604847.
[512] L. Zhou, F. Wu, J. Yu, Q. Deng, F. Zhang, G. Wang, Titanium carbide (Ti3C2Tx) MXene: a novel precursor to amphiphilic carbide-derived graphene quantum dots for fluorescent ink, light-emitting composite and bioimaging, Carbon 118 (2017) 50–57.
[513] G. Liu, J. Zou, Q. Tang, X. Yang, Y. Zhang, Q. Zhang, W. Huang, P. Chen, J. Shao, X. Dong, Surface modified Ti3C2 MXene nanosheets for tumor targeting photothermal/photodynamic/chemo synergistic therapy, ACS Appl. Mater. Interfaces 9 (46) (2017) 40077–40086.
[514] X. Han, J. Huang, H. Lin, Z. Wang, P. Li, Y. Chen, 2D ultrathin MXene-based drug-delivery nanoplatform for synergistic photothermal ablation and chemotherapy of cancer, Adv. Healthcare Mater. 7 (9) (2018), 1701394.
[515] C. Xing, S. Chen, X. Liang, Q. Liu, M. Qu, Q. Zou, J. Li, H. Tan, L. Liu, D. Fan, Two-dimensional MXene (Ti3C2)-integrated cellulose hydrogels: toward smart three-dimensional network nanoplatforms exhibiting light-induced swelling and bimodal photothermal/chemotherapy anticancer activity, ACS Appl. Mater. Interfaces 10 (33) (2018) 27631–27643.
[516] Z. Li, H. Zhang, J. Han, Y. Chen, H. Lin, T. Yang, Surface nanopore engineering of 2D MXenes for targeted and synergistic multitherapies of hepatocellular carcinoma, Adv. Mater. 30 (25) (2018), 1706981.
[517] X. Han, X. Jing, D. Yang, H. Lin, Z. Wang, H. Ran, P. Li, Y. Chen, Therapeutic mesopore construction on 2D Nb2C MXenes for targeted and enhanced chemo-photothermal cancer therapy in NIR-II biowindow, Theranostics 8 (16) (2018) 4491.
[518] K. Rasool, K.A. Mahmoud, D.J. Johnson, M. Helal, G.R. Berdiyorov, Y. Gogotsi, Efficient antibacterial membrane based on two-dimensional Ti3C2Tx (MXene) nanosheets, Sci. Rep. 7 (1) (2017) 1–11.
[519] J. Halim, E.J. Moon, P. Eklund, J. Rosen, M.W. Barsoum, T. Ouisse, Variable range hopping and thermally activated transport in molybdenum-based MXenes, Phys. Rev. B 98 (10) (2018), 104202.
[520] X. Chen, X. Sun, W. Xu, G. Pan, D. Zhou, J. Zhu, H. Wang, X. Bai, B. Dong, H. Song, Ratiometric photoluminescence sensing based on Ti 3 C 2 MXene quantum dots as an intracellular pH sensor, Nanoscale 10 (3) (2018) 1111–1118.
[521] E.S. Muckley, M. Naguib, H.-W. Wang, L. Vlcek, N.C. Osti, R.L. Sacci, X. Sang, R.R. Unocic, Y. Xie, M. Tyagi, Multimodality of structural, electrical, and gravimetric responses of intercalated MXenes to water, ACS Nano 11 (11) (2017) 11118–11126.
[522] E. Lee, A. VahidMohammadi, B.C. Prorok, Y.S. Yoon, M. Beidaghi, D.-J. Kim, Room temperature gas sensing of two-dimensional titanium carbide (MXene), ACS Appl. Mater. Interfaces 9 (42) (2017) 37184–37190.
[523] P.A. Rasheed, R.P. Pandey, K. Rasool, K.A. Mahmoud, Ultra-sensitive electrocatalytic detection of bromate in drinking water based on Nafion/Ti3C2Tx (MXene) modified glassy carbon electrode, Sensor. Actuator. B Chem. 265 (2018) 652–659.
[524] S. Chertopalov, V.N. Mochalin, Environment-sensitive photoresponse of spontaneously partially oxidized Ti3C2 MXene thin films, ACS Nano 12 (6) (2018) 6109–6116.
[525] H. An, T. Habib, S. Shah, H. Gao, M. Radovic, M.J. Green, J.L. Lutkenhaus, Surface-agnostic highly stretchable and bendable conductive MXene multilayers, Sci. Adv. 4 (3) (2018), eaaq0118.
[526] Y.-Z. Zhang, K.H. Lee, D.H. Anjum, R. Sougrat, Q. Jiang, H. Kim, H.N. Alshareef, MXenes stretch hydrogel sensor performance to new limits, Sci. Adv. 4 (6) (2018), eaat0098.
[527] Y. Yue, N. Liu, W. Liu, M. Li, Y. Ma, C. Luo, S. Wang, J. Rao, X. Hu, J. Su, Z. Zhang, Q. Huang, Y. Gao, 3D hybrid porous Mxene-sponge network and its application in piezoresistive sensor, Nano Energy 50 (2018) 79–87, https://doi.org/10.1016/j.nanoen.2018.05.020.
[528] Y. Ma, N. Liu, L. Li, X. Hu, Z. Zou, J. Wang, S. Luo, Y. Gao, A highly flexible and sensitive piezoresistive sensor based on MXene with greatly changed interlayer distances, Nat. Commun. 8 (1) (2017) 1–8.
[529] N. Driscoll, A.G. Richardson, K. Maleski, B. Anasori, O. Adewole, P. Lelyukh, L. Escobedo, D.K. Cullen, T.H. Lucas, Y. Gogotsi, Two-dimensional Ti3C2 MXene for high-resolution neural interfaces, ACS Nano 12 (10) (2018) 10419–10429.
[530] L. Lorencova, T. Bertok, J. Filip, M. Jerigova, D. Velic, P. Kasak, K.A. Mahmoud, J. Tkac, Highly stable Ti3C2Tx (MXene)/Pt nanoparticles-modified glassy carbon electrode for H2O2 and small molecules sensing applications, Sensor. Actuator. B Chem. 263 (2018) 360–368.

[531] J. Zheng, B. Wang, A. Ding, B. Weng, J. Chen, Synthesis of MXene/DNA/Pd/Pt nanocomposite for sensitive detection of dopamine, J. Electroanal. Chem. 816 (2018) 189–194.
[532] H. Zhang, Z. Wang, Q. Zhang, F. Wang, Y. Liu, Ti3C2 MXenes nanosheets catalyzed highly efficient electrogenerated chemiluminescence biosensor for the detection of exosomes, Biosens. Bioelectron. 124 (2019) 184–190.
[533] S.J. Kim, H.J. Koh, C.E. Ren, O. Kwon, H.T. Jung, Metallic $Ti_3C_2T_x$ MXene gas sensors with ultrahigh signal-to-noise ratio, ACS Nano 12 (2) (2018).
[534] L. Lorencova, T. Bertok, E. Dosekova, A. Holazova, D. Paprckova, A. Vikartovska, V. Sasinkova, J. Filip, P. Kasak, M. Jerigova, Electrochemical performance of $Ti_3C_2T_x$ MXene in aqueous media: towards ultrasensitive H2O2 sensing, Electrochim. Acta 235 (2017) 471–479.
[535] E.S. Muckley, M. Naguib, I.N. Ivanov, Multi-modal, ultrasensitive, wide-range humidity sensing with Ti3C2 film, Nanoscale 10 (2018).
[536] E.S. Muckley, M. Naguib, H.-W. Wang, L. Vlcek, N.C. Osti, Multimodality of Structural, Electrical, and Gravimetric Responses of Intercalated MXenes to Water, ACS Nano 11 (11) (2017) 11118–11126.
[537] J. Heo, H. Kim, N. Her, S. Lee, Y.G. Park, Y. Yoon, Natural organic matter removal in single-walled carbon nanotubes–ultrafiltration membrane systems, Desalination 298 (none) (2012).
[538] K.H. Chu, M. Fathizadeh, M. Yu, J.R.V. Flora, A. Jang, M. Jang, C.M. Park, S.S. Yoo, N. Her, Y. Yoon, Evaluation of removal mechanisms in a graphene oxide coated ceramic ultrafiltration membrane for retention of natural organic matter, pharmaceuticals, and inorganic salts, ACS Appl. Mater. Interfaces (2017) acsami.7b14217.
[539] J.R. Werber, C.O. Osuji, M. Elimelech, Materials for next-generation desalination and water purification membranes, Nat. Rev. Mater. 1 (5) (2016), 16018.
[540] K.H. Chu, Y. Huang, M. Yu, J. Heo, J. Flora, A. Jang, M. Jang, C. Jung, C.M. Park, D.H. Kim, Evaluation of graphene oxide-coated ultrafiltration membranes for humic acid removal at different pH and conductivity conditions, Separ. Purif. Technol. 181 (2017) 139–147.
[541] H. Sun, B. Tang, P. Wu, Development of hybrid ultrafiltration membranes with improved water separation properties using modified superhydrophilic metal-organic framework nanoparticles, ACS Appl. Mater. Interfaces (2017), 21473.
[542] Y. Mo, X. Zhao, Y.-x. Shen, Cation-dependent structural instability of graphene oxide membranes and its effect on membrane separation performance, Desalination 399 (2016) 40–46.
[543] R. Pandey, K. Rasool, V. Madhavan, B. Aissa, Y. Gogotsi, Ultrahigh-flux and fouling-resistant membranes based on layered silver/MXene (Ti3C2Tx) nanosheets, J. Mater. Chem. A (2018).
[544] J. Zhu, J. Hou, A. Uliana, Y. Zhang, M. Tian, B. Bruggen, The rapid emergence of two-dimensional nanomaterials for high-performance separation membranes, J. Mater. Chem. 6 (2018).
[545] Ding Li, Wei Yanying, Wang Yanjie, Chen Hongbin, Caro Jürgen, A two-dimensional lamellar membrane: MXene nanosheet stacks, Angew. Chem. Int. Ed. 56 (2016).
[546] K. Rasool, K.A. Mahmoud, D.J. Johnson, M. Helal, Y. Gogotsi, Efficient antibacterial membrane based on two-dimensional Ti3C2Tx (MXene) nanosheets, Sci. Rep. 7 (1) (2017).
[547] K.M. Kang, D.W. Kim, C.E. Ren, K.M. Cho, S.J. Kim, J. Choi, Y.T. Nam, Y. Gogotsi, H.T. Jung, Selective molecular separation on Ti3C2tx-graphene oxide membranes during pressure-driven filtration: comparison with graphene oxide and MXenes, ACS Appl. Mater. Interfaces 9 (2017) 44687–44694, acsami.7b10932.
[548] L. Tang, K.J.T. Livi, K.L. Chen, Polysulfone membranes modified with bioinspired polydopamine and silver nanoparticles formed in situ to mitigate biofouling, Environ. Sci. Technol. Lett 2 (2015) 59–65.
[549] F. Guo, G. Silverberg, S. Bowers, S.P. Kim, D. Datta, V. Shenoy, R.H. Hurt, Graphene-based environmental barriers, Environ. Sci. Technol. 46 (14) (2012) 7717.
[550] Y. Huang, H. Li, L. Wang, Y. Qiao, M. Yu, Ultrafiltration membranes with structure-optimized graphene-oxide coatings for antifouling oil/water separation, Adv. Mater. Interfac. 2 (2) (2014).
[551] Z. Ajma, M.u. Haq, Y. Naciri, R. Djellabi, N. Hassan, S. Zaman, A. Murtaza, A. Kumar, A.G. Al-Sehemi, H. Algarni, O.A. Al-Hartomy, R. Dong, A. Hayat, A. Qadeer, Recent advancement in conjugated polymers based photocatalytic technology for air pollutants abatement: cases of CO_2, NOx, and VOCs, Chemosphere 308 (2022), 136358, https://doi.org/10.1016/j.chemosphere.2022.136358.
[552] J. Li, S. Wang, Y. Du, W. Liao, Enhanced photocatalytic performance of TiO_2@C nanosheets derived from two-dimensional Ti_2CT_x, Ceram. Int. 44 (2018).
[553] K. Ullah, Z.D. Meng, S. Ye, L. Zhu, W.C. Oh, Synthesis and characterization of novel PbS–graphene/TiO_2 composite with enhanced photocatalytic activity, J. Ind. Eng. Chem. 20 (3) (2014) 1035–1042.
[554] L. Yang, M. Yao, A. Zhou, Q. Hu, L. Wang, Preparation and photocatalytic performance of Ti_3C_2/TiO_2/CuO ternary nanocomposites, J. Nanomater. 2017 (2017) 1–5, 2017,(2017-4-3).
[555] H.G. Shiraz, O. Tavakoli, Investigation of graphene-based systems for hydrogen storage, Renew. Sustain. Energy Rev. 74 (2017) 104–109.
[556] M. Gaboardi, N. Sarzi-Amadé, M. Aramini, C. Milanese, D. Pontiroli, Extending the hydrogen storage limit in fullerene, Carbon 120 (2017) 77–82.
[557] S.J. Park, S.Y. Lee, Hydrogen storage behaviors of platinum-supported multi-walled carbon nanotubes, Int. J. Hydrogen Energy 35 (23) (2010) 13048–13054.
[558] A. Ahmed, S. Seth, J. Purewal, A.G. Wong-Foy, M. Veenstra, A.J. Matzger, D.J. Siegel, Exceptional hydrogen storage achieved by screening nearly half a million metal-organic frameworks, Nat. Commun. 10 (1) (2019).
[559] A. Schneemann, J.L. White, S.Y. Kang, S. Jeong, L.F. Wan, E.S. Cho, T.W. Heo, D. Prendergast, J.J. Urban, B.C. Wood, Nanostructured metal hydrides for hydrogen storage, Chem. Rev. 118 (2018).
[560] Q. Hu, D. Sun, Q. Wu, H. Wang, L. Wang, B. Liu, A. Zhou, J. He, MXene: a new family of promising hydrogen storage medium, J. Phys. Chem. 117 (51) (2013), 14253.
[561] G.J. Kubas, Dihydrogen complexes as prototypes for the coordination chemistry of saturated molecules, Proc. Natl. Acad. Sci. U. S. A 38 (17) (2010) no-no.
[562] N.C. Osti, M. Naguib, M. Tyagi, Y. Gogotsi, E. Mamontov, Evidence of molecular hydrogen trapped in two-dimensional layered titanium carbide-based MXene, Phys. Rev. Mater. 1 (2) (2017), 024004.
[563] Q. Hu, D. Sun, Q. Wu, H. Wang, L. Wang, B. Liu, A. Zhou, J. He, MXene: a new family of promising hydrogen storage medium, J. Phys. Chem. A 117 (51) (2013) 14253–14260, https://doi.org/10.1021/jp409585v.
[564] A. Yadav, A. Dashora, N. Patel, A. Miotello, M. Press, D.C. Kothari, Study of 2D MXene Cr_2C material for hydrogen storage using density functional theory, Appl. Surf. Sci. 389 (2016) 88–95, https://doi.org/10.1016/j.apsusc.2016.07.083.
[565] R. Wu, H. Du, Z. Wang, M. Gao, H. Pan, Y. Liu, Remarkably improved hydrogen storage properties of NaAlH4 doped with 2D titanium carbide, J. Power Sources 327 (2016) 519–525.
[566] Y. Liu, H. Du, Z. Xin, Y. Yang, M. Gao, H. Pan, Superior catalytic activity derived from a two-dimensional Ti_3C_2 precursor towards the hydrogen storage reaction of magnesium hydride, Chem. Commun. 52 (2015).
[567] Z. Shen, Z. Wang, Z. Min, M. Gao, J. Hu, D. Fang, Y. Liu, H. Pan, A novel solid-solution MXene $(Ti_{0.5}V_{0.5})_3C_2$ with high catalytic activity for hydrogen storage in MgH_2, Materialia 1 (2018) 114–120. S2589152918300073-.
[568] G. Chen, Y. Zhang, H. Cheng, Y. Zhu, L. Li, H. Lin, Effects of two-dimension MXene Ti3C2 on hydrogen storage performances of MgH2-LiAlH4 composite, Chem. Phys. (2019).
[569] K. Xian, M. Gao, Z. Li, J. Gu, H. Pan, Superior kinetic and cyclic performance of a 2D titanium carbide incorporated 2LiH+MgB2 composite towards highly reversible hydrogen storage, ACS Appl. Energy Mater. 2 (7) (2019) 4853–4864.
[570] F.O. Perreault, F. Andreia, M. Elimelech, Environmental applications of graphene-based nanomaterials, Chem. Soc. Rev. 44 (16) (2015) 5861–5896.
[571] S. Park, K.M. Yeon, S. Moon, J.O. Kim, Enhancement of operating flux in a membrane bio-reactor coupled with a mechanical sieve unit, Chemosphere 191 (Jan) (2017) 573–579.
[572] K. Krishnamoorthy, M. Veerapandian, L.H. Zhang, K. Yun, S.J. Kim, Antibacterial efficiency of graphene nanosheets against pathogenic bacteria via lipid peroxidation, J. Phys. Chem. C 116 (32) (2012) 17280–17287.
[573] Y. Cui, Z. Zhang, B. Li, R. Guo, X. Zhang, X. Cheng, M. Xie, Q. Cheng, Ultrasound assisted fabrication of AgBr/TiO 2 nano-tube arrays photoelectrode and its enhanced visible photocatalytic performance and mechanism for detoxification of 4-chlorphenol, Separ. Purif. Technol. 197 (2018) 189–196.
[574] D.Y. Koseoglu-Imer, B. Kose, M. Altinbas, I. Koyuncu, The production of polysulfone (PS) membrane with silver nanoparticles (AgNP): physical properties, filtration performances, and biofouling resistances of membranes, J. Membr. Sci. 428 (2013) 620–628.
[575] K. Rasool, M. Helal, A. Ali, C. Ren, Y. Gogotsi, K.A. Mahmoud, Antibacterial activity of $Ti_3C_2T_x$ MXene, ACS Nano 10 (2016) 3674.